

HIGH DENSITY NOBLE GAS DETECTORS  
AND  
SEARCH FOR MASSIVE NEUTRINOS IN THE  $\beta$ -DECAY OF  $^{35}\text{S}$

Thesis by  
David A. Imel

In Partial Fulfillment of the Requirements  
for the Degree of  
Doctor of Philosophy

California Institute of Technology  
Pasadena, California

1990

(Submitted May 23, 1990)

## Acknowledgments

First, I wish to thank Professor Felix Boehm for his guidance and support throughout my graduate studies. His encouragement and advice have been crucial to my education here.

I am grateful to Petr Vogel for being a continual source of information on the theoretical background of this thesis, as well as providing helpful criticism of the experiments.

I have enjoyed the friendship and advice of the entire Physics 34 research group, but am especially in debt to Mrs. Elsa Garcia and Mr. Herb Henrikson.

I wish particularly to thank Jim Thomas and Hans-Werner Becker, who served as my mentors and from whom I have learned much about the experiments described. Their patience and ability to teach a junior physicist is dearly appreciated.

I gratefully acknowledge the financial support of the Department of Energy and the California Institute of Technology.

Eloisa, my wife, has patiently stood with me during my studies at Caltech. I am, and will continue to be throughout my life, grateful for her love and understanding.

My parents have not only been the source of my desire to study physics, but have continued to encourage me in the pursuit of science, and it is to them that I dedicate this thesis.

Finally, to the Lord Jesus Christ, the Son of God, I give thanks for all things.

## Abstract

This thesis is divided into two parts. In Part I, I present a series of studies of high density noble gas detectors, the goal of which was to determine the feasibility of a  $^{136}\text{Xe}$   $\beta\beta$ -decay detector. The limitations of liquid, high pressure and solid xenon and argon detectors are described in detail, and it is shown that initial recombination of  $\delta$ -electrons provides the ultimate limit to energy resolution in the condensed media. Ionization spectra in solid xenon are presented for the first time.

Part II describes an experiment which uses the Caltech iron-free double-focusing  $\beta$ -spectrometer to test the possible admixture of a heavy neutrino in the  $\beta$ -spectrum of  $^{35}\text{S}$ . Preliminary data with a statistical uncertainty of  $3\times 10^{-3}$  are presented and show that the  $\beta$ -spectrum is consistent with the allowed shape. Although the data are not accurate enough to verify or deny the existence of the 17 keV neutrino postulated by Simpson, data runs are underway which should clearly confirm it or rule it out.

## Contents

<b>Acknowledgments</b>	<b>ii</b>
<b>Abstract</b>	<b>iii</b>
<b>Contents</b>	<b>iv</b>
<b>Part I</b>	<b>1</b>
<b>1 Introduction</b>	<b>2</b>
1.1 The Xenon Detector	2
1.2 $\beta\beta$ -Decay	4
1.3 Summary of Part One	10
<b>2 A Liquid Ionization Chamber</b>	<b>13</b>
2.1 Introduction	13
2.2 Apparatus	13
2.3 Performance	21
2.4 Summary	33
<b>3 A High Pressure Ionization Chamber</b>	<b>36</b>
3.1 Introduction	36
3.2 Design and Construction	40
3.3 Performance	47
3.4 Conclusions	61
<b>4 A Solid Xenon Ionization Chamber</b>	<b>62</b>

4.1 Motivation	62
4.2 Principles of Operation for a Radial Ionization Chamber	64
4.3 The Experimental Apparatus	70
4.4 Performance	82
4.5 Conclusions	98
<b>5 Conclusions</b>	<b>102</b>
<b>A Derivation of the Recombination Model</b>	<b>106</b>
<b>B Energy Resolution and <math>\delta</math>-Electron Recombination</b>	<b>121</b>
B.1 Introduction	121
B.2 Sources of Energy Resolution Degradation	122
B.3 $\delta$ -Electron Production and the Statistics of Charge Collection	130
B.4 Conclusions	146
<b>C Spectra from High Pressure Ionization Chambers</b>	<b>149</b>
C.1 Argon Spectra	149
C.2 Xenon Spectra	152
C.3 Improving Energy Resolution by Field Shaping	154
<b>D Spectra from Radial Ionization Chambers</b>	<b>161</b>
D.1 Introduction	161
D.2 0.3 M Detector with Argon	161
D.3 0.3 M Detector with Xenon	177

D.4 0.9 M Detector with a Small Anode Wire	182
D.5 0.9 M detector with Argon	191
D.6 0.9 M Detector with Xenon	201
<b>References (Part I)</b>	<b>217</b>
<b>Part II</b>	<b>222</b>
<b>1 Introduction</b>	<b>223</b>
1.1 Neutrino Mass	223
1.2 Previous Limits	227
1.3 Experimental Considerations	228
1.4 Evidence for a 17 keV Neutrino	229
1.5 Exclusions of the 17 keV Neutrino	232
1.6 Remarks on the Experiments	236
<b>2 Apparatus</b>	<b>238</b>
2.1 Spectrometer	239
2.2 Source	240
2.3 Detector and Electronics	242
2.4 Power Supply and Stability	244
2.5 Spectrometer Settings	245
2.6 Earth Field	250
<b>3 Data</b>	<b>251</b>
3.1 Calibration	251

3.2 $^{35}\text{S}$ Spectrum	256
<b>4 Discussion</b>	<b>259</b>
4.1 Discussion of Data	259
4.2 Analysis Procedure	261
4.3 Outlook	263
<b>References (Part II)</b>	<b>264</b>

# **PART I**

**HIGH DENSITY NOBLE GAS DETECTORS**



## CHAPTER ONE

### Introduction

#### 1.1 The Xenon Detector

The noble gases argon and xenon are known to be important detector media in nuclear and particle physics<sup>1</sup>. In addition, xenon appears to be a promising detector medium for  $\gamma$ -ray astronomy<sup>2,3</sup> as well as for  $\beta\beta$ -decay<sup>4-6</sup>. While argon at low and moderate densities has been widely used as a detector gas in proportional counters and ionization chambers, much less is known about the properties and suitability of high density argon and xenon detectors for particles or radiation. Although we have been primarily interested in the development of high density xenon ionization chambers for  $\beta\beta$ -decay, we have also conducted research on high density argon since it serves as an inexpensive test gas.

Because of its large cross section for photoabsorption<sup>7</sup>, xenon ( $Z = 54$ ) is an ideal detector for high energy  $\gamma$ -rays. With the density<sup>8</sup> of condensed xenon ranging from about  $2.8 \text{ g/cm}^3$  to about  $3.7 \text{ g/cm}^3$ , depending on pressure and temperature, a condensed xenon detector has a large stopping power.

The average energy,  $W$ , required to create an ion-electron pair from condensed xenon has been measured<sup>9</sup> to be 15.6 eV. (In argon<sup>10</sup> it is 23.3 eV.) Thus, a 1 MeV electron should generate about 64,000 ion-electron pairs. The Fano factor<sup>11</sup>, which expresses the deviation from Poisson statistics in the amount of fluctuation in the charge created, has been estimated<sup>10</sup> in xenon to

be between 0.04 and 0.06. Thus the fluctuation in the number of ion-electron pairs generated by a 1 MeV electron should be less than about 60 pairs. (See appendix B for more detail.) If all of the electrons were collected, the energy resolution (full-width at half-maximum height of the peak, or FWHM) of a detector which converts charge to an energy signal would be about 0.2%, or 2 keV, which is comparable to the energy resolution obtained with a germanium detector. Thus, one might expect that xenon would provide a detector with the energy resolution of a germanium detector, but with increased efficiency and decreased cost.

Two of the naturally occurring isotopes in xenon may decay via  $\beta\beta$ -decay. In fact,  $^{136}\text{Xe}$ , which has a natural abundance of 8.9% (and can be obtained enriched to 90% or higher), has a relatively high endpoint energy for the decay, making it a favored candidate for a  $\beta\beta$ -decay experiment using xenon as both the source and the detector.

When beginning this thesis research on xenon, the intended goal of the studies on high density xenon counters was the investigation of the two modes of  $\beta\beta$ -decay in  $^{136}\text{Xe}$ . As the work progressed it was found that the resolution of 0.2% at 1 MeV cannot be attained. The research into the resolution and other properties of high density xenon counters was then chosen as Part I of this thesis, while the  $\beta\beta$ -decay research was postponed. Nevertheless, in order to document the original goal, a brief introduction to  $\beta\beta$ -decay will be presented.

## 1.2 $\beta\beta$ -Decay

### *Description*

$\beta\beta$ -decay<sup>12,13</sup> may occur in two modes, the so-called  $2\nu$  and  $0\nu$  modes. The labels refer to the number of neutrinos emitted in the decay. For  $2\nu$   $\beta\beta$ -decay:



and for the  $0\nu$  mode:



The  $2\nu$  mode is a standard model process, a second-order electroweak decay, and must occur. The  $0\nu$  mode, where a “virtual” neutrino emitted by one neutron stimulates the decay of a second neutron in the nucleus, can only occur if the neutrino is the same as its antiparticle, i.e., if the neutrino is a Majorana particle. In addition, this decay may only take place if the neutrino has a non-zero mass, since a neutrino with left-handed helicity is emitted, but a neutrino with right-handed helicity is absorbed. In fact,  $0\nu$   $\beta\beta$ -decay may be the most sensitive test for neutrino mass.

The shapes of the electron spectra for the two modes are quite different, since the electrons share the decay energy with the neutrinos in the  $2\nu$  mode, but in the  $0\nu$  mode the electrons get all of the energy. Since neutrinos are not

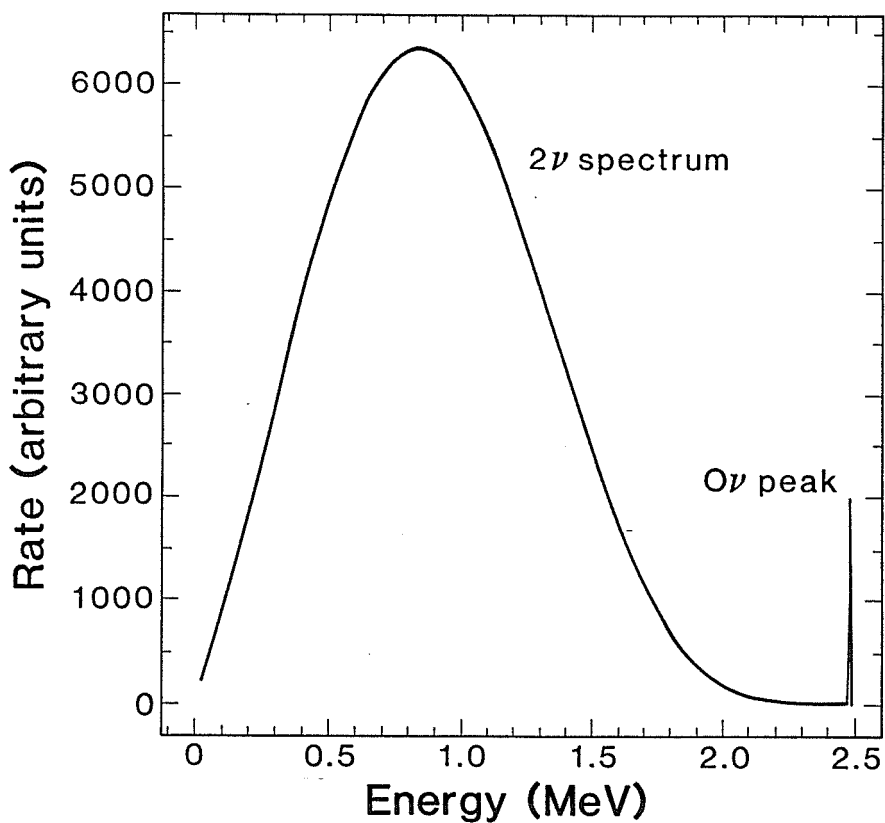


Figure 1-1. Electron-sum energy spectrum for  $^{136}\text{Xe}$   $\beta\beta$ -decay. The relative rates of the  $0\nu$  and  $2\nu$  modes shown here are arbitrarily chosen.

detected by ordinary detectors, only the energy carried by the electrons is seen. Fig. 1-1 shows the shape of the electron-sum energy spectrum for the  $2\nu$  and  $0\nu$  modes. (The protons take up the recoil momentum of the decay, but their kinetic energy is clearly negligible compared to that of the electrons and neutrinos.)

*Lifetimes*

The rates for the  $0\nu$  and  $2\nu$  modes of  $\beta\beta$ -decay may be calculated. For the  $2\nu$  mode, the lifetime  $\Gamma$  is given by<sup>12,13</sup>:

$$\Gamma^{-1} = G^{2\nu} \left| M_{GT}^{2\nu} - \frac{g_V^2}{g_A^2} M_F^{2\nu} \right|^2 \quad (1-3)$$

where  $G$  is the contribution from the phase space of the decay, and  $M_F$  and  $M_{GT}$  are the Fermi and Gamow-Teller matrix elements, respectively. Similarly, for the  $0\nu$  mode,

$$\Gamma^{-1} = G^{0\nu} \left| M_{GT}^{0\nu} - \frac{g_V^2}{g_A^2} M_F^{0\nu} \right|^2 < m_\nu >^2 \quad (1-4)$$

where  $< m_\nu >$  is a parameter which is approximately proportional to the mass of the neutrino.

Mode	$G^{-1}$ (years)	Predicted Lifetime (years)
$2\nu$	$2.07 \times 10^{17}$	$8 \times 10^{20}$
$0\nu$	$5.52 \times 10^{24}$	$1 - 6 \times 10^{25}$

Table 1-1. Estimated lifetimes for  $\beta\beta$ -decay in  $^{136}\text{Xe}$ . The predicted lifetime entries are based on the matrix element calculations of Vogel *et al*<sup>14</sup>., and the entry for the  $0\nu$  mode lifetime assumes a Majorana neutrino mass of 1 eV.

Although the phase space factors,  $G$ , may be calculated exactly, the nuclear matrix calculations are uncertain. The most recent estimates<sup>14</sup> by Vogel *et al.* for the  $2\nu$  mode matrix elements are listed for xenon in Table 1-1, as are the phase space factors for xenon. Since the phase space contribution to the rate depends on the eleventh power of the endpoint energy of the decay for the  $2\nu$  mode, and the fifth power for the  $0\nu$  mode, it is advantageous to choose an isotope with a fairly large endpoint energy.  $^{136}\text{Xe}$  has an endpoint energy of 2.479 MeV, which is somewhat larger than that of  $^{76}\text{Ge}$  (2.040 MeV) for which the most sensitive tests<sup>15</sup> for  $0\nu \beta\beta$ -decay have been carried out.

Case of  $^{136}\text{Xe}$

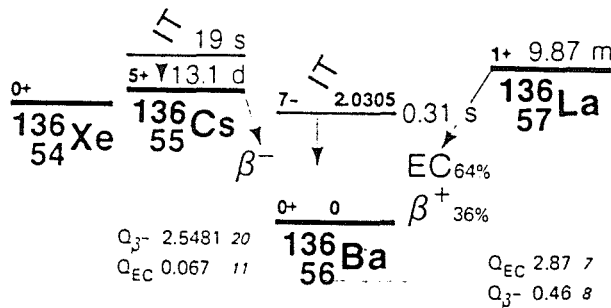


Figure 1-2. Energy diagram<sup>16</sup> for mass  $A = 136$ . The single  $\beta$ -decay of  $^{136}\text{Xe}$  to  $^{136}\text{Cs}$  is clearly energetically forbidden.

With lifetimes of greater than  $10^{20}$  years, in order to observe  $\beta\beta$ -decay one must of course choose an isotope where the single  $\beta$ -decay is suppressed. The best way to do this is to choose candidates where the single  $\beta$ -decay is energetically forbidden. This is the case for  $^{136}\text{Xe}$ , illustrated in Fig. 1-2. A complete list of candidates may be found in Boehm and Vogel<sup>13</sup>.

### *Experiments and Limits*

Until recently,  $\beta\beta$ -decay had only been observed in geochemical<sup>17</sup> experiments. However, the group at UC Irvine reports<sup>18</sup> the observation of  $\beta\beta$ -decay in the  $2\nu$  mode for  $^{82}\text{Se}$  with a lifetime of  $10^{20}$  years.

To date, the most sensitive limit on  $0\nu$   $\beta\beta$ -decay has been obtained with high purity, low background germanium detectors. Several groups have competitive  $^{76}\text{Ge}$   $\beta\beta$ -decay experiments, and the best half-life limit at the present time<sup>15</sup> is about  $10^{24}$  years, which corresponds to a limit on Majorana neutrino mass of approximately 2 to 5 eV.

$\beta\beta$ -decay has not yet been observed in either mode for xenon, although several groups<sup>4-6</sup> have built detectors with xenon. Three are notable. Barabash *et al*<sup>4</sup>. use a high pressure ionization chamber at 25 atm of xenon and obtain a lower limit of  $8 \times 10^{17}$  years for the  $2\nu$  mode and  $3 \times 10^{21}$  years for the  $0\nu$  mode. Their experimental sensitivity is limited by contamination of radon from the purification process for xenon.

The group at Milano<sup>5</sup> is using a multi-wire proportional chamber to obtain two-dimensional track information along with the energy spectrum. The sensitivity of this experiment is also limited by radon background from the titanium vessel used to contain the 10 atm of xenon. Their half-life limit for the  $0\nu$  mode is  $10^{22}$  years.

A Caltech-Neuchatel-SIN collaboration is installing a time projection chamber filled with 5 atm of xenon in the St. Gotthard tunnel in Switzerland<sup>15</sup>. The time projection chamber provides energy information and three-dimensional tracking information, as well as a unique signature for  $\beta\beta$ -decay:

as the two electrons emitted in the decay lose energy, their rate of energy loss increases, as does the magnitude of the average angle through which they are scattered. This leads to a high charge density region (called a “charge blob”) at the end of each electron track. A good  $\beta\beta$ -decay event is one in which there is one extended electron track with a charge blob at each end. This detector will be filled alternately with 60% enriched and depleted  $^{136}\text{Xe}$ , and should be sensitive<sup>6</sup> to a  $0\nu$  lifetime of about  $10^{24}$  years.

#### *Parameters for an Experiment*

There are several considerations in designing a xenon ionization chamber for  $\beta\beta$ -decay. One must have a sufficient number of candidate atoms, at least one mole, in the active volume of the detector. The detector must be stable and noise-free. One would like to be able to see the  $0\nu$  peak if it occurs, so that energy resolution as high as possible is desired. To detect  $0\nu$   $\beta\beta$ -decay, energy resolution of  $\sim 2\%$  should be achieved at the endpoint, whereas for the  $2\nu$  mode, energy resolution as poor as 20% may be sufficient.

In order to detect a few events in a year, one must completely reduce all backgrounds in the detector. For cosmic rays this is most easily done by going far underground, although a surface experiment may be done with much less precision using an active cosmic ray veto. External  $\gamma$ -ray backgrounds may be shielded, but the detector itself must be constructed of very low background materials.

Neutrons are also a troublesome background, both thermal and those from cosmic ray reactions. Thermal neutrons give the reaction:





where  $^{137}\text{Xe}$  is a  $\beta$ -emitter<sup>16</sup> with a Q-value of about 3 MeV. Cosmogenic reactions<sup>19</sup> in materials like copper are also an experimental hazard.

Because the primary, and perhaps only, information from an ionization chamber is the total energy deposited in the detector, there is no way to distinguish these background events from  $\beta\beta$ -decay events, other than the shape of the energy spectrum. In contrast to tracking detectors, which suppress backgrounds by  $dE/dx$  and position information, the ionization chamber must minimize backgrounds by being constructed of low background materials, being heavily shielded from external backgrounds and presenting a low cross-sectional area for external background fluxes. The feasibility of an ionization chamber  $\beta\beta$ -decay experiment depends critically on the above background minimization and the ability of the detector to discern the shape of the  $\beta\beta$ -decay energy spectrum.

### 1.3 Summary of Part One

#### *Liquid Ionization Chamber*

Since previous experiments<sup>20</sup> were limited by the purity of the media used, we built an ultra-pure liquid xenon and liquid argon ionization detector<sup>21</sup>, hoping to observe the high energy resolution expected in these detectors. We discovered instead that the energy resolution of condensed noble gas detectors is limited by the initial recombination<sup>22,23</sup> of high charge density regions produced in the detector by  $\delta$ -electrons. Chapter 2 details the liquid ionization detector, appendix A gives the derivation of our recombination model and

appendix B applies that recombination model to the problem of energy resolution in condensed noble gas detectors. We proposed<sup>23</sup> several ways to reduce the recombination strength of these detectors and so increase the energy resolution.

### *High Pressure Ionization Chamber*

One of the most promising ways to decrease the recombination strength was to increase the separation between atoms in the medium. This was accomplished by lowering the density of the medium, making the liquid into a high pressure gas. We built an ionization detector<sup>24</sup> to test the performance of high pressure argon and xenon gas. We found that the recombination strength was indeed lower in the high pressure gas, and that the energy resolution in high pressure argon was limited only by capacitive and electronic noise and by the statistics of charge production.

However, we found that high pressure xenon was much more sensitive to the presence of electronegative impurities in the detector. Although the performance of the high pressure argon in the same detector was stable over several hours, the xenon spectra showed marked deterioration after just a few minutes. Thus, we found the detector unsuitable for a high energy resolution  $\beta\beta$ -decay experiment in xenon. Chapter 3 describes the high pressure ionization chamber and its performance, and appendix C details spectra from this detector and suggests a possible general improvement for stable, low purity ionization chambers.

### *Radial Ionization Chamber with Liquid and Solid*

Although a  $0\nu$  experiment could not be feasible in liquid or solid xenon because of the difficulties in obtaining high energy resolution, a  $2\nu$  experiment might be possible. We built a radial ionization chamber<sup>25</sup>, taking advantage of the cancellation of the increase in charge induced as electrons are drifted towards the central anode with the decrease in charge as electrons are attached and recombined in the non-uniform electric field of this detector to build a chamber without a grid. This allowed us to test the performance of solid argon and xenon. This is the first time ionization spectra have been reported in solid xenon. The energy resolution obtained in this case was about 16% FWHM, which is marginally sufficient to do a  $2\nu$  experiment in xenon. Chapter 4 describes the radial ionization chamber and appendix D reports the spectra from several studies of this detector.

### *Conclusion*

We have explored the possibility of using solid, liquid and high pressure xenon ionization chambers to detect the  $\beta\beta$ -decay of  $^{136}\text{Xe}$ . We have developed a model to describe initial recombination in these detectors and have successfully applied this model to the problem of energy resolution in condensed noble gas detectors. Although the performance of the high pressure argon detector is excellent, we have found that the energy resolution of condensed and high pressure xenon is insufficient to compensate for the poor background suppression inherent in these detectors. We expect that the 5 atm time projection chamber being installed in the St. Gotthard tunnel will provide a better measurement of the  $\beta\beta$ -decay lifetimes of  $^{136}\text{Xe}$ .

## CHAPTER TWO

### A Liquid Ionization Chamber

#### 2.1 Introduction

A review of the history of liquid ionization detectors is given in Lindblad *et al*<sup>26</sup>. As discussed in chapter one, liquid xenon should be a good detector medium, with energy resolution as good as 2 keV FWHM. Nevertheless, Edmiston and Gruhn<sup>20</sup> and Masuda *et al.*<sup>27</sup> have achieved energy resolutions of only 30 keV and 70 keV FWHM at 1 MeV in LAr and LXe, respectively, and these results have not changed dramatically with improved apparatus.<sup>26,28</sup> We built a liquid xenon and liquid argon ionization chamber to test these limits. We show here that energy resolution significantly better than this cannot be achieved for practical electric drift field strengths. This chapter provides the experimental details and data of the liquid xenon and argon detector work published by us (Imel and Thomas, Nucl. Instrum. Methods, A273, 291, 1988).

#### 2.2 Apparatus

##### *Gas-Handling System*

The experimental apparatus is shown in Figs. 2-1, 2-2 and 2-3. Fig. 2-1 depicts the chamber housing the detector and the gas purification system. The chamber and ion pump have a combined volume of 25 liters. All materials used inside the chamber are high vacuum materials such as stainless steel,

oxygen-free high-conductivity (OFHC) copper, high vacuum epoxy and Macor machinable glass ceramic.

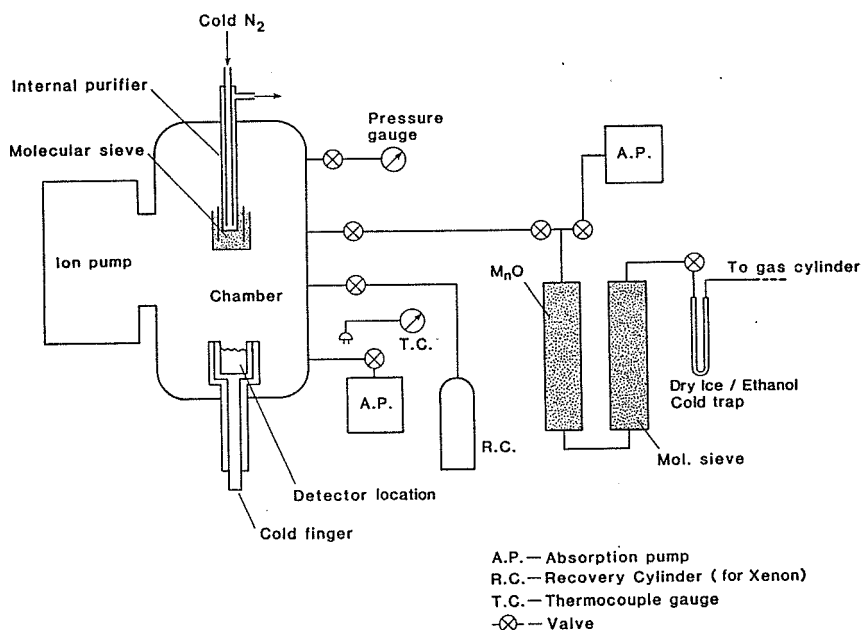


Figure 2-1. The chamber, detector cryostat, and gas-purification system.

The gas purification system consists of a cold trap cooled by dry ice and ethanol and filled with molecular sieve,<sup>29</sup> and purification towers containing MnO and molecular sieve. The towers were kept at room temperature. MnO is used to remove O<sub>2</sub> from the gas and the sieve captures residual water. The MnO was prepared by mixing manganese oxalate in a dispersing agent and then activated by flowing H<sub>2</sub> through the tower while baking it at 300°C. Once activated, the MnO changes color from black to green. The system can be

reactivated with H<sub>2</sub> whenever it becomes saturated with O<sub>2</sub>.

### *Preparation*

Great care was taken in cleaning the chamber and detector. Prior to construction, all metallic parts were etched using standard acid solutions, all Macor parts were etched in Dichrol, and all non-metallic parts were ultrasonically cleaned in methanol. The chamber was baked at 100 °C for 48 hours using a LN<sub>2</sub> cooled sorption pump and then baked into an ion pump at 50-80 °C for a week. In this way we were able to clean the chamber and the molecular sieve filled internal purifier so that a pressure of  $1 \times 10^{-8}$  torr could be maintained at room temperature.

The internal purifier was used as the final stage of purification for the xenon or argon gas. (See Fig. 2-1.) It was driven by cold nitrogen gas flowing through the cold finger. The xenon (or argon) condenses on the finger and then drips into the cup containing cold molecular sieve. Once the cup overflows, the liquid evaporates and the gas circulates through the purifier again.

### *Operation*

In order to condense liquid into the detector cryostat, the cold finger at the bottom of the chamber was cooled (see Fig. 2-2) using LN<sub>2</sub> to condense argon or isopentane (2-methylbutane) to condense xenon. To refrigerate the isopentane, we used a coil of copper tubing, through which cold nitrogen gas flowed at a controlled rate. Using a cold finger (as opposed to submerging the entire chamber) greatly reduced microphonic noise.

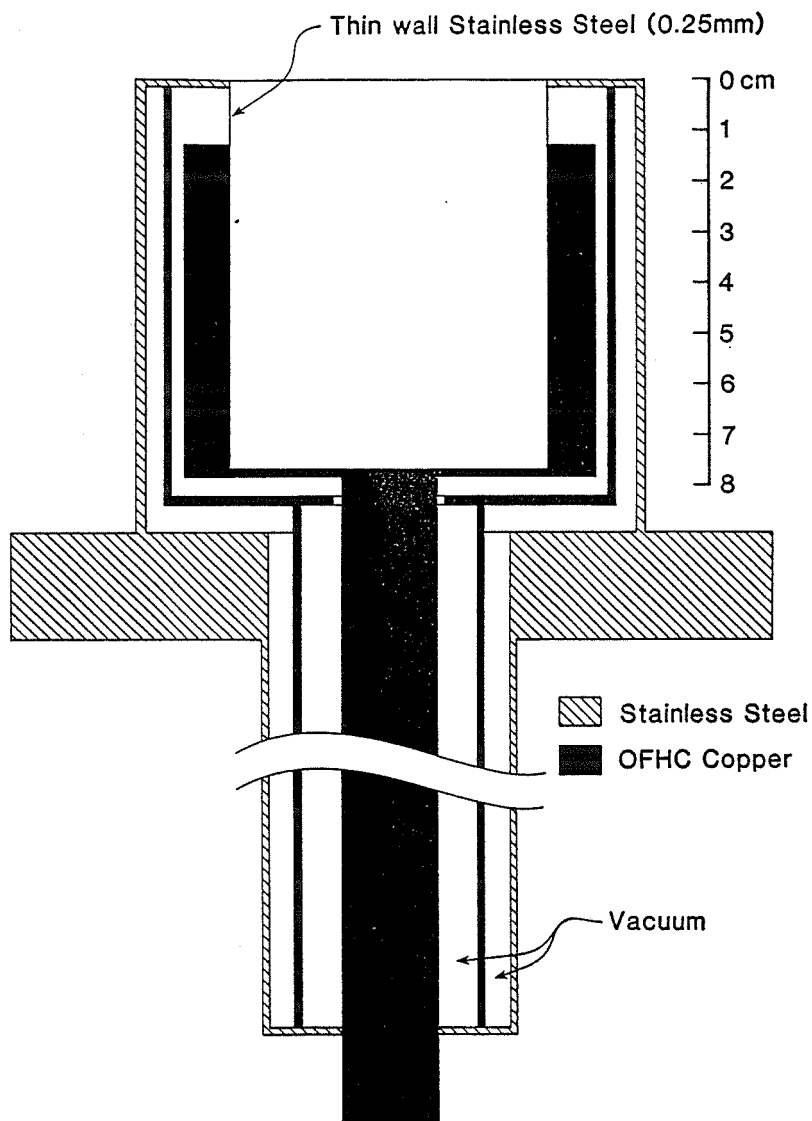
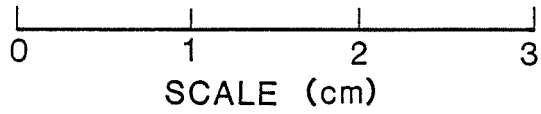
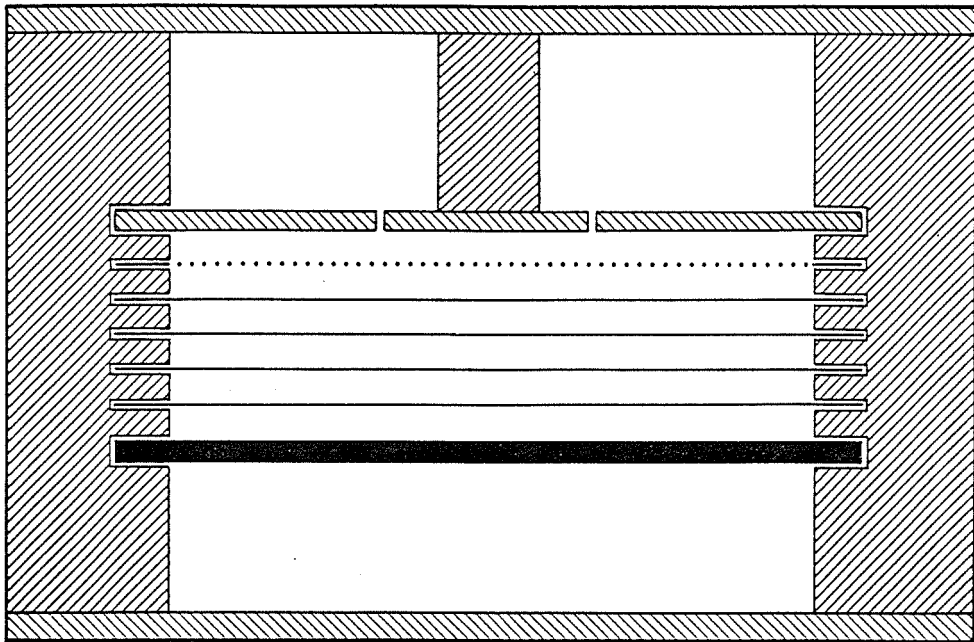


Figure 2-2. The detector cryostat is a double walled dewar which is cooled by liquid nitrogen or cold isopentane. The inner dewar wall serves to cool the top of the outer dewar, reducing thermal losses via the outer wall, and a thin stainless steel wall between the detector cup and the outer wall further reduces these thermal losses. The detector cup has 1 cm thick copper walls to reduce the vertical thermal gradients.






-  MACOR Machinable Glass
-  Stainless Steel
-  OFHC Copper

Figure 2-3(a). Schematic diagram of the ionization detector with the segmented anode, the Frisch grid, and the guard rings shown. The outer stainless steel plates are merely for mechanical support.



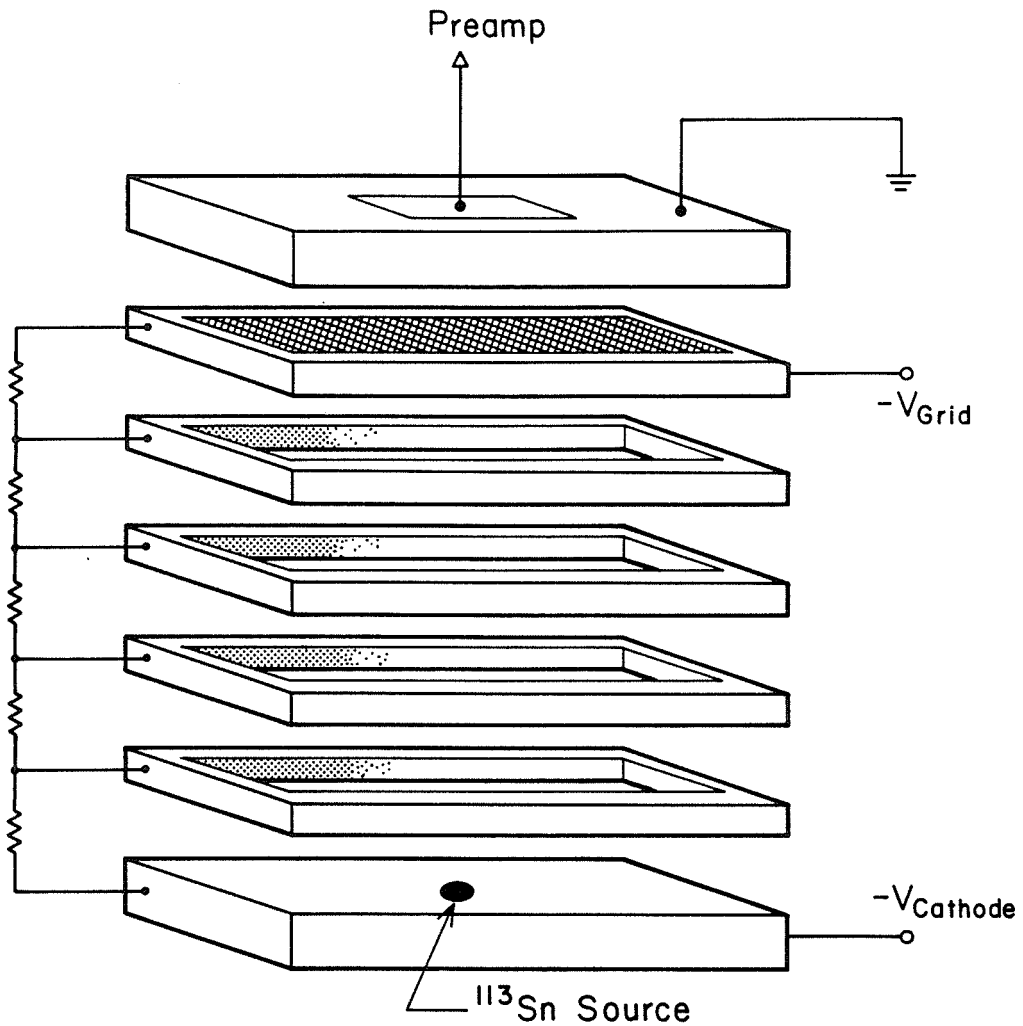


Figure 2-3(b). Exploded schematic of detector, not to scale.

### *Detector*

The detector is shown in Fig. 2-3. Fig. 2-4 is a picture of an earlier version of our detector which is similar to the one in Fig. 2-3. It is a gridded ionization chamber with a stainless steel segmented anode, four stainless steel field shaping rings, and an OFHC copper cathode upon which was plated a  $^{113}\text{Sn}$  source.

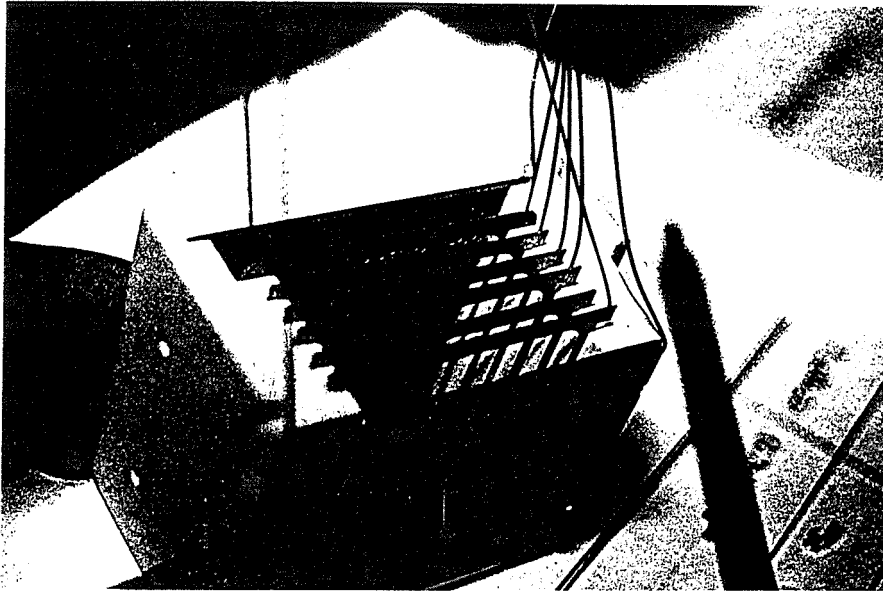


Figure 2-4. Picture of an earlier model of the detector. The Macor housing, field-gradient rings and grid (an older mesh than that discussed in the text) are shown. In this model, the anode and cathode were not shielded as in the schematic of Fig. 2-3.

(See Table 2-1.) The  $^{113}\text{Sn}$  source was prepared by electroplating a  $\text{SnCl}_4$  solution containing  $^{113}\text{Sn}$  onto the cathode. It was then diffused into the cathode by baking for two hours at  $200^\circ\text{C}$ . Finally it was sanded and acid etched in  $\text{HCl}$  to ensure that the source was as clean as the other parts of the detector and chamber. A  $\text{Si}(\text{Li})$  spectrum obtained from that source is shown in Fig. 2-5.

A chain of metal film resistors coated with high-vacuum epoxy keeps the field gradient rings at their appropriate potentials in order to ensure field uniformity. The resistor leads were stripped of their tin coating and were etched in  $\text{HCl}$ . The resistors themselves were ultrasonically cleaned in methanol and then checked to ensure that they were uniform in resistance to within 0.5%.

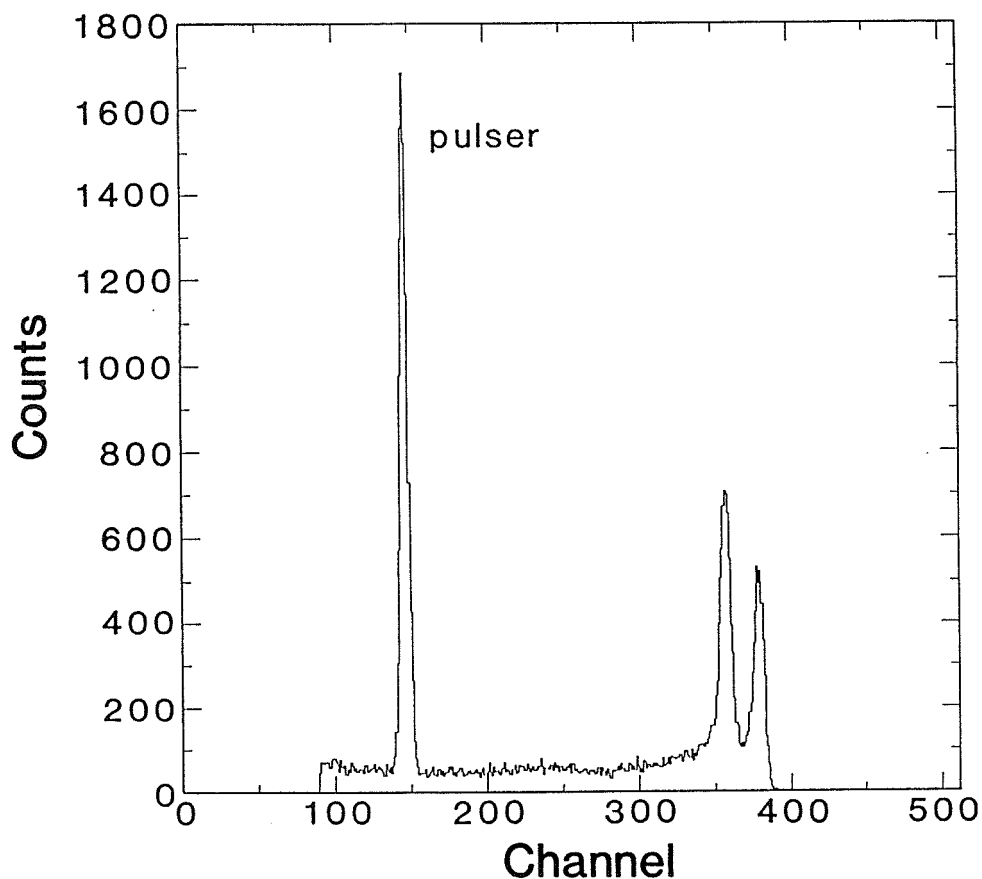


Figure 2-5. Cooled Si(Li) detector spectrum of the  $^{113}\text{Sn}$  source used in this experiment. The peak near channel 150 is a pulser peak.

The grid was formed by spot welding a 3 cm x 3 cm square of electroformed Nickel mesh<sup>30</sup> onto one of the stainless steel field gradient rings. The mesh spacing is 220  $\mu\text{m}$  and the mesh wire diameter is 36  $\mu\text{m}$ . Typical drift fields are 1 kV/cm, and the ratio of the field in the grid-anode region to the drift field is 5 : 1 to ensure charge transmission through the grid. (See Figs. 2-11 and 2-12 and the discussion in section 2.3.) The plates and rings are 3 cm x 3 cm, and the drift distance from cathode to grid is 1 cm. The spacing between rings is 2 mm,

and the active region of the anode is the central 1 cm<sup>2</sup>.

### *Electronics*

The anode is connected to a room temperature preamplifier (EG&G Ortec 142A) immediately outside the chamber. The preamplifier pulses are shaped and amplified by a spectroscopy amplifier and fed into a multi-channel pulse-height analyzer, and the spectra are stored on a computer. Typical shaping times are 2  $\mu$ s. We use a pulser to measure the contribution of the electronic noise to the width of the signal, and to assist in calibration. The calibration was accomplished by using the same electronics with a cooled Si(Li) detector and assuming an average pair creation energy of 3.6 eV for silicon.<sup>31</sup> (We assume that the pair creation energies for LXe and LAr are 15.6 eV and 23.3 eV, respectively.<sup>9,10</sup>) The absolute charge calibrations are uncertain by  $\pm 5\%$ .

## **2.3 Performance**

### *<sup>113</sup>Sn Spectra*

Spectra in liquid xenon and liquid argon are shown in Figs. 2-6 and 2-7. A spectrum taken at a field strength of only 25 volts/cm in liquid xenon is shown in Fig. 2-8, and illustrates the extreme purity of our detector media by the ability of the detector to drift electrons at extremely low voltages.

### *Charge Collection and Energy Resolution*

In order to measure the intrinsic resolution of the detector, we compared the observed signal to the convolution of the expected spectrum shape and detector response functions. To calculate the relative intensities of the two

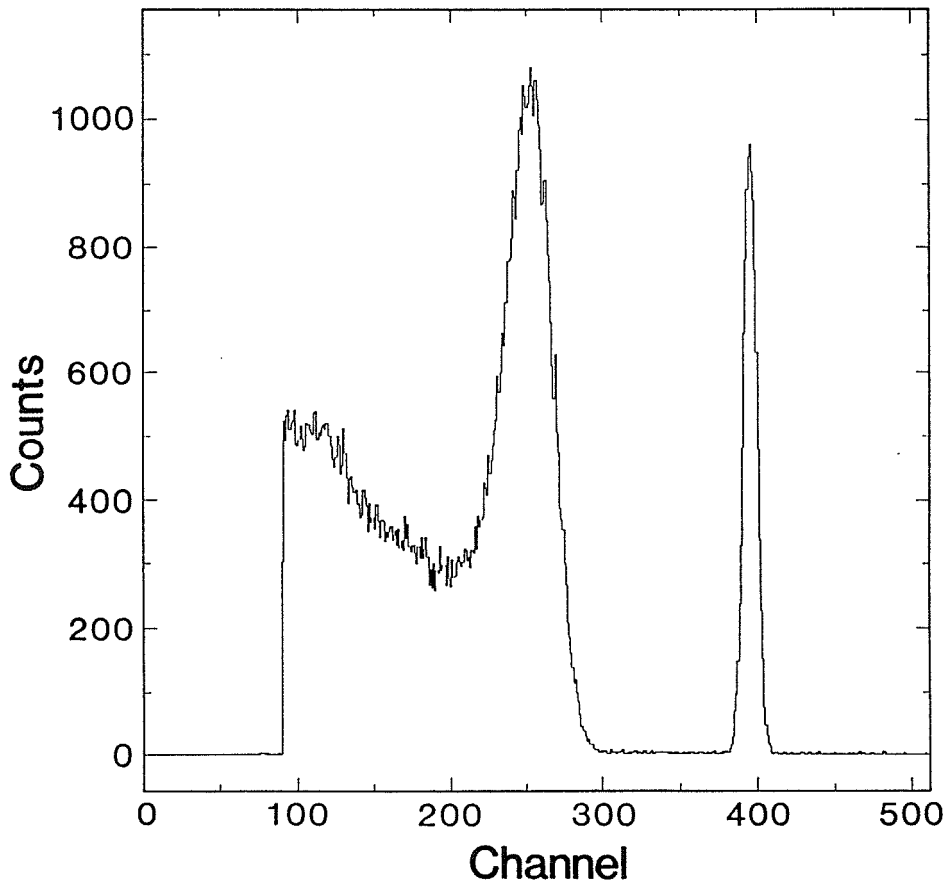


Figure 2-6. Typical MCA spectrum for the liquid xenon detector. The lower energy peak is composed of the two  $^{113}\text{Sn}$  lines at 384 keV, and the other peak is a pulser peak.

peaks in xenon or argon, we include the ratio of conversion electrons to  $\gamma$ -rays emitted by the source and the efficiency of the detector for absorption of both the  $\gamma$ -ray and the x-ray. (See Table 2-1.) The efficiency for absorption of a 392 keV  $\gamma$ -ray is estimated to be about 3% in liquid argon and 14% in liquid xenon,<sup>7</sup> and the efficiency for the absorption of the 24 keV and 4 keV x-rays following conversion electron emission is 100% in both liquids. (We lose 50% of these x-rays due to solid angle, assuming isotropic x-ray emission.) The range<sup>32</sup>

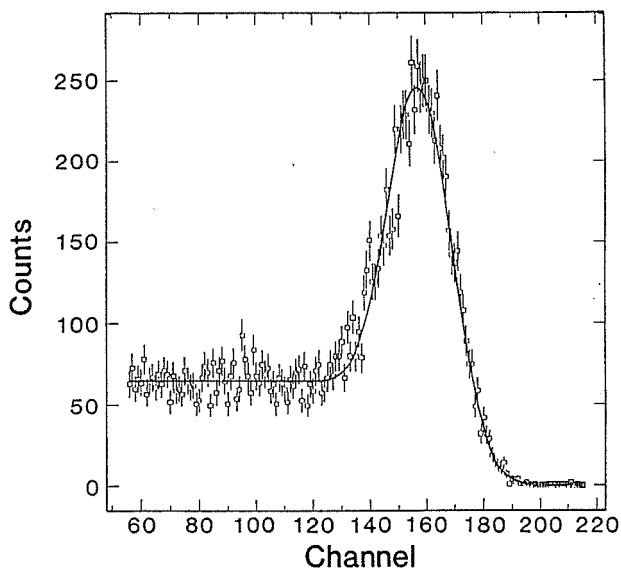


Figure 2-7. Fit to a typical  $^{113}\text{Sn}$  spectrum observed in liquid argon. The fit takes into account the presence of two peaks. (See text.) The fitted energy resolution is 14% FWHM, or 13% if the pulser width is subtracted in quadrature.

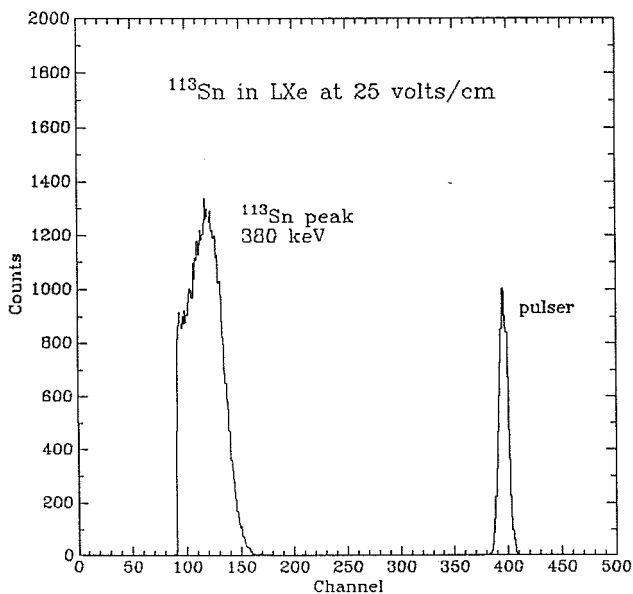


Figure 2-8. Energy spectrum of  $^{113}\text{Sn}$  taken in liquid xenon at an electric drift field strength of only 25 volts/cm. The grid-anode to drift field ratio is 5 : 1 here as in all other spectra shown in this chapter.

of the 364 keV and 388 keV conversion electrons<sup>16</sup> is less than the length of the inner anode segment, so all of the electrons are captured in the active region of the detector. Thus, the ratio of the peak at 364 keV to the full energy (392 keV) peak is 1 : 2.3 in liquid argon and 1 : 3.4 in liquid xenon.

<sup>113</sup> Sn source		LAr	LXe
Full energy	(391.7 keV)	55.2	100.0
e <sub>L</sub>	(387.6 keV)	38.4	38.4
e <sub>K</sub>	(363.8 keV)	40.6	40.6
Effective range of e <sub>K</sub>		0.8 mm	0.4 mm

Table 2-1. The estimated relative intensities of the lines from the <sup>113</sup>Sn source in the detector are tabulated. The source strength was 0.1 μCi and half-life was 115.1 days. It was electroplated onto the cathode in a spot less than 1 mm in diameter. The full energy peak consists of absorption of the γ-rays and the coincident capture of the conversion electrons and their respective x-rays.

We fit our observed spectra in argon with a pair of Gaussian peaks superimposed on a flat background below the peak. The energy calibration of the spectrum and ratio of the two peaks (K-conversion and full-energy) for the <sup>113</sup>Sn source is fixed so the only free parameter in the fit is the width of the

peaks. For example, Fig. 2-7 shows a typical fit to a spectrum in liquid argon. It is clear that even after correcting for electronic noise broadening and the double peak of the  $^{113}\text{Sn}$  source, the energy resolution of the detector is poorer than that predicted by the Fano factors for xenon and argon.

Our data of charge collected and energy resolution as a function of drift field are plotted in Figs. 2-9 and 2-10. Several effects can contribute to the degradation of performance we observe: 1) electrons may be trapped in the grid; 2) drifting electrons may be "scavenged" by electronegative impurities such as  $\text{O}_2$  and  $\text{N}_2$ ; and 3) electrons may be lost by recombining with other positive ions. (See also Appendix B.)

Bunemann *et al.* have shown<sup>33</sup> that for our grid parameters, a ratio of the field in the grid-anode region to the field in the drift region of 3 : 1 will be sufficient for 100% transmission of the electrons through the grid, and gives only 1% shielding inefficiency. His solution for ensuring 100% transmission through a parallel wire grid is:

$$\frac{E_g}{E_d} > \frac{1+\rho}{1-\rho}, \quad (2-1)$$

where  $E_g$  is the electric field strength in the grid-anode region,  $E_d$  is the drift field strength and  $\rho = 2\pi r/d$ , where  $2\pi r$  is the circumference of the grid wires and  $d$  is their center-to-center spacing. With a grid-anode separation of  $s$ , his solution for the shielding inefficiency,  $\sigma$ , is:

$$\sigma = \frac{d}{2\pi s} \log_e \rho^{-1}. \quad (2-2)$$

Note especially that these parameters and solutions refer to an array of parallel



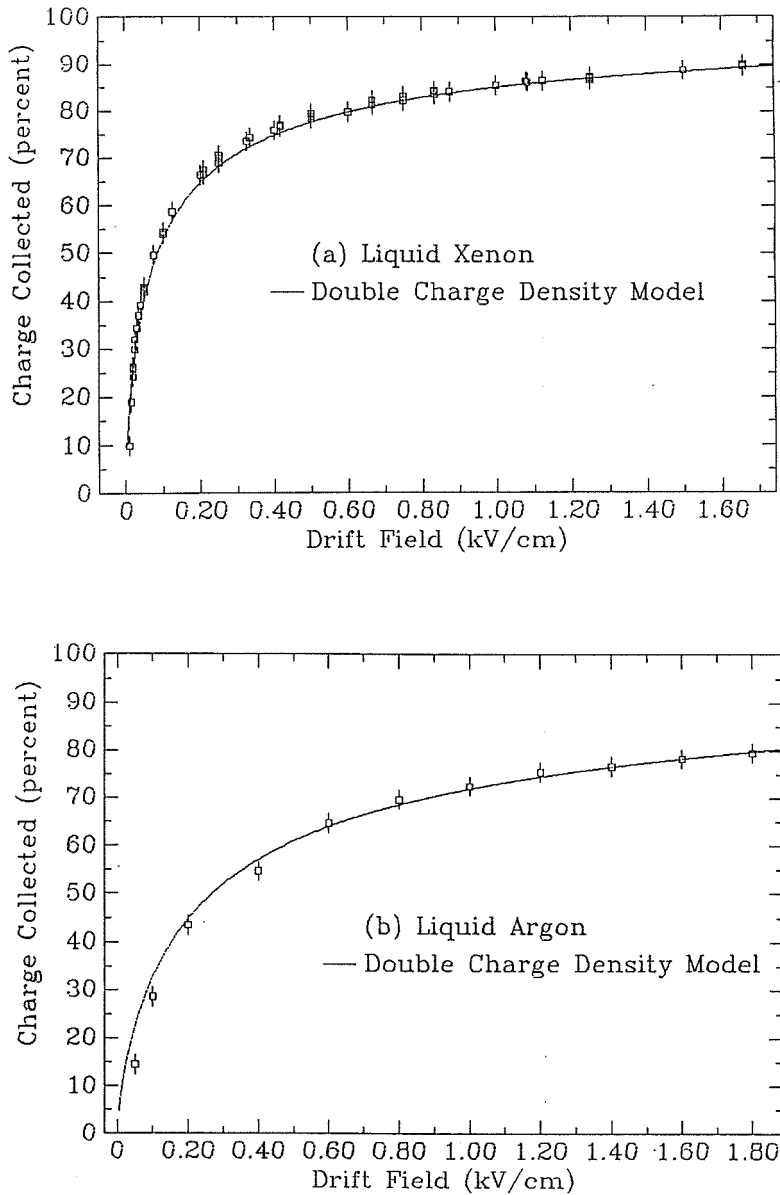


Figure 2-9. Charge collected as a function of drift field for (a) LXe and (b) LAr.

wires, not a mesh. In the case of a crossed-wire mesh grid, the problem is much more difficult to solve, but it is safe to assume that the both the transmission and the shielding efficiency will be decreased for the same wire diameter

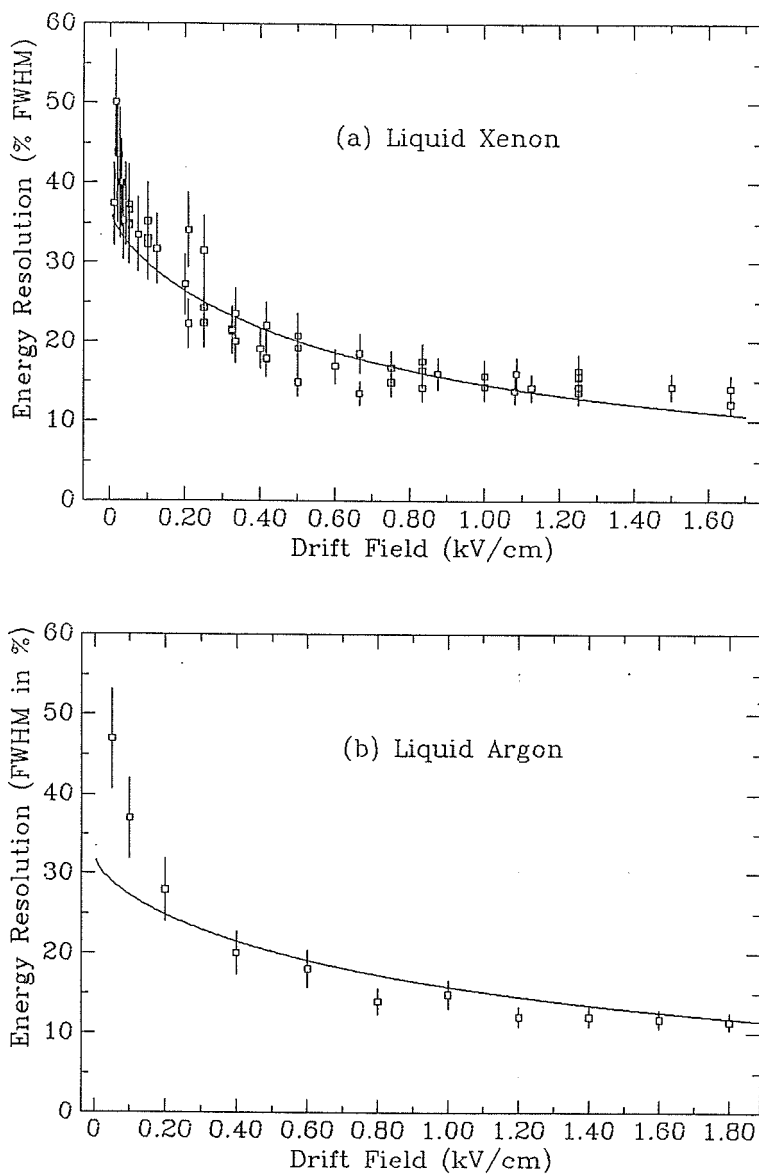


Figure 2-10. Energy resolution as a function of drift field for (a) LXe and (b) LAr.

and spacing. Thus, we must simply ensure the transmission of electrons through the grid.

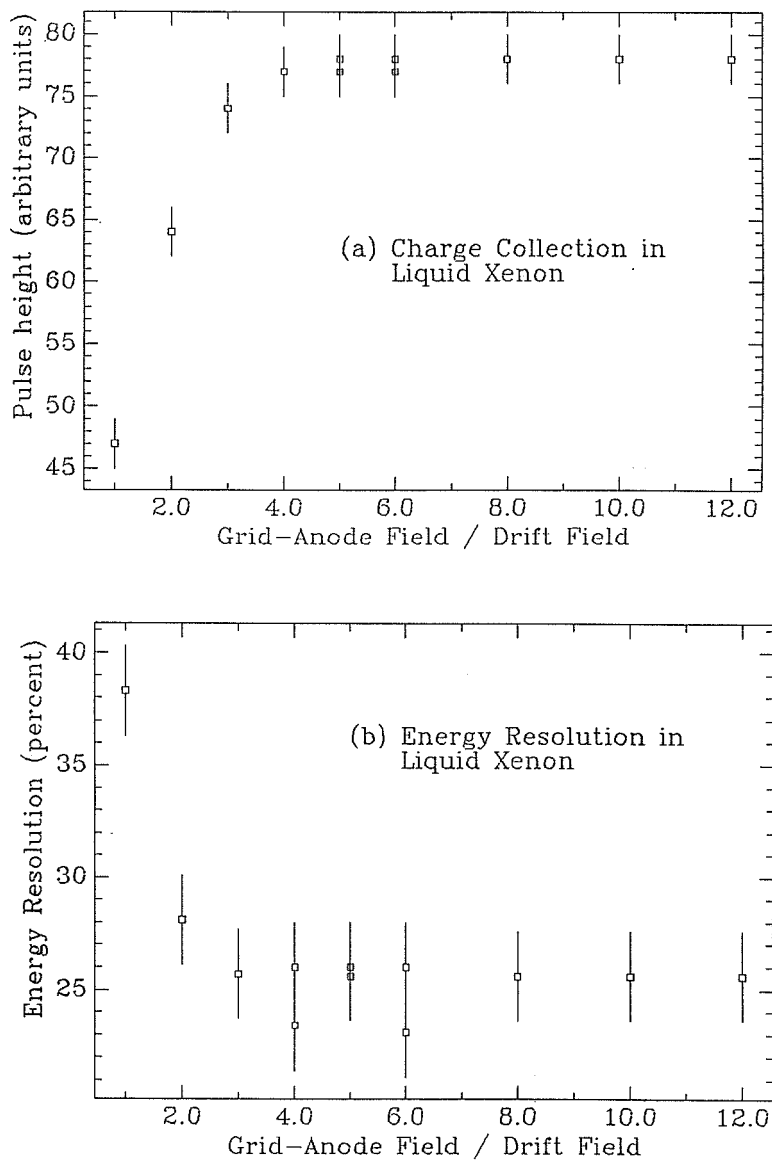


Figure 2-11. (a) Charge collection and (b) energy resolution in LXe as a function of the field ratio in the grid-anode region to the drift field region, plotted for a constant drift field of 0.25 kV/cm.

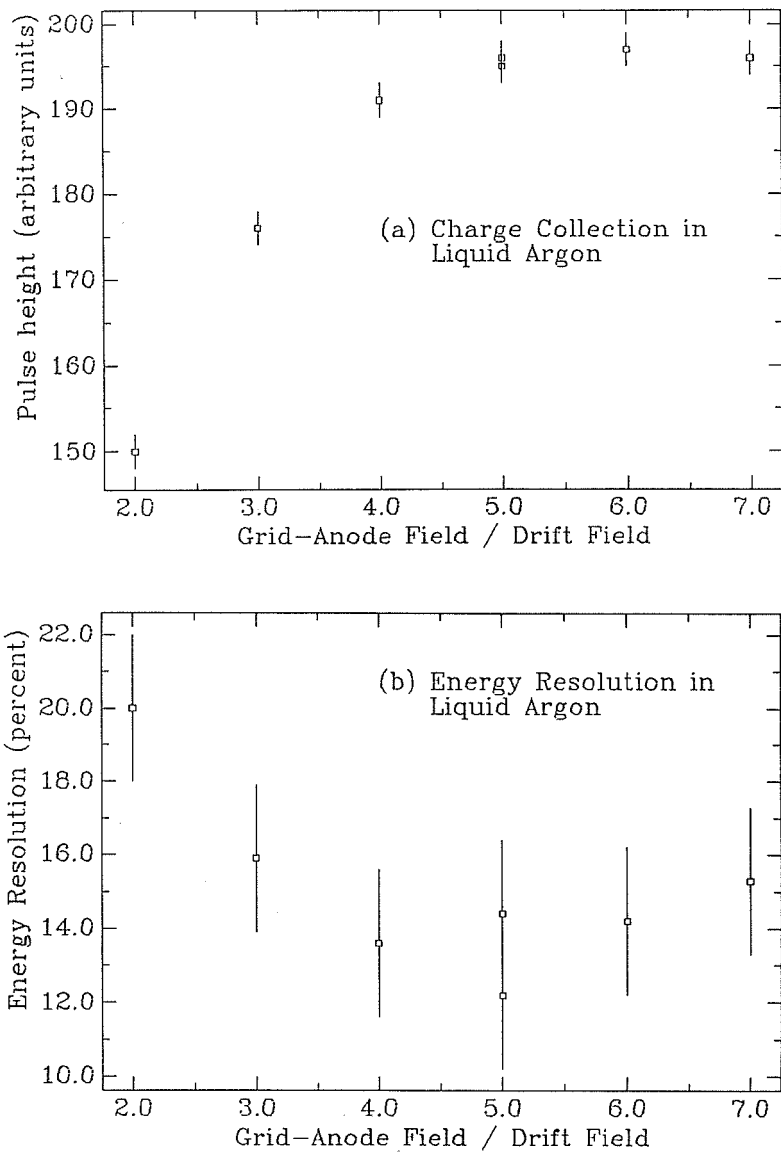


Figure 2-12. (a) Charge collection and (b) energy resolution in LAr as a function of the field ratio in the grid-anode region to the drift field region, plotted for a constant drift field of 1.08 kV/cm.

We measured charge collection and energy resolution as a function of  $E_g/E_d$  for fixed drift field,  $E_d$ . The data are displayed in Figs. 2-11 and 2-12. Based on these observations, we operate at a field ratio of 5 : 1, well into the saturation region for charge collection.

By analyzing the charge collection data in LAr, we can set an upper limit on the amount of electronegative impurities in our detector. The work of Hoffman *et al.*,<sup>34</sup> and especially that of Scalettar *et al.*,<sup>35</sup> shows that attachment of electrons to electronegative impurities can be described by a simple exponential process:

$$Q = Q_0 e^{-\frac{d}{\lambda}}, \quad (2-3)$$

where  $Q$  is the charge collected after drifting a distance  $d$ ,  $Q_0$  is the initial charge created, and  $\lambda$  is the attenuation length and is measured to be proportional to the drift field strength,  $E$ , and inversely proportional to the impurity concentration,  $\rho$ :

$$\lambda = \beta \frac{E}{\rho}. \quad (2-4)$$

In argon,  $\beta$  is 0.15 cm - ppm / (kV/cm).<sup>35</sup> With a drift distance of 1 cm, 73% charge collection at 1 kV/cm implies  $\lambda \geq 3$  cm, and  $\rho \leq 50$  ppb.

We estimate the spreading of a charge collection peak due to a conversion electron source placed on the cathode by comparing the charge collected for electrons emitted parallel to the cathode to that for electrons emitted perpendicular to the cathode. We find that the spreading is approximately given by  $r/\lambda$ , where  $r$  is the effective range of the conversion electrons. Since the

effective range of 364 keV electrons in LAr is  $<1$  mm, the spreading of the conversion electron peak due to electronegative impurities, when  $\lambda=3$  cm, should be less than 4%, which is also approximately the contribution of electronic noise to the energy resolution. This compares with the observed value of 15% FWHM at 1 kV/cm in both liquids. (In LXe, the 14% of the counts which come from the  $\gamma$ -ray itself will interact over the entire volume of the detector. In this case, the spreading is given approximately by  $d/\lambda$ , where  $d$  is the drift length of the detector.) Thus, the effects of electronegative impurities do not account for the degraded energy resolution we observe. We must also consider the initial recombination of the ions and electrons.

When the medium is first ionized by the charged particle, the ionized atom and its electron have a finite probability of recombining. In the absence of  $\delta$ -electron production, this process can be described by a single parameter model<sup>22</sup> (see Appendix A):

$$Q = Q_0 \frac{\ln(1+\xi)}{\xi}, \text{ where} \quad (2-5)$$

$$\xi = \frac{N_0 \alpha}{4a^2 \mu_- E}. \quad (2-6)$$

$N_0$  is the charge deposited in one ionization event (normally 1 electron),  $\alpha$  is a phenomenological recombination coefficient,  $a$  is the size scale of the distribution,  $\mu_-$  is the electron mobility, and  $E$  is the drift field strength. Thus the recombination strength,  $\xi$ , depends inversely upon the drift field strength.

We fit the Irvine data<sup>35</sup> of charge collected versus drift field strength in LAr (see Fig. A-3) where the effects of electronegative impurities have been

removed and we find<sup>4</sup>  $\xi E = 0.80 \pm 0.02$  kV/cm. We then fit our data by fixing the value of  $\xi E$  in the LAr data to that of the UC Irvine data and by including an attenuation length. From this we estimate the purity of the liquid. We have consistently been able to achieve impurity levels of  $\lesssim 2$  ppb O<sub>2</sub> equivalent. (Our method of measuring electronegative impurities becomes insensitive below 2 ppb due to the short drift distance in the detector. It would be sensitive to lower concentrations at larger drift distances.) This means that the contribution to the energy resolution at 1 kV/cm due to impurities must be less than 1% FWHM, in view of our previous discussion following (2-4).

Therefore, the only significant contribution to the experimentally observed resolution is due to the statistics of ion-electron recombination. In Appendix B it is shown that the production of  $\delta$ -electrons affects the recombination rates and therefore requires a model<sup>23</sup> with two recombination strengths corresponding to two charge densities. One density describes the minimum ionizing track and the other describes the more heavily ionizing region at the end of each  $\delta$ -electron track. Including  $\delta$ -electrons, the total charge existing after recombination is:

$$Q = Q_0 \left[ a \frac{\ln(1+\xi_0)}{\xi_0} + (1-a) \frac{\ln(1+\xi_1)}{\xi_1} \right] \quad (2-7)$$

where  $Q_0$  is the charge created in the detector.  $\xi_1 E = 0.34 \pm 0.12$  kV/cm,  $\xi_0 E = 3.4 \pm 0.7$  kV/cm in argon and  $\xi_1 E = 0.13 \pm 0.04$  kV/cm,  $\xi_0 E = 1.9 \pm 0.5$  kV/cm in xenon. Also,

$$a \approx 0.291 + \frac{16.7}{E_P} \quad (\text{Argon}) \quad (2-8a)$$

$$a \approx 0.203 + \frac{12.2}{E_P} \quad (\text{Xenon}) \quad (2-8b)$$

where  $E_P$  is the energy of the primary particle in keV. The shape of this curve is very similar to the shape predicted by the single density model because the charge collected from the high charge density region is a small perturbation on the charge collection process. However, this perturbation has a large effect in (2-9) which describes energy resolution.

The statistical fluctuations in the charge collection process create a fundamental limit to the observed resolution which is given in the double density model by:

$$\% \text{ FWHM} \times \frac{Q}{Q_0} = \frac{235.5}{\sqrt{E_P}} b \left[ \frac{\ln(1+\xi_1)}{\xi_1} - \frac{\ln(1+\xi_0)}{\xi_0} \right] \quad (2-9)$$

where  $b \approx (4.52 + \frac{157}{E_P})^{\frac{1}{2}}$  in argon; in xenon  $b \approx (6.76 + \frac{216}{E_P})^{\frac{1}{2}}$ . Fits of these functions to our data are shown in Fig. 2-10.

## 2.4 Summary

We have constructed ionization chambers filled with both liquid argon and liquid xenon. In the liquid argon detector we collect  $78\% \pm 5\%$  of the charge in an electric drift field of 1.6 kV/cm, but in the liquid xenon detector at the same field strength we collect  $90\% \pm 5\%$  and at 10 V/cm we collect  $10\% \pm 3\%$  of the charge. In both detectors, the energy resolution is  $12\% \pm 1\%$  FWHM at 380 keV, which is comparable to the results of Lindblad *et al.*<sup>26</sup> and Masuda *et al.*<sup>27</sup>, and the purity of the liquids is better than 2 ppb O<sub>2</sub> equivalent. The ob-



served resolution is a fundamental limit imposed by the statistics of  $\delta$ -electron production.

### *Improving Energy Resolution*

In order to improve the energy resolution of these ionization detectors, we must decrease the recombination strength,  $\xi$ , of the ion-electron pairs. There are several ways to do this:<sup>22,23</sup>

- Increase the field strength
- Increase the electron mobility
- Decrease the charge density
- Add the recombination light back to the signal

Increasing the electric field strength improves the observed energy resolution<sup>20</sup>, but fields as high as 60 kV/cm are necessary to overcome the recombination problem. This is impractical for building  $\beta\beta$  decay detectors with drift distances of 10 cm or more.

Increasing the electron mobility may be possible by cooling the detector to liquid He temperatures. Mobility has been observed to increase<sup>36</sup> with decreasing temperatures as  $T^{-3/2}$ . However, the recombination constant,  $\alpha$ , may be proportional to the mobility, which could leave the recombination strength  $\xi$  unchanged. In any event, it is worth pursuing because a crystalline detector would have the additional advantage that it could be purified by zone-refining since impurities are more soluble in the liquid than in the solid.

The charge density can be decreased by lowering the pressure over the medium, transforming the liquid into a high pressure gas or low density liquid

above its critical point.

Organic dopants such as Triethylamine may be added to convert ultraviolet photons given off in the recombination process to free electrons. This process will occur away from the ions and so these electrons will not be subject to recombination. Doke<sup>9</sup> and others<sup>37,38</sup> have observed large gains in charge collection in this way, but the effect of these dopants on energy resolution has not been examined.

Finally, one may attempt to directly observe the ultraviolet photons from recombination using photomultiplier tubes. This has given good improvement of the energy resolution for spectra of heavy ions, where recombination is very strong. However, it has not been shown yet to be effective in the case of the energy resolution of electron (and  $\gamma$ -ray) spectra.

## CHAPTER THREE

### A High Pressure Ionization Chamber

#### 3.1 Introduction

##### *Motivation*

In order to decrease the recombination strength of the detector medium we chose to examine the performance of ionization chambers at high pressures where the density is still high but the atomic spacing should be significantly less than it is in condensed gases. Our model for the recombination strength,

$$\xi = \frac{N_0\alpha}{4a^2\mu-E}, \quad (3-1)$$

if taken to be valid over a large density range, would predict that the recombination strength should scale as  $\xi \propto 1/a^2$ , i.e.,  $\xi \propto \rho^{2/3}$ , where  $\rho$  is the density of the medium. In 30 atm of xenon this would correspond to a factor of  $\approx 6$  reduction from liquid xenon. According to (2-9) this should mean energy resolution three times better than that of liquid xenon.

We were additionally motivated by reports that the group headed by Pomansky<sup>4</sup> had achieved at least 3.5% FWHM energy resolution at 1.3 MeV using 30 atm of xenon in an ionization chamber. This chapter provides the details of the results of our high pressure xenon and argon detector studies

published in Imel and Thomas, Nucl. Instrum. and Methods, B40/41, 1208, 1989.

### *Design Considerations*

We designed the ionization chamber with the intent of using it as a detector for  $\beta\beta$ -decay, should it prove to be stable and have sufficient energy resolution. Thus, there were several design criteria for the detector:

- Size
- Efficiency
- Drift Characteristics
- Reduction Background
- Active Volume
- Strength

In order to be sensitive to  $\beta\beta$ -decay, we needed to have enough  $^{136}\text{Xe}$  to be sensitive to a lifetime of  $\sim 10^{20-22}$  years. Thus a detector for use with  $\sim 1$  mole of  $^{136}\text{Xe}$  in the active volume was designed. This translates to a physical volume of  $\sim 1$  liter.

We wish to maximize the efficiency of the detector for containing a  $\beta\beta$ -decay event. Tables 3-1(a) and (b) give the densities<sup>39</sup> and ranges<sup>32</sup> of 400 keV and 1 MeV electrons in argon and xenon. The effective range<sup>42</sup> may be as little as 2/3 of the actual range of the electrons because of multiple scattering in the detector medium at these high densities. In order to contain two 1 MeV electrons from  $\beta\beta$ -decay in the detector filled with xenon, it is clear that we would like to operate at the highest pressure possible. The maximum pressure is

Density and Range in Xenon				
Pressure (atm)	5	10	20	30
Density (g/cm <sup>3</sup> )	0.028	0.057	0.121	0.197
Range (cm), 400 keV e <sup>-</sup>	8.03	3.95	1.86	1.14
Range (cm), 1 MeV e <sup>-</sup>	25.6	12.59	5.93	3.63
Pressure (atm)	40	50	60	70
Density (g/cm <sup>3</sup> )	0.290	0.415	0.616	0.887
Range (cm), 400 keV e <sup>-</sup>	0.78	0.54	0.37	0.25
Range (cm), 1 MeV e <sup>-</sup>	2.49	1.72	1.18	0.80

Table 3-1(a). Density<sup>39</sup> and range<sup>32</sup> of electrons in high pressure xenon.

limited by the drifting characteristics of the gas.

Balanced against efficiency is the desire to have the smallest drift distance possible in order to minimize the effects of electron attachment to electronegative impurities in the detector. These effects become more severe at higher pressures. Thus, the highest pressure at which we could operate in xenon was 30 atm. Therefore the minimum drift distance at which we could still contain most of the 1 MeV electrons was about 5 cm.

Density and Range in Argon				
Pressure (atm)	10	40	70	100
Density (g/cm <sup>3</sup> )	0.0163	0.0664	0.1178	0.1699
Range (cm), 400 keV e <sup>-</sup>	11.1	2.72	1.53	1.06
Range (cm), 1 MeV e <sup>-</sup>	36.7	9.01	5.08	3.52

Table 3-1(b). Density<sup>39</sup> and range<sup>32</sup> of electrons in high pressure argon.

Although external backgrounds can be shielded from the detector, we must use a design which minimizes any radioactive background in the construction materials themselves. Thus, we used only OFHC copper and plastics such as Delrin and Teflon, all of which have been examined by a shielded Ge detector and shown to be low-background materials.

We anticipated that we would alternately fill the detector with enriched and depleted xenon. In contrast to the case of condensed xenon where the liquid is placed only in the cooled part of the detector, the xenon in a high-pressure detector is distributed throughout the entire system, both active and non-active volumes. We desire to maximize the active volume of the detector, since enriched xenon is very expensive. This means that we must minimize the volume of the gas-handling system as well as the volume of the non-active part of the detector.

Finally, for a 1 liter detector at 30 atm, the force on the surfaces is on the order of 4 tons. We must use strong materials to contain this pressure. OFHC copper has this strength, as does Delrin. However, we found that other plastics such as polypropylene and high-molecular weight polyethylene, while having superior outgassing characteristics, had insufficient strength to withstand the pressures in the system.

## 3.2 Design and Construction

### *Geometry*

The detector is shown in Figs. 3-1 and 3-2. It is a design which completely maximizes the active volume of the detector by using the copper field-gradient rings and Delrin insulating rings as the containment vessel. The entire volume of gas in the detector is active, with the exception of the regions between the grid and anode and between the anode and flange. For convenience in applying high voltage to the detector we use a double-detector system where the cathode is at negative high voltage and the anodes are at ground potential. This system also removes the difficulty of obtaining high-voltage, high-pressure, high-vacuum and low-background feedthroughs. The field-gradient rings, the cathode plate and the anode plate serve as the feedthroughs for this system. The vessel is held together by 16 0.95 cm diameter OFHC copper bolts and 2 OFHC copper flanges. The gas inlet and outlet were electron-beam welded to the copper flanges to minimize any possibility of radioactive contamination.

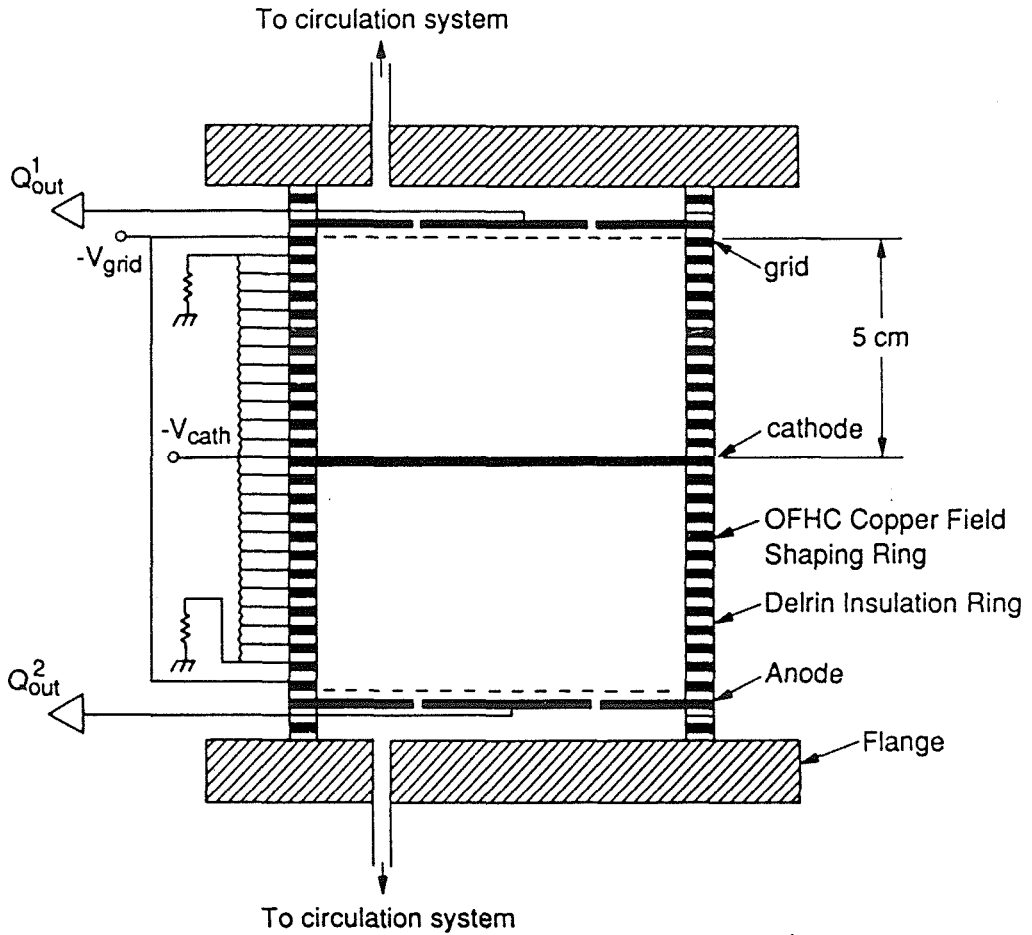


Figure 3-1. Schematic of the high pressure double ionization chamber. The gas is contained by the field gradient rings, which are insulated with Delrin rings. The anodes are segmented to reduce capacitive noise. The chamber is held together by 16 OFHC copper bolts (not shown). This system withstood pressures of greater than 120 atm.

### *Rings*

Standard 12.0 cm diameter and 1.8 mm thick OFHC copper gaskets<sup>41</sup> normally marketed for use with conflat flanges were used as the field-gradient



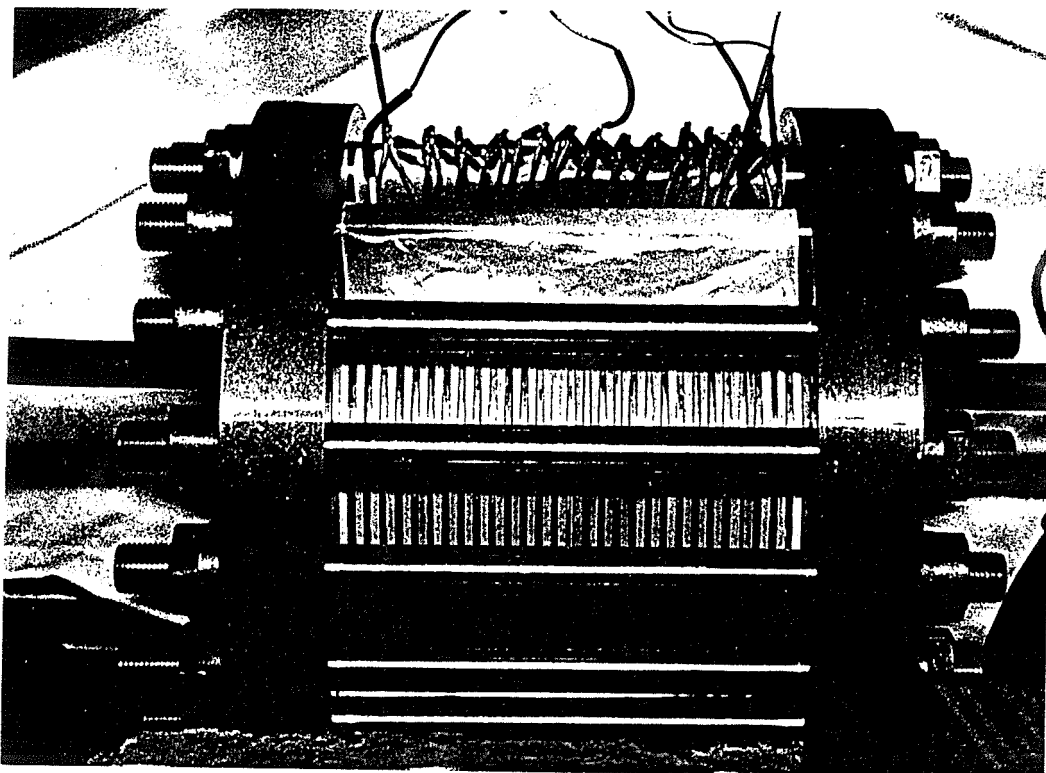


Figure 3-2. The high pressure ionization chamber and resistor chain. The Faraday cage has been removed for this picture.

rings. In order to ensure a good pressure seal between the copper and Delrin rings, each ring was meticulously hand polished on a flat plate until the surface was free of scratches and was flat to within  $0.1 \mu\text{m}$ . The Delrin rings were 12.2 cm in diameter (to help decrease arcing between the copper rings) and had the same thickness as the copper rings. Teflon gaskets ( $50 \mu\text{m}$  thick) with the same shape as the copper rings were used for each high pressure seal in the detector.

### *Grid*

The grid is an OFHC copper mesh<sup>30</sup> with a wire diameter of  $33\ \mu\text{m}$  and a center-to-center spacing of  $230\ \mu\text{m}$ . The grid-anode spacing is 3.6 mm. Thus, the Bunemann<sup>33</sup> results discussed in chapter 2 give 0.8% shielding efficiency and a grid-anode to drift field ratio of 2.6 : 1 for 100% electron transmission for this grid. The grid was attached to a ring by sandwiching the grid between the ring and a smaller diameter inner ring.

### *Anode and Cathode*

The anode was initially a single OFHC copper plate with the same thickness and diameter as the rings. However, the plate proved to have a capacitance so high that capacitive noise limited the energy resolution of the detector. Thus, a segmented anode was used. The inner segment was anchored by using Delrin spacers and high-vacuum, low-background epoxy. In these experiments the signal from the inner segment was fed outside behind the anode using a pair of Delrin rings and a thin copper strip. In a  $\beta\beta$ -decay experiment the outer anode would have been segmented into four sections. The cathode is a simple OFHC copper plate with four holes drilled in it in order to allow the gas to pass from one side of the detector to the other.

### *Voltage and Electronics*

Two filtered power supplies were used: one for the cathode and field gradient rings and one for the grid. The resistor chain was formed with  $20\ \text{M}\Omega$  resistors. The connection between the rings and the voltage supplies and electronics was made by putting a small longitudinal slit in the side of each ring, anode, cathode and grid. A wire could then be crimped in the slit. A Faraday

cage of OFHC copper was used to shield the detector from stray power and radio-frequency fields.

The signal was fed from the central anode segment to an Ortec 142A preamplifier. A Canberra 2010 amplifier shaped the pulses and amplified them for input to a multi-channel analyzer. The spectra could then be dumped to our Tektronix computer. Calibration of the electronics was accomplished in the same way as in chapter 2.

### *Gas Handling system*

The gas handling system used 6.4 mm inner diameter tubing to minimize the quantity of gas outside the detector. Xenon was stored at high pressure in a bottle filled with molecular sieve. High pressure argon was obtained by condensing from a commercial gas bottle into a smaller bottle filled with molecular sieve. When the bottle was full of liquid argon the argon was allowed to warm up, giving pressures up to 140 atm.

A circulation system employing two SAES getters<sup>42</sup> was used to purify the gas. A magnetically coupled rotary pump pushed the gas through the getters. We found that the pump would bind at high pressure, so we replaced the brass interior of the pump with a Delrin rotor. In this way the pump could be left running for at least a week at a time.

### *Diagnostic Sources*

Three diagnostic radioactive sources were used for these experiments. In the early prototyping stages of this experiment a  $^{113}\text{Sn}$  source (the same as in chapter 2) was placed in the center of the cathode. This was replaced with a  $^{207}\text{Bi}$  source (Table 3-2 and Fig. 3-3) in later tests. Both of these are

conversion electron sources mounted internal to the detector.

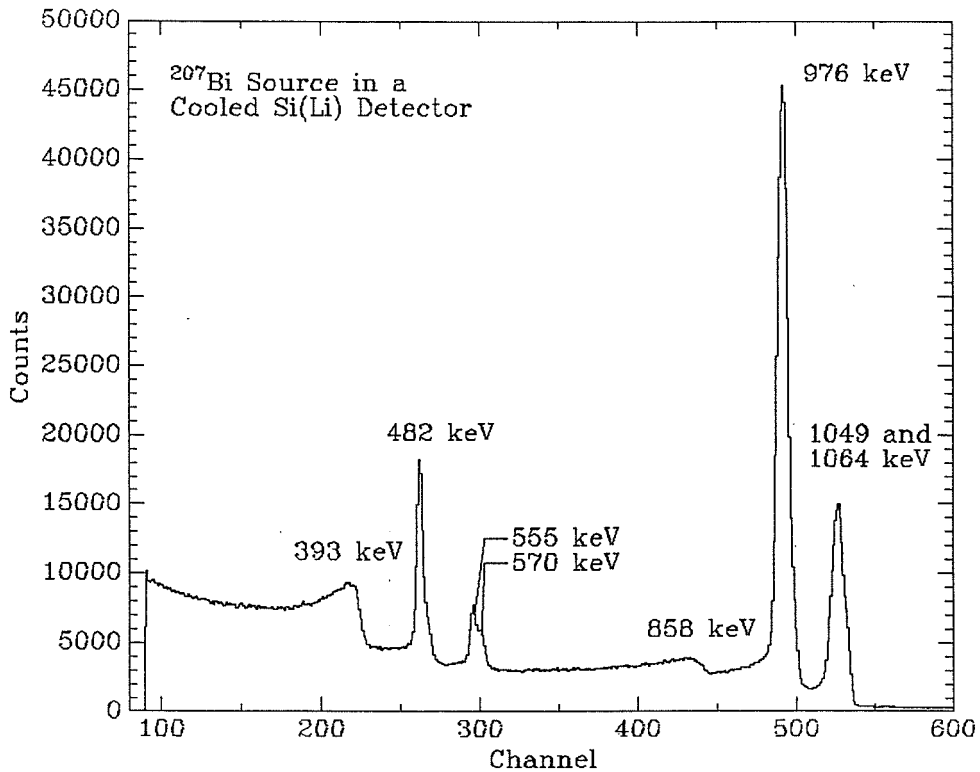


Figure 3-3. Spectrum in a cooled Si(Li) detector of the  $^{207}\text{Bi}$  source used in these experiments.

An external 62 mCi  $^{137}\text{Cs}$  source was placed in a lead housing which sat on rollers. The lead housing had a narrow slit such that the 662 keV  $\gamma$ -rays were emitted in a beam no more than 2 mm wide. With this source, the drift characteristics of the detector could be checked. Not only could the attenuation length of the detector be measured by observing the charge collected as the source was scanned along the drift length of the detector, but the recombination strength could be measured by extracting the charge collected after the

Energy (keV)	Spectrum Feature	Abs. Intensity
393.3	Compton edge of $\gamma_{570}$	
481.7	$e_K$ of $\gamma_{570}$	1.55
555.0	$e_L$ of $\gamma_{570}$	0.45
569.65	$\gamma_{570}$	97.74
698.9	Compton edge of $\gamma_{898}$	
809.8	$e_K$ of $\gamma_{898}$	0.003
857.6	Compton edge of $\gamma_{1064}$	
883.1	$e_L$ of $\gamma_{898}$	0.001
897.8	$\gamma_{898}$	0.14
975.6	$e_K$ of $\gamma_{1064}$	7.27
1048.9	$e_L$ of $\gamma_{1064}$	1.94
1063.64	$\gamma_{1064}$	73.79
1225.2	Compton edge of $\gamma_{1442}$	
1354.2	$e_K$ of $\gamma_{1442}$	0.0003
1427.5	$e_L$ of $\gamma_{1442}$	0.0001
1442.2	$\gamma_{1442}$	0.15
1546.9	Compton edge of $\gamma_{1770}$	
1682.2	$e_K$ of $\gamma_{1770}$	0.024
1755.5	$e_L$ of $\gamma_{1770}$	0.005
1770.2	$\gamma_{1770}$	6.79

Table 3-2. Summary<sup>16</sup> of the most important features in the spectrum of <sup>207</sup>Bi. The energies are listed for  $\gamma$ -rays, K-conversion electrons, the weighted average of the L-conversion electrons and the Compton edges of the  $\gamma$ -rays.

effects of attenuation have been removed.

### 3.3 Performance

#### *Spectra*

Spectra from the detector in 30 atm of xenon and 108 atm of argon using the  $^{207}\text{Bi}$  source are shown in Figs. 3-4 and 3-5. Fig. 3-6 shows the linearity of these spectra and Fig. 3-7 shows the energy resolution of these spectra as a function of energy. A more extensive display and discussion of spectra from this detector is in Appendix C.

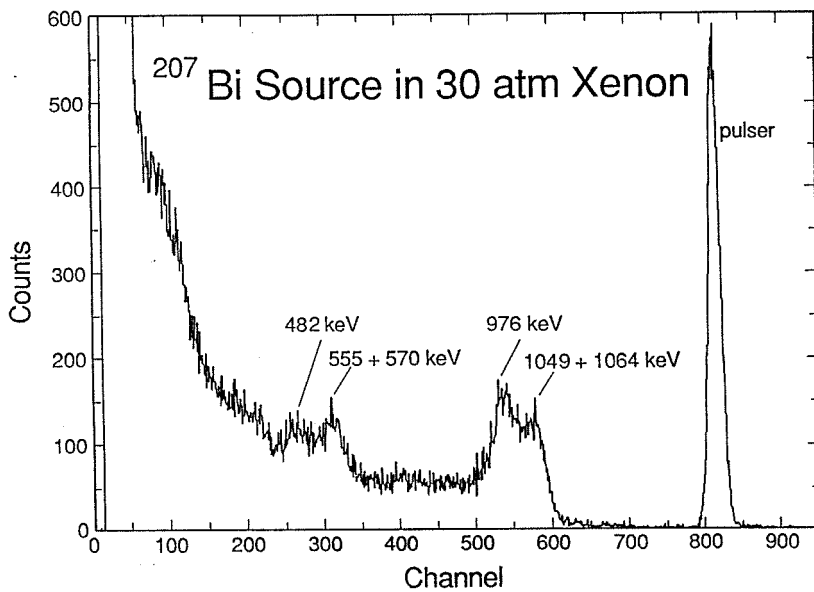


Figure 3-4. Spectrum from internally mounted  $^{207}\text{Bi}$  conversion electron source in 30 atm xenon. Electric drift field strength is 0.7 kV/cm.

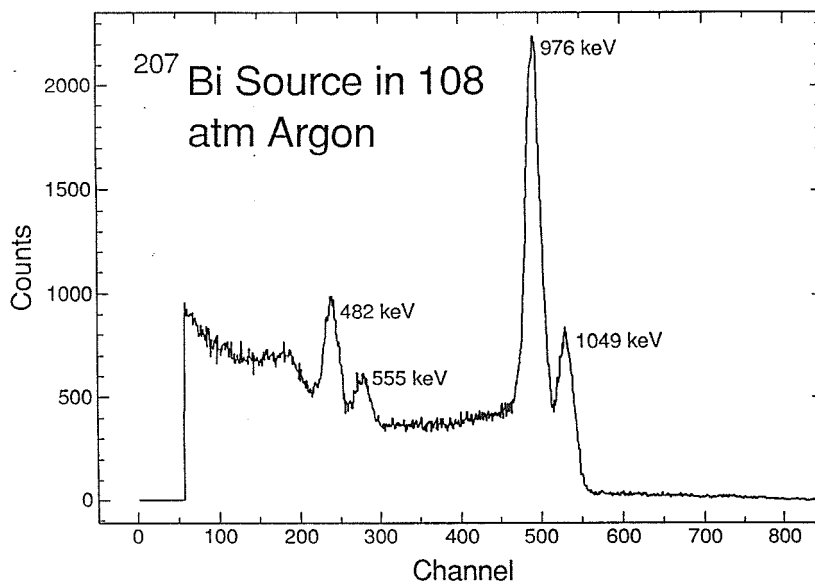


Figure 3-5. Spectrum from internally mounted  $^{207}\text{Bi}$  conversion electron source in 108 atm argon. Electric drift field strength is 0.5 kV/cm.

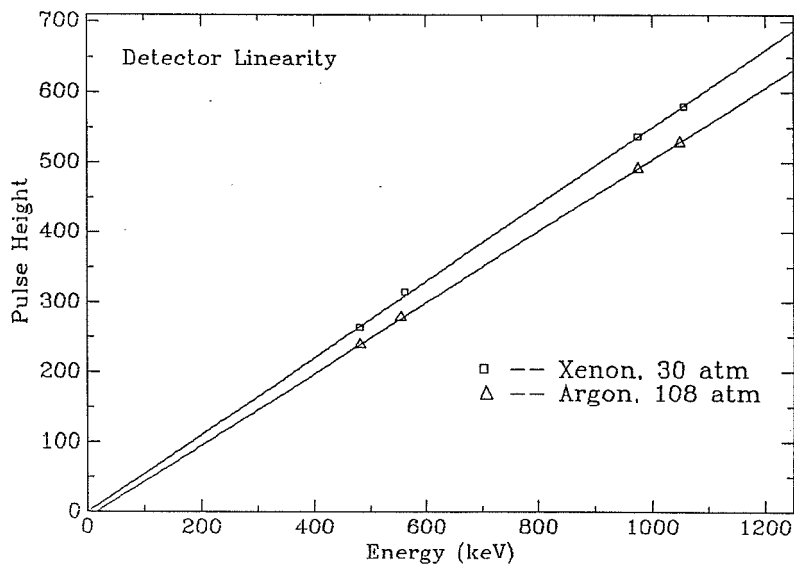


Figure 3-6. Charge collected versus energy in argon and xenon. (Taken from Figs. 3-4 and 3-5.)

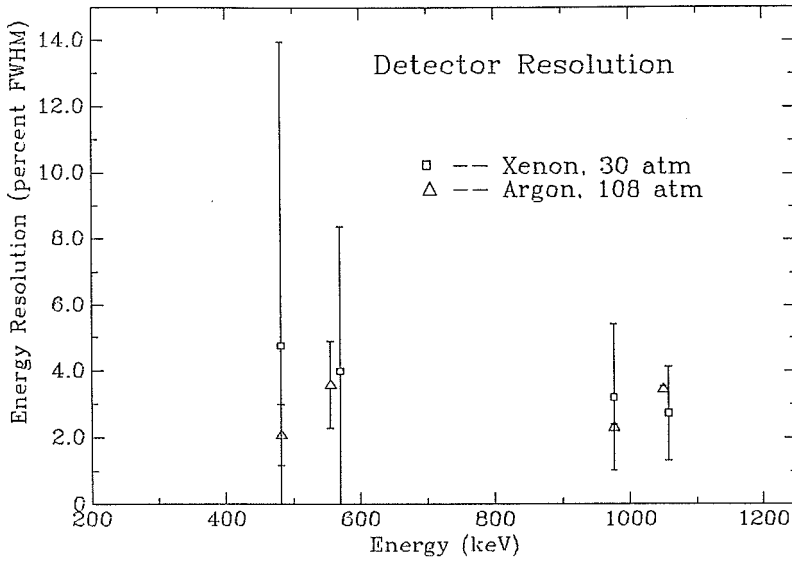


Figure 3-7. Energy resolution versus energy in argon and xenon. The energy resolution data have been corrected for capacitive and electronic noise by subtracting in quadrature the width of the pulser peak.

### Charge Collection

The charge collection using the internally mounted  $^{207}\text{Bi}$  source was measured as a function of pressure in argon. During these measurements, the electronegative impurity concentration was kept constant by starting at high pressures and only decreasing the pressure in the system. These data were accumulated over a time period (2 hours) short compared to the time (> 7 hours) of known stability of the argon detector with respect to charge collection. Fig. 3-8 shows that these data are well modeled by:

$$\frac{Q}{Q_0} = e^{-d/\lambda}, \quad \lambda = \beta \frac{E}{\rho}, \quad \beta = CP^{-n}, \quad (3-2)$$

where  $Q/Q_0$  is the percentage of charge surviving the drift to the anode,  $E$  is



the drift field strength,  $\rho$  is the electronegative impurity concentration,  $C$  is a constant and  $P$  is the pressure. The fit to the data shows that  $n = 2.05 \pm 0.06$ , that is, the attenuation length scales approximately inversely as the inverse of the pressure squared,  $\lambda \propto P^{-2}$ . This suggests that the loss of drifting electrons is a binary process, i.e., it takes two collisions to lose an electron by attachment to an impurity ion: one to attach the electron to the ion and a second collision to de-excite the impurity atom to its ground state.

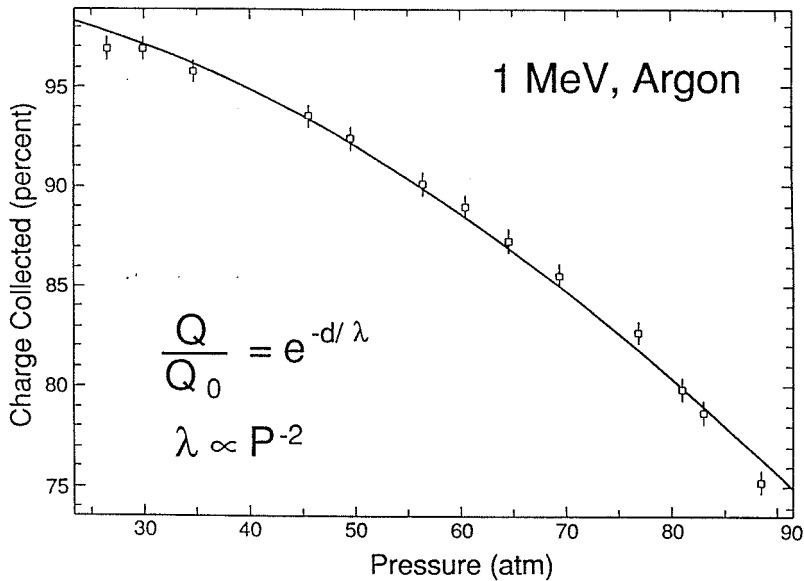


Figure 3-8. Charge collection as a function of pressure in argon. These measurements were performed starting at the highest pressure and letting gas out of the detector for subsequent measurements. The entire set was collected in a time small compared to the poisoning time of the argon. The electric drift field strength for this data set was 0.7 kV/cm.

### *Attenuation*

Direct attenuation length measurements were made in argon and xenon as a function of pressure, purification, voltage and time. Some of these

measurements are plotted in Figs. 3-9 and 3-10. Fig. 3-9 shows that the attachment of drifting electrons is described well by the attenuation model in both xenon and argon. In addition, the prediction of the model,  $\lambda \propto E$ , is compared to data in argon in Fig. 3-10 and is seen to be accurate.

While the attenuation length achievable in pure argon is at the limit of the sensitivity of the apparatus,  $\lambda \approx 2$  m at 0.6 kV/cm, the best attenuation length obtained in purified xenon was  $\lambda \approx 50$  cm at 0.6 kV/cm. Drifting is much more difficult in xenon than in argon for equal densities.

### *Recombination*

By measuring the attenuation length as a function of the drift field applied and extrapolating the charge collected to zero drift distance, we obtain the charge collection independent of the effects of electron attachment, i.e., the charge surviving initial recombination. Fig. 3-11(a) shows data for 45 atm argon at several drift field strengths. Fig. 3-11(b) shows the data for liquid argon. These data show that the recombination strength at this pressure is less than 3% of that in liquid argon. (We use the single-density model for simplicity, since it is sufficiently accurate for an approximate description of the charge collection data.)

Fig. 3-12(a) shows the data in 30 atm xenon, and Fig. 3-12(b) that in liquid xenon. The high pressure xenon data are less precise because of the rapid poisoning of the xenon. The effect of impurities has been removed from the data in both high pressure argon and xenon in order to measure the recombination strength, but this rapidly becomes a large correction in xenon, and therefore the latter data are uncertain.

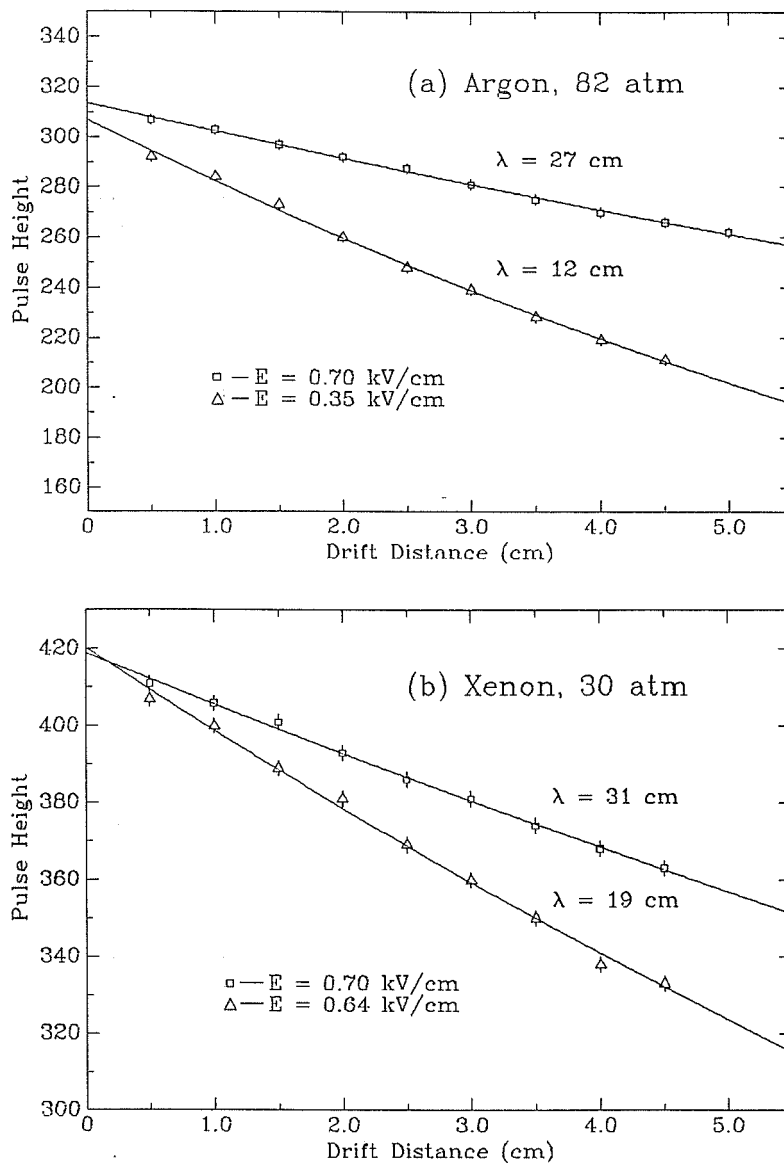


Figure 3-9. Charge collected as a function of drift distance using an external, collimated  $^{137}\text{Cs}$  source. In (a) argon the Compton edge of the 662 keV  $\gamma$ -ray was used, whereas in (b) xenon the full-energy peak at 662 keV was used.

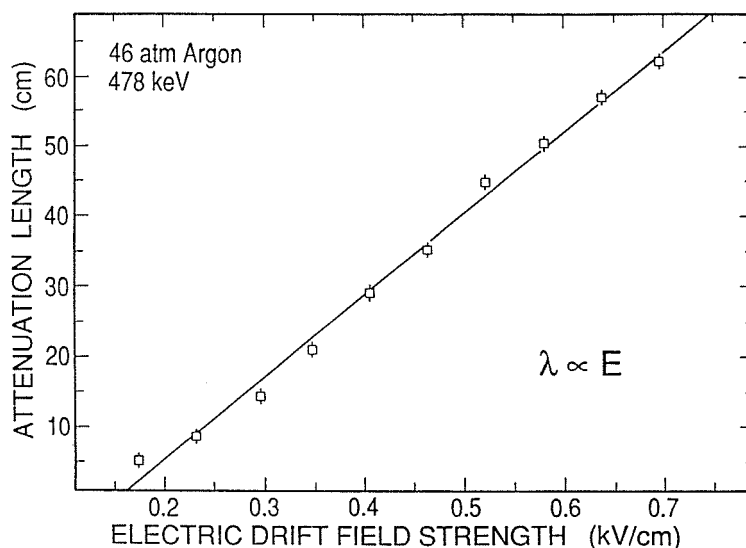


Figure 3-10. Attenuation length in 46 atm argon as a function of electric drift field strength. The half-maximum position of the Compton edge of the 662 keV  $\gamma$ -ray of an external, uncollimated  $^{137}\text{Cs}$  source was used for these measurements.

### *Results and Difficulties*

The best energy resolution obtained in argon (at a pressure of 108 atm and an electric drift field of 0.7 kV/cm) was 2% FWHM at 976 keV after subtracting in quadrature the contribution from electronic noise as measured by the pulser. The best energy resolution in xenon (at a pressure of 30 atm and an electric drift field of 0.6 kV/cm) was 3% FWHM at 1060 keV (after noise subtraction).

The typical energy resolution obtained in 70 atm of argon is 4% FWHM (without any subtraction). Recombination of  $\delta$ -electrons contributes an amount given by (2-9) which is negligible for the magnitude of the recombination strengths we measure in argon at this density range. The W-value in 70 atm argon has not been measured, but should be near the 50 atm value of

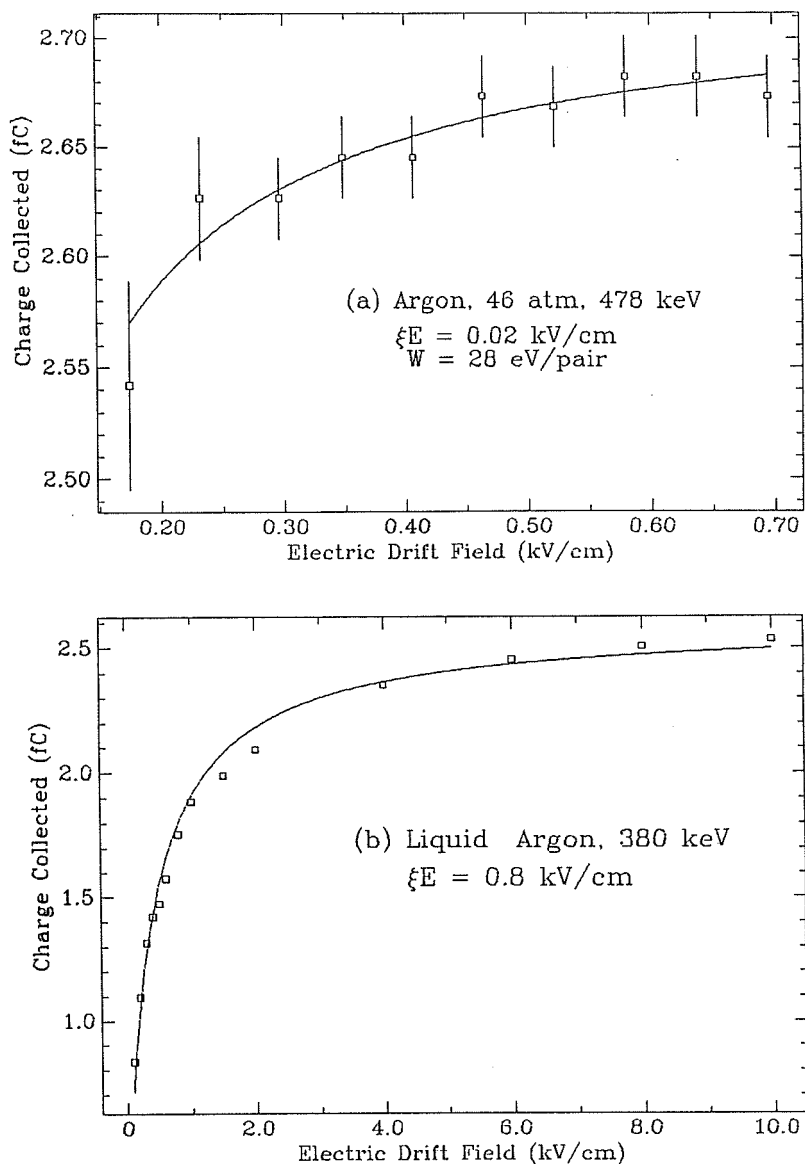


Figure 3-11. (a) Recombination strength measurement in 46 atm argon. The best fit to the single-density model is  $\xi E = 0.02$  kV/cm. (b) Recombination strength measured<sup>35</sup> in liquid argon. The best fit to the single-density recombination model is  $\xi E = 0.8$  kV/cm.

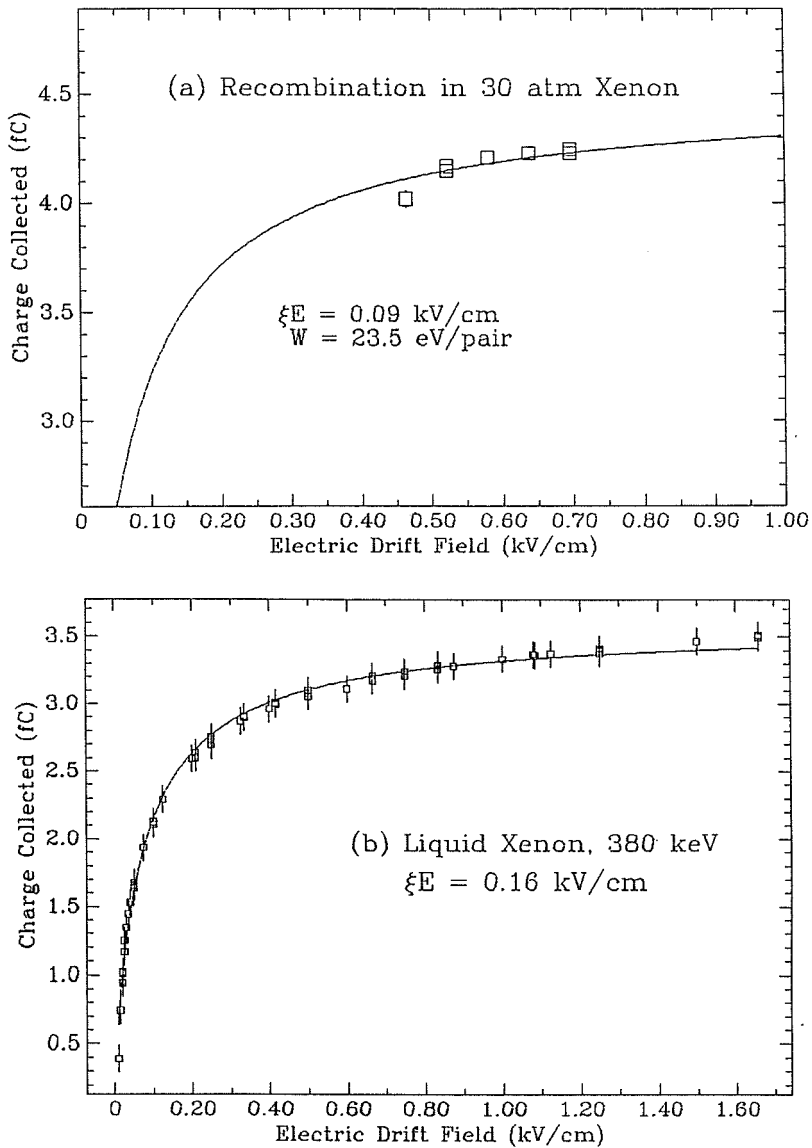


Figure 3-12. (a) Recombination strength measurement in 30 atm xenon. Because of the rapid poisoning of the xenon, the data are uncertain. The best fit to the single-density recombination model is for  $\xi E = 0.09$  kV/cm. (b) Recombination strength measurement in liquid xenon from chapter 2. The best fit to the single-density recombination model is for  $\xi E = 0.16$  kV/cm.

Component	$\Delta Q/Q$
$\delta$ -electron Recombination	0.3%
Shielding Inefficiency of Grid	0.8%
Poisson Statistics	1%
Electronegative Impurities	2%
Capacitive and Electronic Noise	3%

Table 3-3. Contributions to energy resolution at 1 MeV in 70 atm argon detector. Total energy resolution obtained by summing contributions in quadrature is about 4%, in good agreement with the observed energy resolution.

28 eV/pair. Thus, at 1 MeV the rms fluctuation is 190 electrons out of 35,700 produced and the contribution to the energy resolution is about 1% FWHM. The effective range of a 1 MeV electron in 70 atm of argon is about 3 cm, and the attenuation length achievable is about 2 m. Thus, the contribution of electronegative impurities to the energy resolution is about 2%. The electronic noise is typically 30 keV FWHM. Table 3-3 summarizes these estimated contributions to the energy resolution.

In xenon we observe the energy resolution deteriorate rapidly due to decreasing charge collection. Fig. 3-13 shows decreasing charge collection and worsening energy resolution in the space of a few minutes in 30 atm of xenon. Another indication of the deterioration of the xenon detector is shown in

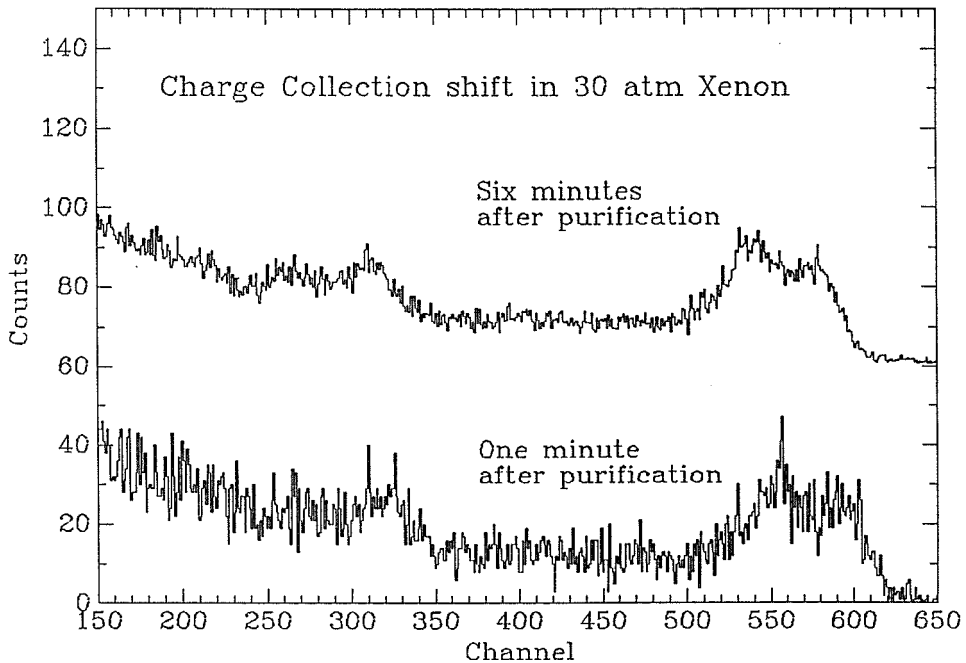


Figure 3-13. Xenon spectra show rapid poisoning. Notice the shift in charge collection in a five minute interval. The shifting charge smears the conversion electron peaks.

Fig. 3-14 where the attenuation length scaled to constant drift fields is plotted as a function of time. Using the variation of the charge collection over the effective range,  $r$  of the 1 MeV electrons, we observe that  $r/\lambda \approx 5\%$  for the best measured attenuation length (50 cm) in xenon. This agrees well with the observed energy resolution.

These data clearly indicate that the xenon is being poisoned. It is not clear what the cause of this poisoning is. One possibility is that the Delrin rings are outgassing. However, one would expect to observe this effect in high pressure argon as well as in the xenon. Fig. 3-14 demonstrates that this effect is



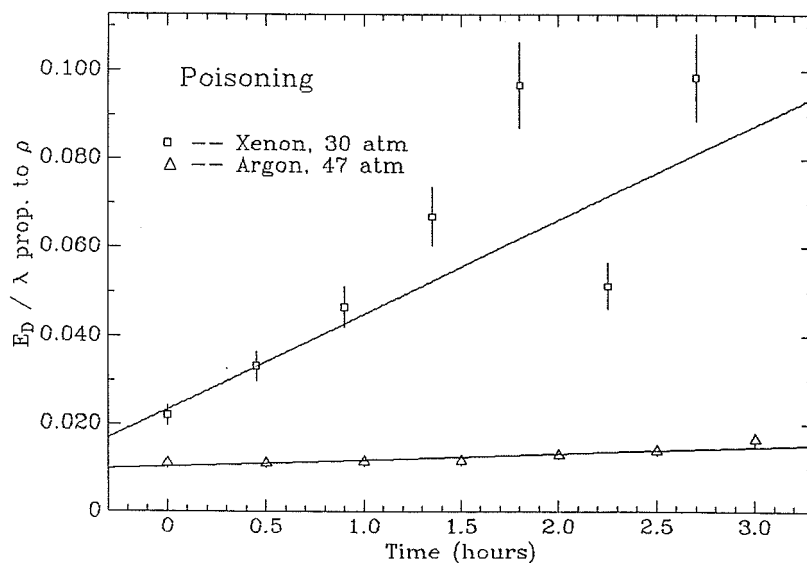


Figure 3-14. Comparison of poisoning in 30 atm xenon and 46 atm argon. The ratio of the electric field strength to the attenuation length (which is proportional to the electronegative impurity concentration,  $E/\lambda \propto \rho$ ) is plotted as a function of time. The argon is obviously much less affected by poisoning than the xenon.

very small in argon. Fig. 3-15 shows a spectrum in 80 atm argon which was accumulated for about 7 hours. The shifting of charge collection apparent in this spectrum is much less than in xenon. Another possibility is that the xenon itself is somehow affected, but the mechanism for this has not been studied by us.

### *Improvements*

In order to improve the energy resolution of the xenon detector, the attenuation length for drifting electrons must be increased and stabilized. One way this may be accomplished would be to add another gas such as methane or hydrogen to improve the drift velocity of the electrons. We attempted to add hydrogen to the xenon detector, but found no improvement at either of the

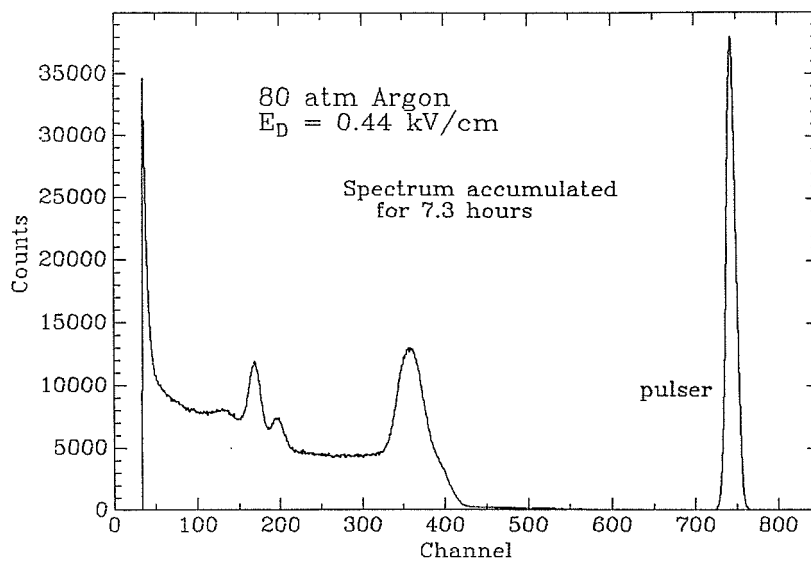


Figure 3-15. The stability of the argon detector, even at high pressures, is illustrated by this spectrum which was accumulated over 7 hours at a pressure of 80 atm. The shift in charge collection is evidently small as demonstrated by the sharp peaks at 482 keV and 555 keV. (The 1 MeV peak is somewhat broad due to incomplete absorption of the electrons in the active region of the detector.)

concentrations attempted: 0.04% and 1.2% hydrogen. In fact, the attenuation length in xenon with hydrogen admixed was slightly worse than that in pure xenon.

One way to maintain a constant attenuation length for drifting electrons would be to use continuous circulation. Indeed, that was the goal of our circulation system. However, any active pumping system generates too much noise in the electronics for a low background experiment. This noise comes both from the vibration of the pump itself along the tubes of the gas-handling system and from the fluctuation in capacitance of the detector due to the small fluctuation in xenon density as it is pushed through the system. By using a

getter between the pump and the chamber on both the inlet and the outlet we were able to reduce the latter noise somewhat, and the former could be reduced by clamping the pump and the gas-handling system. However, the noise cannot be eliminated entirely and provides a catastrophic background even if it has no effect on energy resolution.

We also attempted continuous circulation through the "chimney effect": the purifier was placed in a vertical position and the gas lines for the entire column were heated (as well as the getter) while the return line was cooled. However, the purifier had a large impedance which completely blocked any thermal convection in the column. Other getters with lower impedances could be tried, but the experience of this group<sup>43</sup> is that they introduce microscopic dust particles which contaminate the detector and lead to voltage breakdown.

We suspect that the Delrin may be the major source of the electronegative contamination. We attempted to replace the Delrin rings with other plastics such as polypropylene and high molecular weight polyethylene which were known to be much less hygroscopic than Delrin. These plastics had insufficient strength to serve as a containment vessel for the high pressure gas. We also considered removing the insulating rings altogether and using the Teflon gaskets as insulators for the copper rings. However, the capacitance of such an arrangement is overwhelming (about 7000 pF compared to 200 pF for the detector of Fig. 3-1).

Finally, in Appendix C I discuss a way to improve the energy resolution of an ionization detector for the case of a poor, but constant purity level.

### 3.4 Conclusions

#### *Summary*

We have built and tested a high pressure ionization chamber. We measure the (noise-subtracted) energy resolution at 30 atm of xenon to be 3% FWHM at 1 MeV for a 0.7 kV/cm drift field, and at 108 atm of argon to be 2% FWHM at 1 MeV for a 0.5 kV/cm drift field. The detector is limited by capacitive noise when operated in argon and by the ability to drift electrons in xenon.

The recombination strength in high-pressure argon has been shown to be drastically reduced from that of liquid argon, and it is observed that recombination of  $\delta$ -electrons is no longer a significant contribution to the energy resolution in this density regime.

The dependence of the attenuation length for drifting electrons in the presence of electronegative impurities has been measured. It is found that  $\lambda \propto P^{-2}$  for a constant electronegative impurity concentration.

We conclude that although the high pressure argon detector provides both good energy resolution and stopping power, the high pressure xenon detector is unsuitable for a  $\beta\beta$ -decay experiment because of the inability to stabilize charge collection while simultaneously achieving good energy resolution.

## CHAPTER FOUR

### A Solid Xenon Ionization Chamber

#### 4.1 Motivation

We have now examined noble gases in the liquid and high-pressure phases. What remains is the solid phase. As mentioned in chapter 2, it is possible that recombination in the solid will be somewhat less than in the liquid, since the electron mobility may improve at lower temperature<sup>36</sup>. This improvement may be offset by the decrease in lattice parameter with decreasing temperature<sup>8</sup>.

The solid state of xenon may have other advantages over the liquid and gaseous phase. From an experimental point-of-view, a solid xenon ionization chamber is advantageous in that once a crystal is condensed, the temperature need only be kept below the freezing point. In addition, the density<sup>8</sup> of solid xenon ( $3.4 \text{ g/cm}^3$  at 160 K to  $3.7 \text{ g/cm}^3$  at 77 K) is somewhat higher than liquid xenon ( $2.8 \text{ g/cm}^3$ , pressurized, at 195 K to  $3.1 \text{ g/cm}^3$  at the boiling point, 165 K). The increased density would mean shorter electron tracks and therefore higher efficiency. It also means that for a given number of candidate atoms the exposure to background radiation is diminished.

Much research has been done<sup>28,44</sup> with liquid argon ionization chambers, especially by Hoffmann<sup>34</sup> and Chen<sup>45</sup>. Solid argon ionization chambers have

been studied by Grebinnik<sup>46</sup>, Cobb<sup>47</sup> and Aprile<sup>48</sup>. Fewer groups have studied liquid xenon ionization chambers<sup>20,27,49,50</sup>, although the group at Waseda University led by Tadayashi Doke has conducted a long-running series of liquid xenon studies. (See for example ref. 27.) Finally, although Gullikson<sup>51</sup> has studied secondary-electron emission in thin films of solid xenon, Pisarev<sup>52</sup> has studied charge production and Miller<sup>36</sup> and Gushchin<sup>53</sup> have studied charge transport in solid xenon, there is no previous report of solid xenon ionization spectra. This chapter presents the work in solid and liquid xenon and argon radial ionization detectors which has been submitted for publication (Imel, submitted to Nucl. Instrum. Methods A, 1990).

Previous attempts by Doke<sup>27</sup>, Barabash<sup>49</sup> and Aprile<sup>50</sup>, as well as our own<sup>21</sup>, to build liquid xenon ionization detectors have usually employed a parallel-plate gridded design. This is probably unsuitable for a solid xenon detector because it is difficult to grow the crystal through a grid. Thus, a gridless radial ionization chamber is preferable due to its simplicity. In a gridless detector, the charge induced on the anode will be a function of event position. Thus, one assumes at first that a gridless detector will have poor or no energy resolution. However, the electric field in a radial detector is a function of radial position, and thus so is the recombination strength. By adjusting the geometry and the electric field strength in the radial detector, using the competing processes of charge induction on the anode, recombination and attachment of drifting electrons, one may cancel most of the position-dependence of the charge collection, and achieve energy resolution in the range of 10%-20% FWHM. This should be sufficient for a  $2\nu$   $\beta\beta$ -decay experiment.

Pisarev<sup>52</sup> built a radial solid xenon ionization chamber. However, the geometry was not optimized as described in the previous paragraph. In fact, a very small anode (10  $\mu\text{m}$ ) was used in order to achieve charge multiplication and Geiger mode operation. This had the effect of sacrificing any energy resolution otherwise achievable. No energy spectrum was reported from that work.

## 4.2 Principles of Operation for a Radial Ionization Chamber

Three factors influence the charge collection in radial ionization chambers, as discussed by Knoll<sup>31</sup>: image charge induction, recombination and attachment to electronegative impurities during electron drifting.

### *Image charge*

The detector has a non-linear electric field strength:

$$E(r) = \frac{V}{\log_e(B/A)} \frac{1}{r}, \quad (4-1)$$

where  $A$  and  $B$  are the radii of the anode and cathode,  $V$  is the potential difference, and  $r$  is the radial coordinate. Thus, the image charge induced is a function of position of the event and, in the absence of attachment to electronegative impurities, is given by:

$$\frac{Q_i}{Q_r}(r) = \frac{\log_e(r/A)}{\log_e(B/A)}, \quad (4-2)$$

where  $Q_i$  is the charge induced on the anode,  $Q_r$  is the charge which survives initial recombination of the electrons and ionized atoms in the drift medium,

and  $r$  is the radial position of the event.

Recombination Parameters		
Parameter	LXe	LAr
$\xi_0 E$	$1.9 \pm 0.5$ kV/cm	$3.4 \pm 0.7$ kV/cm
$\xi_1 E$	$0.13 \pm 0.3$ kV/cm	$0.34 \pm 0.12$ kV/cm
$b$	$(6.76 + 216E_p^{-1})^{\frac{1}{2}}$	$(4.52 + 157E_p^{-1})^{\frac{1}{2}}$
$a$	$0.203 + 12.2E_p^{-1}$	$0.291 + 16.7E_p^{-1}$

Table 4-1. The measured<sup>21</sup> recombination parameters in liquid xenon and argon. Since  $\xi \propto 1/E$ , what is actually measured is the product,  $\xi E$ , of the recombination strength and the electric field strength.  $E_p$  is the energy of the primary particle, in keV.

### Recombination

We use our model<sup>22,23</sup> for the charge surviving recombination:

$$\frac{Q_r}{Q_0} = a \frac{1}{\xi_0} \log_e(1 + \xi_0) + (1 - a) \frac{1}{\xi_1} \log_e(1 + \xi_1), \quad (4-3)$$

where  $Q_0$  is the initial charge created by the ionization event,  $\xi_{0,1}$  are the recombination strengths of the high and low charge density regions created by  $\delta$ -electrons and the minimum-ionizing portion of the electron track, respectively. The recombination strengths are inversely proportional<sup>22</sup> to the electric



field,  $\xi_{0,1}(r) \propto 1/E(r)$ . The “ $\delta$ -electron ratio”,  $c$ , expresses the portion of ionization in each of the charge density regions. The recombination strengths and  $\delta$ -electron ratio for xenon and argon have been experimentally determined by us<sup>21</sup>. (See Table 4-1.) Other models<sup>54-56</sup> for recombination also based on the principle of separate recombination strengths for the high and low charge density regions have been empirically derived and have an electric field dependence similar to that of (4-3).

#### *Attachment*

Finally, the charge surviving attachment<sup>34,57</sup> to electronegative impurities is approximately given (for constant electric field) by:

$$\frac{Q_a}{Q_r}(d) = e^{-\frac{d}{\lambda}}, \quad (4-4)$$

where  $d$  is the drift distance, and  $\lambda$  is the attenuation length given by  $\lambda = \alpha E / \rho$ , for  $E$  in kV/cm,  $\rho$ , the impurity concentration, in parts-per-million (ppm) O<sub>2</sub> equiv., and  $\alpha$  a measured<sup>34,35</sup> constant, 0.15 cm<sup>2</sup>-ppm/kV in argon and 0.2 cm<sup>2</sup>-ppm/kV in (xenon). In the spatially-varying electric field of (4-1), attachment is given by:

$$dQ = -Q \frac{\rho dx}{\alpha E(r)}, \quad (4-5)$$

where  $dx$  is a small drift distance. Collecting terms, we define a new constant  $\kappa$ :

$$\frac{dQ}{Q} = -2 \frac{r dx}{\kappa^2}, \quad (4-6)$$

where

$$\kappa^2 \equiv \frac{2\alpha V}{\rho \log_e(B/A)}. \quad (4-7)$$

( $\kappa$  is the analogue of the attenuation length,  $\lambda$ , in the case of a radial geometry.)

Now integrate both sides from zero distance drifted ( $x = 0$ ) until the electrons reach the anode ( $x = r - a$ ):

$$\frac{Q_a}{Q_r}(r) = e^{-\frac{r^2 - A^2}{\kappa^2}}. \quad (4-8)$$

To calculate the charge induced on the anode as drifting electrons are attenuated, one must integrate the *attenuated* charge induced as it drifts into the anode:

$$\frac{Q_{a,i}}{Q_r} = \frac{1}{\log_e(B/A)} \int_A^r \frac{dx}{x} e^{-\frac{r^2 - x^2}{\kappa^2}} \quad (4-9)$$

$$\frac{Q_{a,i}}{Q_r} = \frac{e^{-\frac{r^2}{\kappa^2}}}{2\log_e(B/A)} \left[ \text{Ei}\left(\frac{r^2}{\kappa^2}\right) - \text{Ei}\left(\frac{A^2}{\kappa^2}\right) \right]. \quad (4-10)$$

$\text{Ei}(x)$ , the exponential-integral, is defined<sup>58</sup> by:

$$\text{Ei}(x) \equiv \int_{-\infty}^x \frac{dt}{t} e^t. \quad (4-11)$$

The previous expression can be approximated<sup>58</sup> to 1% for  $\kappa > 2r$  by:

$$\frac{Q_{a,i}}{Q_r}(r) \approx \frac{\log_e(r/A)}{\log_e(B/A)} e^{-\frac{r^2}{\kappa^2}} \left[ 1 + \frac{r^2 - A^2}{2\kappa^2 \log_e(r/A)} \right]. \quad (4-12)$$

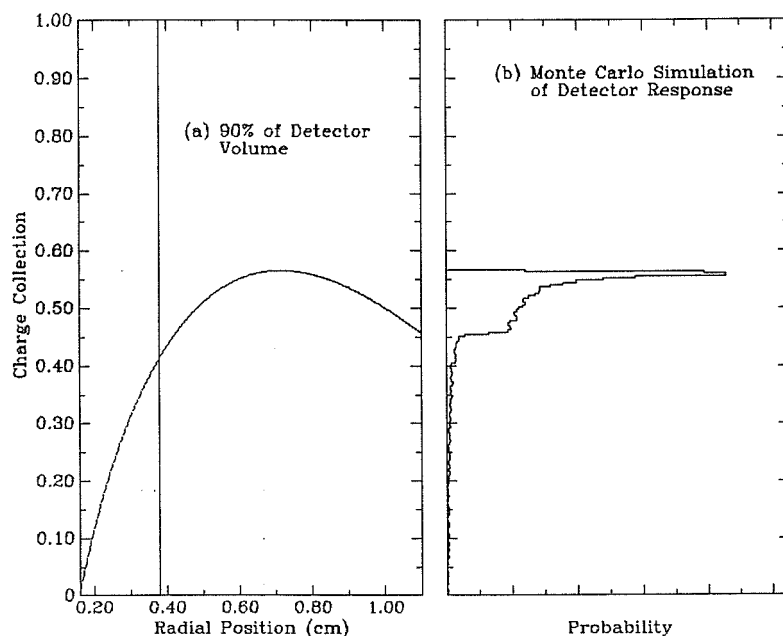


Figure 4-1. (a) Calculation using (4-3) and (4-12) of the charge collection as a function of radial distance from the anode of a (gridless) cylindrical ionization chamber. The charge collection is approximately constant over 90% of the detector volume. This curve is for the case of a liquid argon detector with a 2.2 cm diameter cathode, 3.2 mm anode, an electronegative impurity concentration of 300 ppb  $O_2$  equivalent, and 2.5 kV potential difference across the detector. (b) Monte Carlo simulation of the detector lineshape using the parameters of the charge collection curve in (a). The y-axes of (a) and (b) correspond, and the x-axis of (b) is proportional to the number of counts per bin.

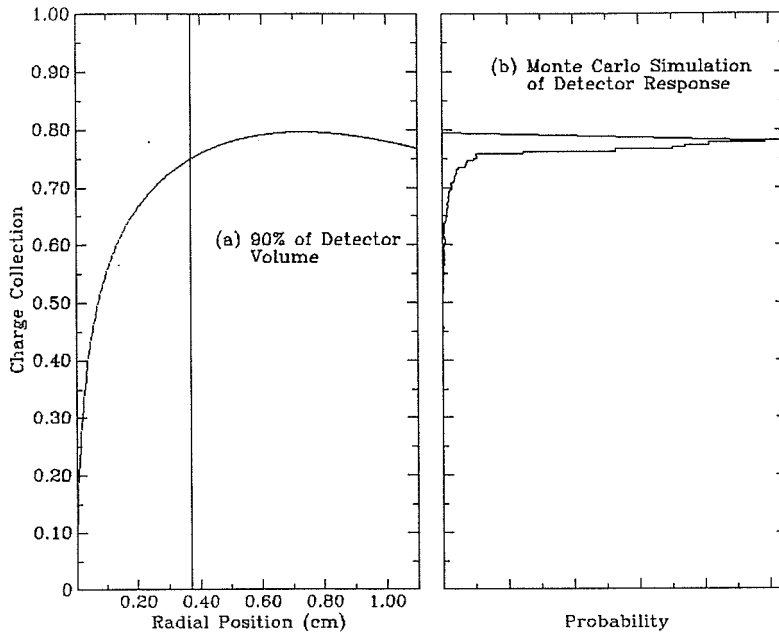


Figure 4-2. (a) Calculation of charge collection in a radial detector as in Fig. 4-1. The parameters in this case are: 2.2 cm cathode diameter, 0.1 mm anode diameter, 20 ppb impurity concentration and 3.0 kV potential difference. (b) Simulation of detector lineshape for the parameters of the detector described in (a).

### *Lineshape*

These three effects, which cause the charge collection to be a function of radial position, can be adjusted to approximately cancel each other and thus provide almost uniform charge collection over the majority of the detector. Fig. 4-1a shows the total charge collection ( $[Q_{a,i}/Q_r] \times [Q_r/Q_0]$ ) as a function of  $r$ . By optimizing the anode diameter for a given purity level, detector size, and voltage range, the effects of image charge induction, attachment to electronegative impurities, and initial recombination have been caused to cancel, making the charge collection approximately uniform over 90% of the detector volume.

This is a larger active volume than most gridded ionization detectors achieve. Fig. 4-1b shows a Monte Carlo simulation of the lineshape for one set of detector parameters. The response has a long tail, but 90% of the events occur within 5% of 52% charge collection. This means that the energy resolution should be better than 20% FWHM in an actual detector with these parameters. With lower electronegative-ion concentrations, the geometry can be optimized such that the energy resolution is better than 10% FWHM. (See Fig. 4-2.)

It should be noted that although these calculations use constants measured in liquid xenon and argon, one expects that the behavior of electrons will be approximately the same in the solid. Comparisons between the solid and liquid phase in the same detector should prove to be interesting.

### 4.3 The Experimental Apparatus

#### *Design*

Two detector geometries were used in the experiments and are shown in Figs. 4-3 and 4-4. The chamber and gas-handling system are constructed entirely of high-vacuum materials such as stainless steel and OFHC (oxygen-free, high-conductivity) copper. A window<sup>41</sup> was placed above both detectors so that the crystal condensation process may be observed. This was a critical addition to the apparatus. The importance of being able to see the detector medium was made clear when, during an early experiment where the count rate for a strong source seemed excessively low, the detector was removed

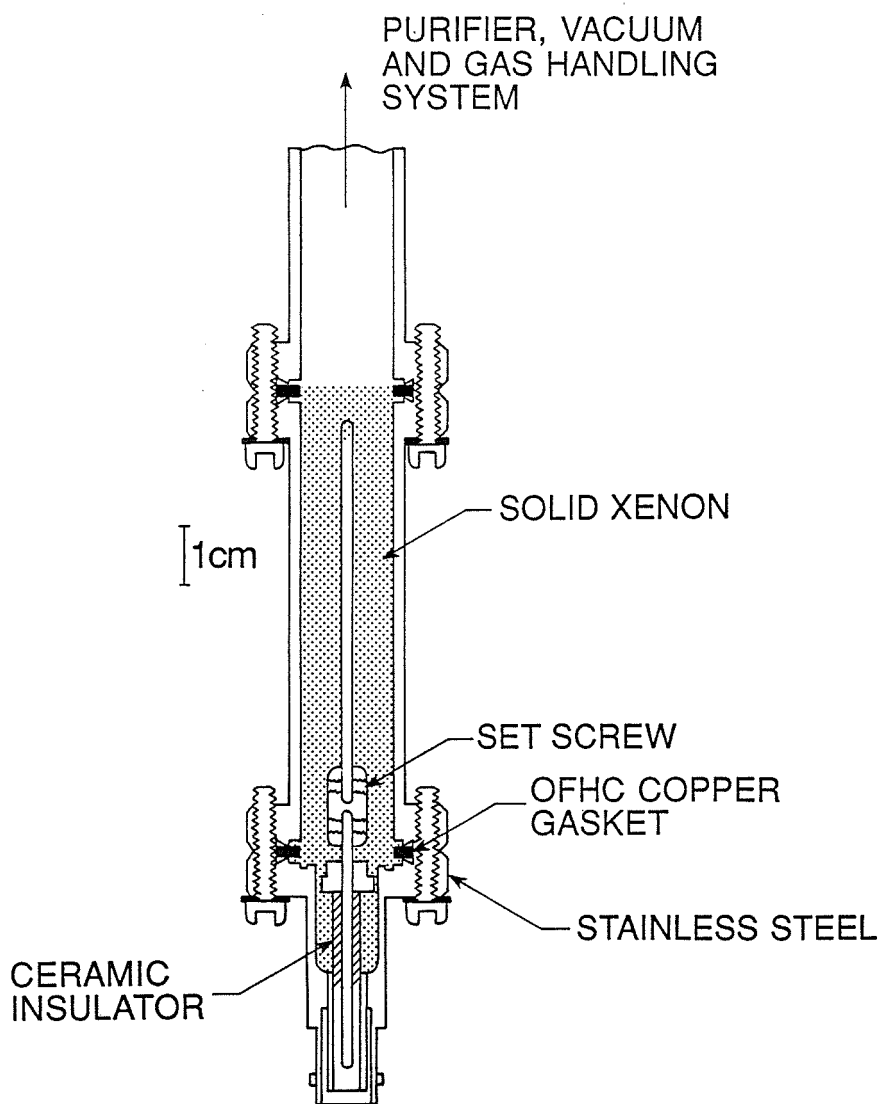


Figure 4-3. The 0.3 mole detector.

while still cold and found not to have any argon condensed at all. The window also allowed observation of the quality of the crystal which was condensed, as well as how much of the detector was filled with liquid and how much was

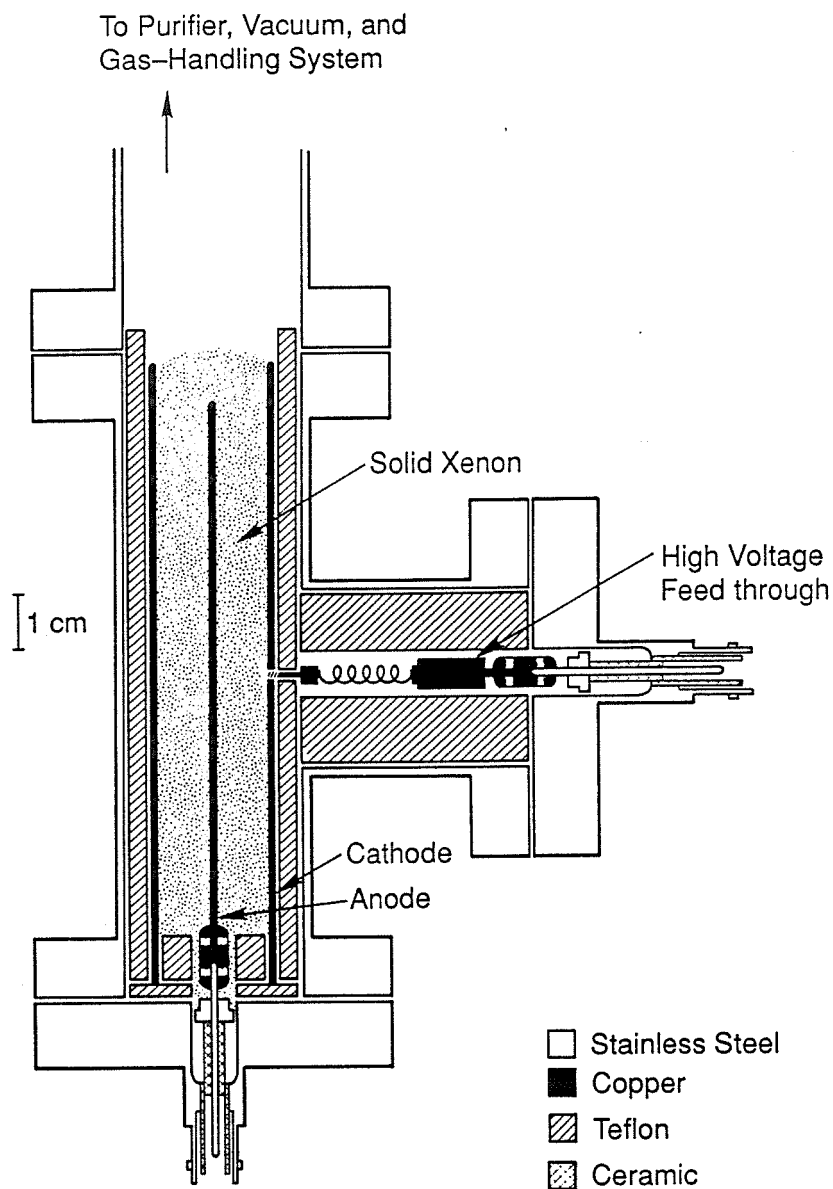


Figure 4-4. The 0.9 mole detector.

solid.

The detector in Fig. 4-3 has an active volume of 0.3 mole and was constructed using stainless steel tubing and feedthroughs<sup>41</sup>. The anode wire

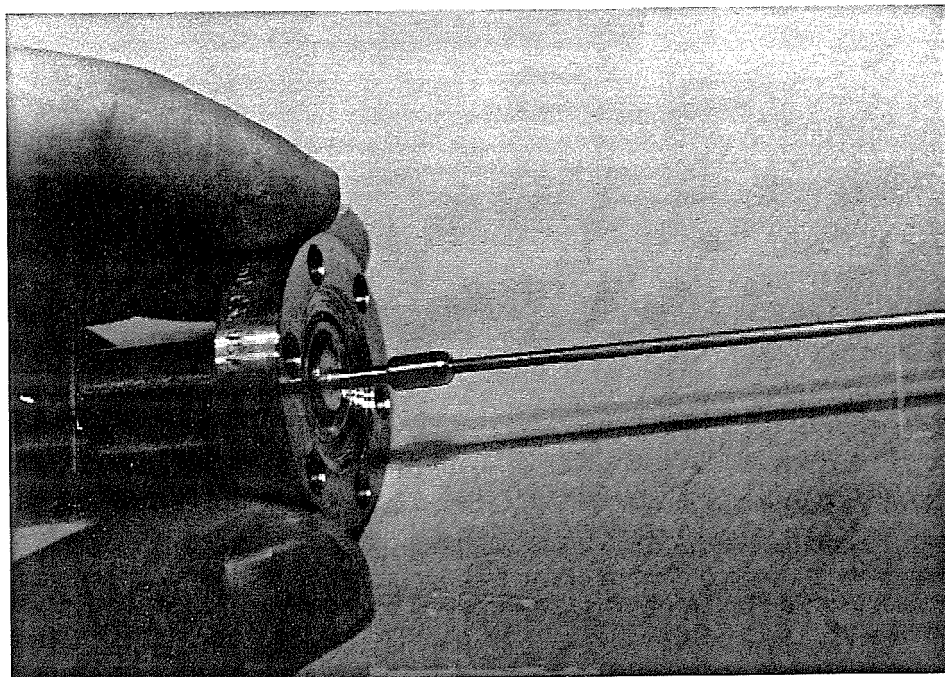


Figure 4-5. Signal feedthrough and anode wire for the 0.3 mole detector.

(Fig. 4-5) is 1.6 mm in diameter and the cathode wall has a diameter of 1.6 cm. In this detector, the high-voltage was applied to the anode. The anode wire was joined to the feedthrough with the only specially machined part in this experiment.

In the detector of Fig. 4-4, the high-voltage was applied to the cathode and the anode was at ground potential. This allowed the latter to operate at much higher voltages than the former. This 0.9 mole detector was constructed using a BNC signal feedthrough, high-voltage feedthrough (Fig. 4-6) and a standard high-vacuum tee into which were inserted a Teflon tube for insulation and a copper tube to serve as the high-voltage cathode. The anode wire is 3.2 mm in diameter and 10 cm long. The cathode wall has an inner diameter of 2.2 cm.



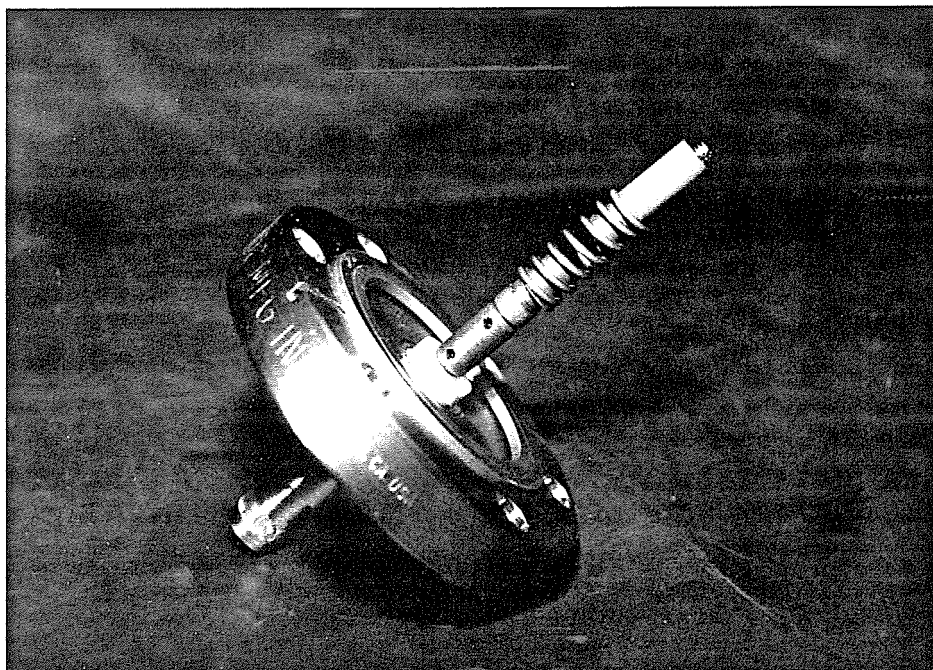


Figure 4-6. The high-voltage feedthrough for the 0.9 mole detector.

In order to avoid small pockets of trapped air (virtual leaks), flats were cut on the outside of the copper and Teflon cylinders and a slot was cut in the screw attaching the high-voltage feedthrough to the copper cylinder. The anode was attached to the signal feedthrough using a double socket. The feedthrough and anode were anchored using small copper-beryllium set-screws which were recessed into the body of the socket when tightened so as not to provide a sharp point for high-voltage discharges.

#### *Preparation*

Before assembly, all components of the detector were cleaned according to the standard techniques listed in chapter 1. After assembly, the system is evacuated to better than  $10^{-8}$  torr with the help of a turbo-molecular pump.

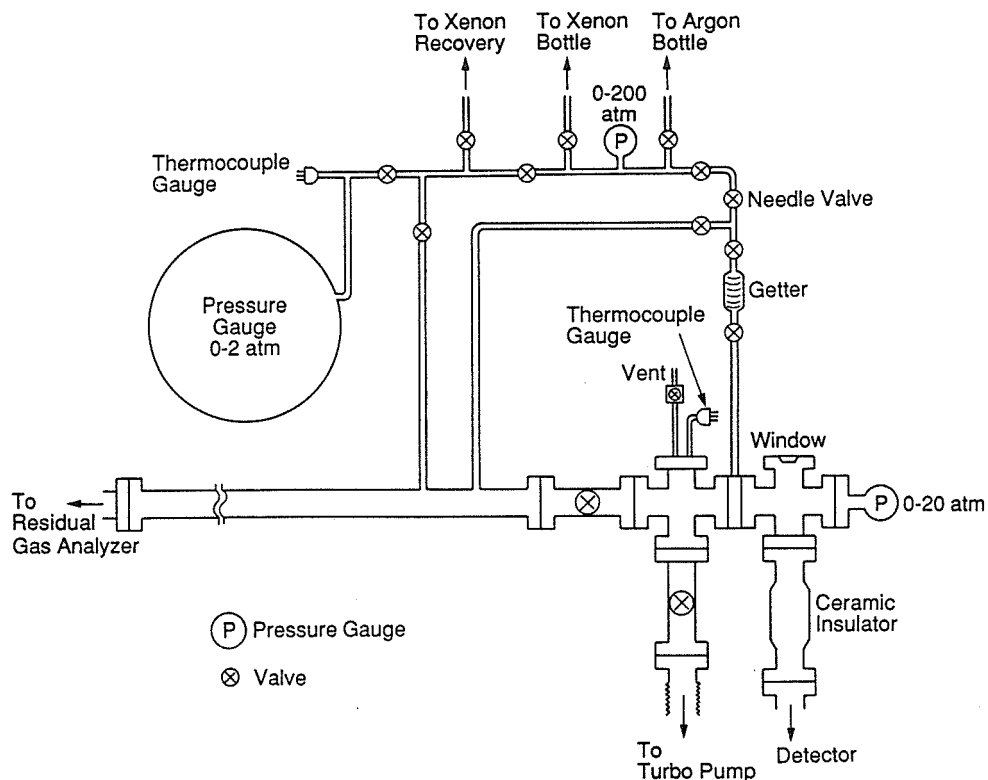


Figure 4-7. Gas handling and purification system for the radial ionization detector.

The 0.3 mole detector is warmed during pumping for about 60 hours to approximately 400 °C (monitored with a thermocouple gauge). The 0.9 mole detector could only be warmed to 100 °C because of the Teflon pieces inside which begin to lose their shape at higher temperatures. The residual gas analyzer (RGA) installed in the gas-handling system was useful in determining the sources of outgassing or leaks, but was too insensitive to determine the purity of the argon or xenon gas used as a detector medium. Fig. 4-7 is a schematic of the gas-handling system for this series of experiments.

### *Purification*

The gas is purified by passing through a SAES (Zr-V-Fe) getter<sup>42</sup> which removes all electronegative impurities typically encountered in these gases.

The purifier has a volume of 150 ml and is installed in a vertical position to prevent channeling. It is prepared by heating in vacuum to 450 K for one hour prior to the first use. The temperature is maintained by a thermocouple-controlled regulator at 400 K during the condensation process. The purifier is placed immediately above the detector and is the last stage in the gas-handling system before condensation, so that contamination due to outgassing from the gas-handling system walls is minimized.

### *Condensation*

In order to condense liquid and solid argon, the detector was submerged in a liquid nitrogen bath. First, the liquid would condense. When the liquid argon level reached the liquid nitrogen level outside the detector, the argon could either be frozen or maintained as a liquid by controlling the pressure of the argon. This was accomplished by adjusting the amount of argon allowed into the detector from the purifier. The competition between condensation and incoming argon determined the pressure and thus the phase of the detector medium.

Two methods were used to condense and freeze xenon: a cryostat and a pentane bath. A copper-constantan-copper thermocouple<sup>59</sup> was used to monitor the temperature of the detector. One end of the thermocouple was attached to the detector, and the other was placed in a liquid nitrogen bath in order to provide a constant, known reference temperature. The calibration curve<sup>59</sup> for this thermocouple is plotted in Fig. 4-8. Good empirical fits to this curve are given by:

$$V = a_0 + a_1 \left( \frac{T}{T_0} \right) + a_2 \left( \frac{T}{T_0} \right)^2 + a_3 \left( \frac{T}{T_0} \right)^3 \quad (4-13a)$$

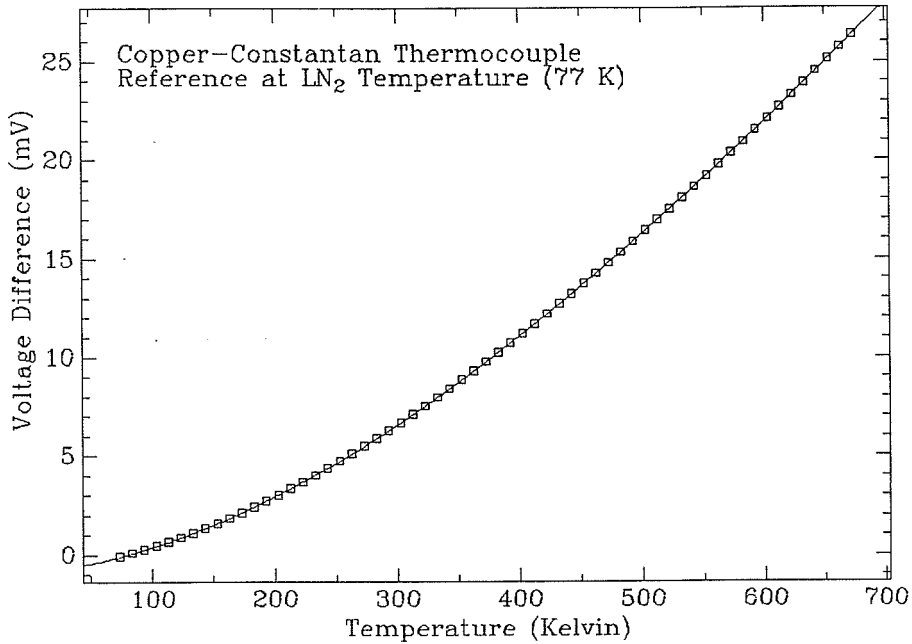


Figure 4-8. Calibration curve for copper-constantan thermocouple, referenced to liquid nitrogen bath. The smooth line is the fit of (4-13) and Table 4-2.

and

$$T = T_0 + b_1 \left( \frac{V}{V_0} \right) + b_2 \left( \frac{V}{V_0} \right)^{\frac{1}{2}} + b_3 \left( \frac{V}{V_0} \right)^{\frac{1}{3}}, \quad (4-13b)$$

where  $V$  is the potential difference between the measured temperature,  $T$ , and the liquid nitrogen reference temperature (77 K). Table 4-2 gives the values of the coefficients in this fit.

A cryostat cooled by liquid nitrogen (Fig. 4-9) was used to condense xenon in the 0.3 mole detector. The copper cold-finger which conducted heat from the detector to the liquid nitrogen bath was insulated by a stainless steel tube and vacuum ( $< 10^{-3}$  torr). A thin stainless-steel bellows<sup>41</sup> soldered to the

Thermocouple Parameters			
Parameter	Value (mV)	Parameter	Value (K)
$V_0$	1.0	$T_0$	77
$a_0$	-0.891		
$a_1$	0.470	$b_1$	5.71
$a_2$	0.424	$b_2$	142
$a_3$	-0.0138	$b_3$	-95.2

Table 4-2. The values of the parameters for the fit to the thermocouple potential difference temperature-dependence, (4-13a,b).

copper cold-finger and a flange allowed the cold finger to make a good thermal connection with the detector while still being insulated from the cryostat and the atmosphere. Styrofoam (6 cm thick) was used to insulate the detector from the environment. In this way, the temperature of the detector saturated at 162 K, just above the freezing point of xenon, and allowed a stable operating temperature to be achieved.

A pentane bath cooled by liquid nitrogen to as low as 145 K was used to condense and freeze solid xenon in the 0.9 mole detector. Other possible baths for use with condensed xenon are shown in Table 4-3.

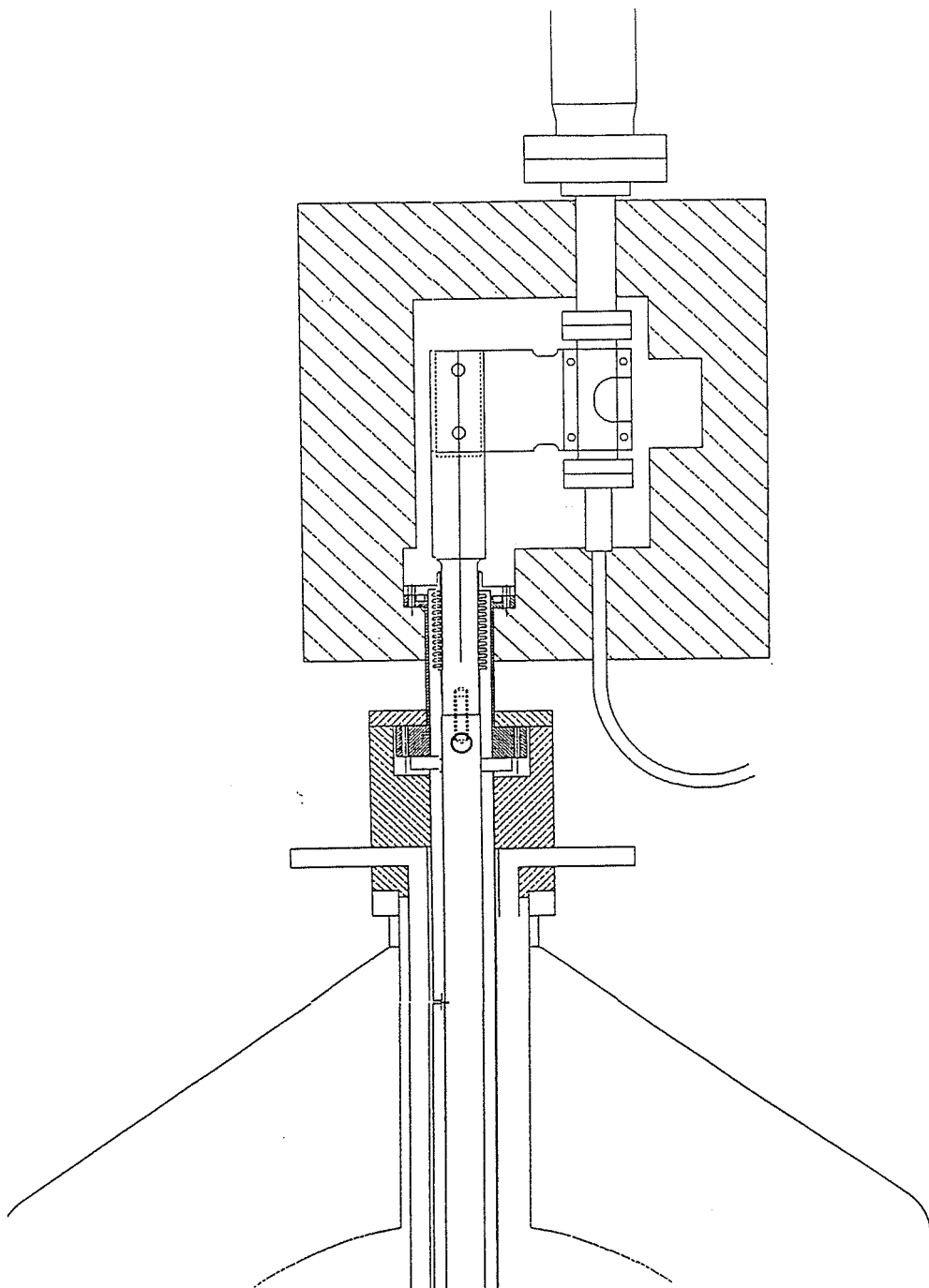


Figure 4-9. The cryostat for the 0.3 mole detector.

Typically, the crystals condensed from the melt using these methods would be initially translucent, and then rapidly become opaque. Occasionally, however, a crystal would remain translucent so that comparisons in

Low Temperature Liquid Baths	
Compound	Melting Point
Isopentane (2-Methyl butane)	113.3 K
Methyl cyclopentane	130.8 K
Allyl chloride	138.7 K
n-Pentane	143.5 K
Allyl alcohol	144.2 K
Ethyl alcohol	155.9 K
Carbon disulfide	162.4 K
Isobutyl alcohol	165.2 K

Table 4-3. Liquid baths useful for condensing xenon. (This table is condensed from ref. 59.)

performance between an opaque and translucent crystal could be made. No difference in energy resolution was observed between these two cases in either argon or xenon.

#### *Electronics*

The anode is connected to a room temperature preamplifier (EG&G Ortec 142A). The preamplifier pulses are shaped and amplified by a spectroscopy amplifier and fed into a multi-channel pulse-height analyzer. The usual

shaping time for the amplifier is  $12 \mu\text{s}$ , although shaping times as short as  $1 \mu\text{s}$  have been explored. The spectra are stored on a computer. A pulser is used to assist in calibration and to determine the contribution of electronic noise to the energy resolution. The typical noise contribution to the energy resolution is 30 keV in xenon. The capacitive noise is dominated by the capacitance of the cable, which was about 100 pF/m, whereas the detector capacitance was about 10 pF.

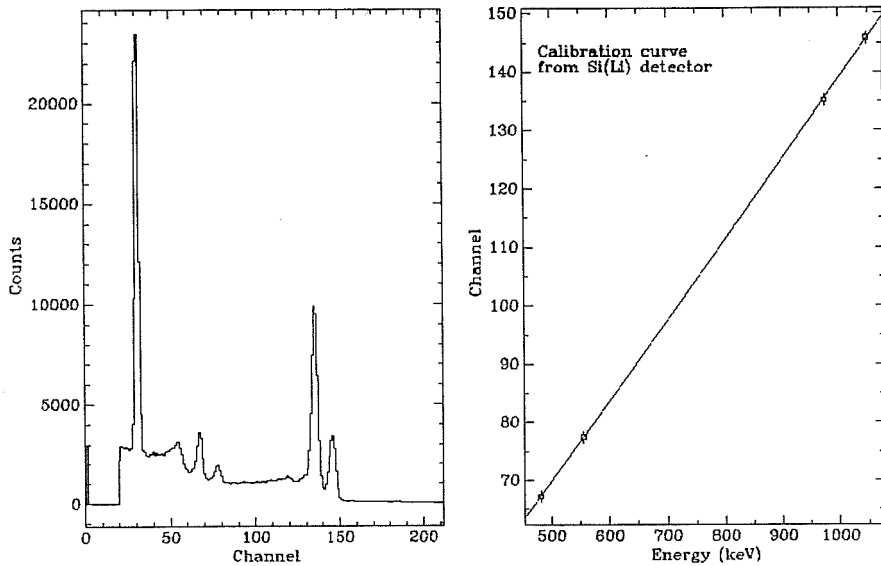


Figure 4-10. Calibration of pulser. (a)  $^{207}\text{Bi}$  spectrum taken in a cooled semiconductor detector. The large peak around channel 30 is the pulser peak. (b) Calibration curve using features of spectrum in (a).



### *Calibration*

The absolute charge calibration was accomplished (to within  $\pm 5\%$ ) by using the same electronics with a cooled Si(Li) detector and a  $^{207}\text{Bi}$  source. Fig. 4-10(a) shows the spectrum from this source. The peaks from the  $^{207}\text{Bi}$  source are fit with a straight line in Fig. 4-10(b). Thus, the pulser dial was calibrated to be  $3.25 \pm 0.2$  fC/division, and the absolute charge collected in any spectrum could be calculated using the pulser as a reference.

## **4.4 Performance**

### *Spectra*

Spectra in argon from the 0.3 mole detector are displayed in Fig. 4-11 and in xenon in Fig. 4-12. Figs. 4-13 and 4-14 display spectra in argon and xenon, respectively, from the 0.9 mole detector. Detailed comparisons of spectra taken in these detectors with different condensation techniques, voltages, pressures, filling levels and sources are shown in Appendix D.

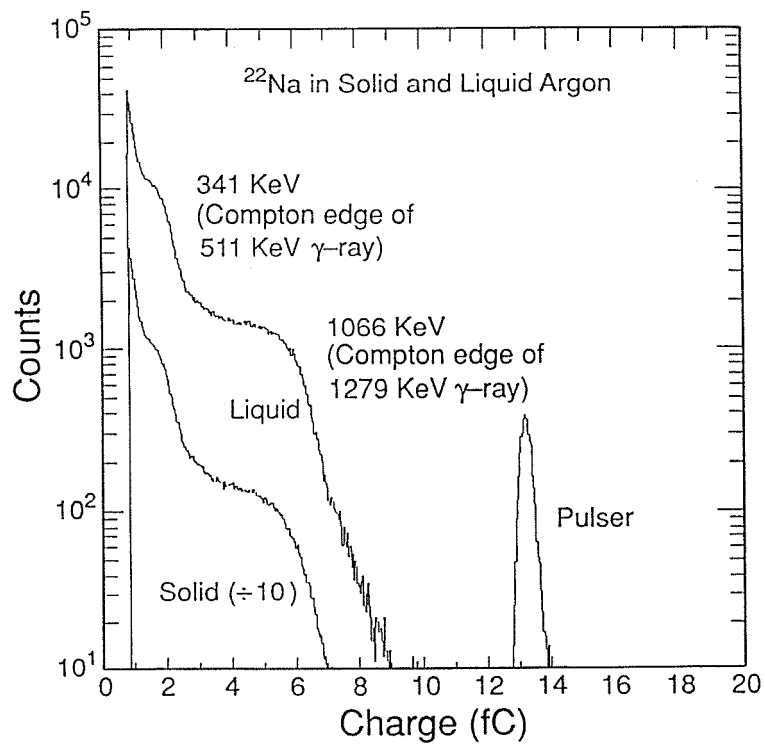


Figure 4-11. Liquid and solid argon spectra from the 0.3 mole detector. The voltage between anode and cathode is 3.0 kV.

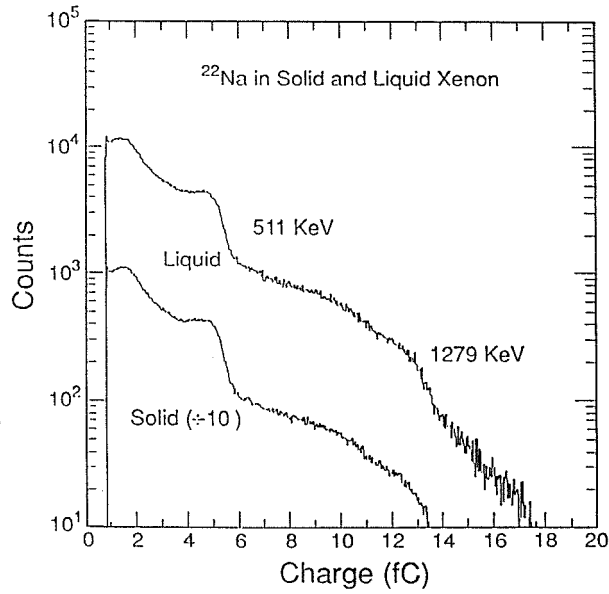


Figure 4-12. Liquid and solid xenon spectra from the 0.3 mole detector. The voltage between the anode and cathode is 2.1 kV.

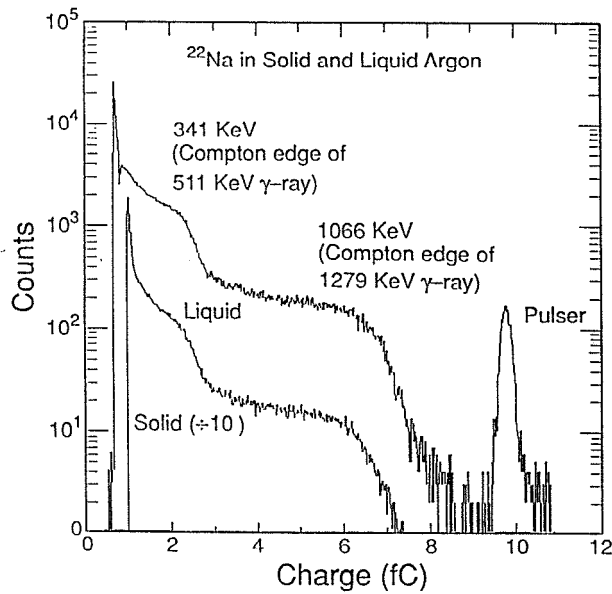


Figure 4-13. Liquid and solid argon spectra from the 0.9 mole detector. The voltage between the anode and cathode is 3.0 kV.

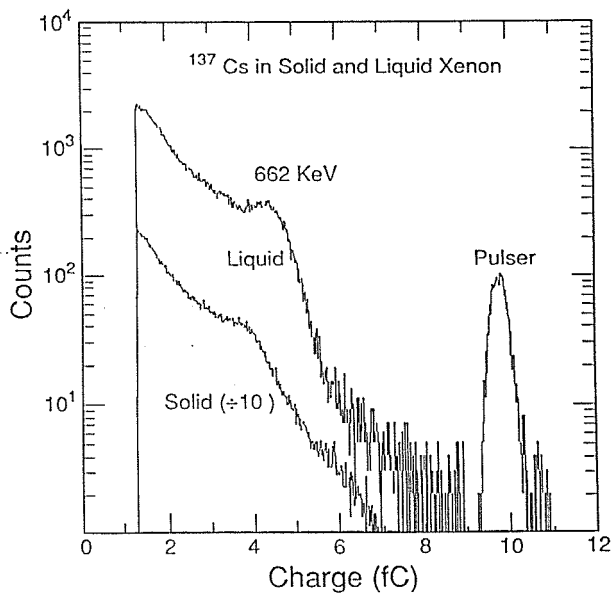


Figure 4-14. Solid and liquid xenon spectra from the 0.9 mole detector. The liquid spectrum was accumulated with a voltage of 1.1 kV and the solid, 0.6 kV.

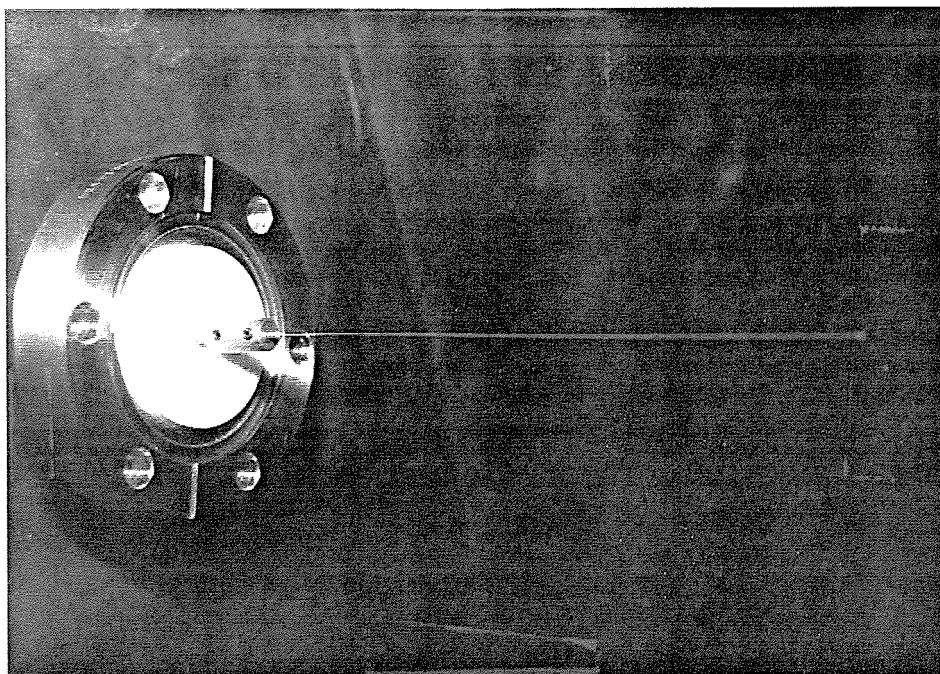


Figure 4-15. Small diameter anode with connector, feedthrough and Teflon insulator.

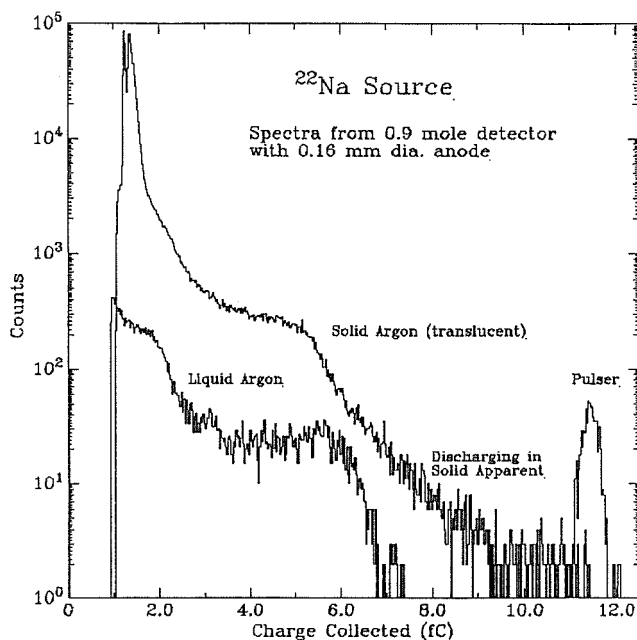


Figure 4-16. Spectrum in solid and liquid argon using the 0.9 mole detector with the small diameter anode. Note especially the micro-discharging evident in the solid argon spectrum.

### *Test of a Smaller Anode*

A smaller diameter (0.16 mm) anode (Fig. 4-15) was tested with solid argon in the 0.9 mole detector. In order to center this anode, a Teflon cross was installed at the top of the Teflon tube, with a locating hole at the center of the cross. In this way, not only was the anode centered in the detector, but it was also insulated against discharging at the point of the anode.

The energy resolution was somewhat worse, typically 20% FWHM at 1066 keV. With this anode, proportional multiplication was observed at voltages as low as 3 kV in the solid, causing further deterioration of the energy resolution. Spectra using this anode are displayed in Fig. 4-16, and a more extensive discussion and display of spectra from this detector is in Appendix D.

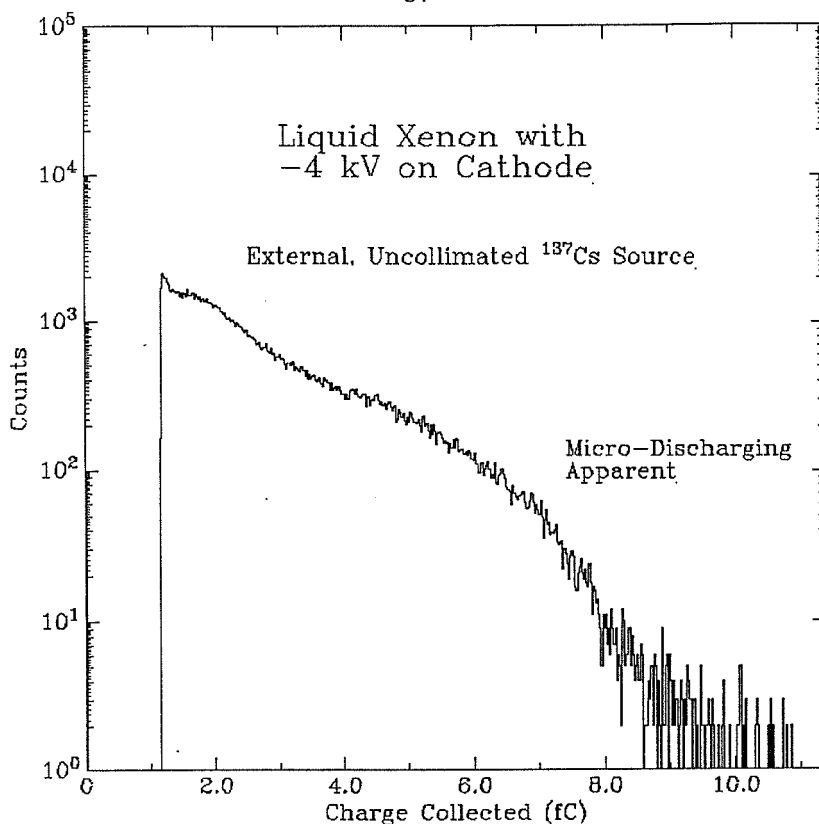


Figure 4-17.  $^{137}\text{Cs}$  spectrum using liquid xenon in 0.9 mole detector at high voltage. Spectrum is smeared out considerably by micro-discharging.

### *Discharging*

One difficulty in using xenon (both solid and liquid) is that at voltages above 2 kV micro-discharging occurs in both detectors. This was not observed in either liquid or solid argon at voltages up to 7 kV. An example of discharging in xenon spectra is shown in Fig. 4-17.

### *Linearity and Charge Collection*

The linearity of the 0.3 mole solid xenon detector is shown in Fig. 4-18a, and of the 0.9 mole liquid argon detector in Fig. 4-18b. From these data the percentage charge collection, assuming the liquid W-values of 15.6 eV for xenon and 23.3 eV for argon, may be calculated at these voltages. In Fig. 4-18a

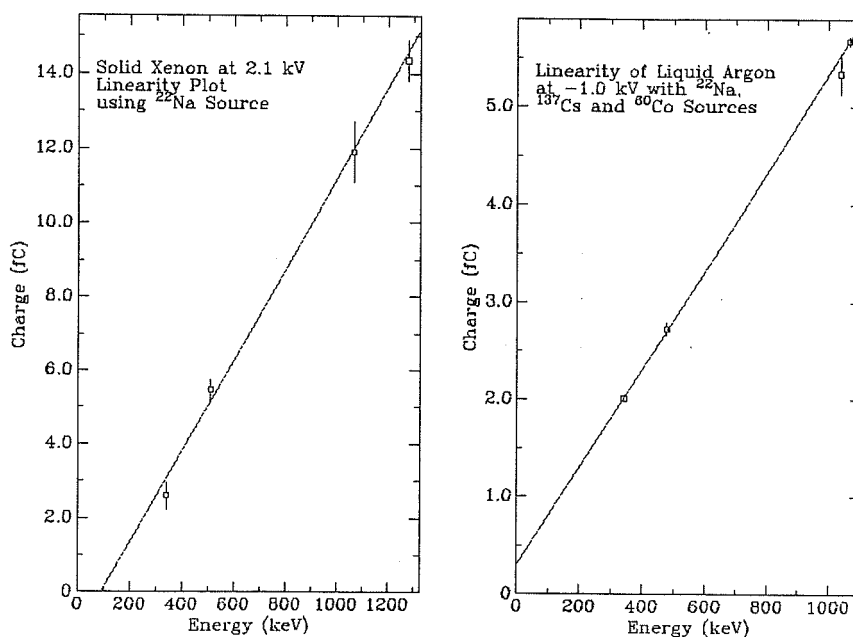


Figure 4-18. Linearity of charge collection in the radial ionization detectors with (a) solid xenon and (b) liquid argon.

(0.3 mole solid xenon, 2.1 kV), the charge collection is  $98\% \pm 5\%$ , and in Fig. 4-18b (0.9 mole liquid argon, -1.0 kV),  $82\% \pm 5\%$ . For comparison, the percent charge collection in the 0.9 mole detector filled with liquid xenon is  $62\% \pm 4\%$  at -1.0 kV and  $64\% \pm 4\%$  at -1.5 kV. In the 0.9 mole detector with solid xenon, the percent charge collection is  $55\% \pm 4\%$  at 0.6 kV. Finally, in the 0.3 mole argon detector at 1 kV the percent charge collection is  $76\% \pm 4\%$ . The absolute charge collection as a function of voltage is graphed in Fig. 4-19a for the 0.9 mole liquid argon detector, and the associated energy resolution at each voltage is graphed in Fig. 4-19b.

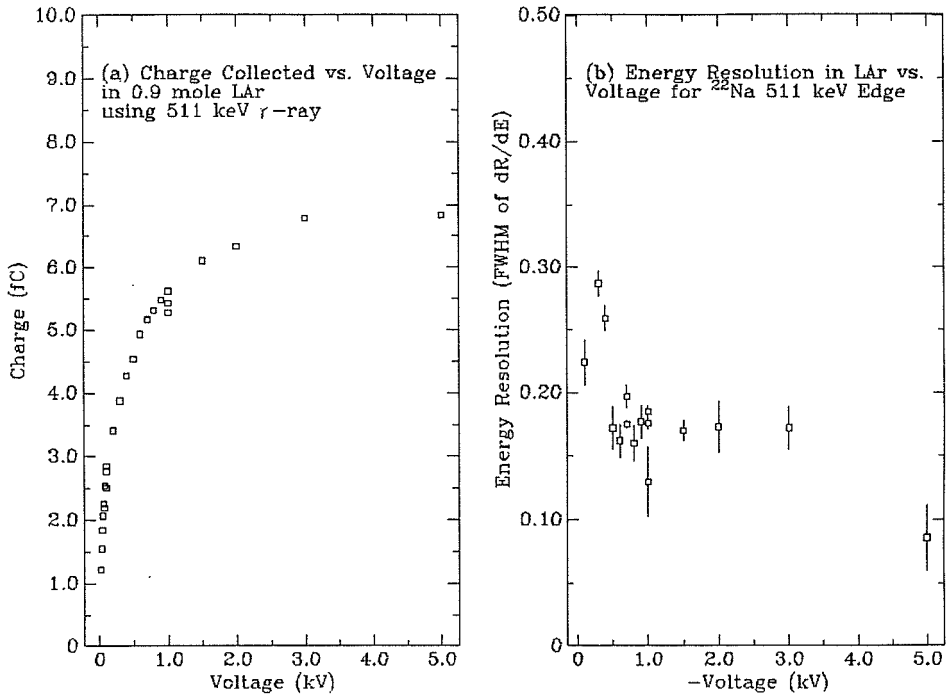


Figure 4-19. (a) Charge collection and (b) energy resolution as a function of applied voltage in the 0.9 mole liquid argon detector.

### *Energy Resolution*

The detector energy resolution in each xenon spectrum is obtained by subtracting in quadrature the electronic noise FWHM (full-width at half-maximum height) from the full-absorption peak FWHM. In argon, the FWHM of the derivative of the Compton edge is used, since the full energy (photo-absorption)  $\gamma$ -ray peak in the argon spectra is too small to be seen. The FWHM of each peak was obtained by fitting a Gaussian peak superimposed on a linear background to the spectrum. Fig. 4-20 shows an example fit to the derivative of a Compton edge in argon, and Fig. 4-21 shows a fit to an



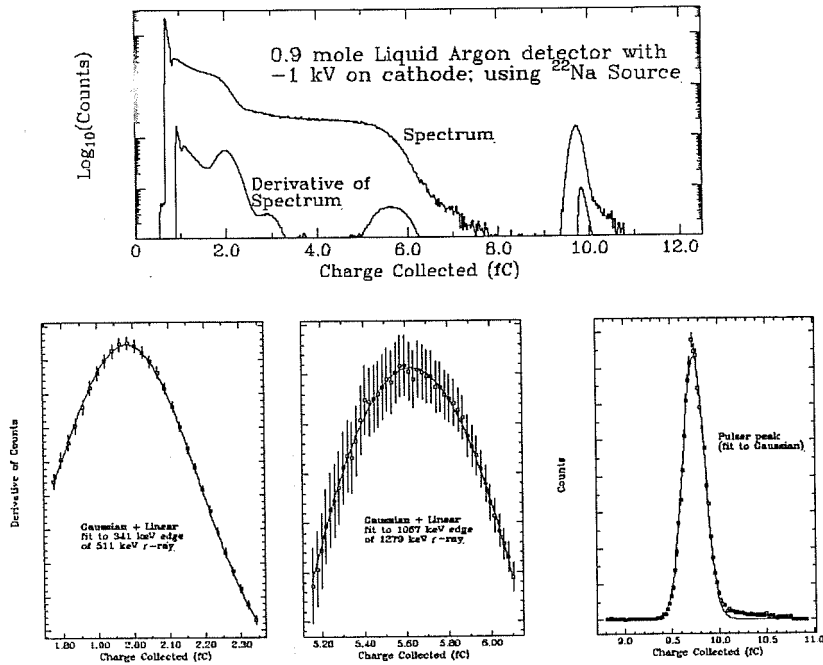


Figure 4-20. Using derivative of energy spectrum to obtain energy resolution in 0.9 mole liquid argon detector. Gaussians superimposed on a linear background are fit to the derivative of the edge of the 511 keV  $\gamma$ -ray, the 1.28 MeV  $\gamma$ -ray and the undifferentiated pulser peak.

absorption peak in xenon. The energy resolution results are displayed in Table 4-4.

Besides the contribution by the electronic noise (which has been removed from the results in Table 4-4) and the position-dependence of the charge collection in the detector discussed in section 4.2, there is an additional source of broadening due to the charge-density fluctuations caused by the statistics of  $\delta$ -electron production. It has been shown<sup>21,23</sup> that the width of a peak due to

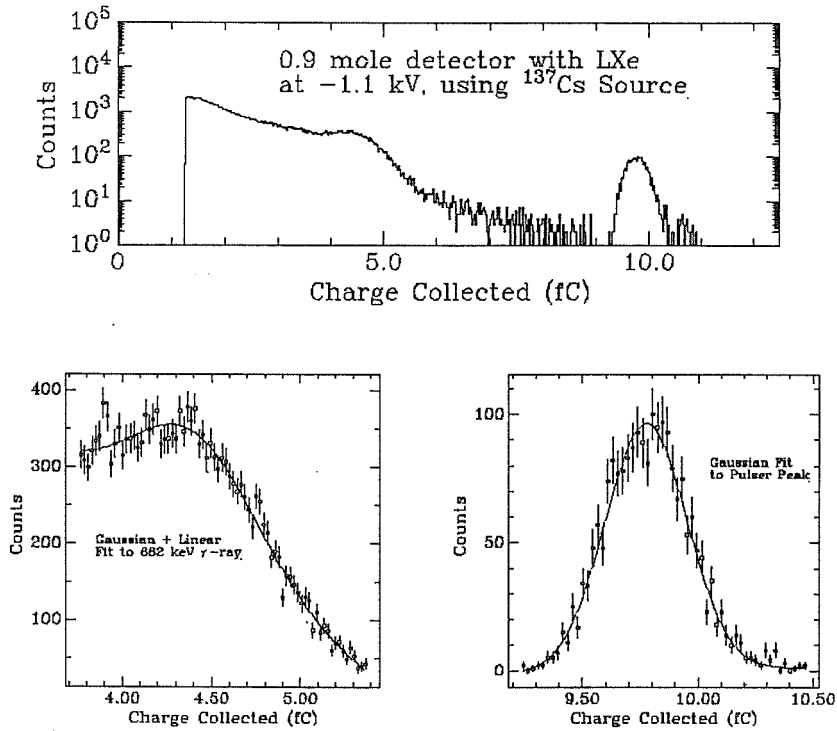


Figure 4-21. Fitting energy resolution in 0.9 mole liquid xenon detector. The  $^{137}\text{Cs}$  full energy peak at 662 keV and the pulser peak are fit with Gaussians superimposed on a linear background.

recombination of these charge fluctuations is given by:

$$\% \text{ FWHM} \times \frac{Q_r}{Q_0} = \frac{235.5}{\sqrt{E_p}} b \left[ \frac{\log_e(1+\xi_1)}{\xi_1} - \frac{\log_e(1+\xi_0)}{\xi_0} \right], \quad (4-14)$$

where  $\frac{Q_r}{Q_0}$ ,  $\xi_0$ ,  $\xi_1$ ,  $b$  and  $E_p$  are defined in (4-3) and Table 4-1. When this contribution is removed from the values of energy resolution in Table 4-4, the remaining energy resolution is due entirely to position-dependent charge

Energy Resolution		
Medium	0.3 Mole Detector	0.9 Mole Detector
Liquid Argon	14% at 341 keV	21% at 341 keV
	29% at 1066 keV	14% at 1066 keV
Solid Argon	14% at 341 keV	18% at 341 keV
	29% at 1066 keV	17% at 1066 keV
Liquid Xenon	16% at 511 keV	17% at 662 keV
Solid Xenon	16% at 511 keV	18% at 662 keV

Table 4-4. Energy resolution obtained in liquid and solid argon and xenon for both the 0.3 mole and 0.9 mole detectors. See Figs. 4-11 through 4-14 for the spectra from which these results are obtained.

collection, and is about 10% to 15% FWHM.

#### *Charge Accumulation*

The stability of solid xenon and argon against charge accumulation was tested using a  $^{207}\text{Bi}$  conversion electron source with an activity of  $1\ \mu\text{Ci}$ . The source was electroplated onto a nickel substrate<sup>60</sup>. After observing it with a cooled Si(Li) detector, the source was mounted on a plug and inserted into a mini-conflat tee. (Figs. 4-22 through 4-24.) Thus, the geometry was approximately the same as that of the 0.3 mole detector, with a conversion electron

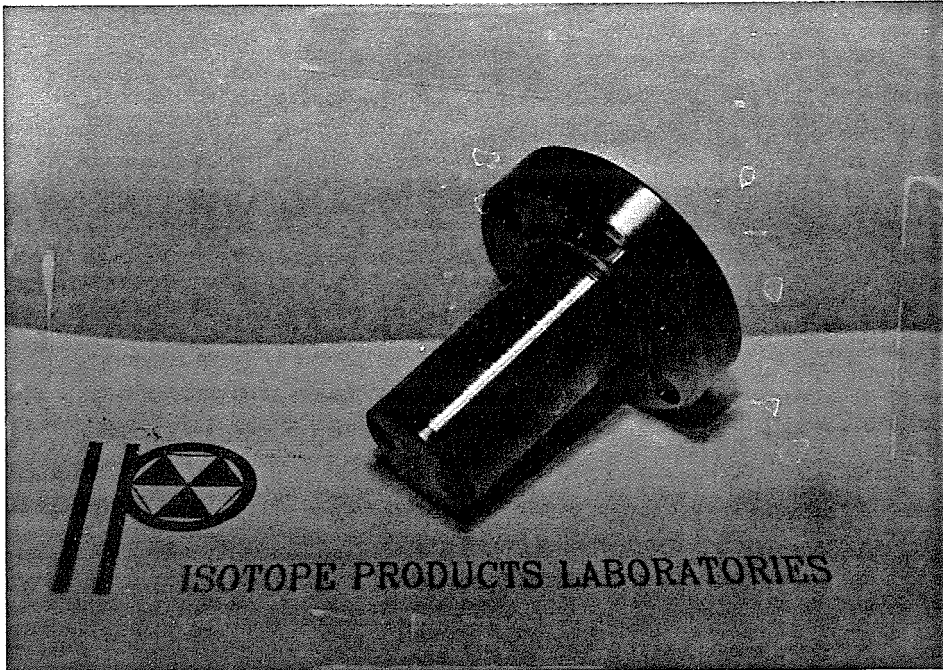


Figure 4-22. The  $^{207}\text{Bi}$  source, mounted on a plug. The plug is fixed to the flange with a set-screw and may be mounted into a tee.

source mounted at the wall half-way along the length of the detector.

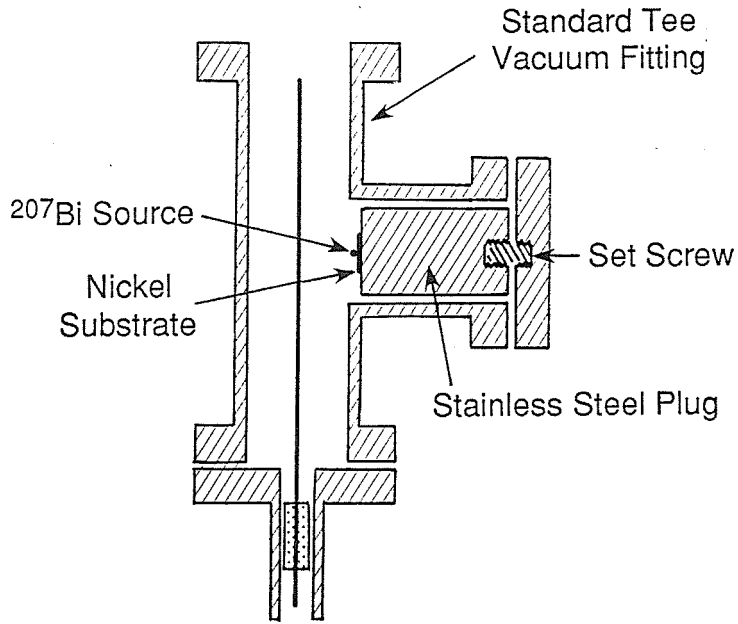


Figure 4-23. Schematic of the 0.3 mole tee detector used to test the stability of the detector against charge accumulation.

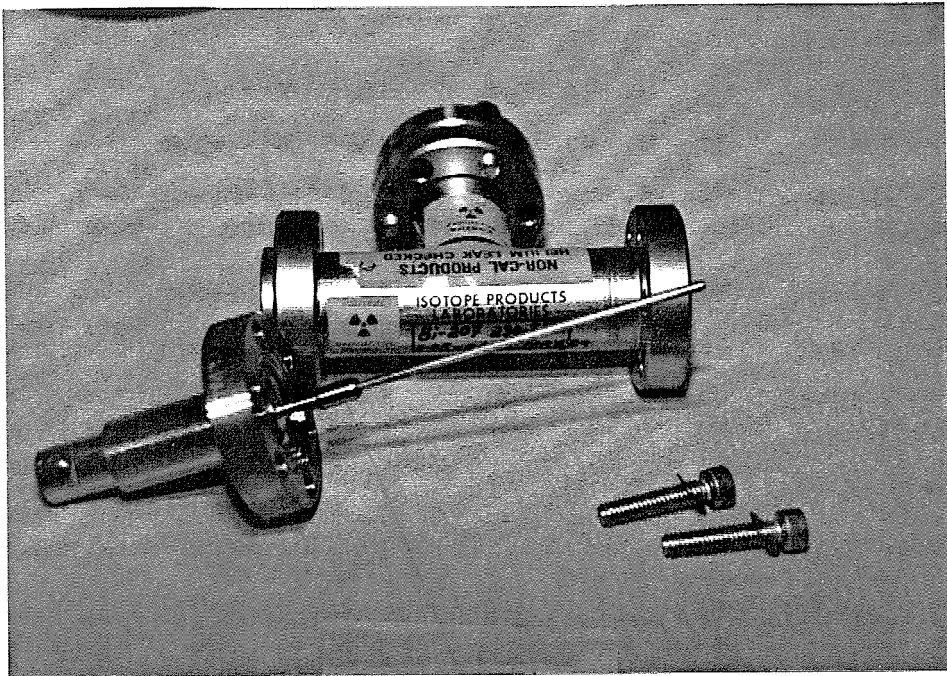


Figure 4-24. The 0.3 mole tee detector.

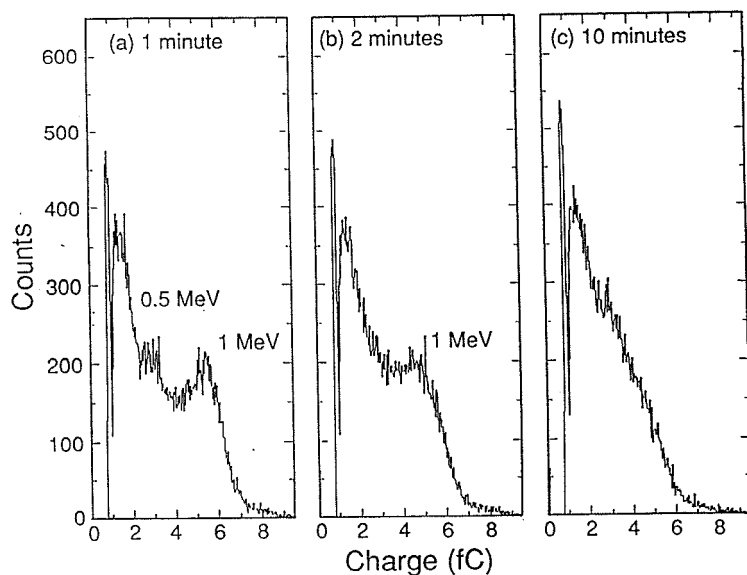


Figure 4-25. Charge accumulation with an internal  $^{207}\text{Bi}$  conversion electron source mounted in the 0.3 mole liquid argon tee detector. (a) One minute after voltage is applied, (b) two minutes and (c) ten minutes after voltage is applied.

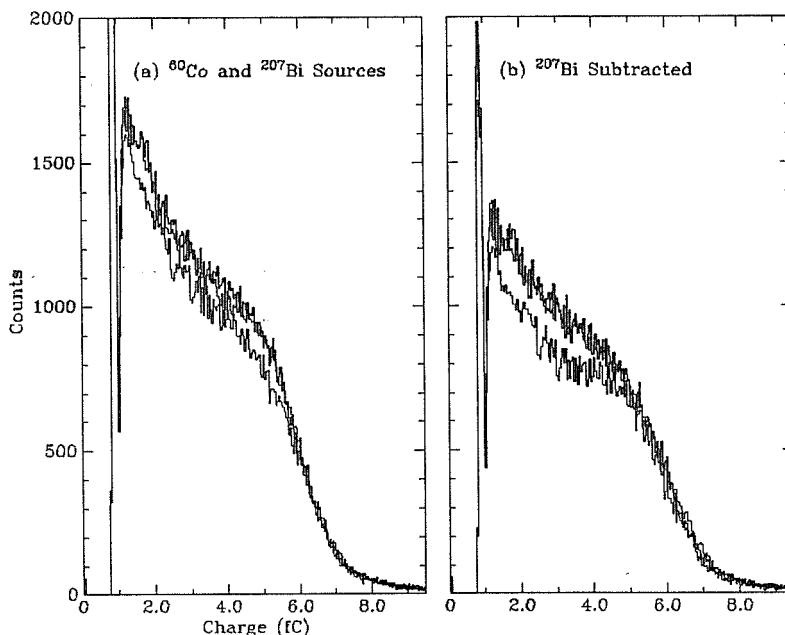


Figure 4-26. Stability of the 0.3 mole tee detector against charge accumulation is illustrated here by the detector's ability to acquire a  $\gamma$ -ray spectrum using the majority of

the volume of the detector while a small region near the internally mounted  $^{207}\text{Bi}$  source is accumulating charge. (a) Raw spectra and (b) spectra with the  $^{207}\text{Bi}$  spectrum subtracted. Both (a) and (b) display three spectra accumulated at the same time intervals as Figs. 4-25(a), (b) and (c).

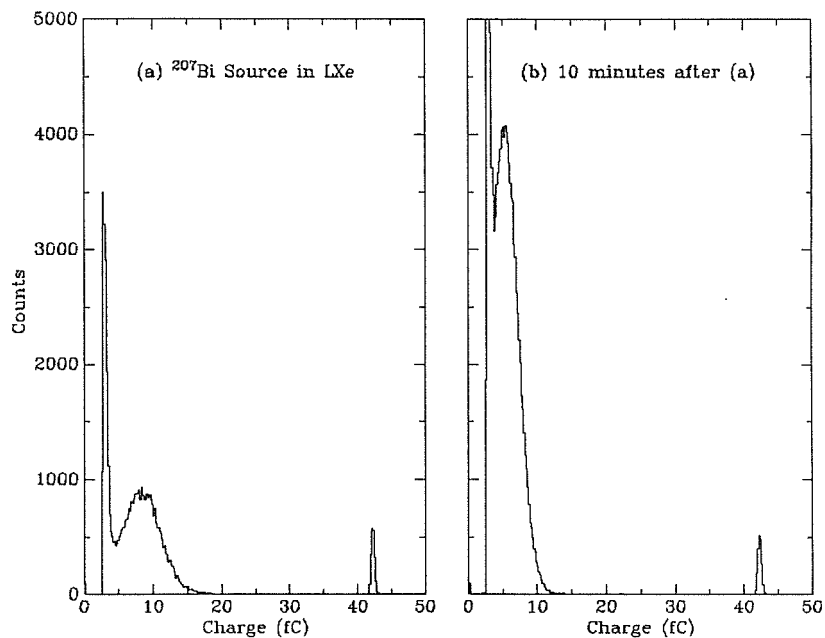


Figure 4-27. Charge accumulation in the 0.3 mole liquid xenon tee detector. The spectrum in (b) was taken 10 minutes after that displayed in (a), which was acquired immediately after applying voltage to the system.

The spectra in solid argon (Fig. 4-25) show rapid deterioration with time. However, the detector continued to operate satisfactorily with an external  $\gamma$ -ray source at the same time that the charge collection of the internal conversion-electron spectrum was deteriorating, Fig. 4-26. This seems to indicate that the deterioration in electron drifting only occurs at the local area ionized by the strong electron source. Thus, the solid detector is probably more

useful for applications involving rare processes such as  $\beta\beta$ -decay. The effect of deterioration of charge collection due to charge accumulation in the solid seems to be reversible by switching the direction of the electric field. After applying 3 kV of the opposite polarity for approximately 2 minutes, the charge collection returned to its initial value and the experiment could be repeated. The spectra in solid xenon show a similar effect, Fig. 4-27.

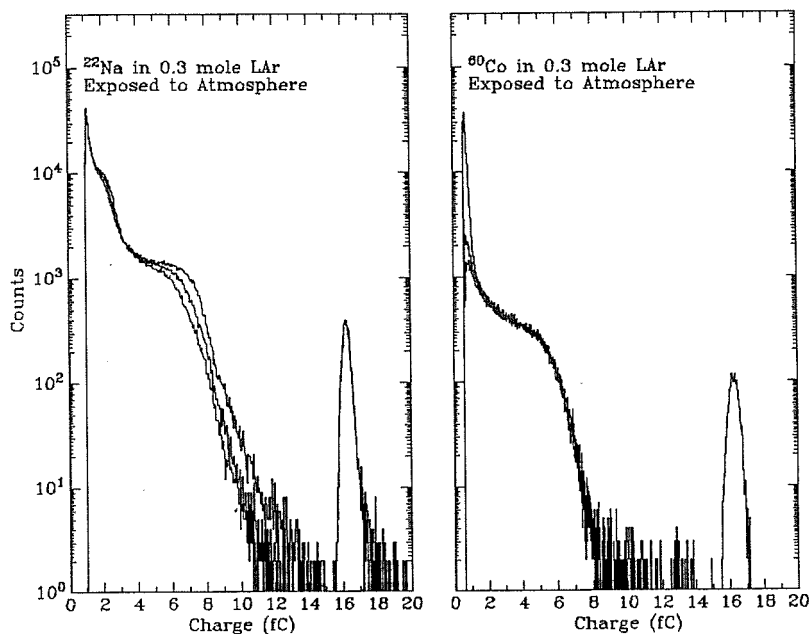


Figure 4-28. In these spectra, liquid argon in the 0.3 mole detector was exposed to the atmosphere. The spectra show little shift in charge collection or energy resolution with time.

#### *Exposure to atmosphere*

The 0.3 mole detector was filled with liquid and solid argon. In order to gauge the effects of outgassing and to see whether material outgassed from the



walls of the detector would migrate into the liquid, a small amount ( $\ll 1 \text{ cm}^3$ ) of air was allowed into the detector. No difference in the spectrum shape or charge collection was observed. Increasing amounts of air were introduced into the system, until the detector was left open to the atmosphere for 2 hours. Fig. 4-28 shows spectra in liquid argon before air was admitted, immediately after opening to the atmosphere and after up to 2 hours of exposure to the atmosphere. Little change was observed in charge collection or energy resolution in the liquid argon during this test. This test was repeated and the same results obtained on two different occasions. One must conclude that the oxygen and nitrogen in the air do not mix readily with the already-condensed liquid argon.

## 4.5 Conclusions

### *Summary*

The possibility of using solid xenon as a detector medium has been demonstrated and studied with a simple apparatus. The best energy resolution obtained in solid xenon is 16% FWHM at 511 keV and in solid argon is 14% FWHM at 341 keV, both for external, uncollimated  $\gamma$ -rays. This detector design seems promising for an experiment to measure  $2\nu \beta\beta$ -decay in  $^{136}\text{Xe}$ .

### *Comparison with Other Experiments*

For comparison, the best energy resolution reported in the literature in liquid xenon is 4.5% FWHM at 2.6 MeV<sup>27</sup> and 6% FWHM at 569 keV<sup>50</sup>, and for liquid argon, 3% FWHM at 1 MeV<sup>28</sup>. These were obtained in parallel-

Medium	Resolution	Energy	Author
Liquid Argon	3%	1 MeV	Aprile <i>et al.</i> <sup>28</sup>
	14%	1 MeV	<b>Present Thesis</b>
	14%	0.34 MeV	<b>Present Thesis</b>
Liquid Xenon	4.5%	2.6 MeV	Masuda <i>et al.</i> <sup>27</sup>
	6.0%	0.57 MeV	Aprile <i>et al.</i> <sup>50</sup>
	16%	0.51 MeV	<b>Present Thesis</b>
Solid Argon	14%	0.48 MeV	Grebinnik <i>et al.</i> <sup>46</sup>
	14%	0.34 MeV	<b>Present Thesis</b>
Solid Xenon	(no previous report)		
	16%	0.51 MeV	<b>Present Thesis</b>

Table 4-5. Energy Resolution reported in the literature and present thesis for liquid and solid ionization detectors.

plate, gridded ionization chambers. In solid argon, the only spectra shown<sup>46</sup> appear to have an energy resolution of about 14% FWHM at 478 keV. This experiment employed a radial, gridless geometry with a 10  $\mu\text{m}$  diameter anode wire. (No solid xenon ionization spectra have been reported.)

### Improvements

In order to improve the energy resolution in the solid xenon ionization chamber, higher voltages must be applied with a smaller anode wire in order to reduce the position-dependent effect of recombination, and to reduce the fluctuation of charge collection due to  $\delta$ -electron charge deposits. This may be difficult, since, as noted above, micro-discharging is already occurring in the solid xenon at voltages above 2 kV. In addition, electronegative impurities in the xenon should be minimized. A separate test, with several cycles of purification, condensation, use as a ionization detector and evaporation, showed no improvement in charge collection or energy resolution with re-purification of the detector medium.

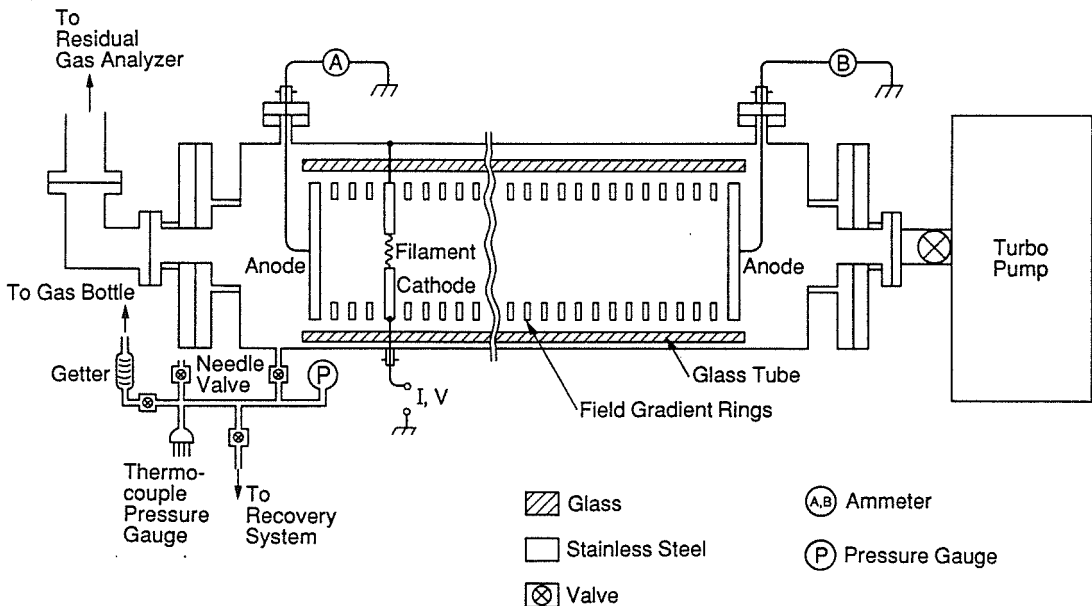


Figure 4-29. Schematic of the gas purity monitor.

Ideally, one would like to have a separate gas-purity monitor. One possible design for this is shown in Fig. 4-29. Electrons are emitted from a thoriated tungsten filament and a drifted in 5 atm of gas. A weak field provided by a

small voltage potential applied across the filament and anode increase the sensitivity of the drifting electrons to electronegative impurities. Field gradient rings ensure that the electric field is uniform along the two drift lengths of the monitor, 10 cm and 100 cm. Electron currents of about  $1 \mu\text{A}$  in magnitude are used, so that detection is accomplished with sensitive current meters instead of charge-sensitive preamplifiers, and shaping times may be ignored. This system does not require a grid. The differential attenuation of currents indicates the purity of the gas. This differential attenuation can be calibrated by adding a small known amount of oxygen (or any other electronegative impurity) into the system. The sensitive of such a system may be estimated<sup>61</sup>:

$$\lambda = \frac{7.8 \times 10^{-3} \text{ cm}}{P_{\text{Xe}}^2 \rho_{\text{O}_2}} \quad (4-15)$$

for an electron drift velocity of  $2.3 \times 10^6$  cm/s, where  $\lambda$  is the attenuation length,  $P_{\text{Xe}}$  is the pressure of xenon gas in atm, and  $\rho_{\text{O}_2}$  is the fractional quantity of  $\text{O}_2$ -equivalent electronegative impurities. Thus, at 5 atm pressure, and assuming a 1% maximum current sensitivity, sensitivity to  $\lambda = 100$  cm implies sensitivity to  $\rho_{\text{O}_2} \sim 1$  ppb.

## CHAPTER FIVE

### Conclusions

#### *Liquid Ionization Detector*

We designed, built and tested a high-purity liquid argon and liquid xenon ionization detector. We achieved medium energy resolution in liquid argon and liquid xenon at lower electric field strengths and electron energies than previously reported, 12% FWHM at 380 keV in an electric drift field of less than 2 kV/cm. The purity of our liquid media is illustrated by our ability to drift electrons at electric fields of only 10 V/cm.

From studies of our detector data and that of others, we deduced the limitation to the energy resolution of these detectors. We derived a physically realistic model for recombination,

$$\frac{Q}{Q_0} = \frac{1}{\xi} \log_e(1+\xi) \quad (5-1)$$

where  $\frac{Q}{Q_0}$  is the fraction of charge which survives recombination, and  $\xi$  is the recombination strength, a single parameter which depends on constants of the media and is inversely proportional to the electric field strength. Using this model we fit the charge collection and energy resolution data for liquid argon and liquid xenon ionization detectors and showed that the initial recombination of the high charge-density regions produced by  $\delta$ -electrons limited the energy

resolution. The limit to energy resolution in these liquid noble gas detectors is:

$$\% \text{ FWHM} \times \frac{Q}{Q_0} = \frac{235.5}{\sqrt{E_P}} b \left[ \frac{\log_e(1+\xi_1)}{\xi_1} - \frac{\log_e(1+\xi_\delta)}{\xi_\delta} \right], \quad (5-2)$$

where  $E_P$  is the energy of the primary electron in keV,  $\xi_1$  and  $\xi_\delta$  are the recombination strengths in the minimum ionizing and high charge density portions of the electron track, respectively, and  $b$  is a function of the medium and the energy of the primary electron. (See Table 4-1 for a convenient summary of the values of these parameters.) The result of (5-2) is that the energy resolution in liquid xenon at 1 MeV is no better than 1.6% FWHM at the highest practical electric fields (10 kV/cm) instead of the 0.3% FWHM originally expected for such a detector.

Appendix A contains the details of the recombination model, and the application of this model to the energy resolution of liquid noble gas ionization detectors is described in Appendix B.

### *High Pressure Ionization Chamber*

In order to reduce the limitations of recombination on the liquid noble gas detectors, we built and tested a high pressure double ionization chamber designed specifically for application to  $\beta\beta$ -decay. For this detector we employed a unique design which maximized the active volume of the detector while removing the difficulty of manufacturing high-pressure, high-vacuum, low-background high-voltage feedthroughs.

This detector withstood pressures of up to 140 atm. The energy resolution achieved in 108 atm argon was 2% FWHM at 1 MeV in a 0.5 kV/cm field

and in 30 atm xenon was 3% FWHM at 1 MeV for a 0.7 kV/cm field. The energy resolution of the detector using argon was limited by capacitive noise and the statistics of charge production in the argon – not by purity or recombination of  $\delta$ -electrons. The energy resolution in the detector with xenon was limited by the attachment of the electrons to electronegative impurities. Whereas attenuation lengths of greater than 2 meters could be achieved in argon, the best attenuation length achieved in xenon was 50 cm. The attenuation length decreased rapidly in xenon although it was stable in argon with identical detector parameters. Spectra from these detectors are included in Appendix C, as is a possible way to improve the energy resolution of stable, medium purity ionization detectors.

#### *Radial Liquid and Solid Ionization Detectors*

Using the cancellation of the effects of recombination, attachment and charge induction of drifting electrons, two radial ionization detectors with volumes of 0.3 mole and 0.9 mole were built and tested, allowing the first observation of solid xenon ionization spectra. In contrast to the case of high pressure xenon, solid xenon appears to be stable over the time periods (~ few hours) studied in these experiments. The energy resolution achieved in these detectors in solid xenon is 16% FWHM at 0.5 MeV. The energy resolution is limited by the uniformity of charge collection over the volume of the detector and the initial recombination of high charge density regions produced by  $\delta$ -electrons. Detailed documentation of the spectra obtained in these detectors is included in Appendix D.

*Outlook for  $\beta\beta$ -Decay in  $^{136}\text{Xe}$*

In view of these results, a  $0\nu$   $\beta\beta$ -decay experiment using high-density xenon does not seem very promising. A  $2\nu$   $\beta\beta$ -decay experiment may be practical using the radial ionization detector with condensed xenon in a subtraction experiment, where the spectrum obtained with enriched  $^{136}\text{Xe}$  is compared with that in depleted  $^{136}\text{Xe}$ .

These tests show that our attempts to design and build a simple high density xenon detector cannot compete with our experiment soon to become operational in the St. Gotthard tunnel in Switzerland based on a 5 atm xenon time projection chamber, described in chapter 1. This experiment should be sensitive to lifetimes in excess of  $10^{22}$  years for the  $2\nu$  mode of  $\beta\beta$ -decay and  $10^{23}$  years for the  $0\nu$  mode, both with an *unambiguous* signature for  $\beta\beta$ -decay.



## APPENDIX A

### Derivation of the Recombination Model

#### *Introduction*

In this appendix I derive the recombination model we have used to fit our charge collection data in liquid and gas ionization chambers and to explain the loss of energy resolution due to initial recombination of highly ionized regions ( $\delta$ -electron “charge blobs” – see Appendix B) in these detectors. This is an expanded version of our earlier published work, Thomas and Imel, Phys. Rev. A36, 614, 1987, where we presented the box model solution to (A-5a,b).

We begin with the charge transport equations<sup>62</sup>:

$$\frac{\partial N_+}{\partial t} = -\mu_+ \mathbf{E} \cdot \nabla N_+ + d_+ \nabla^2 N_+ - \alpha N_- N_+ , \quad (\text{A-1a})$$

$$\frac{\partial N_-}{\partial t} = \mu_- \mathbf{E} \cdot \nabla N_- + d_- \nabla^2 N_- - \alpha N_+ N_- , \quad (\text{A-1b})$$

where  $N_+$  and  $N_-$  are the ion and electron charge distributions,  $\mu_+$  and  $\mu_-$  are the mobilities,  $d_+$  and  $d_-$  are the diffusion constants,  $\alpha$  is the recombination constant and  $\mathbf{E}$  is the external electric field. The first term on the rhs represents the motion due to the electric field, the second, that due to diffusion, and the third, recombination of the electrons and ions, the rate of which is assumed in the model to be proportional to the product of their charge

densities.

In 1913, Jaffe<sup>62</sup> attempted to solve these equations by including the recombination term as a perturbation with the boundary condition that the initial distribution is a column of charge around the primary track. His semi-empirical formula for the fraction of charge surviving recombination,

$$\frac{Q}{Q_0} = (1+kE^{-1})^{-1}, \quad (\text{A-2})$$

where  $Q_0$  is the charge produced in an ionization event,  $Q$  is the charge surviving initial recombination,  $E$  is the externally-applied electric field strength and  $k$  is a constant which is a function of the medium, has received extensive use in the literature. This is no doubt partially due to its functional simplicity.

Kramers<sup>63</sup> pointed out in 1952 that in an external field the diffusion term is much smaller than the drift or recombination terms and so introducing the recombination term as a perturbation of the solution to the diffusion equation is unreliable. He solved the same equations by ignoring the diffusion term, including the columnar boundary conditions and assuming that the electron and ion mobilities are equal. Diffusion was added later as a perturbation. Kramers' solution is

$$\frac{Q}{Q_0} = \frac{2}{\sqrt{\pi}} \frac{E}{E_0} \int_0^\infty \frac{\sqrt{\eta} d\eta}{\frac{E}{E_0} e^\eta + 1}, \quad (\text{A-3a})$$

which has high and low field strength approximations:

$$\frac{Q}{Q_0} = \left(1 - \frac{E_0}{E\sqrt{8}}\right), \quad \text{for } \frac{E}{E_0} \gg 1 \text{ and} \quad (\text{A-3b})$$

$$\frac{Q}{Q_0} = \frac{2}{3} \frac{E}{E_0} \left[ \log_e \left( \frac{E_0}{E} \right) \right]^{\frac{3}{2}}, \quad \text{for } \frac{E}{E_0} \ll 1, \quad (\text{A-3c})$$

where  $E_0$  is the saturation electric field strength. Although Kramers' and Jaffe's solutions are useful in empirically fitting recombination data, they seem physically unrealistic. We will see in the next section that rather than being described as a column of charge, an ionization track is much better described as many individual ionization events. Also, the assumption of equal mobilities for ions and electrons is completely wrong for liquid and high-pressure gases.

Onsager<sup>64</sup> assumed (as we will here) that the individual ionizations are separated – the germinate theory assumption – and that the effect of the electric field was a perturbation on Brownian motion. His solution at low field strengths,

$$\frac{Q}{Q_0} \propto 1 + E/E_0, \quad (\text{A-4})$$

where  $E_0$ , the slope-at-zero-field-intercept predicted by his theory, is a function of pressure and temperature ( $E_0 \propto T^{-2}$ ). The prediction of a non-zero charge collection offset at zero electric field strength was shown not to be true in the case of liquid argon by Scalettar *et al.*<sup>35</sup>, and later in both liquid and high-pressure argon and liquid and high-pressure xenon by us. (See chapter 2 for liquid argon and xenon and chapter 3 for high-pressure gases.)

Thus, there is a need for a physically realistic solution to the charge transport equations. We hoped that in better understanding the process of recombination in high-density xenon and argon detectors, we might gain insight into the apparent energy resolution limitations of these devices.

### *Approximations*

In liquid argon and xenon, the diffusion term is very small. The electron diffusion rate is of the order of millimeters per meter of drift<sup>65,66</sup>. In addition, the ion drift mobility is three to five orders of magnitude smaller than the electron drift mobility<sup>36,67,68</sup>. Thus the diffusion term in (A-1a,b) can be dropped, and the positive ion mobility set to zero. This simplifies the equations and they can be solved analytically subject to the realistic boundary condition that each electron-ion pair is isolated. We prefer this germinate theory boundary condition because the ion-electron sites are so widely separated. For example, a 1 MeV electron will generate<sup>9,10</sup> 64,000 electron-ion pairs over a range<sup>32</sup> of about 2 millimeters in liquid xenon. Since the lattice spacing<sup>8</sup> in liquid xenon is about 6Å, this corresponds to about one electron-ion pair for every 50 xenon atoms along the track of the ionizing particle. The potential from the ions and electrons is well shielded<sup>22</sup> by surrounding atoms, so that these ionizations may be considered to be isolated. (A modification to this assumption will be presented in Appendix B.)

With a constant electric field applied along the z axis,  $\mathbf{E} = E\hat{z}$ , (A-1a,b) become:

$$\frac{\partial N_+}{\partial t} = -\alpha N_- N_+ , \quad (\text{A-5a})$$

$$\frac{\partial N_-}{\partial t} = -\mu_- E \frac{\partial N_-}{\partial z} - \alpha N_+ N_- . \quad (\text{A-5b})$$

*Derivation*

In solving (A-5a,b) we will take the following procedure: First, using the equations themselves, we can solve for one distribution in terms of the other. Next, after integrating the resulting equation over time and applying the initial conditions, we will transform coordinates to obtain a simple integral which gives the ion distribution at any later time as a function of the initial ion distribution. Finally, since we are not interested in the details of the ion and electron distributions, but only in how much charge is left over after initial recombination, we will use some simple initial distribution for each, let the time-evolution of the distributions go to infinity, and integrate one distribution over all space. This integral is simply the charge surviving initial recombination which is available to be collected at the plate of an ionization chamber. (Because of charge conservation, we may integrate either the positive distribution or the negative one. In practice, it is convenient to integrate the former.) The details of this derivation follow.

(A-5a) may be substituted into (A-5b) and integrated over time to find:

$$-\frac{1}{\alpha} \frac{\partial N_+}{\partial t} \Big|_t + \frac{1}{\alpha} \frac{\partial N_+}{\partial t} \Big|_0 = N_+ \Big|_t - N_+ \Big|_0 - \frac{\mu_- E}{\alpha} \frac{\partial \log_e N_+}{\partial z} \Big|_t + \frac{\partial \log_e N_+}{\partial z} \Big|_0. \quad (\text{A-6})$$

We can use the initial conditions and (A-5a)

$$N_+ \Big|_0 = N_- \Big|_0 = -\frac{1}{\alpha} \frac{\partial \log_e N_+}{\partial t} \Big|_0, \quad (\text{A-7})$$

(i.e., the electrons and ions are created in approximately the same place) to cancel the second term on both sides of this equation.

$$\frac{\partial \log_e N_+}{\partial t} = \frac{u-E}{\alpha} \frac{\partial}{\partial z} \left[ \log \frac{N_+(t)}{N_+(0)} \right] - \alpha N_+(t) . \quad (\text{A-8})$$

Now, noting that  $\frac{\partial}{\partial t} [N_+(0)] = 0$  (since  $N_+(0)$  is a constant) and defining  $G(t) \equiv N_+(t) / N_+(0)$  we obtain:

$$\frac{\partial G}{\partial t} = \mu-E \frac{\partial G}{\partial z} - \alpha N_+(0) G^2 . \quad (\text{A-9})$$

We introduce new variables:

$$v = t - \frac{z}{\mu-E}, \quad w = t + \frac{z}{\mu-E}, \quad (\text{A-10})$$

where  $w$  and  $v$  form a skewed coordinate system rotated with respect to the  $(z,t)$  coordinate system. Applying the boundary condition  $v = -w$  and  $G = 1$  at  $t = 0$ , the resulting equation is:

$$\frac{\partial [G(v,w)]^{-1}}{\partial v} = \frac{\alpha}{2} N_+(0). \quad (\text{A-11})$$

Finally, we define  $Y \equiv G^{-1}$  and integrate from  $v' = -w$  to  $v' = v$ , holding  $w$  fixed:

$$Y(v,w) = 1 + \frac{\alpha}{2} \int_{-w}^v N_+(0) dv' . \quad (\text{A-12})$$

This equation gives the ion distribution as a function of time and space by an integral of the initial ion distribution. From here, we choose an initial distribution which seems physically reasonable, let the distribution evolve in time and integrate the resulting distribution at large times over all space, giving the total charge surviving initial recombination.

### *Box Model*

We may choose any physically reasonable charge distribution for  $N_+(0)$ . A simple model is that the ion-electron pairs are isolated and the initial distribution of  $N_0$  ions and electrons uniformly populates a box of dimension  $2a$ . The box model is:

$$N_+(x, y, z; t=0) = \frac{N_0}{8a^3} \times \begin{cases} 1; & -a \leq x, y, z \leq a \\ 0; & \text{elsewhere} \end{cases} \quad (\text{A-13})$$

We transform back into the  $t$  and  $z$  variables for the indicated integration using  $dz' = -(1/2)\mu_- E dv'$ :

$$Y(x, y, z; t) = 1 + \frac{N_0 \alpha}{16a^3} [1 - \theta(x-a)][1 - \theta(y-a)]\theta(x+a)\theta(y+a) \times \\ \frac{2}{\mu_- E} \int_z^{z+\mu_- Et} dz' \theta(z'+a)[1 - \theta(z'-a)] \quad , \quad (\text{A-14})$$

where  $\theta(x)$  is the usual Heaviside step function,  $\theta(x) = 0$  for  $x < 0$  and  $\theta(x) = 1$  for  $x > 0$ . Before performing the integration, we let  $t \rightarrow \infty$ , which corresponds to letting the electrons drift completely out of the ion charge distribution so that no further recombination will occur. The charge that survives will be the

charge which may be collected in an ionization chamber. We substitute back in for  $Y(x,y,z;t)$  and integrate over all space to get:

$$\int_{-\infty}^{+\infty} dx' \int_{-\infty}^{+\infty} dy' \int_{-\infty}^{+\infty} dz' N_+(x',y',z';t \rightarrow \infty) = \frac{N_0}{2a} \int_{-a}^a dz' \left( 1 + \frac{N_0 \alpha}{8\mu_- E a^3} (z' + a) \right)^{-1}, \quad (\text{A-15})$$

where the integration over  $x$  and  $y$  contributed a factor of  $4a^2$  and  $N_+(t=0)$  in the numerator of the integrand on the rhs [of the equation obtained by substituting for  $Y(x,y,z;t)$ ] limits the integration to the region between  $z = -a$  and  $z = a$ .

But the integrated charge density at long times is just the total charge surviving initial recombination. Thus we have:

$$Q = \frac{N_0}{2a} \int_{-a}^a \frac{dz'}{1 + \frac{\xi}{2} \left( \frac{z' + a}{a} \right)}, \quad (\text{A-16})$$

where

$$\xi \equiv \frac{N_0 \alpha}{4\mu_- E a^2}, \quad (\text{A-17})$$

and finally,

$$\frac{Q}{N_0} = \frac{1}{\xi} \log_e(1 + \xi). \quad (\text{A-18})$$

Note that  $N_0$  is just the number of charge units deposited in each isolated



ionization location, typically  $N_0 = 1$  for our assumptions. Thus, (A-18) should be interpreted as giving the probability of an individual electron surviving recombination. For all of the charge deposited in an ionization track, this model gives for the fraction of charge surviving recombination:

$$\frac{Q}{Q_0} = \frac{1}{\xi} \log_e(1+\xi) . \quad (\text{A-19})$$

### *Gaussian Sphere*

One would like to see that the solution does not depend drastically upon the model of the initial distribution. We can also solve (A-12) choosing as the initial distribution a spherical Gaussian, which is perhaps more physically realistic.

$$N_+(t=0) = \frac{N_0}{(2\pi\sigma^2)^{3/2}} e^{-\frac{\rho^2}{2\sigma^2}} e^{-\frac{z^2}{2\sigma^2}} \quad (\text{A-20})$$

is a spherical Gaussian of full-width at half maximum (FWHM) in each cartesian coordinate of  $2.35\sigma$ . ( $\rho$  is the cylindrical radial coordinate.) Defining

$$\tau \equiv \frac{\sqrt{8\sigma^2}}{\mu - E} , \quad (\text{A-21})$$

$$\eta \equiv \frac{w - v}{\tau} = \frac{z}{\sqrt{8\sigma^2}} , \quad (\text{A-22})$$

( $\tau$  is the characteristic distribution traversal time of the drifting electrons, and  $\eta$  is a dimensionless distance parameter scaled by the distribution size.) (A-12) becomes:

$$Y(v, w) = 1 - \frac{\alpha\tau}{2} \frac{N_0 e^{-\frac{\rho^2}{2\sigma^2}}}{(2\pi\sigma^2)^{3/2}} \int_{\frac{w}{2r}}^{\frac{w-v}{r}} e^{-\eta^2} d\eta. \quad (\text{A-23})$$

Performing the integration and substituting back in for the time and spatial coordinates, and letting  $t \rightarrow \infty$ , we have:

$$Y(\rho, z, \phi; t \rightarrow \infty) = 1 + \xi e^{-\frac{\rho^2}{2\sigma^2}} \left[ 1 - \text{erf}\left(\frac{z}{\sqrt{2\sigma^2}}\right) \right], \quad \text{where} \quad (\text{A-24})$$

$$\xi = \frac{N_0\alpha}{2\pi\sigma^2\mu_- E}. \quad (\text{A-25})$$

Now substitute the definition of  $Y$  and integrate over all space to get the charge collected after all recombination has occurred:

$$Q = \frac{N_0}{(2\pi\sigma^2)^{3/2}} \int_0^{2\pi} d\theta \int_0^\infty \rho d\rho \int_{-\infty}^{+\infty} dz \frac{e^{-\frac{\rho^2}{2\sigma^2}} e^{-\frac{z^2}{2\sigma^2}}}{1 + \frac{\xi}{2} e^{-\frac{\rho^2}{2\sigma^2}} \left[ 1 - \text{erf}\left(\frac{z}{\sqrt{2\sigma^2}}\right) \right]}. \quad (\text{A-26})$$

After performing the polar integrals, the azimuthal integral can be rewritten as:

$$\frac{Q}{N_0} = \frac{1}{\xi} \int_0^\xi \frac{1}{\lambda} \log_e(1+\lambda) d\lambda, \quad (\text{A-27})$$

where

$$\lambda = \frac{\xi}{2} \left[ 1 - \text{erf}\left(\frac{z}{\sqrt{2\sigma^2}}\right) \right]. \quad (\text{A-28})$$

This function is not analytically integrable<sup>58</sup> but can be expanded in an infinite series and integrated term-by-term:

$$\frac{Q}{N_0} = \sum_{n=0}^{\infty} \frac{(-\xi)^n}{(n+1)^2}, \quad (\text{A-29})$$

which converges for  $\xi \lesssim 1.5$ . For  $\xi \gtrsim 1.5$ , one must integrate (A-26) numerically. Note that  $\xi = 0$  gives  $Q = N_0$ , which is what one expects in the absence of recombination.

When computing (A-27), it is convenient to use the rapidly converging series (A-29) for values of  $\xi \leq 1$  and to break the integral into two pieces<sup>40</sup> for values of  $\xi > 1$ :

$$\frac{Q}{Q_0} = \frac{1}{\xi} \left[ \frac{\pi^2}{12} + \int_1^{\xi} \frac{1}{\lambda} \log_e(1+\lambda) d\lambda \right], \quad (\text{A-30})$$

where the integral must be performed numerically. (Numerical integration is inefficient for  $\xi \ll 1$ .)

### *Discussion*

We see that both models provide a solution for the charge surviving recombination which depends upon a single parameter  $\xi$ , which we shall henceforth call the *recombination strength*. Thus for small recombination strengths  $\xi \rightarrow 0$ , the charge surviving recombination approaches unity,  $Q/Q_0 \rightarrow 1$ , and for the case of strong recombination  $\xi \rightarrow \infty$  no charge survives,  $Q/Q_0 \rightarrow 0$ , as expected.

Notice also that  $\xi \propto E^{-1}$ . One way to ensure strong recombination is to apply zero field strength. In the limit that the approximations used for this model are good, specifically that diffusion is negligible in the medium being used, no charge survives recombination at zero electric field strength. This is in direct contradiction to the Onsager model (A-4) where diffusion is assumed to be the dominant effect and a significant amount of charge survives initial recombination at zero external electric field strength.

Fig. A-1 displays the Gaussian sphere and box models, as well as the box model with the parameter  $\xi$  scaled to match the Gaussian sphere model solution. The scaling represents the difference in the definition of the length scales,  $a$  for the box model and  $\sigma$  for the Gaussian sphere. Although the Gaussian sphere model is a slightly sharper function of the recombination strength, it is clear that these two models give approximately the same results. In fact, from Fig. A-2, where the charge surviving recombination is plotted as a function of relative electric field strength ( $E/E_0 \propto 1/\xi$ ), it is clear that all of the recombination models, with the exception of the Onsager model, give approximately the same shape. In Fig. A-2, the box model parameter  $\xi$  is scaled to compare the model with each of the other models, except the Onsager model. Fig. A-3 shows fits of the Onsager model, the Jaffe model, and our box model to “pure” recombination data taken by Scalettar *et al.*<sup>35</sup>, where the effects of drifting electrons to the anode have been removed by using a detector with an adjustable drift length. We have continued to use our box model for recombination data fitting, as has the group<sup>57</sup> working with liquid argon at UC Irvine, because it retains the simplicity of the Jaffe solution while incorporating realistic assumptions about the drift medium.

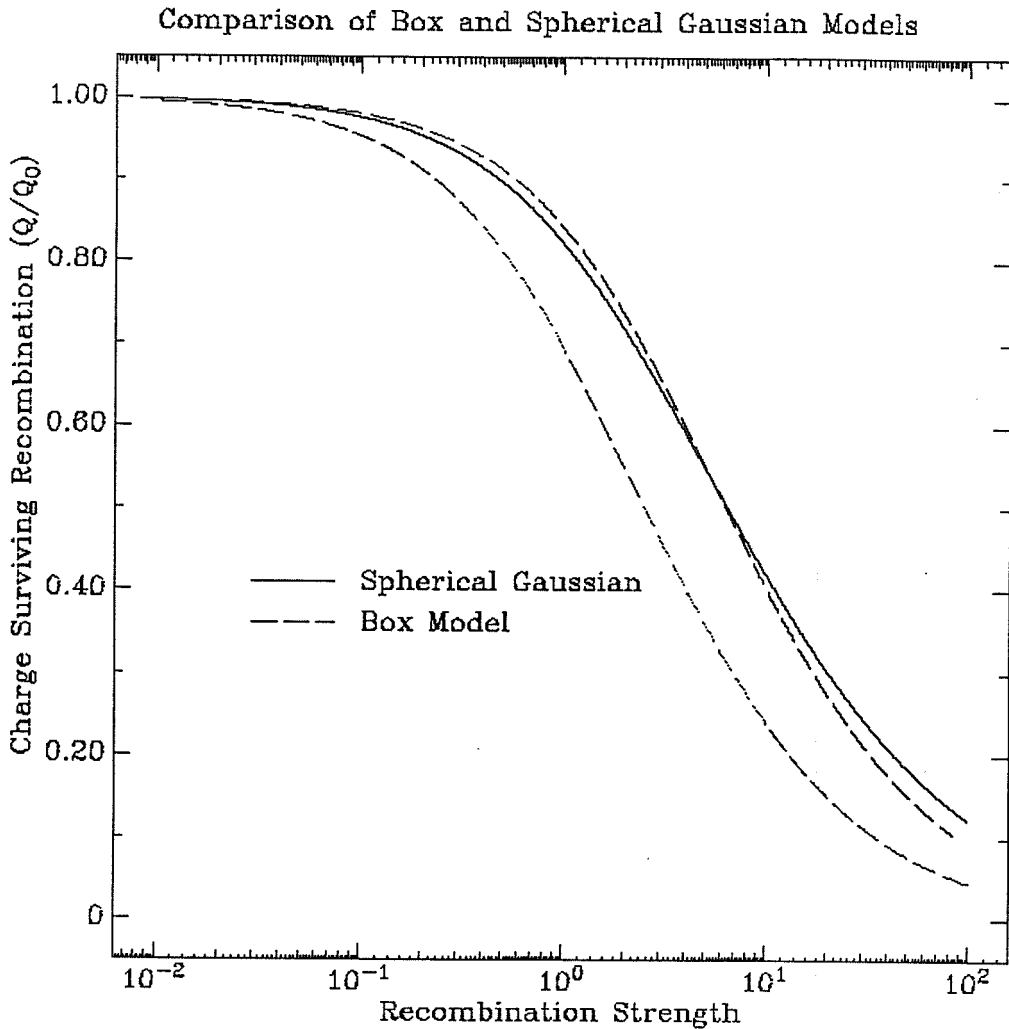


Figure A-1. Plot of charge surviving initial recombination versus recombination strength for both the box and spherical Gaussian initial distributions. The box distribution is also plotted with the resulting recombination strength scaled to that of the Gaussian distribution to compare their shapes, i.e.,  $\xi_{\text{box}} \approx 2.5\xi_{\text{Gaussian}}$ .

### Conclusion

We have solved (A-1a,b) with realistic assumptions for our detector media, and have found good agreement in the solution for the charge surviving recombination with existing data. The model is simple yet physically realistic

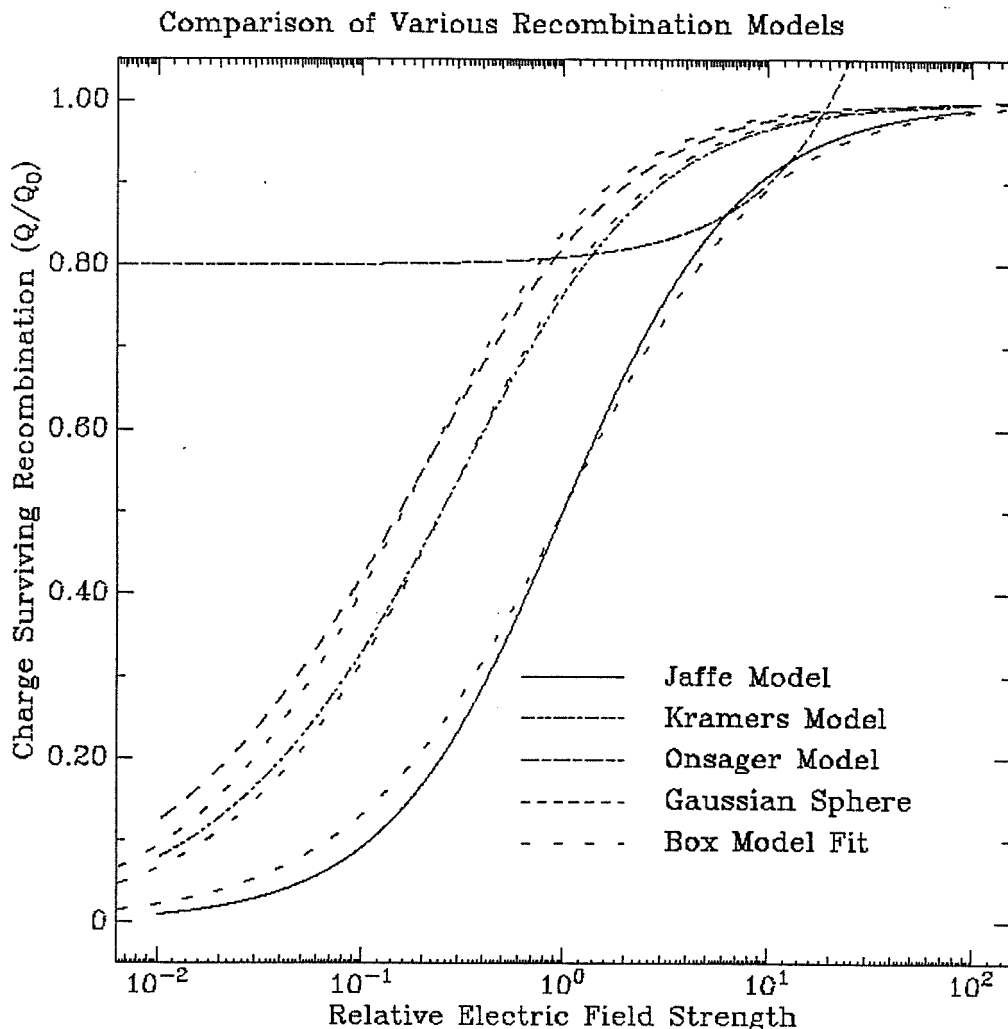


Figure A-2. Comparison of various models for initial recombination. For each other model, the box model with the recombination strength is superimposed for comparison of the shape of the curve. The curve intercepting the vertical axis at  $Q/Q_0 = 0.8$  is the Onsager model. The other curves are, reading from left to right and ignoring the box model curves, the Gaussian sphere, Kramers' model and Jaffe's model.

and is based on good assumptions about the detector media. The solution has a functional form which is convenient for fitting and will facilitate the construction of a more elaborate model for the energy resolution of these detectors. (See Appendix B.)

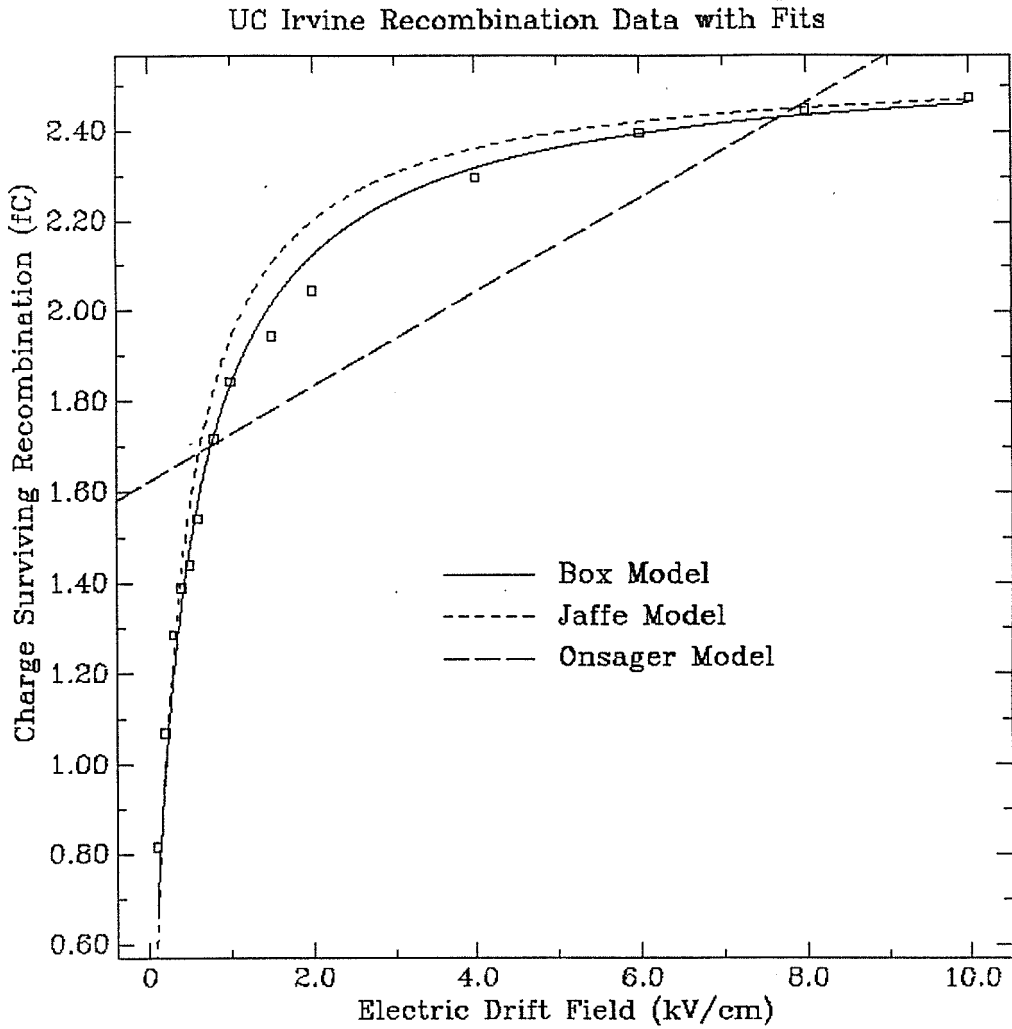


Figure A-3. Data from Scalettar *et al.*<sup>35</sup> used to determine the recombination strength in liquid argon. The best fit of our model to the data is compared with the best fit of the Jaffe model and a typical fit for the Onsager model.

## APPENDIX B

### Energy Resolution and $\delta$ -Electron Recombination

#### B.1 Introduction

In this appendix the recombination model of Appendix A is applied to the problem of the limited energy resolution obtained in liquid argon and liquid xenon ionization chambers. It is shown that the energy resolution limitations correspond not to fluctuations in the total number of electrons produced in an ionization event, but rather in the number of high charge-density regions along the ionization path of a charged particle. This is an expanded version of the work we published earlier, Thomas, Imel and Biller, Phys. Rev. A38, 5793, 1988.

#### *Motivation – Poisson Statistics and the Fano Factor*

Liquid xenon and liquid argon are remarkable media because the energy required to form an ion electron pair is small, 15.6 and 23.6 eV, respectively.<sup>69</sup> The statistical fluctuation in these numbers is small due to the unique solid-state properties of argon and xenon.<sup>70</sup> (We assume that liquid properties are closely related to the solid-state properties.) One way to express the statistical variation in the ionization process is through the Fano factor,<sup>11</sup>

$$\sigma = \sqrt{FE_p W}, \quad (\text{B-1})$$

where  $\sigma$  is the variance of the energy signal,  $F$  is the Fano factor,  $E_p$  the energy



of the primary particle, and  $W$  is the energy required to form an ion-electron pair. The Fano factor is an expression of the deviation of the ionization process away from independent, identically distributed ionization events. For a Poisson process  $F = 1$ , but if all ionization events are identical  $F = 0$ . The Fano factor in xenon is 0.04 to 0.06 and in argon it is 0.12.<sup>67</sup> This is due to the small number of degrees of freedom for the deexcitation of energetic electrons and the small band gap in these materials, 9.3 eV in xenon and 14.3 eV in argon.<sup>9,10,70</sup>

Extremely good energy resolution in liquid argon or xenon should be possible. Estimates based on the Fano factor go as low as 0.4% full width at half maximum (FWHM) at 1 MeV in argon.<sup>9</sup> But only  $\approx 3\%$  resolution has been observed in liquid argon even at extremely high electric fields.<sup>20,26-28</sup> Thus, one wishes to understand the source of energy resolution degradation preventing these detectors from achieving their optimum performance.

## **B.2 Sources of Energy Resolution Degradation**

There are several places where the signal from a monoenergetic event can be broadened by the detector system. We will examine each of these:

- Electronics
- Charge Induction
- Electron Drifting
- Initial Recombination
- Fluctuations in Energy Deposition

It should be noted first, however, that in these systems, the absolute charge is calibrated, usually to within  $\pm 5\%$ , so that the amount of charge induced on the system is known to be tens of thousands of electrons per MeV, and the  $\sqrt{N}$  variation of this number of electrons should be small. Thus, we must look for a process that varies the charge collected as a function of position or as a function of time, rather than simply a process which attenuates the total number of electrons collected.

### *Electronics*

The effect of electronic noise on the system is easily measured by including a monoenergetic test pulse, either at the grid or at the anode of the detector. Any broadening due to the electronics or capacitive noise of the detector will also smear out the test pulse. In fact, most of the results quoted for energy resolution in these detectors have the broadening due to electronic and capacitive noise subtracted out (in quadrature). Thus, we must look elsewhere for the source of the energy resolution problem.

### *Charge Induction*

It is possible that there might be some non-uniformity in the way charge is induced on the anode of the detector, so that from event to event a different amount of charge corresponds to a given energy deposit. The loss of electrons due to incomplete transmission through the grid is eliminated from consideration immediately as it does not provide a mechanism for *variation* in charge collection. (In fact, the grids are designed in these experiments for 100% transmission, and the transmission of electrons through the grid is observed to saturate when the grid-anode field is increased while holding the drift field

constant.)

The shielding inefficiency of the grid could provide a source of energy resolution deterioration. As discussed in chapter 1, the Frisch grid provides a shield for the anode of the electrons drifting between the cathode and the grid. Thus, the only charge induced on the anode is that due to electrons drifting from the grid to the anode. However, no grid is perfect. An inefficiency in the shielding of the grid would allow the anode to see the charge induced by the electrons moving in the drift region. In these experiments, the grids are carefully designed to be less than 1 or 2% inefficient, so that this is a small contribution to the energy resolution compared to the energy resolution observed in these detectors. This effect should be kept in mind as a possible future limitation. It is difficult to design a grid with 100% transmission and lower shielding inefficiency than 1% and still maintain a practical design in terms of the electric field strength required and the active drift volume desired.

Finally, the variation in the distance between the grid and the anode should have no effect on the energy resolution. The charge induced is 100% for electrons which drift the entire distance between the grid and detector, no matter how far the grid is from the anode. The only way there could be an effect with varying grid-anode distance is if the charge is attenuated differently while drifting this distance or if the capacitance somehow varied over the cross-section of the anode face. The latter could only occur in a segmented detector and would be immediately detected through the use of a pulser. The former will be discussed in the section on drifting, below. If the grid-anode distance were non-uniform, there would be a non-uniform electric field between the grid and the anode. This would effect the transmission of electrons through

the grid and could give rise to position-dependent charge collection. However, this potential problem has already been resolved by the aforementioned observation of the saturation of charge collection as a function of grid-anode field.

### *Electron Drifting*

One of the major difficulties in these experiments is to ensure that the detector media are absent of electronegative impurities which attach to drifting electrons. Again, to look for the source of energy resolution loss, we must look for loss of drifting electrons which is a function of position or event, not just for an absolute loss of electrons.

It is possible that when using an uncollimated, external  $\gamma$ -ray source energy deposited in one part of the detector is attenuated differently than in another part of the detector. This could be caused by non-uniform electric fields and by relatively high electronegative impurity levels. The electrons produced by  $\gamma$ -ray interactions at the energies of typical sources used have a range on the order of one or two millimeters. We may test this hypothesis by placing a conversion-electron source internal to the detector volume. Doke<sup>71</sup>, Aprile<sup>28</sup> and we<sup>21</sup> all placed conversion-electron sources at the center of the cathode. Thus, field non-uniformities should be minimal over the track of the electron. One may compute the electronegative impurity concentration required to generate variations in charge collection of a few percent over the range of the electron. For attenuation lengths  $\lambda$  large with respect to the range  $r$  of the electron, the broadening of the electron peak is given by  $r/\lambda$ . For typical field strengths of 1 kV/cm and a range of 2 mm, the minimum impurity level for a 2% variation in charge collection is 20 ppb O<sub>2</sub>-equivalent. But the purity level measured by drifting charges in low electric fields<sup>48</sup> and by measuring the charge

collected as a function of a variable drift length<sup>35</sup> is known to be much better than 20 ppb in these detectors.

*Recombination and Fluctuations in Energy Deposition*

Our model for recombination,

$$\frac{Q}{Q_0} = \frac{\log_e(1+\xi)}{\xi}, \quad (\text{B-2})$$

where the recombination strength  $\xi = N_0\alpha/4a^2\mu_-E$ ,  $E$  is the magnitude of the electric field,  $\mu_-$  the electron mobility,  $N_0$  the charge per unit cell of dimension  $a$  and  $\alpha$  a phenomenological recombination coefficient, showed that the recombination strength was a function of the electric field strength and the charge density in the recombination region. Thus if either of these changed from event to event, the energy resolution would be worsened from its ultimate limit by the variation of recombination from event to event. We can estimate the variation in the recombination strength required to produce an effect by taking the derivative of the charge surviving recombination:

$$\frac{dQ}{Q} = \frac{d\xi}{\xi} \frac{\left| \frac{\log_e(1+\xi)}{\xi} - \frac{1}{1+\xi} \right|}{\frac{\log_e(1+\xi)}{\xi}}. \quad (\text{B-3})$$

A fit of this equation to Aprile's data set<sup>28</sup> is shown in Fig. B-1 where we have assumed that the width of the peaks  $W_{\text{FWHM}} = D dQ/Q$ . The proportionality constant,  $D$ , may depend on the energy of the incident particle and the characteristics of the medium. A reasonable description of the data is achieved if  $\xi E = 0.8$ , a value fixed by the charge collection data alone, and

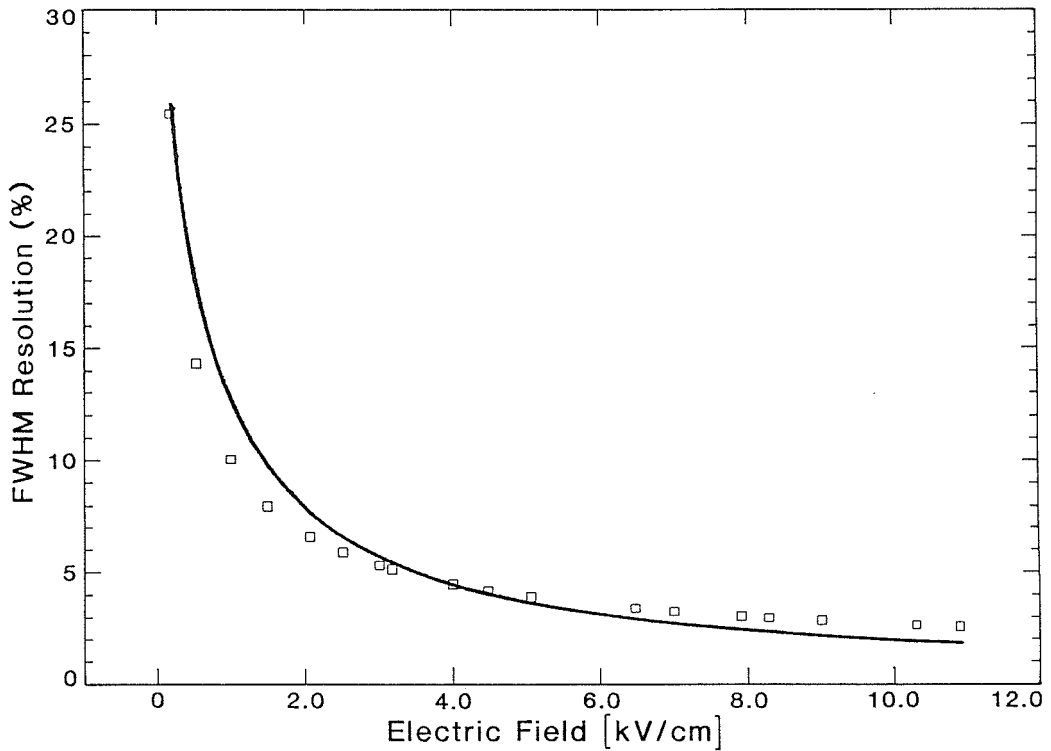


Figure B-1. A fit of (B-3) to the measured resolution of a 976-keV electron in liquid argon (Ref. 28).

$D \, d\xi/\xi = 0.51$ . If  $D$  is simply the proportionality constant between the FWHM of a Gaussian distribution and  $\sigma$ , i.e.,  $D = 2.35$ , then one must ask whether a variation of 20% in the recombination strength is plausible.

The variation in  $\xi$  with respect to electric field strength is  $d\xi/\xi = dE/E$ . But we observe the poor energy resolution in cases where a conversion-electron source is mounted at the center of the cathode, where the field is most uniform. In the case of our detector, where we employed multiple field gradient rings and a shielded, segmented anode, it is very difficult indeed to believe in a 20% variation in electric field strength over the range of the electron trajectory.

Similarly, the variation in  $\xi$  with respect to the charge density is  $d\xi/\xi = dN/N$ . Although we assumed in the construction of our recombination model that the charge deposited in an ionization event was isolated from all other charges by the medium, this is not exactly true. It is well known that charge-density fluctuations exist along the track of an ionizing particle. Fig. B-2 shows an electron traveling through a time projection chamber filled with two atmospheres of argon.<sup>15</sup> As the particle slows down it loses energy at a relatively fixed rate until it becomes nonrelativistic. At about this time, the energy loss increases and the particle loses the remainder of its energy in a relatively short distance (see Fig. B-3). The high charge deposition region, or blob, at the end of the track represents an energy loss of 30-40 keV.<sup>40</sup> Thus, our hypothesis is that the poor energy resolution results are due to intrinsic charge-density fluctuations along the path of an ionizing particle<sup>73</sup> since these fluctuations affect the rate of recombination of the electron-ion pairs.

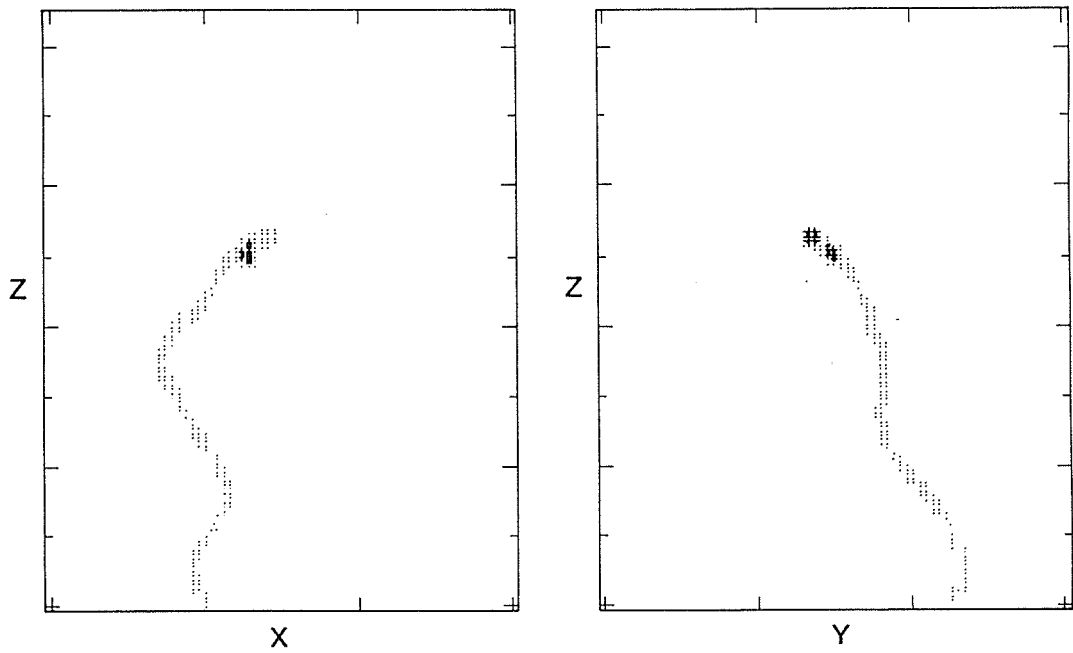


Figure B-2. (a) *X-Z* and (b) *Y-Z* projections of an electron track as it passes into a time projection chamber filled with 2 atmospheres of argon-methane (90/10 mixture). The electron stops near the center of the chamber and deposits 30-40 keV of energy in a well-localized “blob.” The *X* and *Y* axes are 30 cm wide and the *Z* axis is scaled accordingly. (See Ref. 72.)



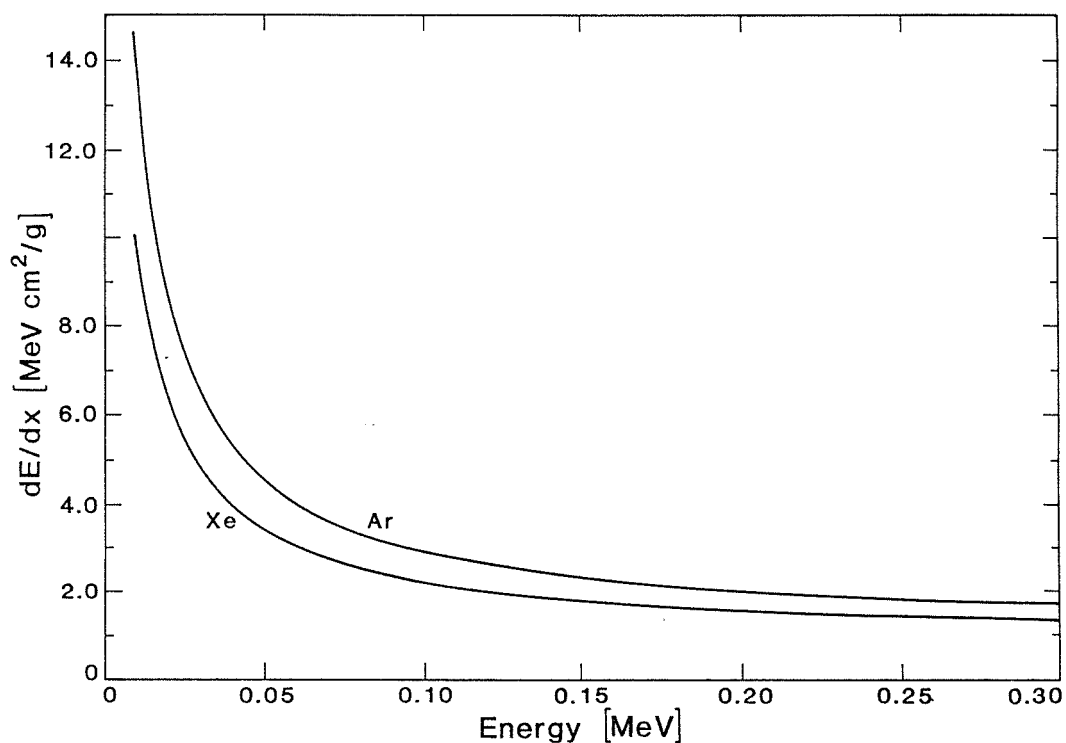


Figure B-3. Energy loss for electrons<sup>32</sup> in argon and xenon as a function of energy.

Note the rapid increase in  $dE/dx$  below 50 keV.

### B.3 $\delta$ -Electron Production and the Statistics of Charge Collection

The effect of charge-density fluctuations on the resolution of liquid noble gas ionization detectors has been discussed in the literature<sup>54</sup> but only in the context of the Jaffe-Kramers theory. (See Appendix A for a critique of this

theory.) It is shown in this section that a fundamental limit to the resolution comes naturally from our more physically realistic model of charge collection.

$\delta$ -electrons are produced by high-energy scatters of the incident primary ionizing particle and may further ionize the medium. A simple description of the  $\delta$ -electron production process is provided by the Rutherford scattering cross section. For nonrelativistic  $\delta$ -electrons (the primary may be relativistic) and for small scattering angles, the momentum transferred to the  $\delta$ -electron is  $p_\delta = p\theta$ , where  $p$  is the momentum of the primary electron. The probability of scattering a  $\delta$ -electron of energy  $E_\delta$  from a target of thickness  $\Delta x$  g/cm<sup>2</sup> is<sup>74</sup>

$$P(E_\delta) dE_\delta = \frac{2\pi N_A e^4}{\beta^2 m_e c^2} \frac{Z}{A} \Delta x \frac{dE_\delta}{E_\delta^2}, \quad (\text{B-4})$$

where  $Z$  is the atomic number of the target,  $A$  its atomic mass,  $m_e$  and  $e$  the mass and charge of an electron, and  $N_A$  is Avogadro's number. (B-4) is valid for a broad range of  $\delta$ -electron energies and will fail only when the scattering angle of the  $\delta$ -electron is large ( $\geq 1$  rad). This expression is also valid for a broad range of primary electron energies and should fail only if the primary electron energy is small ( $\leq 1$ keV) where it is important that the scattering electron is bound rather than free.

(B-4) is more easily expressed in terms of the energy loss of the primary electron. We use the expressions compiled by Pages *et al.*<sup>32</sup> for the energy loss due to ionization

$$\frac{dE}{dx} = \frac{2\pi N_A e^4}{\beta^2 m_e c^2} \frac{Z}{A} \left( \log_e \frac{T^2(T+2)}{2I^2} \right)$$

$$+ \frac{T^2/8 - (2T+1) \log_e(2)}{(T+1)^2} + 1 - \beta^2 \Bigg),$$

(B-5)

where  $T = E/m_e c^2$  and  $I$  is the mean excitation energy of the target in units of  $m_e c^2$ ;  $I m_e c^2 \approx 9.73Z + 58.8Z^{-0.19}$  eV.

The number of  $\delta$ -electrons of energy  $E_\delta$  produced by a primary electron,  $N(E_p, E_\delta)$ , can be calculated by integrating  $P(E_\delta)$  from 0 to  $E_p$  and using (B-5). Then,

$$N(E_p, E_\delta) = F(E_p) \frac{dE_\delta}{E_\delta^2}, \quad (B-6)$$

where

$$F(E_p) = \int_0^{E_p} dE \left[ \log_e \frac{T^2(T+2)}{2I^2} + \frac{T^2/8 - (2T+1) \log_e(2)}{(T+1)^2} + 1 - \beta^2 \right]^{-1} \quad (B-7)$$

can be evaluated numerically and is shown in Fig. B-4 as a function of energy in xenon and argon.  $F(E_p)$  is a smooth function of energy and approximate expressions for  $F$  are

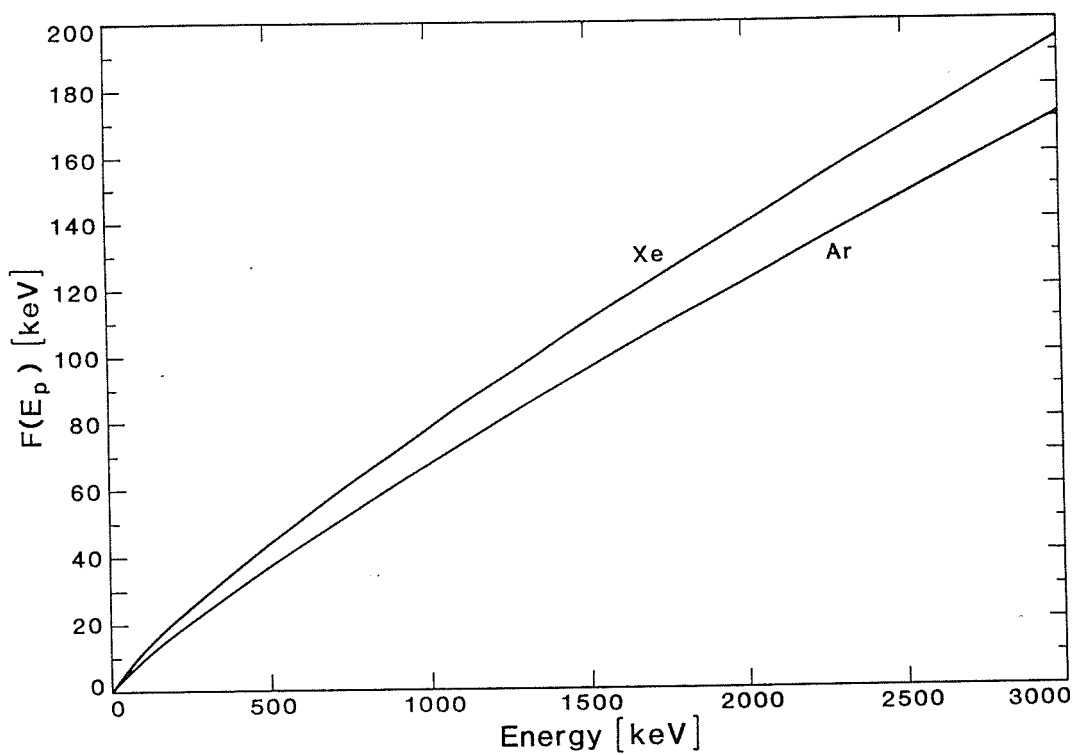


Figure B-4. The function  $F(E_p)$ , defined by (B-7), is essentially linear. Second order fits to these curves are listed in (B-8).

$$F_{\text{Ar}}(E_p) = -4.00 \times 10^{-6} E_p^2 + 6.80 \times 10^{-2} E_p + 2.83 , \quad (\text{B-8a})$$

$$F_{\text{Xe}}(E_p) = -5.12 \times 10^{-6} E_p^2 + 7.84 \times 10^{-2} E_p + 4.28 , \quad (\text{B-8b})$$

where  $E_p$  is the kinetic energy of the primary particle in keV.

An interesting consequence of (B-6) is that the energy carried by the  $\delta$ -electrons,  $NE_\delta$ , in an interval  $dE_\delta$ , is proportional to  $1/E_\delta$  and the fluctuation in the total energy,  $E_\delta\sqrt{N}$ , is a constant. Therefore the effect of the high-energy  $\delta$ -electrons is as important as the more abundant low-energy  $\delta$ -electrons in determining the resolution of an ionization detector.

The  $\delta$ -electrons should in principle carry away all of the energy of the primary electron. But since each high-energy  $\delta$ -electron can produce lower-energy  $\delta$ -electrons, and so on, the distribution of energies predicted by (B-6) should be weighted more heavily toward lower energies. This does not represent a large perturbation since the probability of a high-energy  $\delta$ -electron on a still higher-energy  $\delta$  electron depends on the product of two small probabilities. We approximate these second-order effects by normalizing the integral over all  $\delta$ -electron energies to the energy of the primary particle,

$$E_p \equiv F(E_p) \int_{E_0}^{E_p} \frac{dE_\delta}{E_\delta^2} E_\delta = F(E_p) \log_e \left( \frac{E_p}{E_0} \right). \quad (\text{B-9})$$

$E_0$  represents the minimum kinetic energy of a secondary electron and should be near the ionization energy of the atom since this is where the Rutherford scattering cross section breaks down. We define  $E_0$  such that (B-9) is valid and use this result to normalize the secondary electron distributions in the work that follows. (For the case of a 368-keV primary electron in xenon,  $E_0 = 4.2$  eV.)

We will use a simple double density model to describe the charge-density fluctuations. Along the minimum ionizing part of an electron track the charge

density is described by the parameter  $\xi_1$  and near the end of the electrons range, where  $dE/dx$  increases dramatically, the charge density is described by  $\xi_0$ . Thus every high energy  $\delta$ -electron track has a minimum ionizing portion and a high charge-density blob at its endpoint. The total charge collected from these two regions will be different and we can modify (B-9) to take this into account. The number of  $\delta$ -electrons in a given energy interval is  $dE_\delta/E_\delta^2$  and the energy collected from the  $\delta$ -electrons is  $E_\delta \left[ \log_e(1+\xi) \right] / \xi$ . Being careful to normalize the  $\delta$ -electron distribution we find that the collected energy,  $E_c$ , is

$$\begin{aligned} \frac{E_c}{E_p} = & \left( \int_{E_0}^{E_1} \frac{dE_\delta}{E_\delta^2} E_\delta \frac{\log_e(1+\xi_1)}{\xi_1} + \right. \\ & \int_{E_1}^{E_2} \frac{dE_\delta}{E_\delta^2} E_\delta \frac{\log_e(1+\xi_0)}{\xi_0} + \int_{E_2}^{E_p} \frac{dE_\delta}{E_\delta^2} E_2 \frac{\log_e(1+\xi_0)}{\xi_0} \\ & \left. + \int_{E_2}^{E_p} \frac{dE_\delta}{E_\delta^2} (E_\delta - E_2) \frac{\log_e(1+\xi_1)}{\xi_1} \right) \left( \int_{E_0}^{E_p} \frac{dE_\delta}{E_\delta^2} E_\delta \right)^{-1}. \quad (\text{B-10}) \end{aligned}$$

Those  $\delta$ -electrons with energies lower than  $E_1$  do not produce a high charge-density blob; there are simply too few electron-ion pairs created (at a cost of  $\approx 25$  eV per pair).  $\delta$ -electrons with energies between  $E_1$  and  $E_2$  go entirely into a high charge-density blob. And  $\delta$ -electrons with energies above  $E_2$  expend part of their energy along a minimum ionizing track and the remainder in a high-density blob.

It is trivial to show that (B-10) reduces to

$$\frac{E_c}{E_p} = \left( a \frac{\log_e(1+\xi_0)}{\xi_0} + (1-a) \frac{\log_e(1+\xi_1)}{\xi_1} \right), \quad (\text{B-11})$$

where

$$a \equiv \left( \frac{\log_e \left( \frac{E_2}{E_1} \right) - \frac{E_2}{E_p} + 1}{\log_e \left( \frac{E_p}{E_0} \right)} \right). \quad (\text{B-12})$$

Thus in the limit of small charge-density fluctuations, we recover (B-2).

This model leads to a finite resolution effect in liquid argon that is larger than the Fano factor limited resolution and should be added in quadrature to it. The effect follows from (B-6) which predicts  $N(E_p, E_\delta)$   $\delta$ -electrons of energy  $E_\delta$  with a variance  $\sqrt{N(E_p, E_\delta)}$ . But since the fluctuation in collected energy due to the blob is proportional to the difference in charge collected from the track and the blob, the variance in the observed energy signal is

$$\sigma^2 = \sum N(E_p, E_\delta) E_\delta^2 \left( \frac{\log_e(1+\xi_1)}{\xi_1} - \frac{\log_e(1+\xi_0)}{\xi_0} \right)^2. \quad (\text{B-13})$$

The total variance is the sum, in quadrature, over all  $\delta$ -electron energies that are high enough to create a charged blob. (See the second and third terms in (B-10).) To be more specific, our model is

$$\frac{\sigma^2}{E_c^2} = \left[ F(E_p) \log_e^2 \left( \frac{E_p}{E_0} \right) \frac{E_c^2}{E_p^2} \right]^{-1} \left[ \int_{E_1}^{E_2} \frac{dE_\delta}{E_\delta^2} E_\delta^2 \left( \frac{\log_e(1+\xi_1)}{\xi_1} - \frac{\log_e(1+\xi_0)}{\xi_0} \right)^2 + \int_{E_2}^{E_p} \frac{dE_\delta}{E_\delta^2} E_\delta^2 \left( \frac{\log_e(1+\xi_1)}{\xi_1} - \frac{\log_e(1+\xi_0)}{\xi_0} \right)^2 \right], \quad (\text{B-14})$$

which reduces to a simple expression for the observed width of a peak in a

spectrum:

$$W_{\text{FWHM}}(\%) = \frac{235.5 \left[ F(E_p) \left( 2E_2 - E_1 - \frac{E_2^2}{E_p} \right) \right]^{1/2}}{F(E_p) \log_e \left( \frac{E_p}{E_0} \right) \frac{E_c}{E_p}} \times \left( \frac{\log_e(1+\xi_1)}{\xi_1} - \frac{\log_e(1+\xi_0)}{\xi_0} \right). \quad (\text{B-15})$$

In the limit of small charge fluctuations, it can be shown that (B-15) reduces to (B-3) if

$$D \frac{dN}{N} = \frac{235.5}{E_p} \left[ F(E_p) \left( 2E_2 - E_1 - \frac{E_2^2}{E_p} \right) \right]^{1/2}. \quad (\text{B-16})$$

But now it is possible to model the situation where the charge density fluctuations are not small and we have an explicit prediction of how  $D \frac{dN}{N}$  varies with the energy of the primary particle. In leading order, the percent energy resolution varies as  $E_p^{-1/2}$ .

(B-11) and (B-15) can be tested against experimental data. Figs. B-5, B-6, and B-7 present our model versus our liquid argon data<sup>21</sup> as well as that of Scalettar<sup>35</sup> and Aprile<sup>28</sup>. In Aprile's data sets and ours the O<sub>2</sub>-equivalent impurity concentrations were  $\approx 1$  ppb and so did not affect the resolution in the small chambers used for these studies except at very low fields ( $< 100$  V/cm). Scalettar's data was collected in a large ionization chamber equipped with a movable cathode so that the exponential attenuation of the collected charge, due to the impurities, could be measured directly. So the data presented in



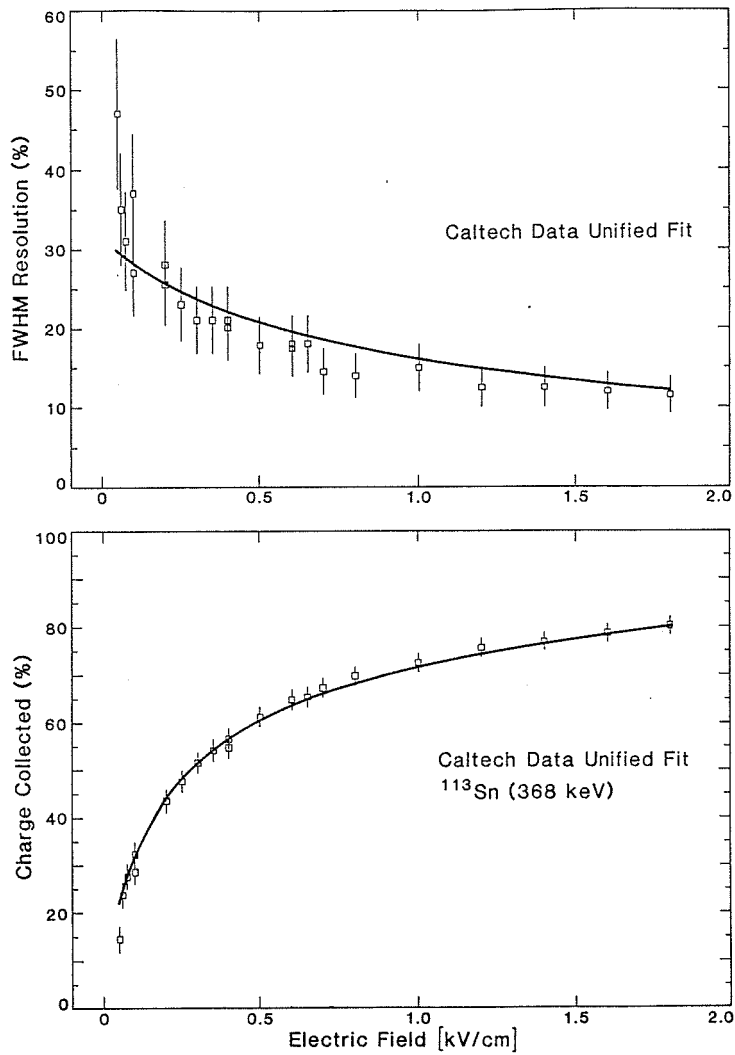


Figure B-5. A simultaneous fit of (B-11) and (B-15) to the (a) energy resolution and (b) charge collected in liquid argon<sup>21</sup>. The data shown in Figs. B-7 and B-8 were fit at the same time. (FWHM error bars are shown.)

Fig. B-7 has had the effect of the impurities removed, for all field strengths, and this was the data set used to determine  $\xi E$ .<sup>22</sup>

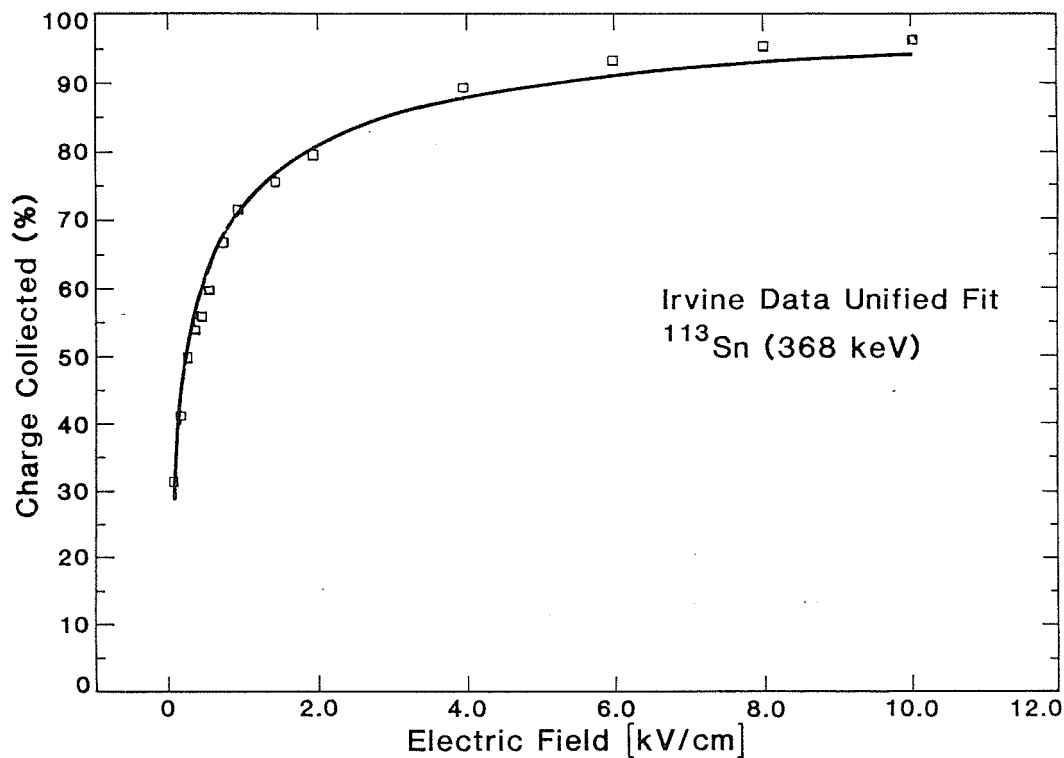


Figure B-6. The unified fit of (B-11) compared to the data in Ref. 35.

The double density model was fit to the data in the following way: our<sup>21</sup> charge collection data sets, Scalettar's<sup>35</sup> and Aprile's<sup>28</sup> were fit simultaneously with the resolution data sets collected by us and Aprile. (Scalettar's publication unfortunately does not include resolution results.) Ours and Scalettar's data were collected using a  $^{113}\text{Sn}$  source which emits 368-keV conversion electrons.

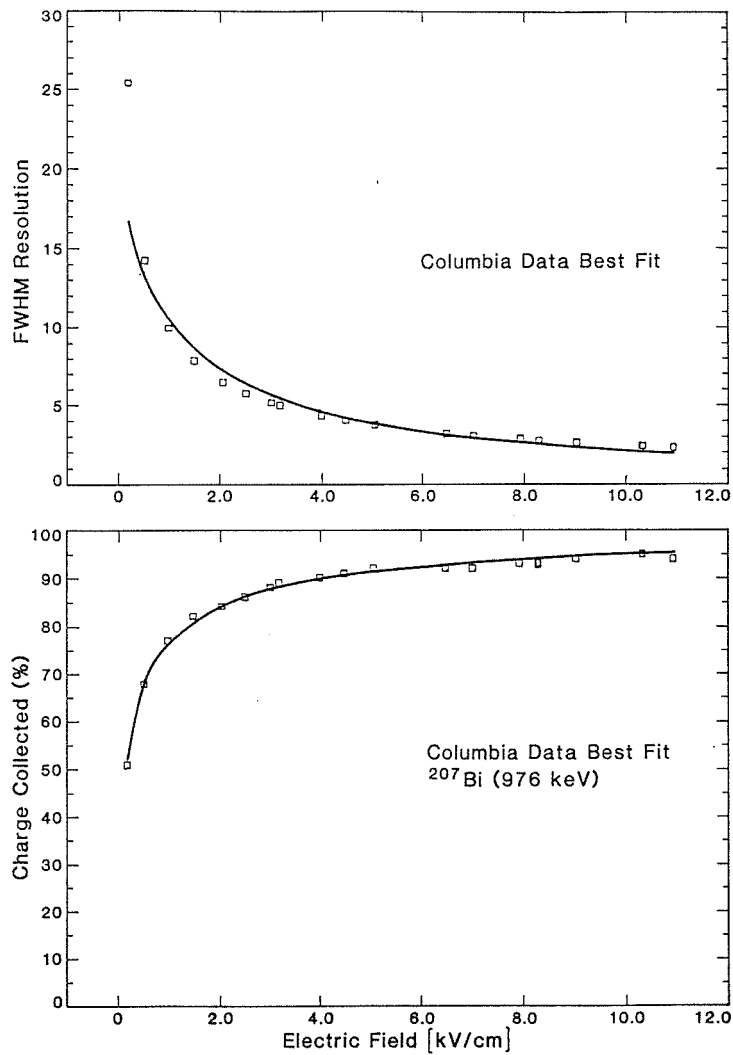


Figure B-7. The unified fit of (B-11) and (B-15) compared to the data in Ref. 28.

Aprile's data were collected using the 976-keV conversion electrons from a  $^{207}\text{Bi}$  source. The errors on Scalettar's and Aprile's data were not published and so we assumed that all three data sets were subject to the same errors for the purpose of the fitting procedure. Also, all of the charge collection data sets were subject to a 5% systematic uncertainty in the calibration of the

electronics. We have taken our data and Aprile's as is, without normalization. Scalettar's data were systematically high in all of the fits and so we reduced his normalization by 2% ( $\approx \frac{1}{2} \sigma$ ) in order to get the best understanding of the shapes of the curves. Thus, the normalizations were fixed and not fit. The resolution data are relative data and so there is no systematic uncertainty in the magnitude of these values.

Ref.	$\xi_1 E$	$\xi_0 E$	$E_2$	$\chi^2$
21	0.337	3.37	36.3	1.37
35	0.337	3.37	36.3	2.85
28	0.337	3.37	36.3	2.21
28	0.217	3.37	40.8	0.68

Table B-1. The universal fit parameters used to draw the theoretical curves shown in Figs. B-5, B-6, and B-7. The last line compares the best fit parameters for Ref. 28 to the universal fit parameters.

A unified fit to all five data sets yields  $\xi_1 E = 0.34 \pm 0.12$ ,  $\xi_0 E = 3.4 \pm 0.7$ , and  $E_2 = 36 \pm 13$  keV, and this fit is shown in Figs. B-5, B-6, and 7. Table B-1 lists the  $\chi^2$  for each fit. Table B-1 also lists the parameters for the best possible

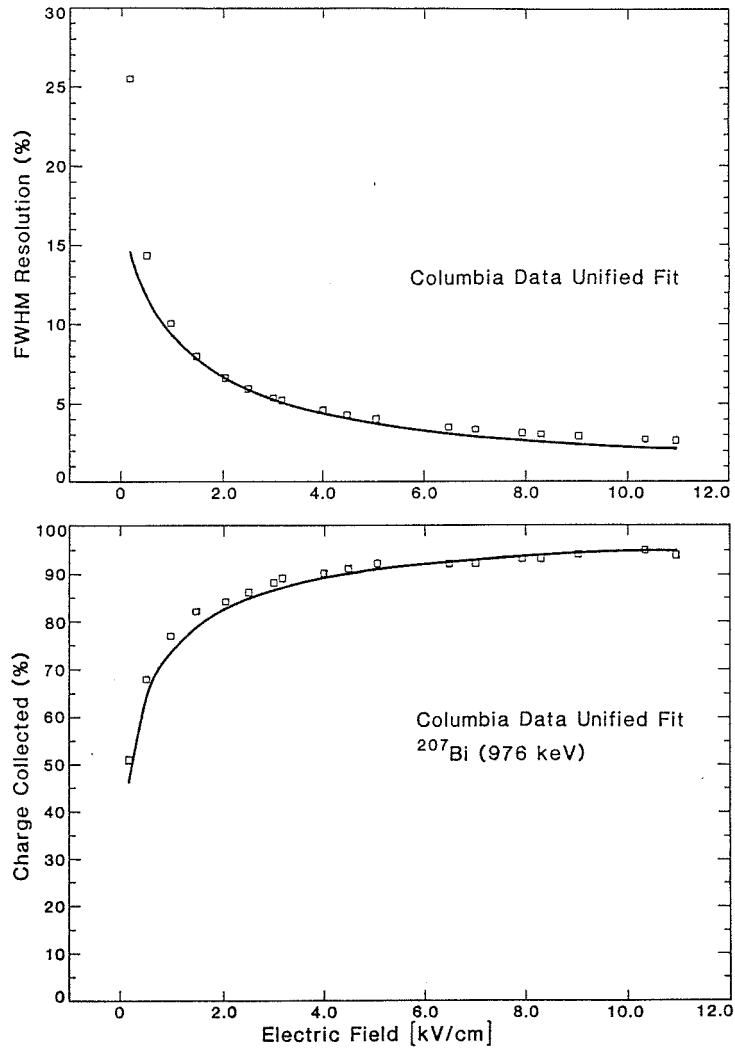


Figure B-8. For comparison to the unified fit, the best fit to the data in Ref. 28 is shown.

fit to Aprile's data just to show how stable the fit parameters are. The best fit parameters represent only a modest change from the universal fit parameters and the fit is shown in Fig. B-8. For all model fits,  $E_0$  was fixed by the normalization of (B-9) and  $E_1$  was fixed at 1 keV. If  $E_1$  were allowed to vary, a broad

range of values gives equally good  $\chi^2$  values, from 0.25 keV to 3 keV. A value of 1 keV was chosen because Rutherford scattering fails to describe the cross section at lower energies and it is reasonable that a  $\delta$ -electron of about 1 keV cannot make a charged blob; there are too few secondary electrons created to make a highly shielded, high charge-density region.

The value of  $E_2$  required by the universal fit,  $36 \pm 13$  keV, has great intuitive appeal. Fig. B-3 shows that the rate of energy loss below 50 keV increases dramatically. This is essential to forming a charged blob at the end of a track, but also the electron must scatter at large, random angles in order to ensure that it remains in a localized region. So we have calculated the angular distribution of electrons traversing a target of finite thickness using Moliere's scattering theory (which is best described by Bethe<sup>40,75</sup>).  $\theta_{\max}$  marks the peak in the angular distribution and it increases at lower energies, as we would expect. Assuming that the product of  $dE/dx$  and  $\Theta_{\max}$  is related to the probability of blob formation, we plot  $\theta_{\max} \times dE/dx$  in Fig. B-9. It rises very rapidly at low energies and the range from 30-40 keV marks the transition from low probability to high probability.

(B-11) and (B-15) can also be fit to charge collection and resolution data collected in liquid xenon. The best fit to our data<sup>21</sup> is shown in Fig. B-10. It is not obvious how to scale the parameters from argon to xenon and more data would be desirable to help understand the scaling mechanism. There are other xenon data sets in the literature<sup>27,49,69,76</sup>, but these data are not as consistent as the argon data.

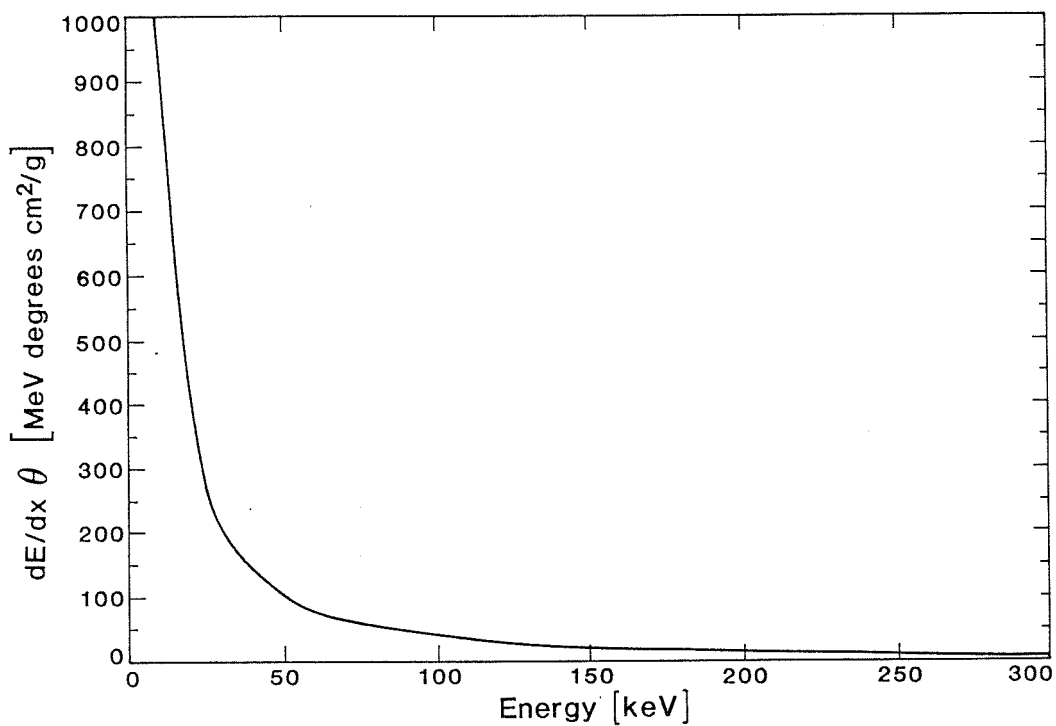


Figure B-9. The product of the average scattering angle and the rate of energy loss is related to the probability of "blob" formation at the end of an electron track.  $\theta$  is the angle associated with the peak in the electron scattering angle distribution. The curve is the same for argon and xenon within the resolution of this figure.

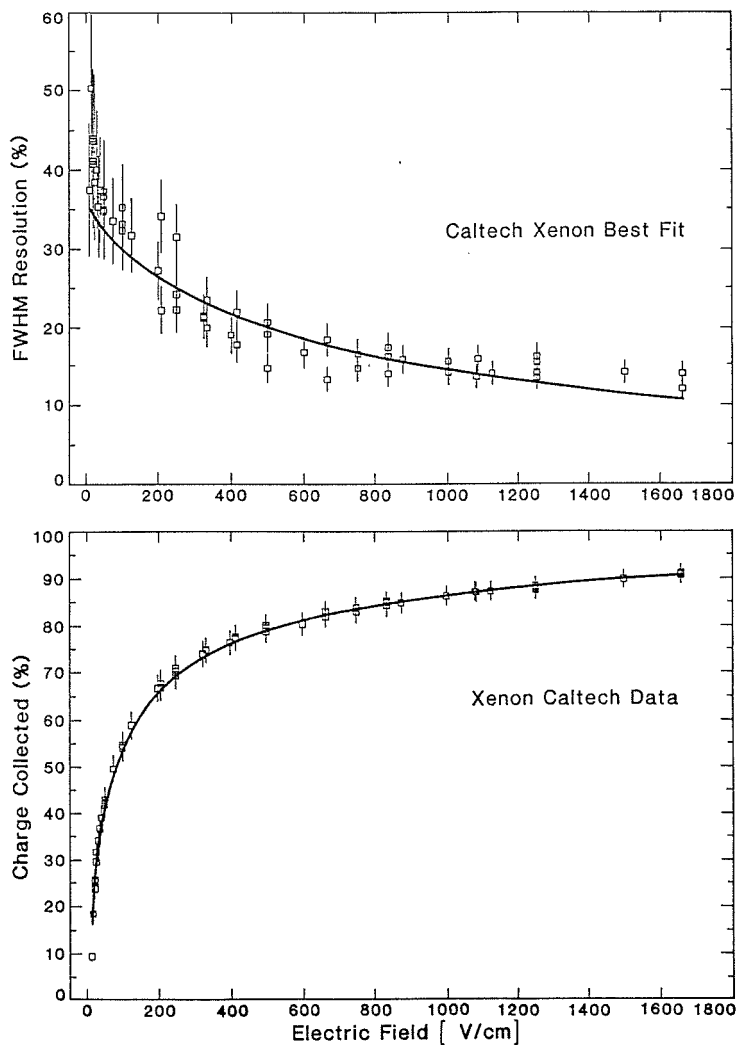


Figure B-10. A simultaneous fit of (B-11) and (B-15) to the (a) energy resolution and (b) charge collected in liquid xenon using a 368 keV *K*-shell conversion electron source. The best fit to these data requires  $\xi_1 E = 0.128$ ,  $\xi_0 E = 1.92$ , and  $E_2 = 51.0$  keV.  $E_1$  was allowed to vary and the best value was 9.6 keV. The data shown here are from Ref. 21.



#### B.4 Conclusions

We have used a physically realistic model to show that there is a fundamental limit to the resolution that can be achieved in liquid argon. The limit is due to charge density fluctuations along an electron track and by the statistics of  $\delta$  electron formation, both of which are fundamental properties of the material and cannot be avoided. These limits are modeled by (B-11) and (B-15) and they can be simplified for experimental analysis by noting that

$$a \approx 0.291 + 16.7/E_p, \quad (\text{Argon}) \quad (\text{B-17a})$$

$$a \approx 0.203 + 12.2/E_p, \quad (\text{Xenon}) \quad (\text{B-17b})$$

and

$$\left[ W_{\text{FWHM}}(\%) \frac{E_c}{E_p} \right] = \frac{235.5}{\sqrt{E_p}} b \left( \frac{\log_e(1+\xi_1)}{\xi_1} - \frac{\log_e(1+\xi_0)}{\xi_0} \right), \quad (\text{B-18})$$

where

$$b \approx \left[ 4.52 + (157/E_p) \right]^{1/2} \quad (\text{Argon}), \quad (\text{B-19a})$$

$$b \approx \left[ 6.76 + (216/E_p) \right]^{1/2} \quad (\text{Xenon}). \quad (\text{B-19b})$$

The best way to improve the resolution of these detectors is to reduce  $\xi_0$  and  $\xi_1$ . Since  $\xi = N_0\alpha/4a^2\mu_-E$ , the simplest way to decrease  $\xi$  is to increase the electric field. Extrapolations of Figs. B-5, B-6, and B-7 suggest that the fluctuations due to  $\delta$ -electrons will be equal to or smaller than the Fano factor fluctuations in argon only at 60 kV/cm. But this is impractical in experiments

which require several centimeter drift distances.

A second approach would be to increase the electron-ion mobility. An order of magnitude estimate of what is required comes by noting that the relative electron-ion mobility in Ge is 50-100 times higher<sup>31</sup> than in argon and xenon, and Ge detectors do not appear to be limited by the statistics of the  $\delta$ -electrons. This suggests that adding methane to the xenon would not be sufficient since we only expect to increase the mobility by a factor of 2.<sup>30</sup> Similarly, changing to the solid phase should only increase the mobility by about a factor of two.<sup>71</sup> But we note that Cohen and Lekner<sup>77</sup> have shown that the low field electron mobility in argon varies as  $T^{-3/2}$ . Decreasing the temperature may give us the required factor of 50 increase in mobility if solid xenon was taken from its triple point to liquid-helium temperatures. There is experimental data<sup>36</sup> suggesting that the low field mobility varies as  $T^{-3/2}$ . But a possible complication is that the recombination coefficient  $\alpha$  may be proportional to the electron mobility<sup>2</sup> and therefore the temperature dependence would cancel out of the problem. Obviously, this approach requires further work.

A third approach would be to lower the charge density along the electron track.  $N_0$  is the charge per unit cell of dimension  $a$ . This could be decreased by increasing  $a$  (i.e., lowering the density of the liquid). Experiments above the critical point, near liquid densities, would be interesting, especially since the value of  $\xi$  may depend nonlinearly on  $N_0/a^2$  because a charge blob would have a highly screened region of charge at its center. The region below  $\frac{1}{2}$  liquid density has been explored<sup>63</sup> with mixtures of hydrogen and xenon and the data supports these ideas.

A fourth approach to improving the resolution of liquid- and solid-Xe detectors would be to decrease the value of  $\alpha$ . This is a phenomenological recombination coefficient that is derived from a simplified Langevin process.<sup>63</sup> It depends on inter-atomic potentials and other invariable quantities. But the effective recombination coefficient may be changed by doping the Ar or Xe with a photosensitive converter such as tetramethylamine or tetraethylamine (TMA, TEA). Doke<sup>9</sup> has observed that when an electron recombines, ultra-violet photons are emitted, and as the electric field is increased, the light output decreases. A photosensitive dopant would absorb these photons and convert them back to electrons so that they could be used to compensate the ionization signal. This effect has already been seen for  $\alpha$  particles in Xe doped with TEA by Suzuki<sup>37</sup> and Ar doped with TMA by Anderson<sup>38</sup>. These authors observed improved resolution, from 15% down to 4%, with the dopant and an  $\alpha$  source but obtained no substantial improvement with an electron source.

## APPENDIX C

### Spectra from High Pressure Ionization Chambers

#### *Introduction*

In this appendix I present and discuss several spectra recorded with the high pressure ionization chamber discussed in chapter 3. I also present a method for improving the energy resolution of ionization chambers with low but constant purity levels.

#### **C.1 Argon Spectra**

The high pressure ionization chamber described in chapter 3 was the final detector in a small series of test detectors built to gauge the performance of high pressure xenon and argon. One of the first limitations discovered in the design was that of capacitive noise. The initial detectors used an anode which was not segmented. This has obvious advantages as far as efficiency and simplicity, as well as providing an automatic high pressure, low background, high vacuum signal feedthrough by the anode itself. However, the capacitance of the detector was so high (for a parallel plate capacitor,  $C \propto A/d$ , where  $A$  is the area and  $d$  is the separation of the plates) that we had to segment the anode into an inner and outer segment, where the inner segment had an area approximately one-fifth that of the whole anode. In a detector where the full active volume would be required, we would further segment the outer segment into four equal segments, Fig. C-1. Fig. C-2 illustrates the improvement in energy

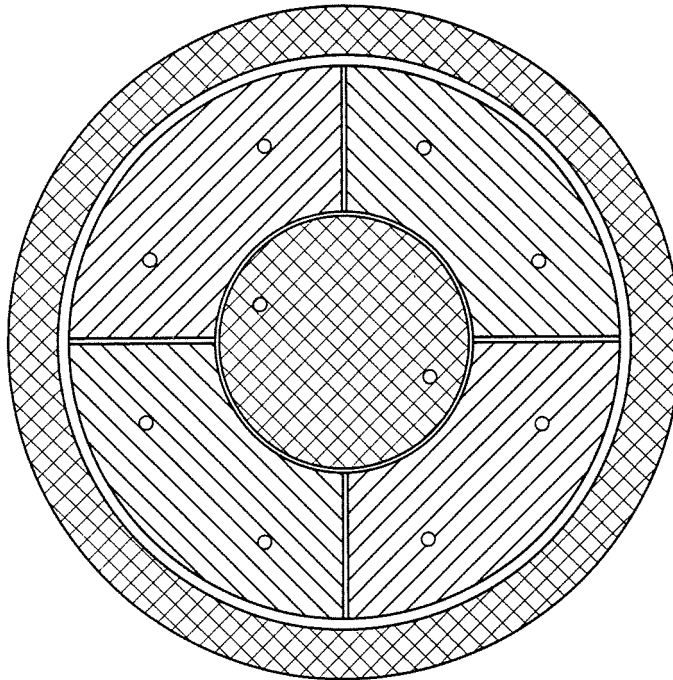


Figure C-1. Design of an anode segmented into five approximately equal area sections. In the detector of chapter 3, this anode was used without dividing the outer ring into four segments as it has been in this drawing. Only the inner anode segment was used in acquiring the spectra shown in this appendix and in chapter 3, with the exception of Fig. C-2a.

resolution which was obtained by segmenting the anode.

The charge collection and energy resolution of the argon detector was stable for at least moderate time periods (~ several hours). A spectrum acquired over a period of about 2 hours is shown in Fig. C-3. The lower level discriminator has been adjusted for this spectrum to allow the Pb x-ray to appear at the low energy end of the spectrum. This indicates that the detector may be used to observe fairly low energy processes. In fact, if the noise were reduced further by additional segmentation of the anode, much lower energy

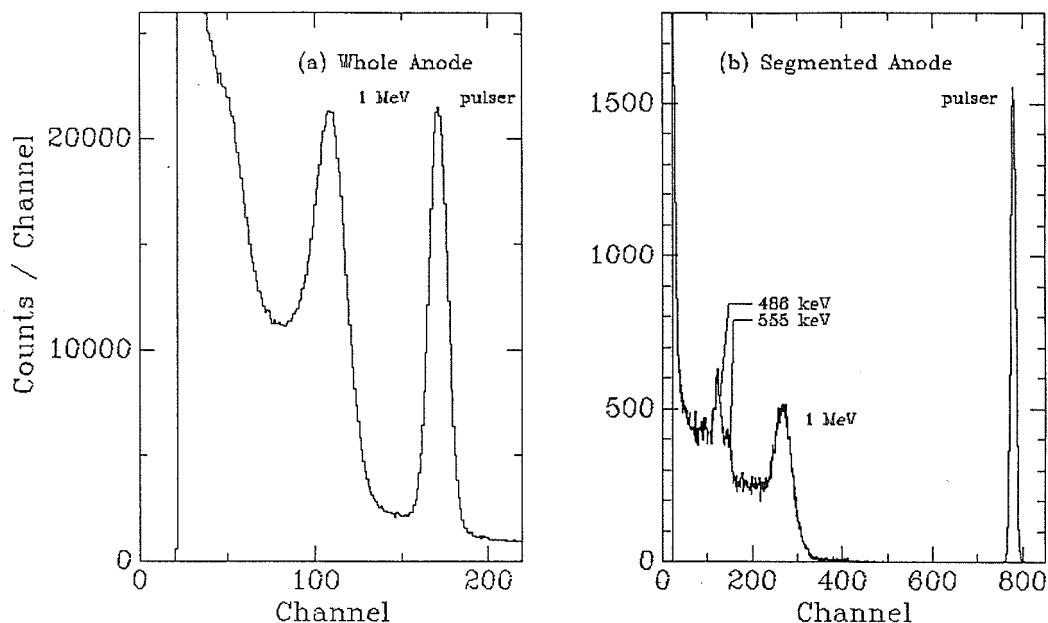


Figure C-2. The effect of segmenting the anode is shown here. Both spectra were acquired using a  $^{207}\text{Bi}$  conversion electron source placed on the center of the cathode. (a) Spectrum taken early in the development of the detector of chapter 3, before the anode was segmented. ( $E_d = 1.0$  kV/cm) (b) Spectrum taken shortly after anode was segmented. ( $E_d = 0.8$  kV/cm) Both spectra show poor charge collection due to electronegative impurities in the argon, which was not purified before it was introduced into the detector. The calibration is different for (a) than it is for (b), but the pulser amplitude is the same for both.

structures might be examined.

Many of the spectra taken in argon show an electron escape tail. This occurs when the electrons which are emitted perpendicular to the drift axis are not stopped with the active region of the anode segment. Fig. C-4 illustrates this effect at three different pressures. In this detector the radius from the

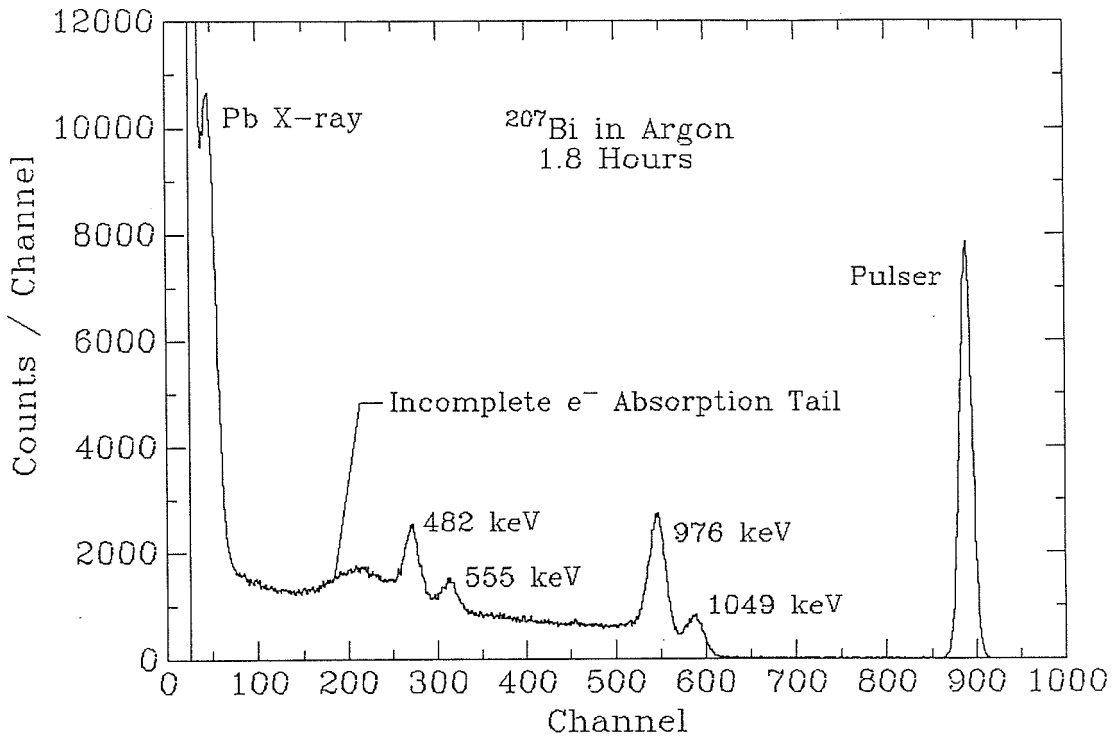


Figure C-3.  $^{207}\text{Bi}$  spectrum in high pressure argon with the lower level discriminator adjusted to show the Pb x-ray. Thus, structure may be observed in these detectors at energies as low as 100 keV.

source of the active region is about 2.3 cm. This compares with the tabulated (effective) range (see Table 3-1b) of a 1 MeV  $e^-$  in argon of 9 cm (6 cm) at 40 atm and 3.5 cm (2.3 cm) at 100 atm.

## C.2 Xenon Spectra

Spectra in high pressure xenon are shown in Figs. C-5 and C-6. Fig. C-5 shows  $^{207}\text{Bi}$  spectra at 20 and 30 atm. The K-conversion electron peaks and the full-energy peaks are barely separated in these spectra. As described in chapter 3, the energy resolution in the xenon detector was limited by the

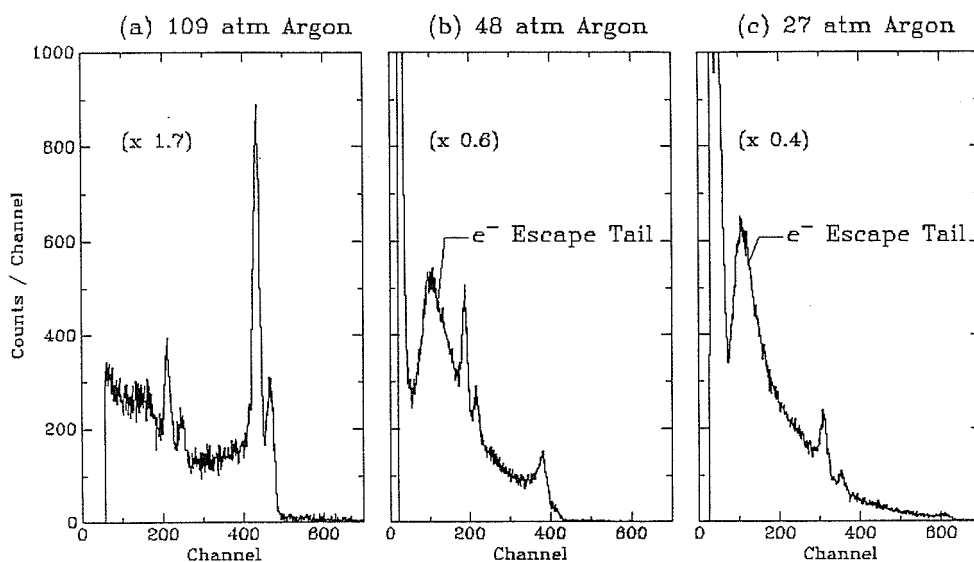


Figure C-4. The effect of incomplete electron absorption, or electron escape, is shown here in spectra taken at (a) 109 atm, (b) 48 atm and (c) 27 atm of argon. In (b) and (c) the tail caused by electrons which escape the active region of the detector is obvious. By contrast, at 109 atm, evidently few or none of the electrons escape. These spectra have been normalized to the same acquisition time, so that the counts / channel axis reflects the efficiency of the detector at a given energy.

inability to drift electrons without attachment to electronegative impurities. This was measured by scanning a collimated  $\gamma$ -ray beam from a 62 mCi  $^{137}\text{Cs}$  source along the drift length of the detector, perpendicular to that length. Fig. C-6 gives spectra obtained in this case. By observing the shift in the pulse height with drift distance the attenuation length could be calculated, and the initial recombination strength could be measured. (See chapter 3.)



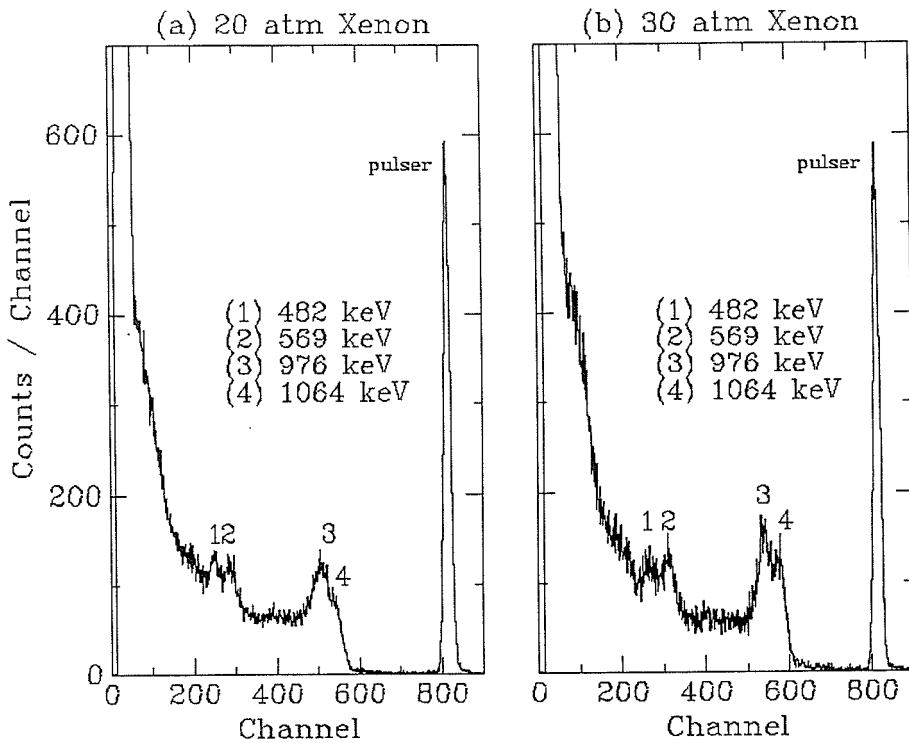


Figure C-5.  $^{207}\text{Bi}$  spectra in (a) 20 atm ( $E_d = 0.6$  kV/cm) and (b) 30 atm of xenon ( $E_d = 0.7$  kV/cm).

### C.3 Improving Energy Resolution by Field Shaping

The primary limitation in the energy resolution of the xenon detector was the attachment to electronegative impurities, which caused the charge collection to be a function of position in the detector, specifically, a function of the drift distance. The obvious way to overcome this problem is to change the materials and the cleanliness of the xenon so that attachment to electronegative impurities is no longer significant. However, when this is not feasible, another possible solution may be the method described in this section.

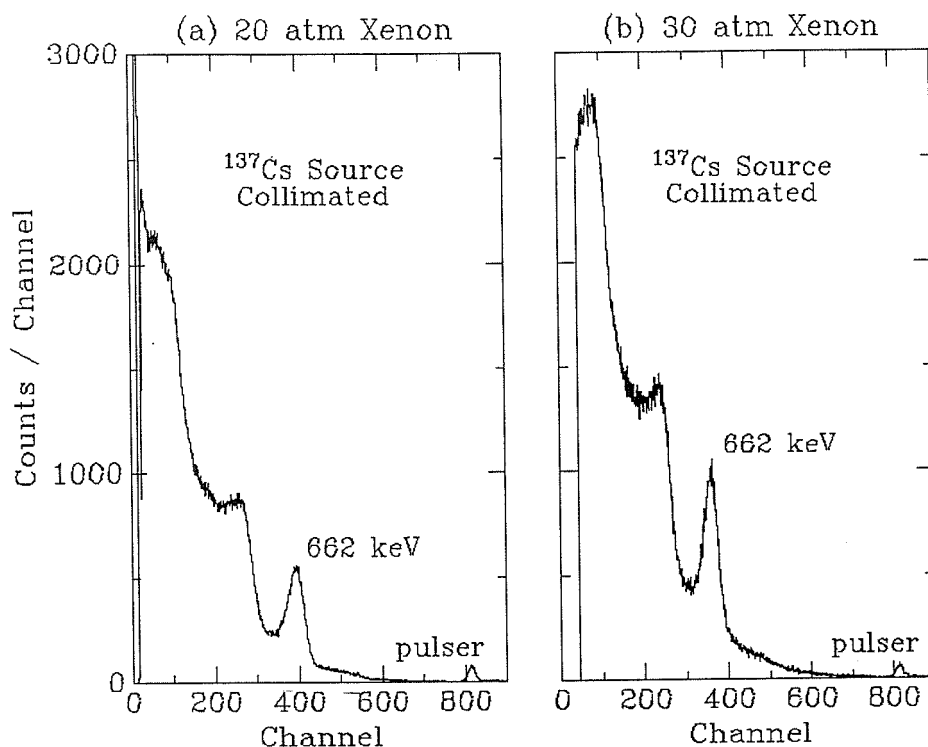


Figure C-6.  $^{137}\text{Cs}$  spectra in (a) 20 atm ( $E_d = 0.6$  kV/cm) and (b) 30 atm of xenon ( $E_d = 0.5$  kV/cm). The  $^{137}\text{Cs}$  external, collimated  $\gamma$ -ray source was located on rollers, and the  $\sim 2$  mm wide beam could be located anywhere along the drift length of the detector in order to measure the attenuation length of the medium. Here, the beam was placed at a drift distance  $d = 2.0$  cm.

Instead of minimizing attachment to electronegative impurities, one may vary the electric field strength to cancel out variations in charge collection with position in the detector. In terms of the individual field gradient rings which set the potentials in these detectors, the condition is that the charge induced on the anode by energy deposited at the position of the  $n$ 'th ring is the same as the charge induced on the anode by an identical amount of energy deposited at the

$n + 1$ 'th ring and subsequently drifted a distance  $d$  to the position of the  $n$ 'th ring:

$$\frac{Q_{n+1}}{Q_n} e^{-\frac{d}{\lambda_{n+1}}} = 1, \quad (\text{C-1})$$

where  $\lambda_{n+1}$  is the attenuation of drifting electrons between the  $n + 1$ 'th and  $n$ 'th ring, and the convention shall be that the first ring is nearest the anode, and the highest numbered ring is nearest the cathode. Typically it is simplest, and it is true in the case of our detector, to assume that the field gradient rings will be equally spaced. Thus for an ionization chamber with a drift distance  $s$  and  $n$  equally spaced field gradient rings,  $s = nd$ .

With a non-constant electric drift field, attachment to electronegative impurities may be described by an attenuation length which is a function of position along the drift length:

$$\lambda_n = \frac{\alpha E_n}{\rho}, \quad (\text{C-2})$$

where  $\alpha$  and  $\rho$  are the usual quantities (chapter 2) and  $E_n$  is the electric field strength between rings  $n$  and  $n - 1$ . Clearly, the charge induced on the anode cannot be made perfectly uniform for any finite value of  $\rho$  and  $E$  by only considering the attachment of electrons to electronegative impurities. In that case the left hand side of (C-1) is less than one always. However, there are two additional modifications to the charge collection process we may include: the recombination strength is also a function of electric field, and in this case, position; and if we remove the grid the charge induced on the anode is a function of the potential through which the charge drifts, i.e., for a constant drift field, the

charge induced on the anode of an ionization chamber without a grid is directly proportional to the distance drifted.

First, we consider the case of a gridded ionization chamber where the field strength is allowed to be a function of position. The desired criterion (C-1) becomes:

$$\frac{\xi_n}{\xi_{n+1}} \frac{\log_e(1+\xi_{n+1})}{\log_e(1+\xi_n)} e^{-\frac{d}{\lambda_{n+1}}} = 1, \quad (\text{C-3})$$

where  $\xi_n = k/E_n$  is the recombination strength between rings  $n$  and  $n-1$ . The  $E_n$  are set by applying the appropriate potentials to the  $n$ 'th and  $n-1$ 'th rings. In principle, this condition may always be met, perhaps by using a separate voltage supply for each field gradient rings, or by using a resistor chain on the rings comprised of variable resistors.

However there are two constraints for this solution. First, the total potential applied must be achievable, otherwise one could always apply an arbitrarily large electric field, and position-dependent charge collection would cease to be a problem. Second, the charge collection must be sufficiently large that electronic and capacitive noise does not dominate the energy resolution. These conditions amount to requiring the gas to be moderately pure, or requiring the variation of the electric field over the drift length of the detector to be moderate. An example solution is provided in Table C-1 for the case of a xenon ionization chamber.

In the case of an ionization chamber without a grid we must replace the attenuation term in (C-3) with a term describing the charge induced on the anode by drifting electrons as they are being attenuated by electronegative

$n$	$E_n$ (kV/cm)	$n$	$E_n$ (kV/cm)
1	0.10	7	0.43
2	0.13	8	0.54
3	0.17	9	0.66
4	0.22	10	0.80
5	0.28	11	0.98
6	0.35	12	1.19

Table C-1. Solution to (C-3) for a xenon ionization chamber with 12 field gradient rings and a drift distance of 5.0 cm. The purity of the detector is assumed to be constant and such that for a constant drift field of 0.5 kV/cm, the attenuation length would be 20 cm (a typical value achievable in the detector described in chapter 3). The recombination strength used was  $\xi E = 0.1$  kV/cm. These field assignments yield a charge collection of 63% and a total applied potential of 2.34 kV.

impurities. Thus, we have:

$$\frac{\xi_n}{\xi_{n+1}} \frac{\log_e(1+\xi_{n+1})}{\log_e(1+\xi_n)} \lambda_{n+1} E_{n+1} \left( 1 - e^{-\frac{d}{\lambda_{n+1}}} \right) = 1. \quad (\text{C-4})$$

If we simplify the situation to that of a constant electric field, we can no longer exactly satisfy (C-4). However, the increase in charge induced on the anode with increasing distance from the anode of an event may be used to

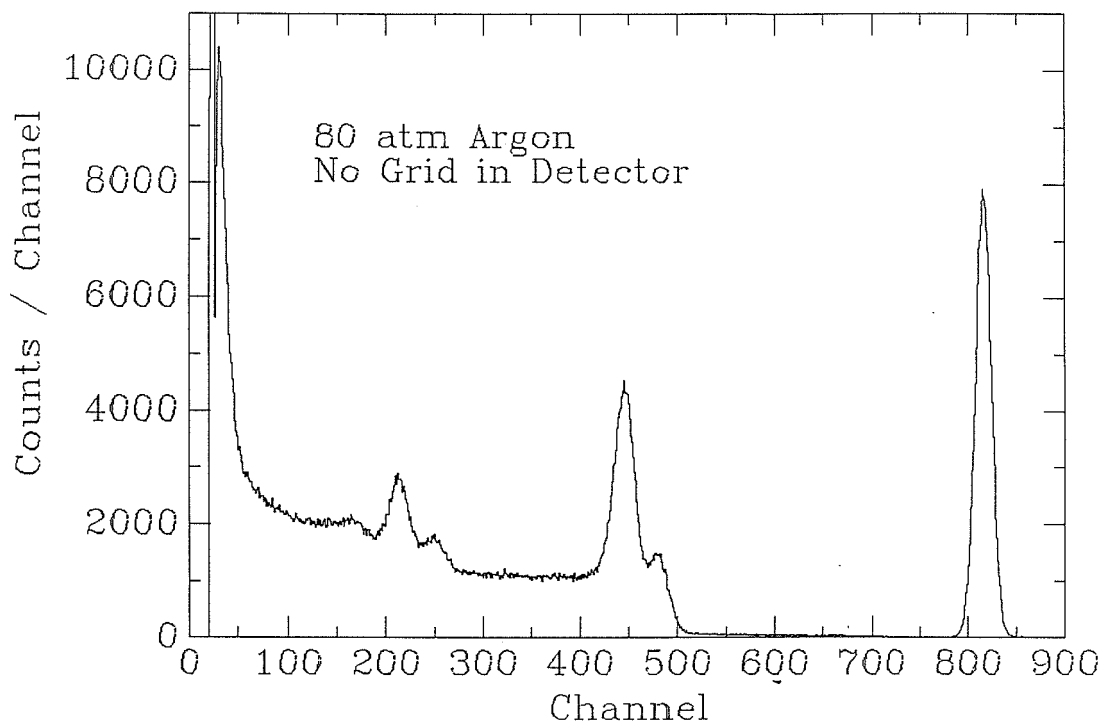


Figure C-7.  $^{207}\text{Bi}$  spectrum taken at 80 atm of argon ( $E_d = 0.6 \text{ kV/cm}$ ) in an ionization chamber *without a grid*.

approximately compensate the increasing attachment of drifting electrons at greater distances from the anode, again producing approximately position-independent charge collection. This is illustrated by the spectrum of Fig. C-7, where the grid has been removed from the detector. In this case, unpurified argon was placed in the chamber. The initial pressure was about 90 atm and the energy resolution was poor, corresponding to an attenuation length of about 10 cm. When the pressure was decreased to 80 atm, the cancellation of charge induction and attachment occurred. The effective attenuation length was measured by scanning the  $^{137}\text{Cs}$  source along the drift length of the detector. This gave  $\lambda_{\text{eff}} \approx -300 \pm 200 \text{ cm}$ , i.e., the charge collection was

approximately position-independent, with a slight increase with distance from the anode. An increase in charge collection with distance from the anode would of course never be observed in a gridded ionization chamber with a constant electric field.

The principle of using the varying charge induced as a function of position in an ionization chamber without a grid to cancel position-dependent charge collection due to attachment of drifting electrons is the fundamental idea behind the detector described in chapter 4.

## APPENDIX D

### Spectra from Radial Ionization Chambers

#### D.1 Introduction

In this appendix I present a more detailed, albeit qualitative description of energy spectra recorded with the liquid and solid radial ionization chambers discussed in chapter 4.

#### *Figures*

Figures containing a total of 115 energy spectra are presented in this appendix. Each of these figures is labeled with the detector and filling medium, the voltage applied between the anode and cathode, the external uncollimated  $\gamma$ -ray source used and the shaping time of the amplifier. In the case of the 0.9 M detectors, the voltage label refers to the absolute magnitude of the (negative) voltage applied to the cathode. A table at the beginning of each section gives these parameters for every spectrum in that section and lists in which figures each spectrum appears.

#### D.2 0.3 M Detector with Argon

Figs. D-1 through D-11 display spectra taken with the 0.3 M detector shown in Fig. 4-3.



Liquid/Solid Argon in 0.3 M Detector				
Source	$ V $ (kV)	$\tau_s$ ( $\mu$ s)	Figure(s)	Misc.
$^{60}\text{Co}$	1.7	4	D-1	
$^{22}\text{Na}$	1.7	4	D-1,2	
$^{22}\text{Na}$	2.0	4	D-2	
$^{22}\text{Na}$	3.0	4	D-2,11	Mostly LAr
$^{22}\text{Na}$	3.0	4	D-11	Mostly SAr

Table D-1. Summary of spectra from the 0.3 M detector filled with liquid argon and solid argon near the anode.

*Liquid with a solid core*

Figs. D-1 and D-2 display spectra of the 0.3 M detector in liquid argon with a solid argon core. Table D-1 summarizes the parameters of the spectra displayed in these figures.

Although the energy resolution is obviously poor (about 20% FWHM), it is clear from Fig. D-1 that the individual energy features (1066 keV Compton edge of the 1279 keV  $\gamma$ -ray of  $^{22}\text{Na}$ , 341 keV Compton edge of the 511 keV annihilation radiation from  $^{22}\text{Na}$  and about 1 MeV Compton Edges of the 1.1 MeV and 1.3 MeV  $\gamma$ -rays of  $^{60}\text{Co}$ ) may be discerned. The charge collection clearly improves with increasing voltage, as shown in Fig. D-2.

Solid Argon in 0.3 M Detector				
Source	$ V $ (kV)	$\tau_s$ ( $\mu$ s)	Figure(s)	Misc.
$^{60}\text{Co}$	0.2	12	D-5	
$^{60}\text{Co}$	0.3	12	D-5	
$^{60}\text{Co}$	0.5	12	D-5	
$^{60}\text{Co}$	1.0	12	D-7	
$^{60}\text{Co}$	1.0	12	D-7	
$^{60}\text{Co}$	1.5	12	D-3	
$^{60}\text{Co}$	1.5	12	D-4	Unpurified
$^{137}\text{Cs}$	1.5	12	D-3	
$^{137}\text{Cs}$	1.5	12	D-4	Unpurified
$^{22}\text{Na}$	0.7	12	D-6,8	
$^{22}\text{Na}$	0.7	12	D-6	After V. rev.
$^{22}\text{Na}$	0.7	12	D-8,10	Low Pressure
$^{22}\text{Na}$	1.4	12	D-10	Low Pressure
$^{22}\text{Na}$	1.5	12	D-10	Low Pressure
$^{22}\text{Na}$	1.5	12	D-4	Unpurified
$^{22}\text{Na}$	1.8	12	D-10	High Pressure
$^{22}\text{Na}$	2.0	12	D-9,10	Low Pressure
$^{22}\text{Na}$	2.0	12	D-9	
$^{22}\text{Na}$	3.0	4	D-11	
$^{22}\text{Na}$	3.0	4	D-11	Translucent

Table D-2. Summary of spectra from the 0.3 M solid argon detector.

*Solid*

Figs. D-3 through D-11 display spectra of the 0.3 M detector with solid argon. Table D-2 summarizes the parameters of the spectra displayed in these figures.

Figs. D-3 and D-4 show the effect of purifying the argon. There is a significant increase in charge collection with argon that has been passed through the purifier described in chapter 4, instead of simply using argon straight from the gas bottle. The ability of the detector to operate at lower voltages is shown in Fig. D-5 and the effect of reversing the voltage for a period of time in Fig. D-6. It was noticed, particularly in the case of an internal conversion electron source mounted inside the detector, that reversing the voltage for a few moments and then applying the usual voltage again would improve the charge collection. This effect was drastic for electron sources mounted internally to the detector, but as Fig. D-6 shows, it was a small effect for external, uncollimated  $\gamma$ -rays.

The difference in charge collection for argon crystals of different quality is shown in Fig. D-7. Surprisingly, the translucent crystal (expected to have fewer grain boundaries which trap drifting electrons) actually had a lower charge collection. This seemed to always be the case, so that efforts to achieve a perfect single crystal did not seem warranted for this detector.

The effect of changing the pressure over the solid argon was examined. Although it was thought that perhaps changing pressure might change the density of the crystal, and therefore the mobility of the drifting electrons, no effect on charge collection or energy resolution was noticed. Figs. D-8 and D-9 display this study. Fig. D-10 shows the charge collection as a function of voltage at 0.2 atm pressure over the argon crystal. As expected, charge collection increases with voltage at low pressure as it does at standard pressure.

Fig. D-11 shows the effect of condensing argon in different ways and compares the spectra under identical conditions for different states of argon filling

the detector. There is no evident difference in energy resolution between liquid argon, solid argon quickly frozen (and opaque) and solid argon carefully frozen (translucent) in the 0.3 M detector.

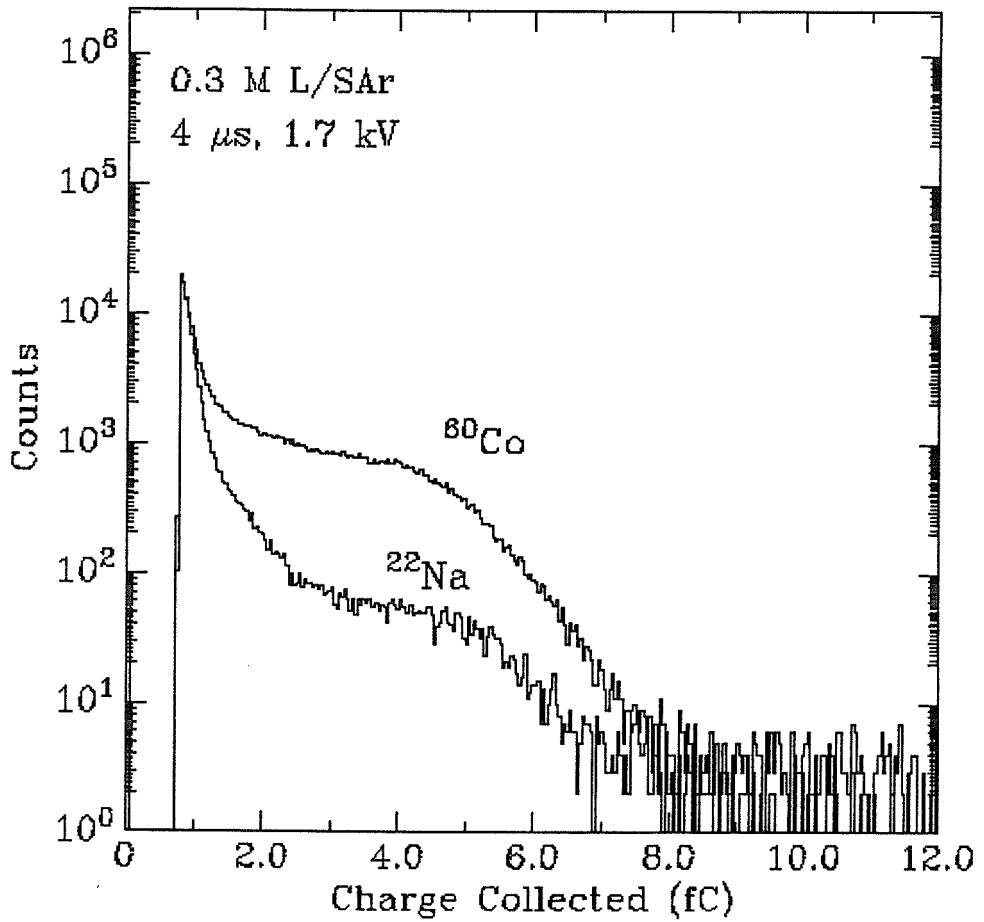


Figure D-1. Comparison of  $^{22}\text{Na}$  and  $^{60}\text{Co}$  sources in the 0.3 M detector filled with argon. The argon was liquid with a solid core near the anode.

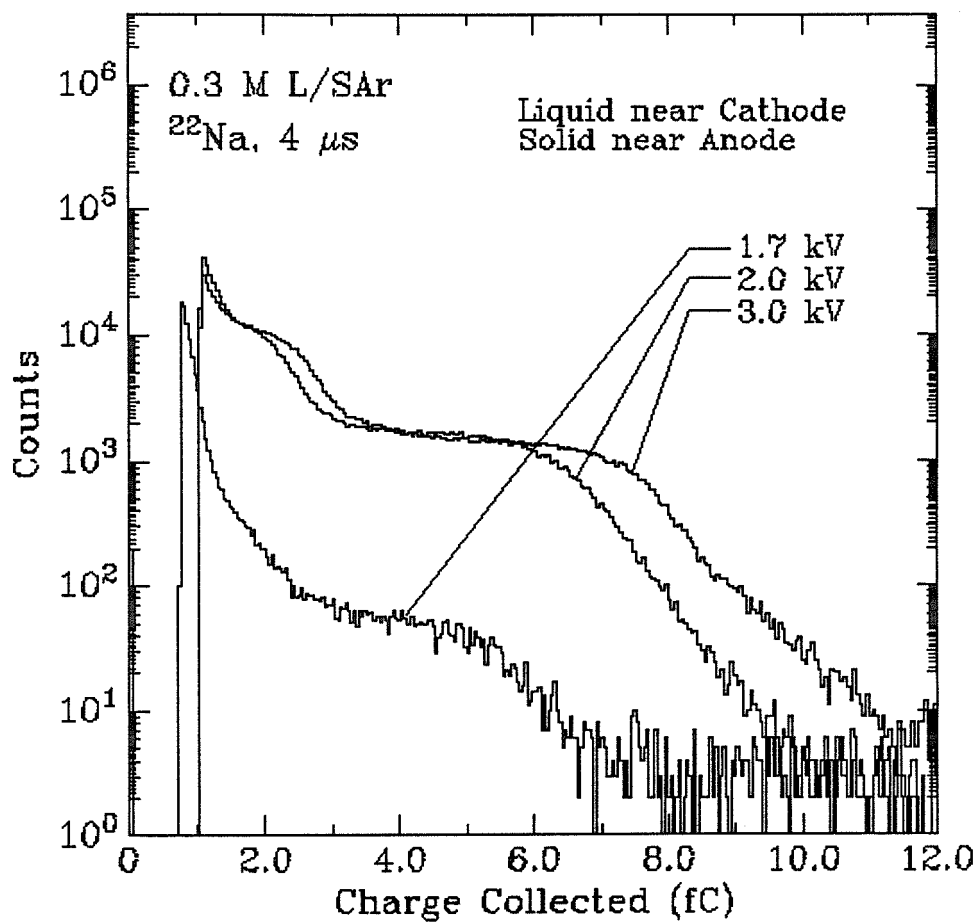


Figure D-2. Energy spectra at different applied voltages in 0.3 M detector filled with argon. The argon was liquid with a solid core near the anode.

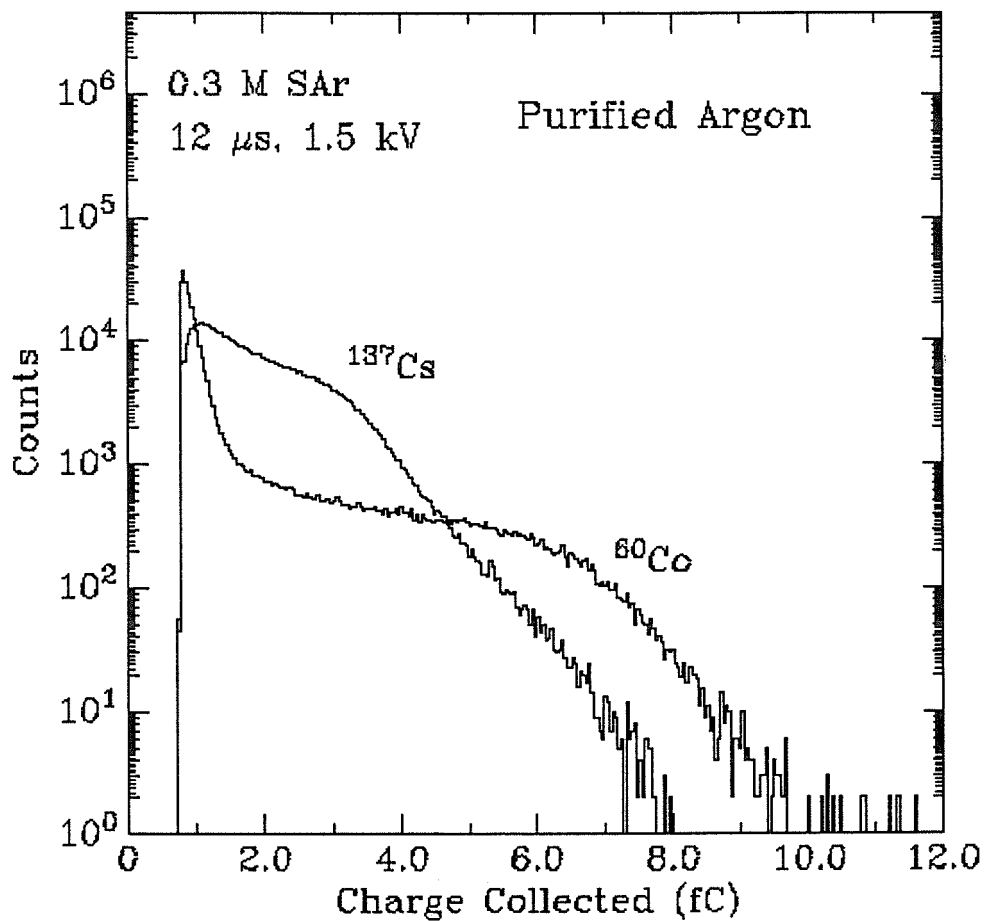


Figure D-3. Solid argon in 0.3 M detector at 1.5 kV with  $^{60}\text{Co}$  and  $^{137}\text{Cs}$  sources.

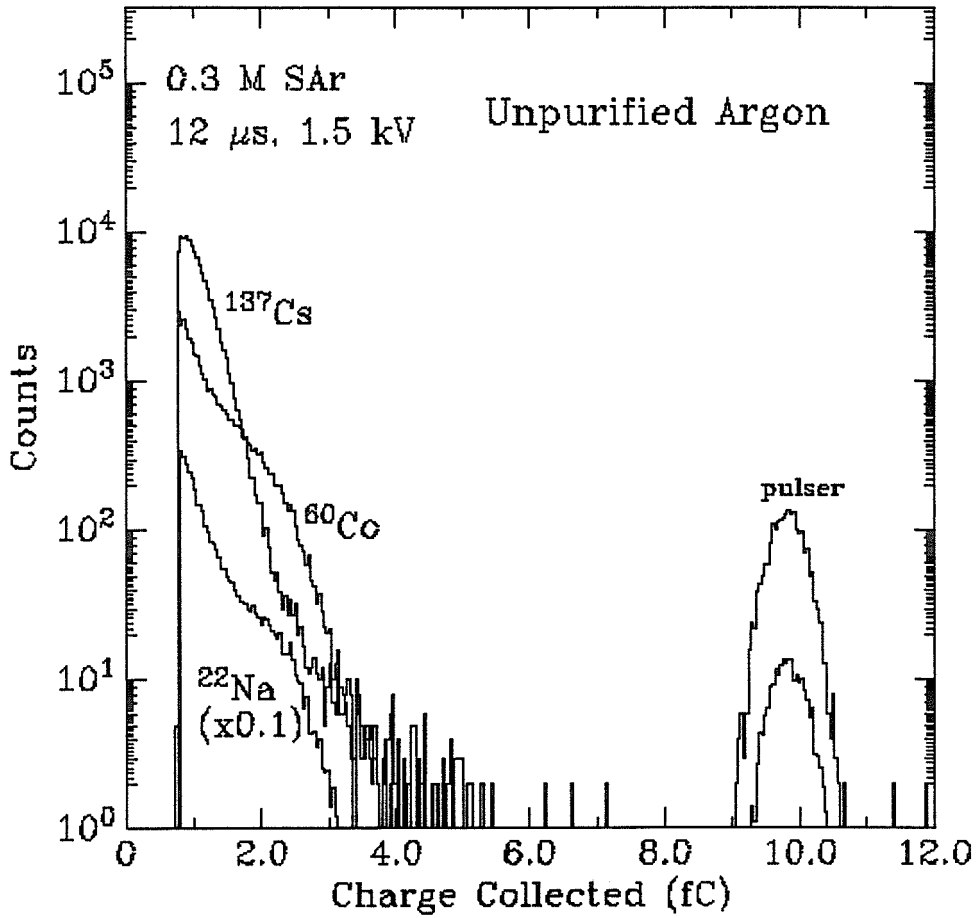


Figure D-4. Solid (unpurified) argon in 0.3 M detector at 1.5 kV. Compare with Fig. D-3.



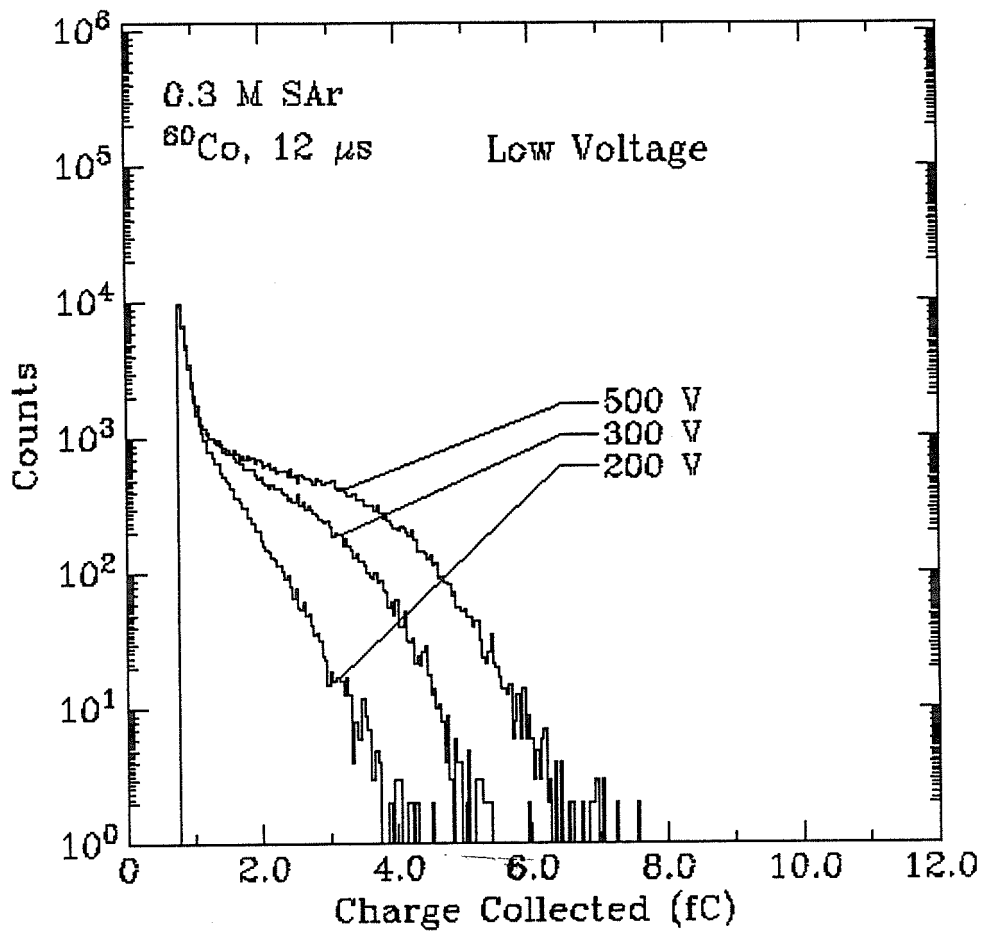


Figure D-5. Solid argon in 0.3 M detector at low voltages with a  $^{60}\text{Co}$  source.

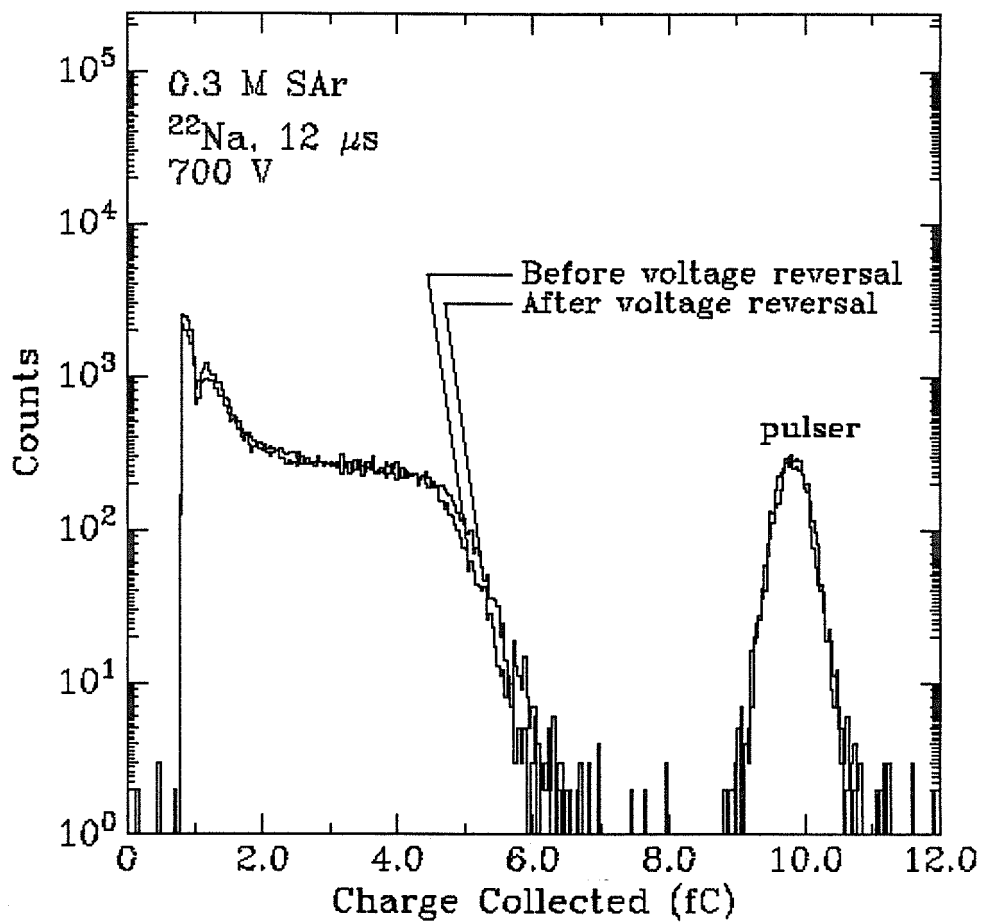


Figure D-6. Solid argon in 0.3 M detector at 700 volts. The effect of reversing the voltage is shown.

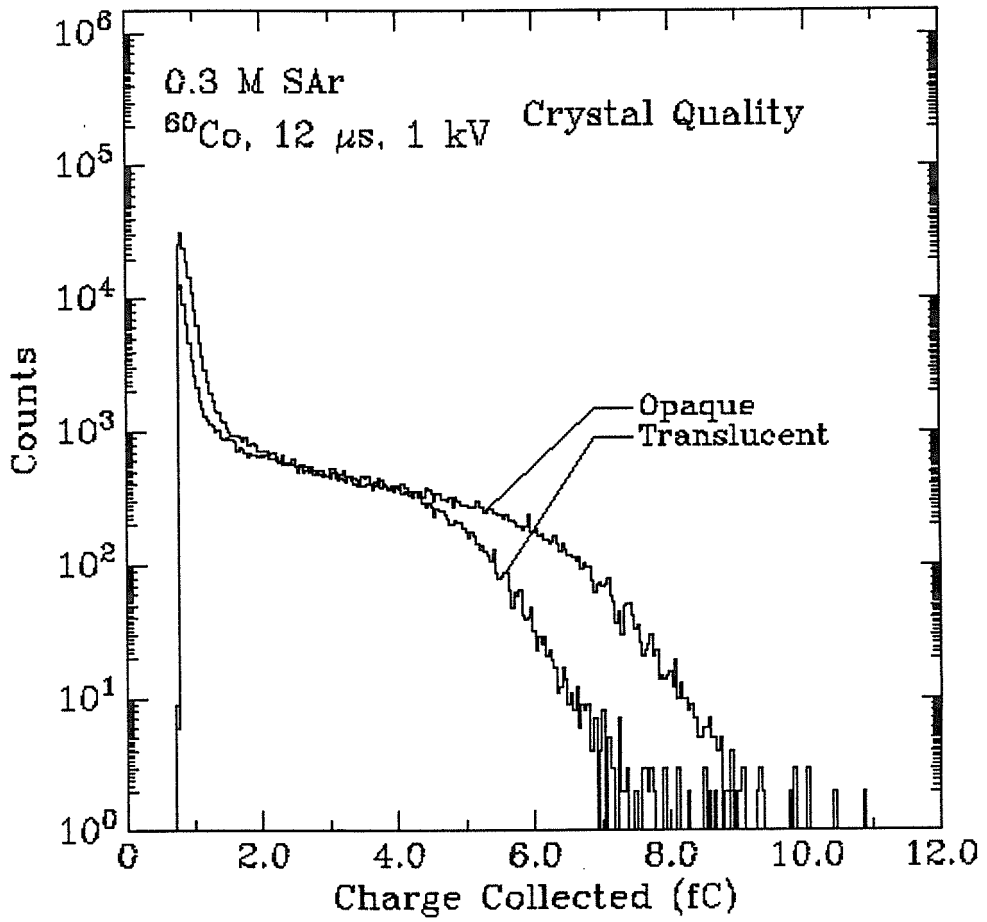


Figure D-7. The effect of crystal clarity is shown here for the 0.3 M detector filled with solid argon and 1 kV applied.

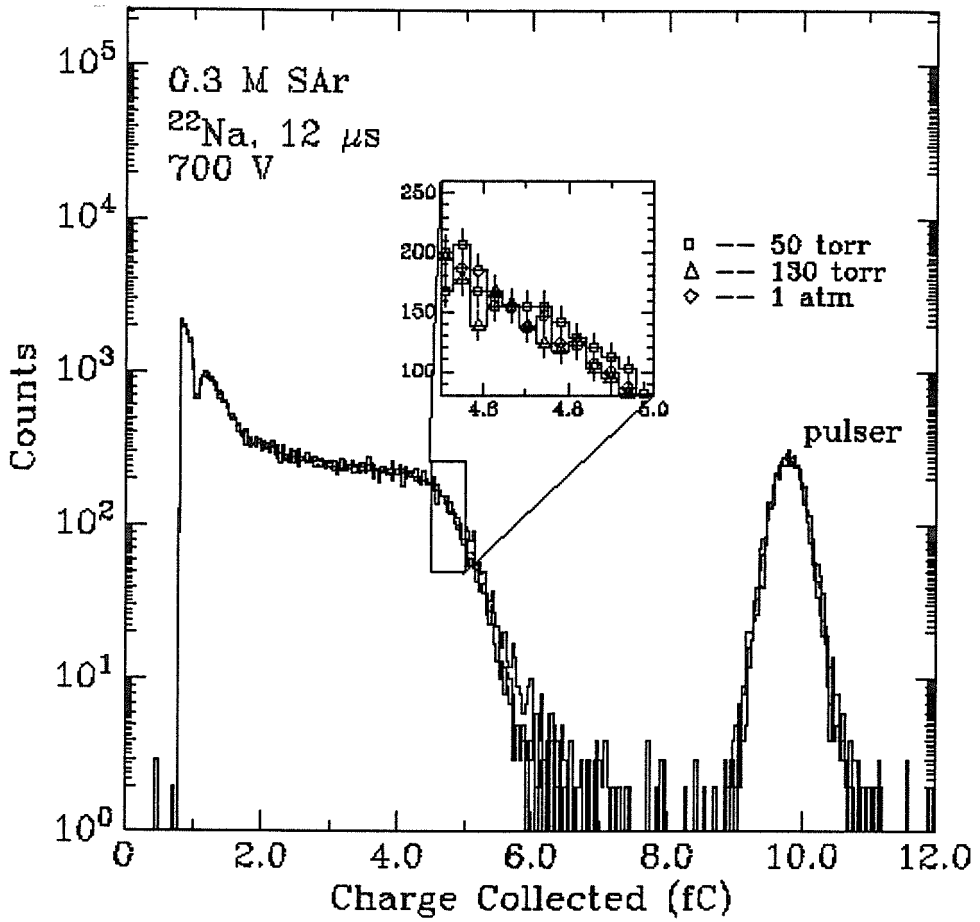


Figure D-8. Comparison of spectra taken with the 0.3 M detector filled with solid argon with different pressures of argon over the solid. Spectra were taken at a constant voltage, 700 volts.

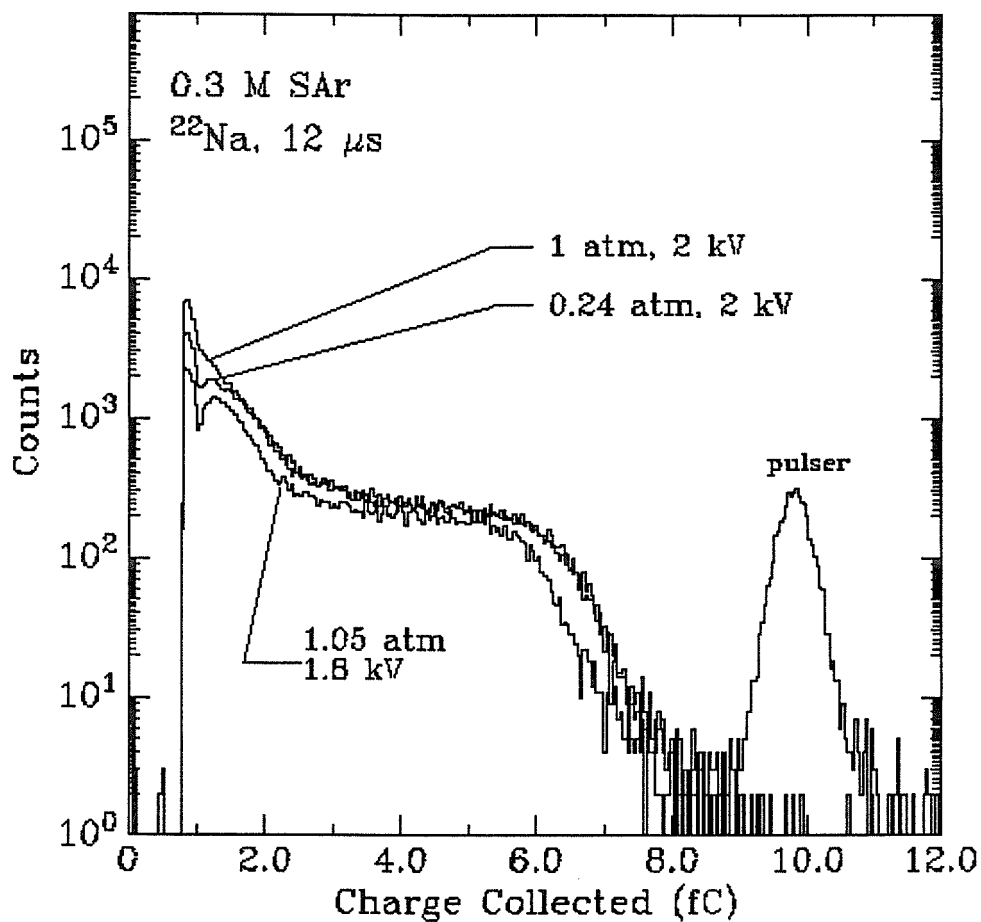


Figure D-9. Comparison of spectra taken with the 0.3 M detector filled with solid argon with different pressures of argon over the solid. Spectra were taken at higher voltages than in Fig. D-8.

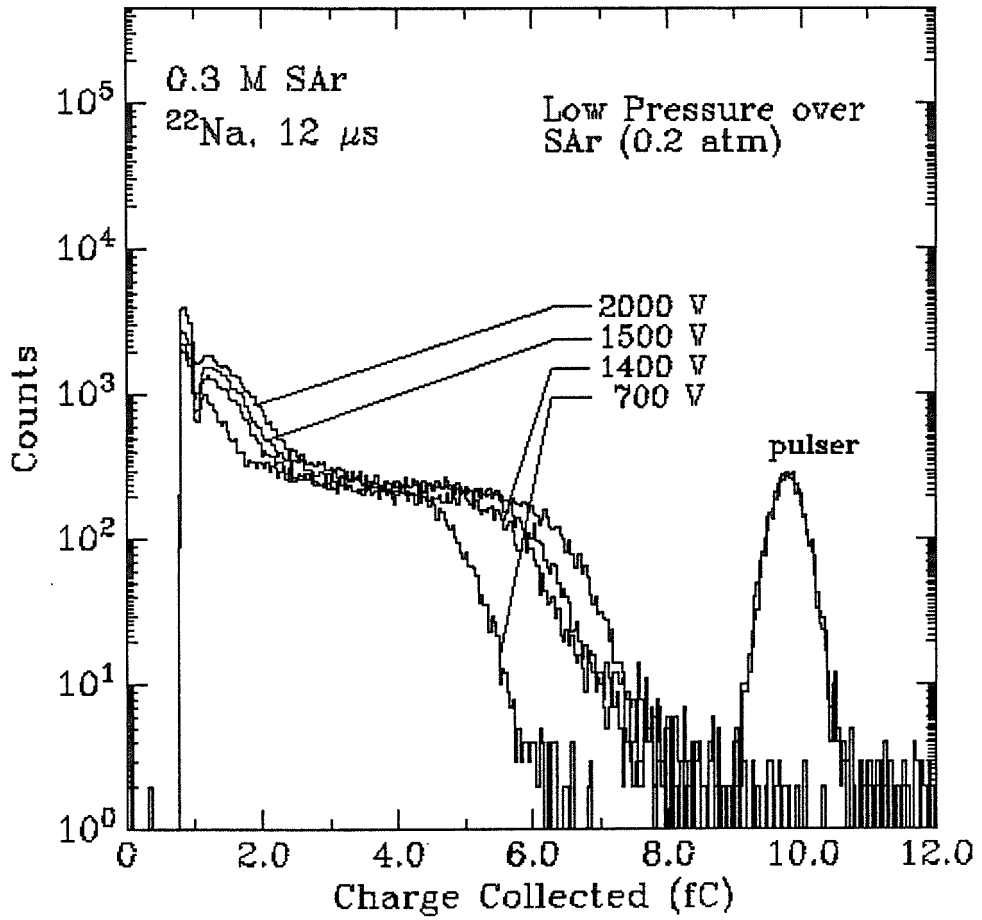


Figure D-10. Effect of voltage on energy spectra in 0.3 M solid argon detector with 0.2 atm of argon over the solid.

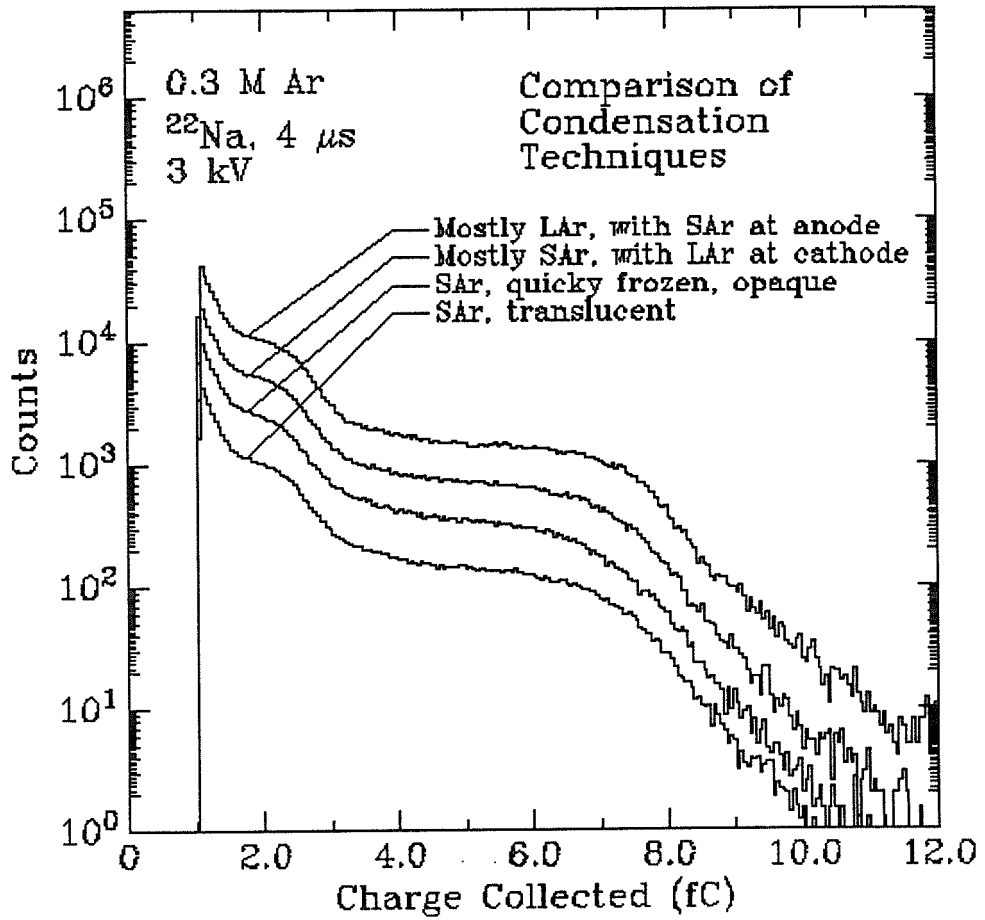


Figure D-11. Comparison of different argon detector media for the 0.3 M detector at 3 kV applied, with a 4  $\mu\text{s}$  shaping time constant on the amplifier.

### D.3 0.3 M Detector with Xenon

Figs. D-12 through D-14 compare the performance of the 0.3 M detector in liquid and solid xenon for different voltages and filling media. The spectra are summarized in Tables D-3 and D-4.

Liquid/Solid Xenon in 0.3 M Detector				
Source	$ V $ (kV)	$\tau_s$ ( $\mu$ s)	Figure(s)	Misc.
$^{22}\text{Na}$	1.6	12	D-12	
$^{22}\text{Na}$	2.1	12	D-12,13	$t = t_0$
$^{22}\text{Na}$	2.1	12	D-13	$t = t_0 + 10$ min.
$^{22}\text{Na}$	2.1	12	D-13	$t = t_0 + 30$ min.
$^{22}\text{Na}$	3.0	12	D-12	

Table D-3. Summary of spectra from the 0.3 M detector filled with liquid xenon and solid xenon near the anode.

Spectra taken at different voltages are shown in Fig. D-12. There is only a slight (<10%) increase in charge collection with a factor of two increase in voltage. The stability of the detector filled with liquid xenon (with a solid xenon core) for small time-scales is shown in Fig. D-13. Although these spectra only span 30 minutes, one might compare them with those of the high-pressure xenon detector (Fig. 3-13) which showed noticeable deterioration in just a few minutes.



Solid Xenon in 0.3 M Detector			
Source	$ V $ (kV)	$\tau_s$ ( $\mu$ s)	Figure(s)
$^{22}\text{Na}$	0.5	12	D-14
$^{22}\text{Na}$	1.0	12	D-14
$^{22}\text{Na}$	1.1	12	D-14
$^{22}\text{Na}$	1.5	12	D-14
$^{22}\text{Na}$	2.1	12	D-14

Table D-4. Summary of spectra from the 0.3 M detector filled with solid xenon.

Finally, spectra in solid xenon at different voltages are displayed in Fig. D-14. Again, the charge collection and energy resolution appear to have saturated at 1 kV, and a factor of two increase in the voltage brings only a marginal increase in the charge collection and energy resolution; whereas a factor of two decrease in the voltage drastically reduces the charge collection and energy resolution in this detector.

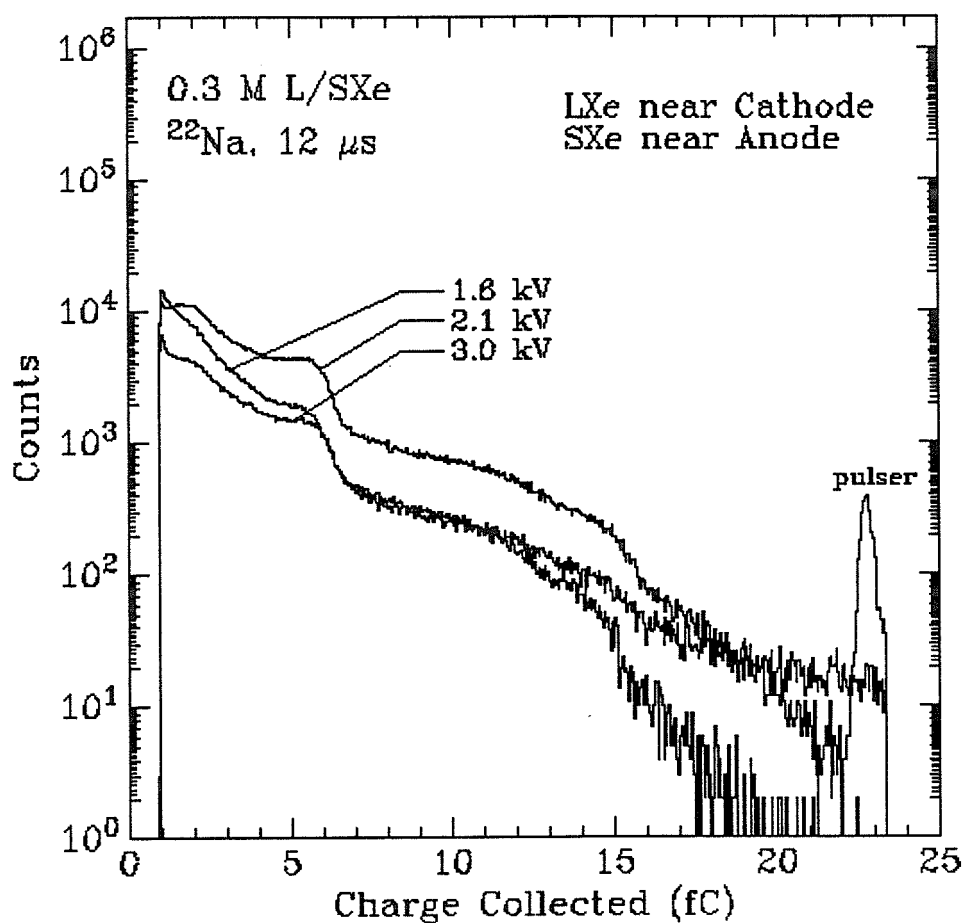


Figure D-12. Spectra with different voltages applied to the 0.3 M detector filled with liquid xenon and a solid xenon core near the anode.

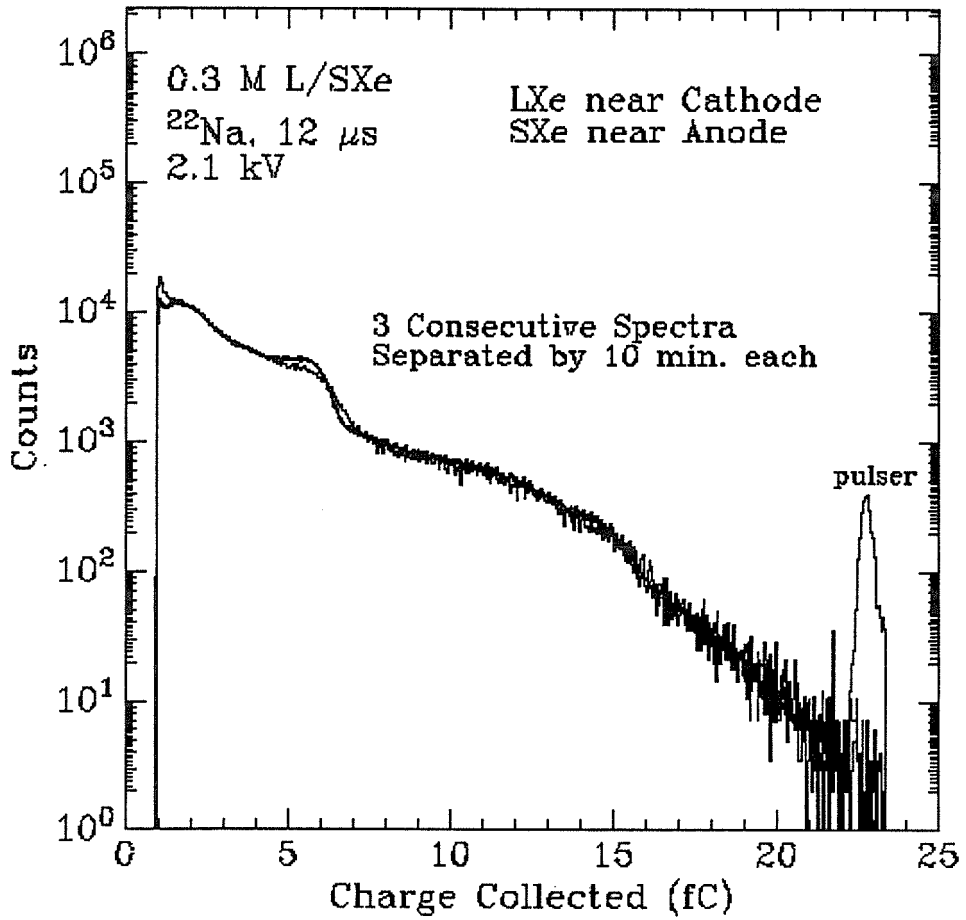


Figure D-13. Spectra taken at 10 minute intervals in the 0.3 M detector filled with liquid xenon and a solid xenon core near the anode.

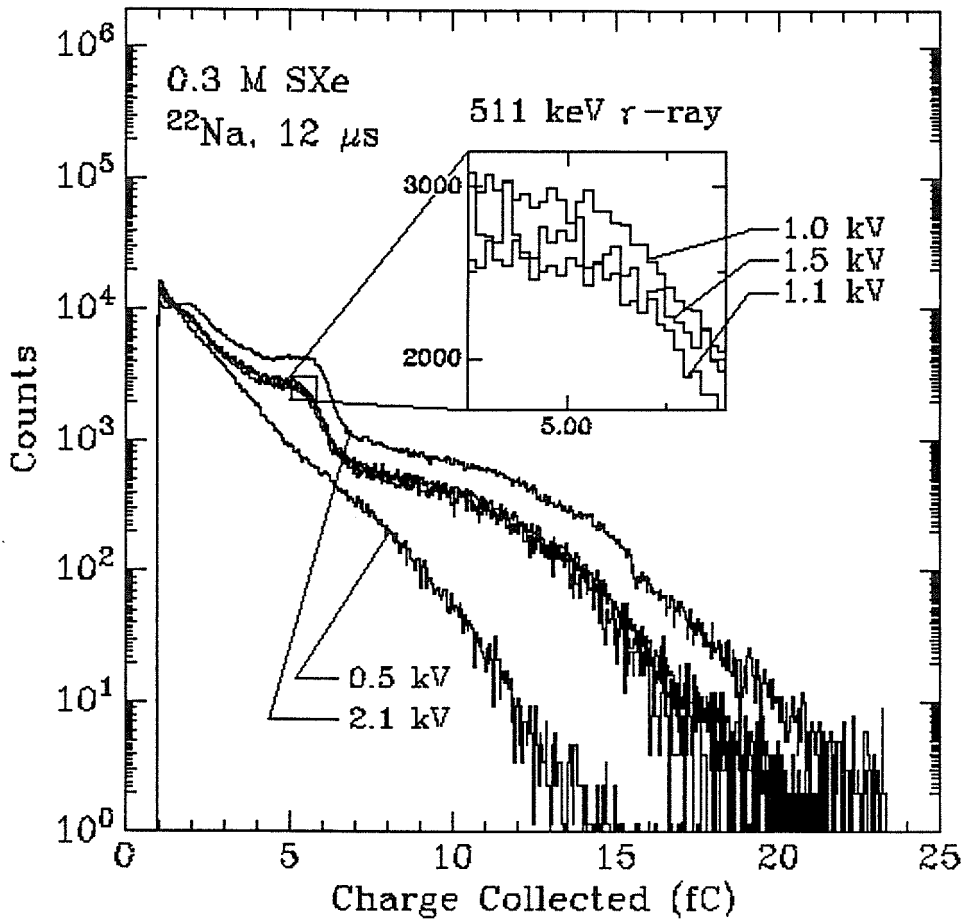


Figure D-14. Spectra taken at different voltages in the 0.3 M detector filled with solid xenon.

#### D.4 0.9 M Detector with a Small Anode Wire

Spectra from the 0.9 M detector employing a small diameter anode wire are displayed in Figs. D-15 through D-18.

##### *Liquid Argon*

Table D-5 summarizes the spectra obtained in liquid argon with the small diameter anode emplaced in the 0.9 M detector.

Liquid Argon in 0.9 M Detector with Small Anode				
Source	$ V $ (kV)	$\tau_s$ ( $\mu$ s)	Figure(s)	Misc.
$^{22}\text{Na}$	1.5	12	D-16	
$^{22}\text{Na}$	3.0	12	D-17	Unpurified
$^{22}\text{Na}$	3.0	12	D-15	$t = t_0$ , half-full
$^{22}\text{Na}$	3.0	12	D-15,16,17	$t = t_0 + 10$ min.
$^{22}\text{Na}$	3.0	12	D-15	$t = t_0 + 30$ min.
$^{22}\text{Na}$	4.0	12	D-16	
$^{22}\text{Na}$	5.1	12	D-16	
$^{22}\text{Na}$	7.0	12	D-16	
$^{22}\text{Na}$	7.0	0.25	D-18	solid at anode
$^{22}\text{Na}$	7.0	12	D-18	solid at anode

Table D-5. Summary of spectra from the 0.9 M liquid argon detector with a small diameter anode.

Fig. D-15 compares spectra from the detector operating only half-full with liquid argon to those obtained at later times with the detector full of liquid argon. The energy resolution is quite good in the former case, as is the

uniformity of charge collection over the volume of the detector, but deteriorates by the time the detector is filled with liquid argon. An interesting effect is that the charge collection improves with time for the detector full of liquid argon.

In Fig. D-16 spectra of the 1066 keV Compton edge of the 1.28 MeV  $\gamma$ -ray from  $^{22}\text{Na}$  are displayed as a function of applied voltage. Above 3 kV, the edge is quite sharp. However, the constancy of the charge collection over the volume of the detector is clearly poor, since the slope of the Compton spectrum is so large below the edge.

Purified and unpurified argon spectra are contrasted in Fig. D-17. This comparison showed that the purifier was saturated, and a new one was substituted which gave improved spectra in later tests of the larger diameter anode.

In Fig. D-18 the spectra are of the detector with a solid argon core surrounded by liquid argon. The energy resolution seems to improve at shorter shaping times, which may imply that charge multiplication is occurring in the solid, washing out the energy spectrum at longer integration times.

### *Solid Argon*

Table D-6 summarizes the spectra obtained in the 0.9 M solid argon detector using a small diameter anode wire.

Fig. D-19 shows the Compton edges of  $^{22}\text{Na}$  spectra accumulated at different applied voltages. A very short shaping time was best in this detector, as longer shaping time constants allowed the proportional multiplication which was occurring in the solid argon near the wire to be integrated along with charge induced by the drifting electrons, washing out the energy spectrum.

Solid Argon in 0.9 M Detector			
Source	$ V $ (kV)	$\tau_s$ ( $\mu$ s)	Figure(s)
$^{22}\text{Na}$	1.0	0.25	D-19
$^{22}\text{Na}$	2.0	0.25	D-19
$^{22}\text{Na}$	3.0	0.25	D-19
$^{22}\text{Na}$	4.0	0.25	D-19
$^{22}\text{Na}$	5.0	0.25	D-19
$^{22}\text{Na}$	6.0	0.25	D-19,20
$^{22}\text{Na}$	6.0	1	D-20
$^{22}\text{Na}$	6.0	12	D-20

Table D-6. Summary of spectra from the 0.9 M solid argon detector with a small diameter anode wire.

Fig. D-20 clearly illustrates why such a short shaping time was necessary when using this anode.

It seems clear that with the marginal purity levels of the gasses available for the detector, along with the occurrence of proportional multiplication in the solid, that the small diameter wire is not the optimum geometry for a  $\beta\beta$ -decay detector.

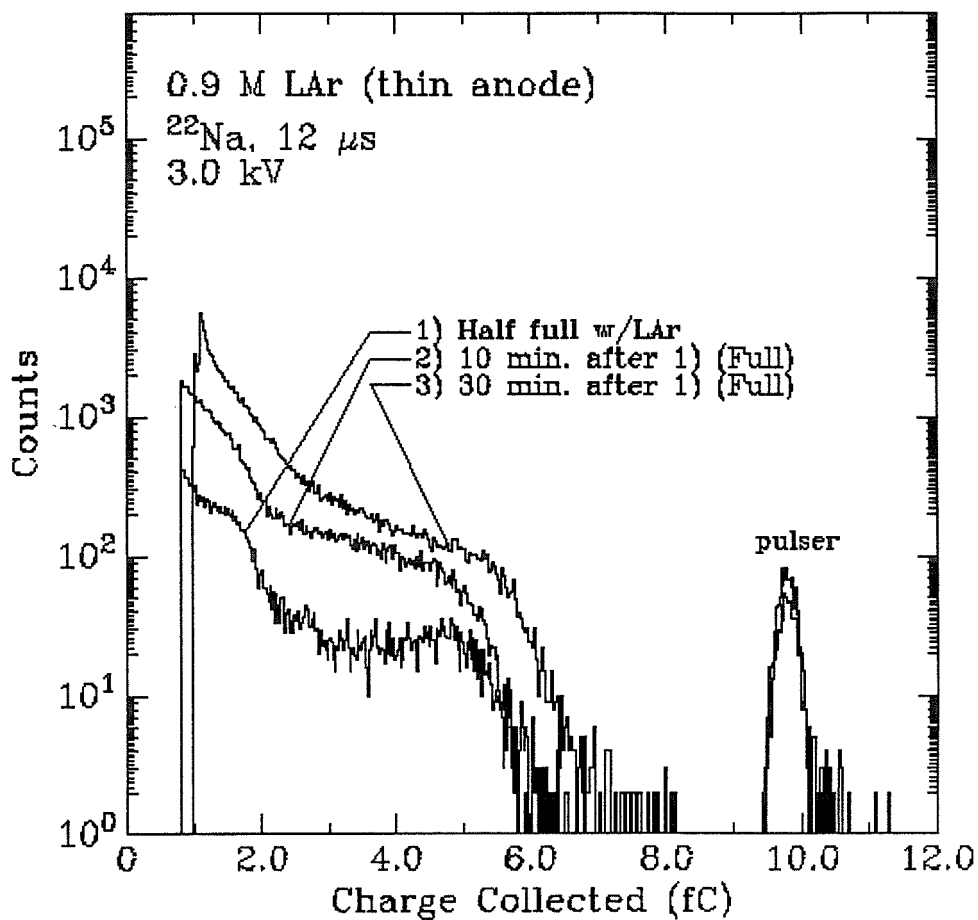


Figure D-15.  $^{22}\text{Na}$  spectra taken in the 0.9 M detector using the small anode wire and  $-3\text{ kV}$  on the cathode. The spectra are for: 1) detector half-filled with liquid argon, 2) detector full of liquid argon and 3) detector full of liquid argon. Spectrum 2) was obtained 10 minutes after spectrum 1), and 20 minutes before spectrum 3).



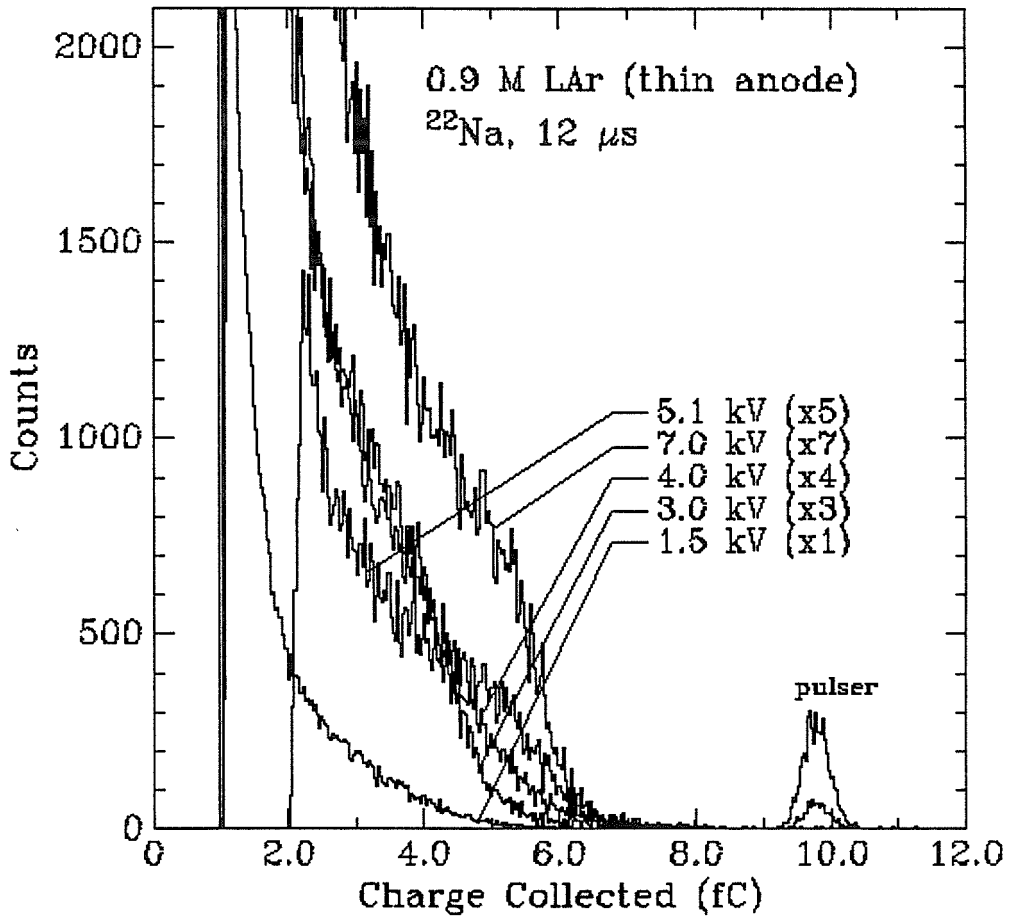


Figure D-16. Spectra at various voltages taken with the 0.9 M detector with a small anode wire, using liquid argon.

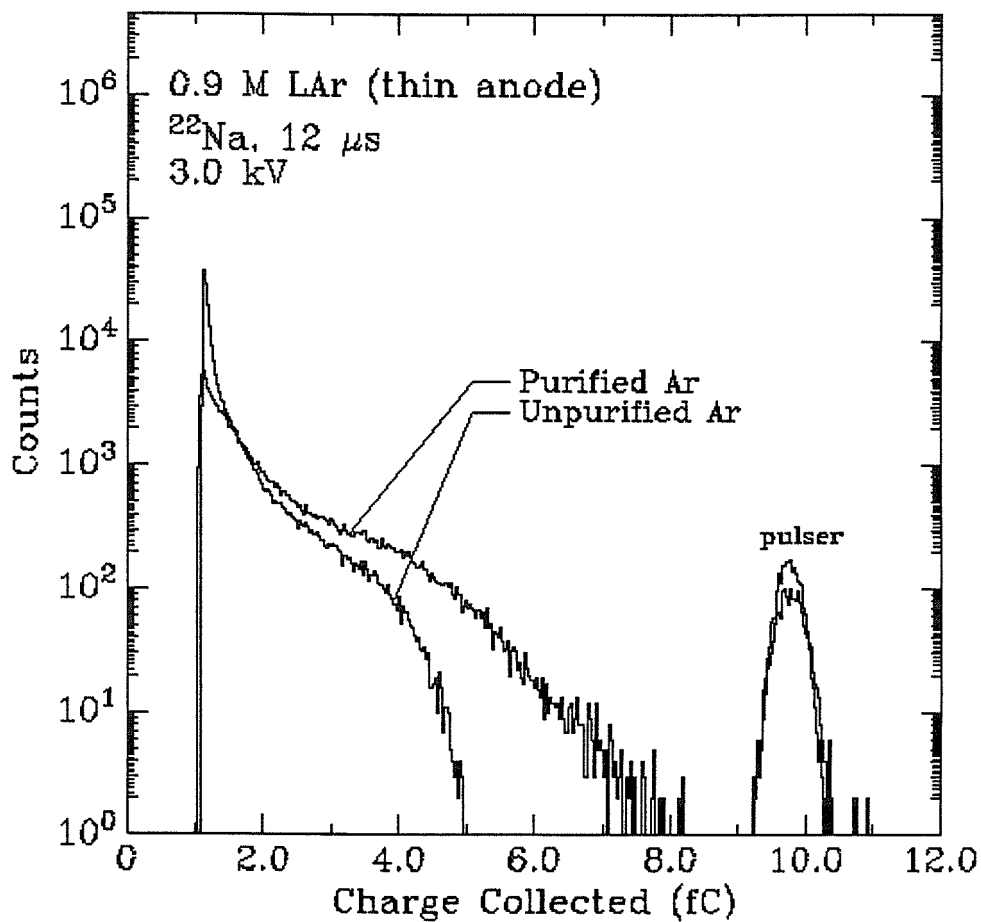


Figure D-17. Comparison of spectra taken with purified and unpurified argon, using the 0.9 M liquid argon detector with a small anode wire.

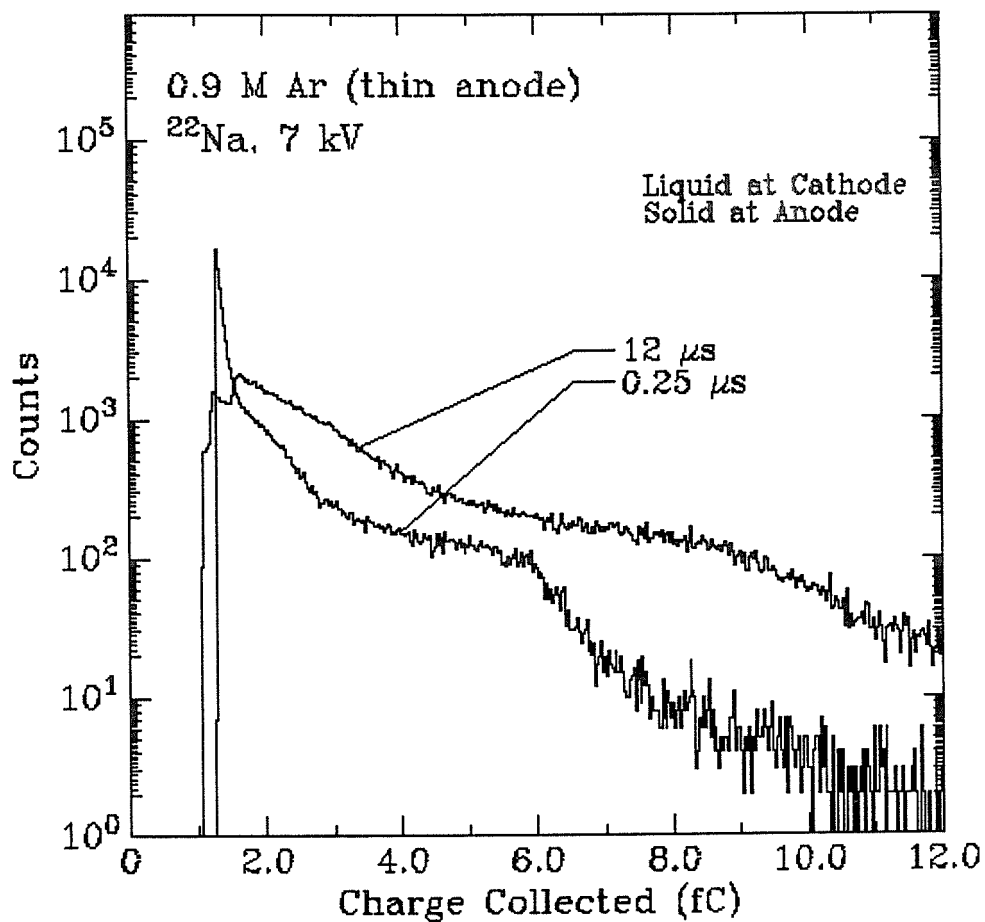


Figure D-18. Spectra taken with different shaping time constants in the 0.9 M thin anode detector filled with liquid argon with a solid argon core at the anode.

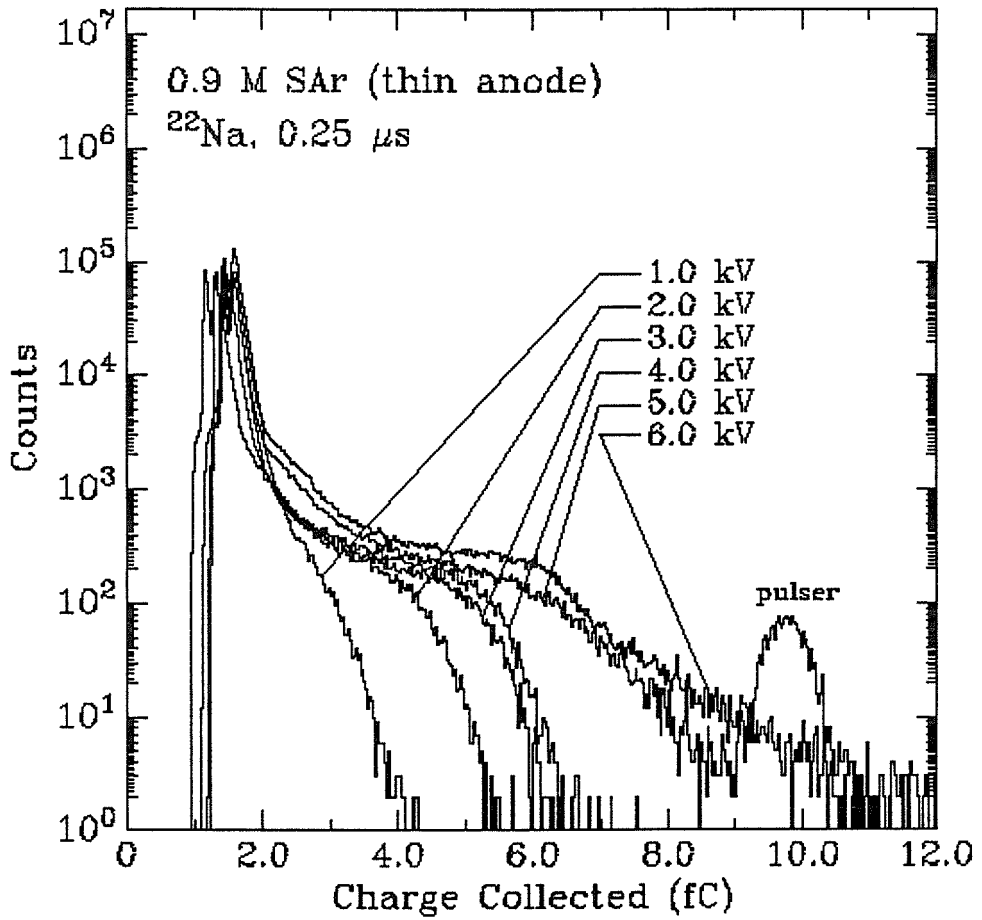


Figure D-19. Spectra taken at various voltages in the 0.9 M detector filled with solid argon, using the small anode wire.

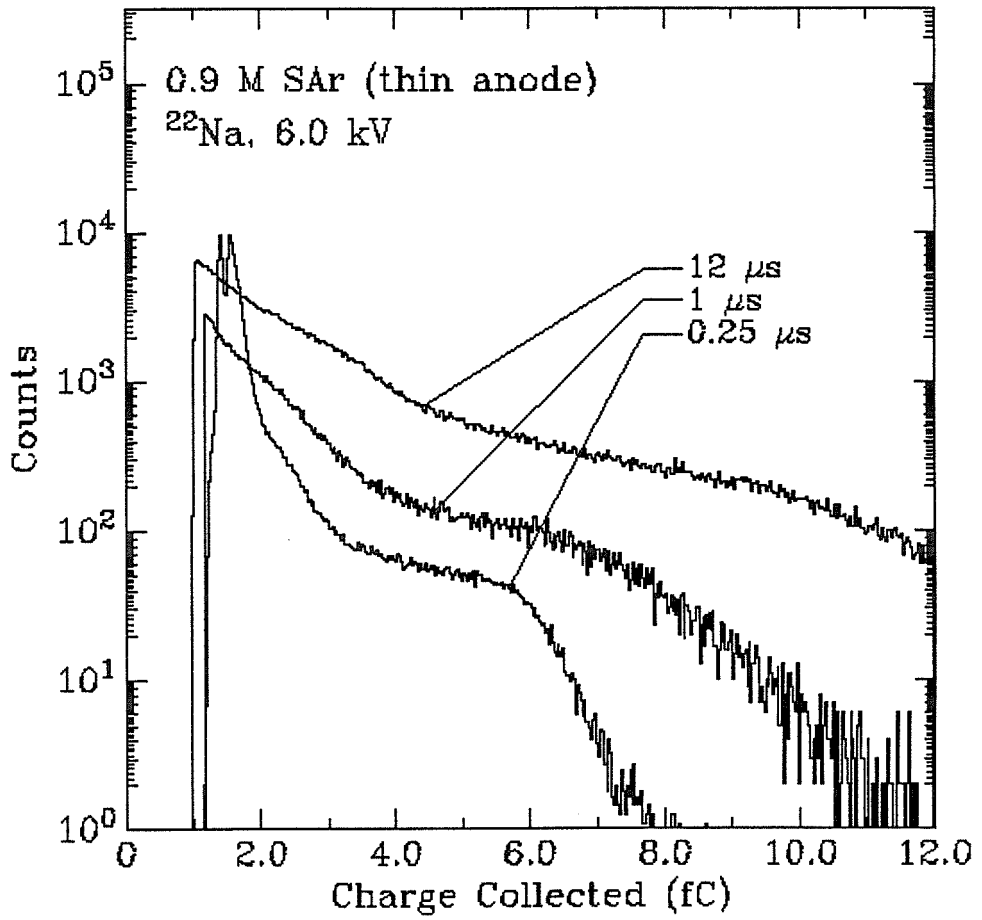


Figure D-20. Spectra taken with different shaping time constants in the 0.9 M thin anode detector filled with solid argon.

### D.5 0.9 M detector with Argon

Figs. D-21 through D-26 display spectra of the 0.9 M detector in argon.

#### *Liquid*

Table D-7 summarizes the spectra from the 0.9 M liquid argon detector displayed in Figs. D-21 through D-24.

Liquid Argon in 0.9 M Detector				
Source	$ V $ (kV)	$\tau_s$ ( $\mu$ s)	Figure(s)	Misc.
$^{60}\text{Co}$	0.7	12	D-23	
$^{60}\text{Co}$	1.0	12	D-23	
$^{137}\text{Cs}$	0.7	12	D-23	
$^{137}\text{Cs}$	1.0	12	D-23	
$^{22}\text{Na}$	0.02	12	D-22	
$^{22}\text{Na}$	0.04	12	D-22	
$^{22}\text{Na}$	0.06	12	D-22	
$^{22}\text{Na}$	0.1	12	D-22	
$^{22}\text{Na}$	0.2	12	D-22	
$^{22}\text{Na}$	0.4	12	D-22	
$^{22}\text{Na}$	0.7	12	D-24	
$^{22}\text{Na}$	1.0	12	D-21	
$^{22}\text{Na}$	2.0	12	D-21	
$^{22}\text{Na}$	3.0	12	D-21	
$^{22}\text{Na}$	3.0	12	D-27	filled
$^{22}\text{Na}$	3.0	12	D-27	unpurified, filled
$^{22}\text{Na}$	5.0	12	D-21	

Table D-7. Summary of spectra from the 0.9 M detector half-filled (except where noted) with liquid argon.

It was observed that much better energy resolution and charge collection were obtained in the 0.9 M detector when it was only half-full with liquid argon. This detector was able to collect a spectrum at surprisingly low voltages. Fig. D-21 shows the spectra from a  $^{22}\text{Na}$  source at voltages from one to five kilovolts, and Fig. D-22 from 400 volts down to 20 volts. The energy resolution in this detector is much better ( $\sim 10\%$  FWHM) than that of the 0.3 M argon detector. (The Compton edges are much sharper.) Spectra using a  $^{60}\text{Co}$  source and a  $^{137}\text{Cs}$  source are displayed in in Fig. D-23. If the energy resolution obtained in this detector with liquid argon were obtained in solid xenon, it would make a good  $2\nu$   $\beta\beta$ -decay detector.

### *Solid*

Table D-8 summarizes the spectra displayed for the 0.9 M solid argon detector.

The effect of freezing the detector is shown in Fig. D-24. Apparently some loss of charge collection and energy resolution occurs upon freezing in the 0.9 M detector which is only half-full. Note that this did not seem to be the case in the 0.3 M detector and is the opposite of the effect seen in a detector full of argon, mentioned below. Spectra taken at different voltages are shown in Fig. D-25. It is clear that increasing the voltage has a much larger effect in the 0.9 M detector for the same voltage range than in the 0.3 M detector. This is only natural, of course, since the electric field in the 0.9 M detector is smaller than in the 0.3 M detector.

The effect of choosing different shaping time constants is shown in Fig. D-26. There is no obvious improvement in charge collection or energy

Solid Argon in 0.9 M Detector				
Source	$ V $ (kV)	$\tau_s$ ( $\mu$ s)	Figure(s)	Misc.
$^{22}\text{Na}$	0.5	12	D-25	
$^{22}\text{Na}$	0.7	12	D-24	
$^{22}\text{Na}$	1.0	12	D-25	
$^{22}\text{Na}$	1.5	12	D-25	
$^{22}\text{Na}$	2.0	12	D-25	
$^{22}\text{Na}$	2.5	12	D-25	
$^{22}\text{Na}$	3.0	1	D-26	
$^{22}\text{Na}$	3.0	2	D-26	
$^{22}\text{Na}$	3.0	4	D-26	
$^{22}\text{Na}$	3.0	12	D-25, 26, 27	
$^{22}\text{Na}$	3.0	12	D-27	Unpurified

Table D-8. Summary of spectra from the 0.9 M detector filled with solid argon.

resolution at any particular shaping time constant displayed. (A choice of 8  $\mu$ s for the shaping time constant, however, seems to be particularly bad for this detector. It seemed to correspond to some noise time-base in the electronics system, and produced very noisy spectra, none of which have been recorded.)

The effect of purification in the 0.9 M detector is displayed in Fig. D-27. The charge collection for purified argon is clearly superior to that of unpurified argon. However, it is interesting that fairly good spectra are obtained with argon which comes unaltered from the gas bottle. Fig. D-27 also shows that the charge collection in solid argon is somewhat better than that of liquid argon, although the energy resolution is not noticeably improved.



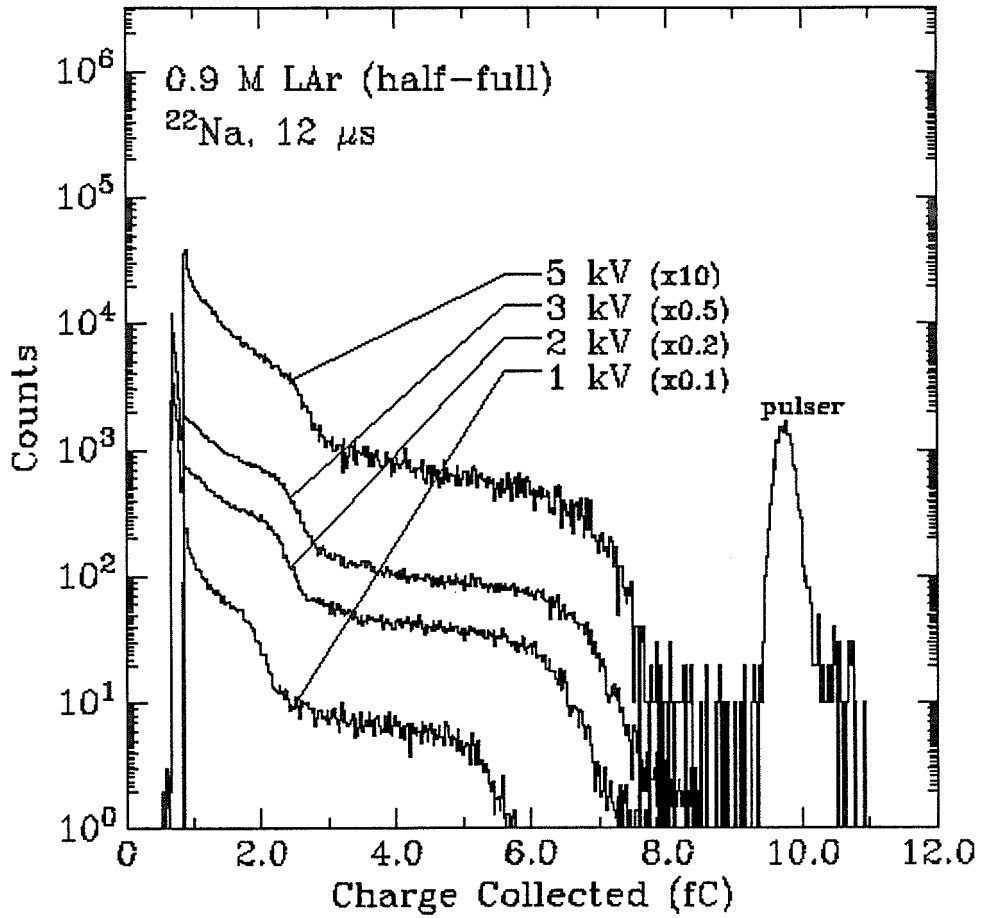


Figure D-21. Spectra taken at different voltages in the 0.9 M detector half-filled with liquid argon.

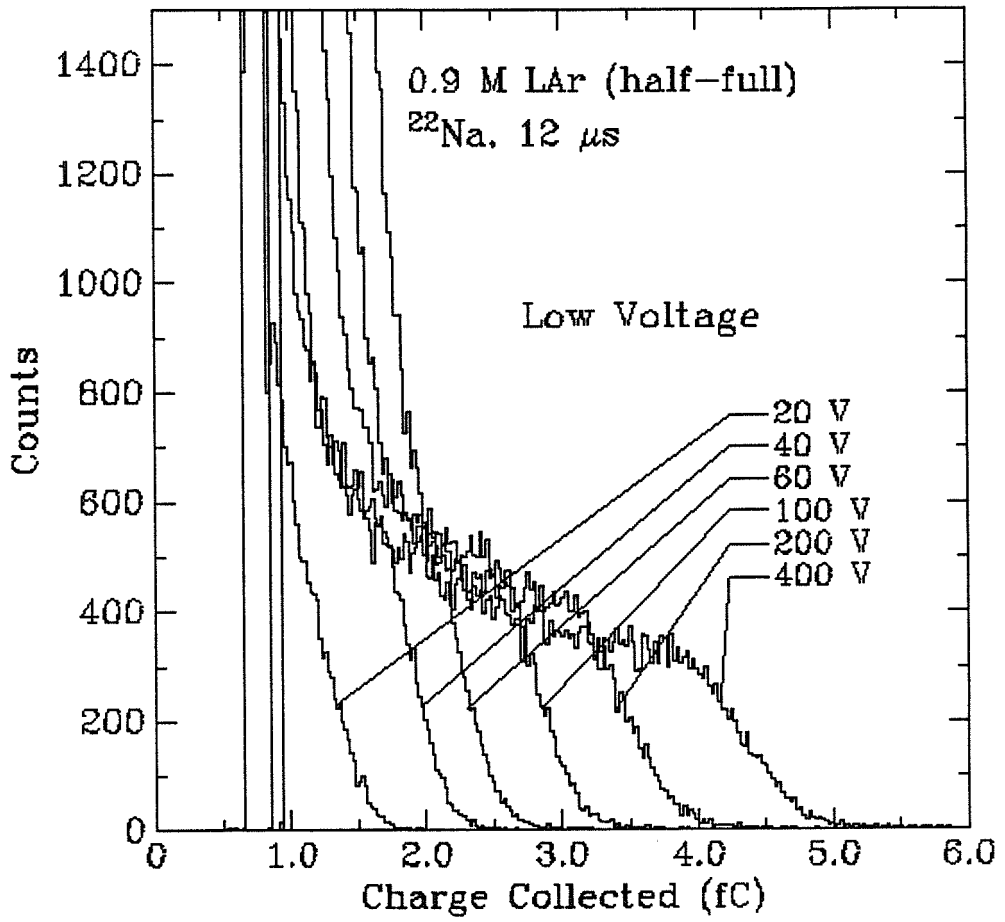


Figure D-22. Spectra taken at low voltages in the 0.9 M detector half-filled with liquid argon.

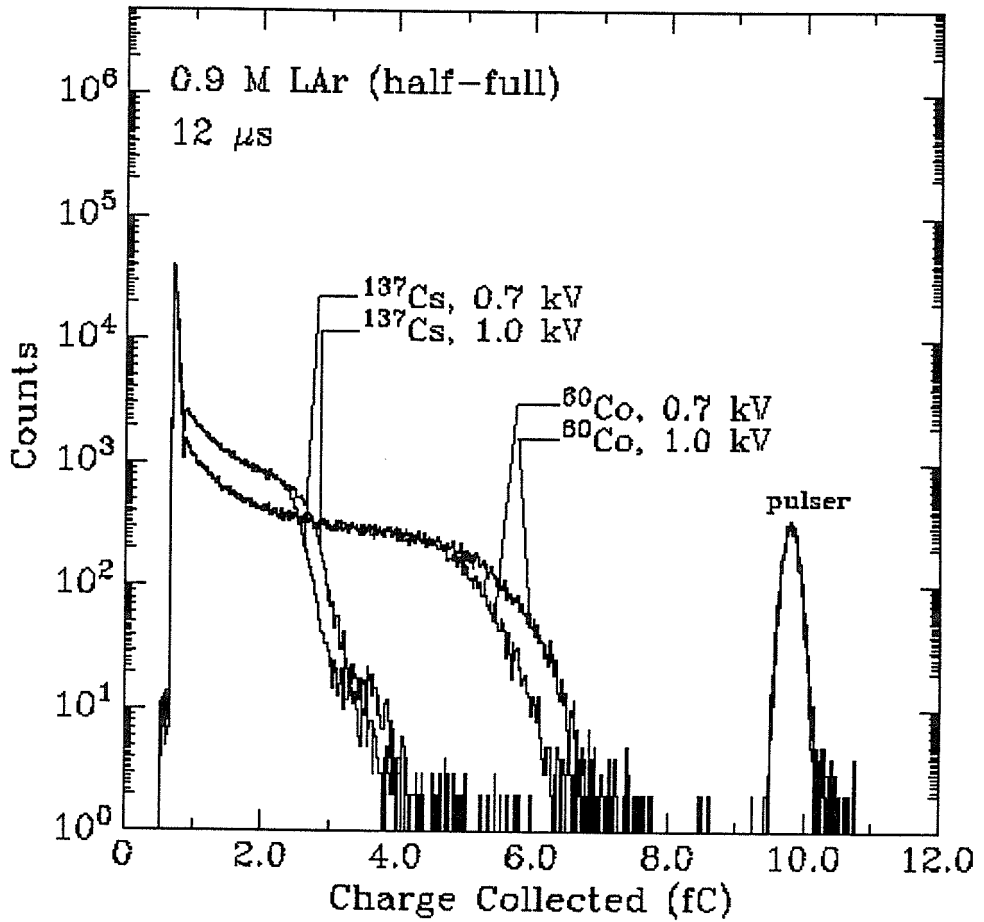


Figure D-23. Spectra taken with different sources in the 0.9 M detector half-filled with liquid argon.

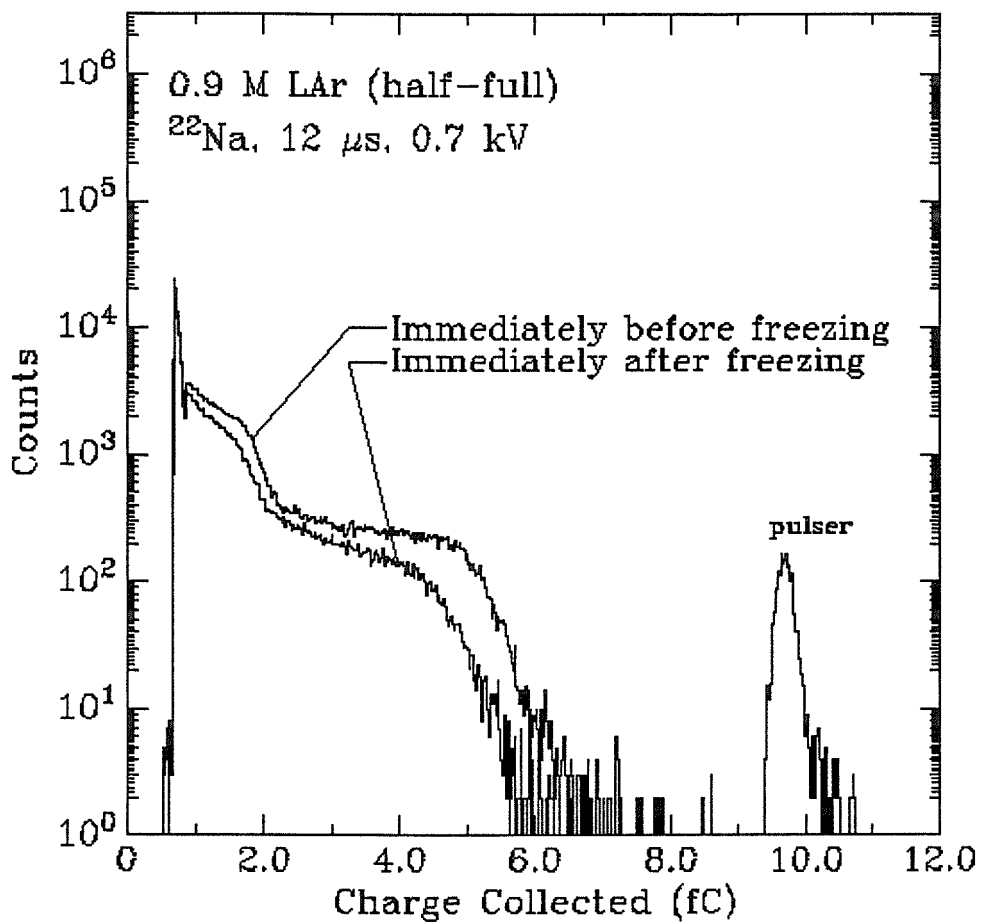


Figure D-24. Spectra taken immediately before and after freezing in the 0.9 M detector half-filled with liquid argon.

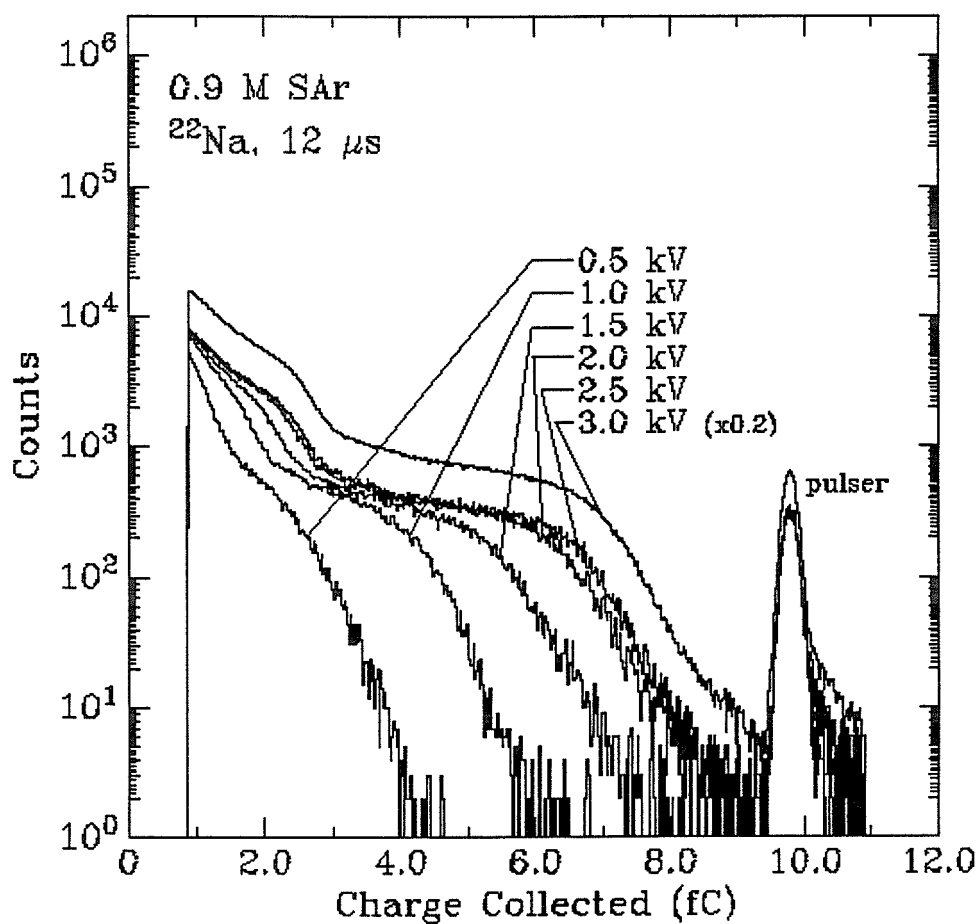


Figure D-25. Spectra taken at different voltages in the 0.9 M detector filled with solid argon.

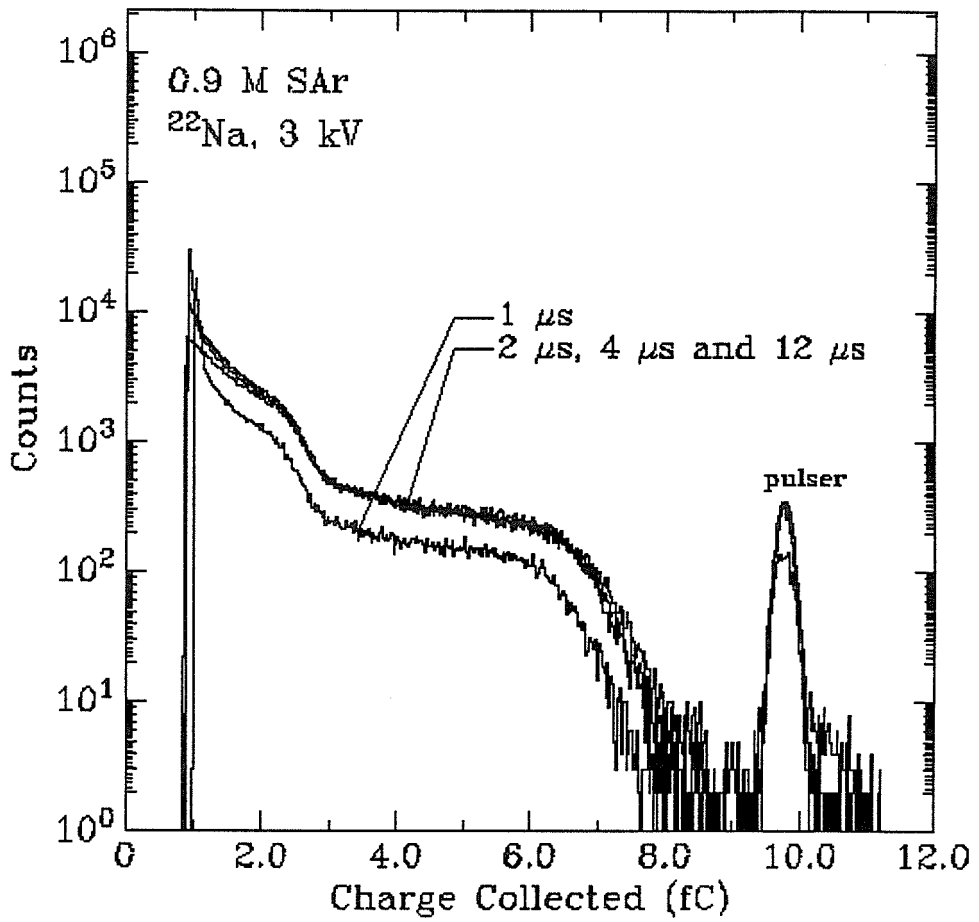


Figure D-26. Spectra taken with different shaping time constants in the 0.9 M detector filled with solid argon.

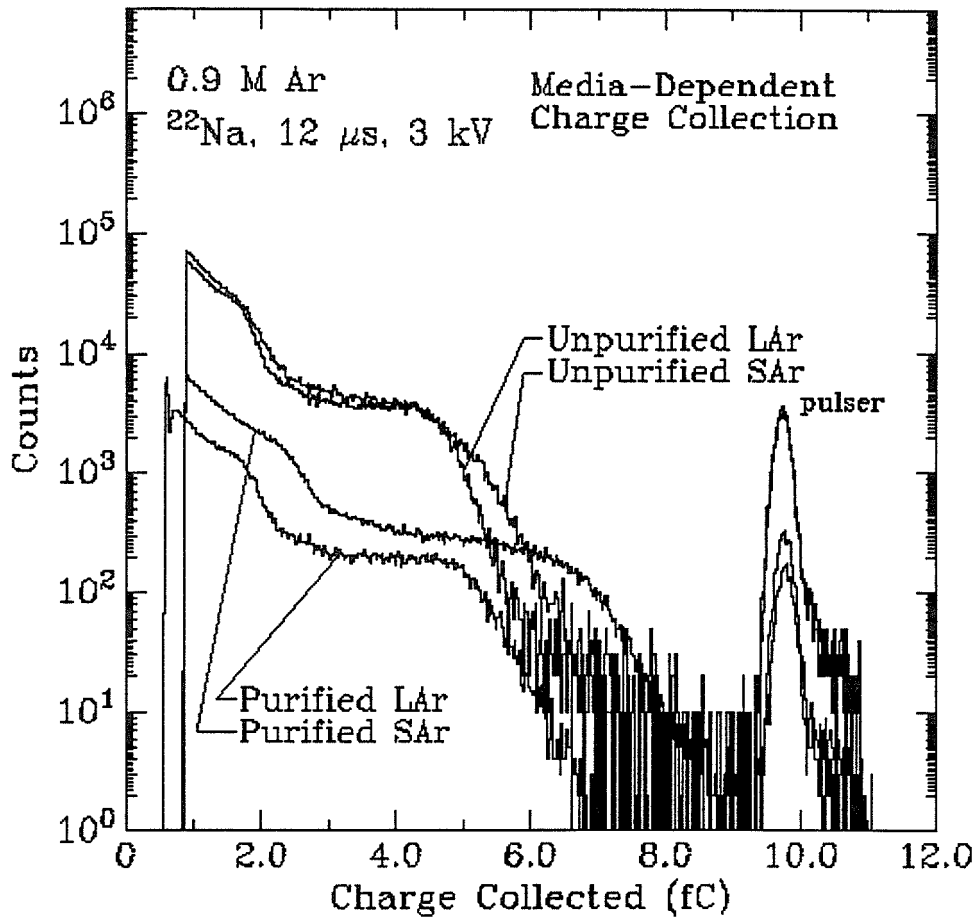


Figure D-27. Spectra taken in different kinds of argon in the 0.9 M detector.

## D.6 0.9 M Detector with Xenon

Spectra taken from the 0.9 M xenon detector are displayed in Figs. D-28 through D-38. Two samples of xenon were used in the detector. The first was xenon (“old”) which had been used and re-used in all of the preceding experiments discussed in chapters 2 through 4. This xenon has probably become contaminated with electronegative impurities after innumerable transfers. The second sample (“new”) was xenon that had been kept in a storage bottle and not transferred since it had been obtained.

### *Liquid*

Table D-9 summarizes the spectra obtained with liquid xenon in the 0.9 M detector.

Figs. D-28 and D-29 show the difference between the old and new samples of xenon. In addition, the difference in energy resolution with shaping times of  $2\ \mu\text{s}$  and  $12\ \mu\text{s}$  is clear. Evidently it takes more than  $2\ \mu\text{s}$  for the electrons to drift the radius of the detector. Spectra from three different sources are compared in Fig. D-30, where the detector was only partially filled with liquid xenon. Although the energy resolution is poor, it is possible to discern the approximate location of the full energy peak for the 662 keV peak of  $^{137}\text{Cs}$  and the full energy peak for the annihilation radiation of  $^{22}\text{Na}$ . By contrast, with a shorter shaping time constant ( $4\ \mu\text{s}$  instead of  $12\ \mu\text{s}$ ), the peaks (Fig. D-31) are sharper.



Liquid Xenon in 0.9 M Detector				
Source	$ V $ (kV)	$\tau_s$ ( $\mu$ s)	Figure(s)	Misc.
$^{60}\text{Co}$	1.1	12	D-30	partly filled
$^{137}\text{Cs}$	0.3	12	D-29	
$^{137}\text{Cs}$	0.6	12	D-29	
$^{137}\text{Cs}$	1.0	12	D-29	
$^{137}\text{Cs}$	1.1	4	D-31	partly filled
$^{137}\text{Cs}$	1.1	12	D-30,37	partly filled
$^{137}\text{Cs}$	1.1	12	D-30,37	
$^{137}\text{Cs}$	1.5	2	D-28	old xenon
$^{137}\text{Cs}$	1.5	12	D-29	
$^{137}\text{Cs}$	2.1	1	D-38	“re-purified”
$^{137}\text{Cs}$	2.1	12	D-38	“re-purified”
$^{137}\text{Cs}$	3.0	2	D-28	old xenon
$^{22}\text{Na}$	1.1	4	D-31	partly filled
$^{22}\text{Na}$	1.1	12	D-30	partly filled

Table D-9. Summary of spectra from the 0.9 M detector with liquid xenon.

*Liquid with a solid core*

Table D-10 summarizes the spectra obtained from the 0.9 M detector filled with liquid xenon, with a core of solid xenon near the anode.

These spectra are displayed in Figs. D-32 through D-34. Fig. D-32 shows  $^{22}\text{Na}$  spectra as a function of applied voltage. Fig. D-33 does the same for  $^{137}\text{Cs}$  spectra. Some deterioration in energy resolution is evident when these are compared to the spectra obtained in liquid xenon with this detector. The effect (which seems to be small) of changing the shaping time constant in this

Liquid/Solid Xenon in 0.9 M Detector				
Source	$ V $ (kV)	$\tau_s$ ( $\mu$ s)	Figure(s)	Misc.
$^{60}\text{Cs}$	0.8	12	D-33	translucent
$^{60}\text{Cs}$	1.0	12	D-33	translucent
$^{60}\text{Cs}$	1.3	12	D-33	translucent
$^{60}\text{Cs}$	1.8	12	D-33	translucent
$^{60}\text{Cs}$	2.5	1	D-33	translucent
$^{22}\text{Na}$	1.0	2	D-32	old xenon
$^{22}\text{Na}$	2.0	2	D-32	old xenon
$^{22}\text{Na}$	3.0	2	D-32	old xenon
$^{22}\text{Na}$	4.5	2	D-32	old xenon
$^{22}\text{Na}$	5.5	1	D-34	old xenon
$^{22}\text{Na}$	5.5	2	D-32,34	old xenon
$^{22}\text{Na}$	5.5	12	D-34	old xenon

Table D-10. Summary of spectra from the 0.9 M detector filled with liquid xenon and solid xenon near the anode.

detector is shown in Fig. D-34.

*Solid*

Table D-11 summarizes spectra obtained with the 0.9 M solid xenon detector.

A beautifully transparent crystal of xenon was condensed by slowly lowering the temperature of a pentane bath. However, the spectra in transparent solid xenon show poor energy resolution. These are shown in Fig. D-35. Fig. D-36 contrasts spectra taken under identical conditions with the old xenon,

Solid Xenon in 0.9 M Detector				
Source	$ V $ (kV)	$\tau_s$ ( $\mu$ s)	Figure(s)	Misc.
$^{137}\text{Cs}$	0.5	12	D-35	transparent
$^{137}\text{Cs}$	0.8	12	D-35	transparent
$^{137}\text{Cs}$	1.1	12	D-37	
$^{137}\text{Cs}$	1.1	12	D-38	“re-purified”
$^{137}\text{Cs}$	1.8	12	D-35	transparent
$^{137}\text{Cs}$	2.1	12	D-38	“re-purified”
$^{22}\text{Na}$	3.0	12	D-31	transparent, old
$^{22}\text{Na}$	3.0	12	D-31	old xenon

Table D-11. Summary of spectra from the 0.9 M detector filled with solid xenon.

except that in one case the xenon crystal was opaque, and in the other, translucent. As in the case of solid argon, the opaque crystal actually had better charge collection than that of the translucent crystal, although the effect is not large.

Three xenon spectra from  $^{137}\text{Cs}$  taken under the same voltage and electronics conditions are displayed in Fig. D-37 for solid and liquid xenon. The solid xenon spectrum shows severe deterioration compared to the liquid xenon spectrum, which actually shows a full energy peak. This deterioration is mostly due to charge multiplication which occurs at fairly low voltages in solid xenon.

Finally, an attempt was made to re-purify the xenon by passing the new xenon through the purifier, storing it in a bottle of molecular sieve, which had been baked out for 4 days in a vacuum, and passing it again through the

purifier before condensation. The spectra from this test are displayed in Fig. D-38 and show no improvement over the singly purified xenon spectra.

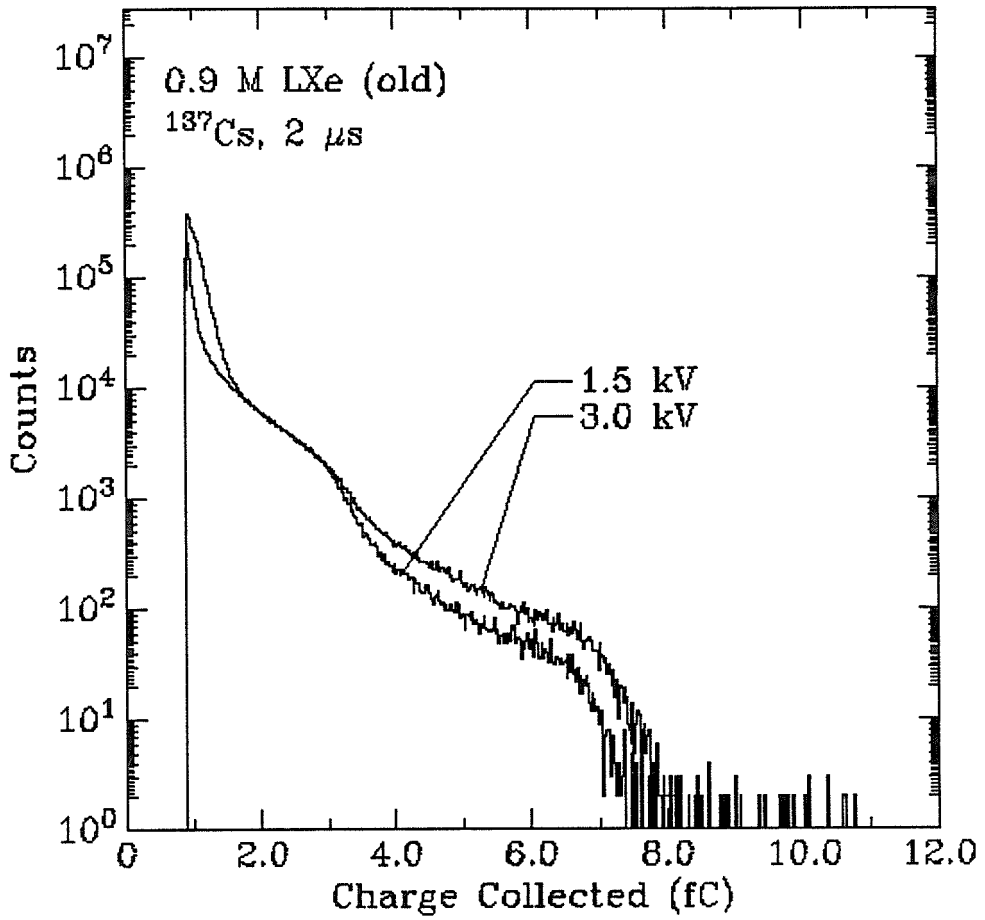


Figure D-28. Spectra taken at two different voltages in the 0.9 M detector filled with liquid xenon. The xenon had been re-used many times and was probably quite contaminated with electronegative impurities even after passing through the purifier.

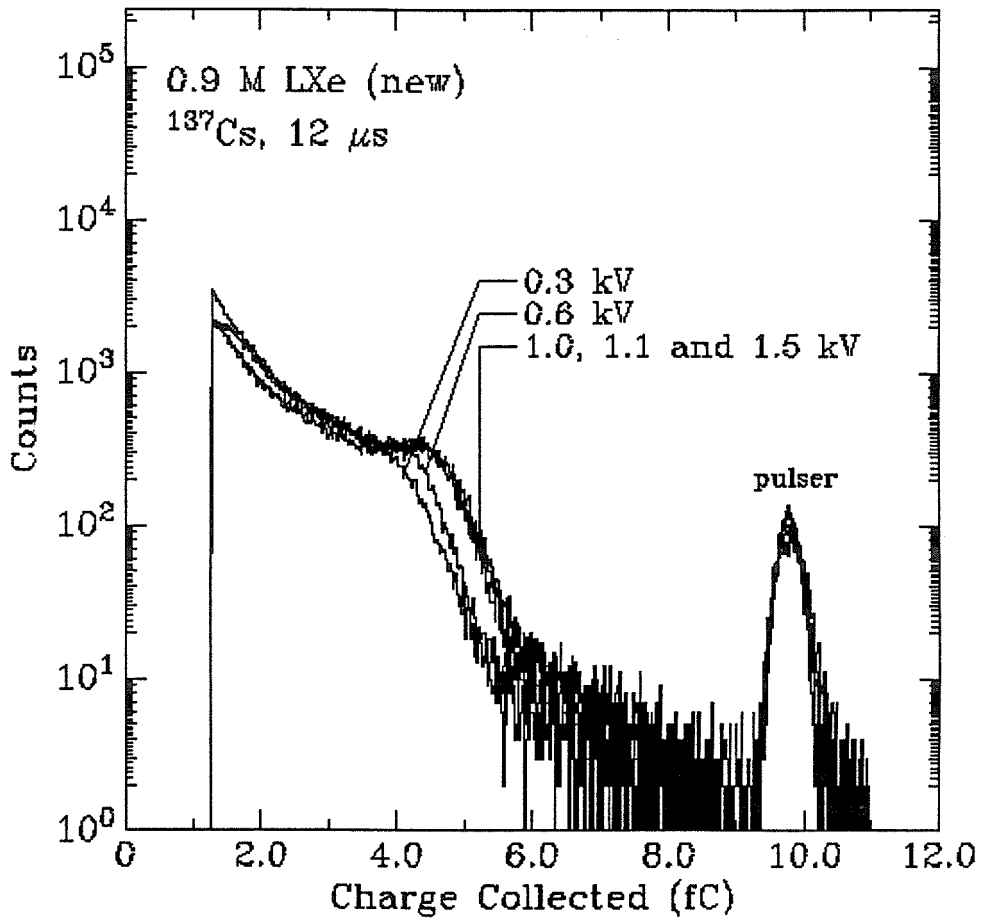


Figure D-29. Spectra taken at different voltages in the 0.9 M detector filled with “new” liquid xenon. (See text.)

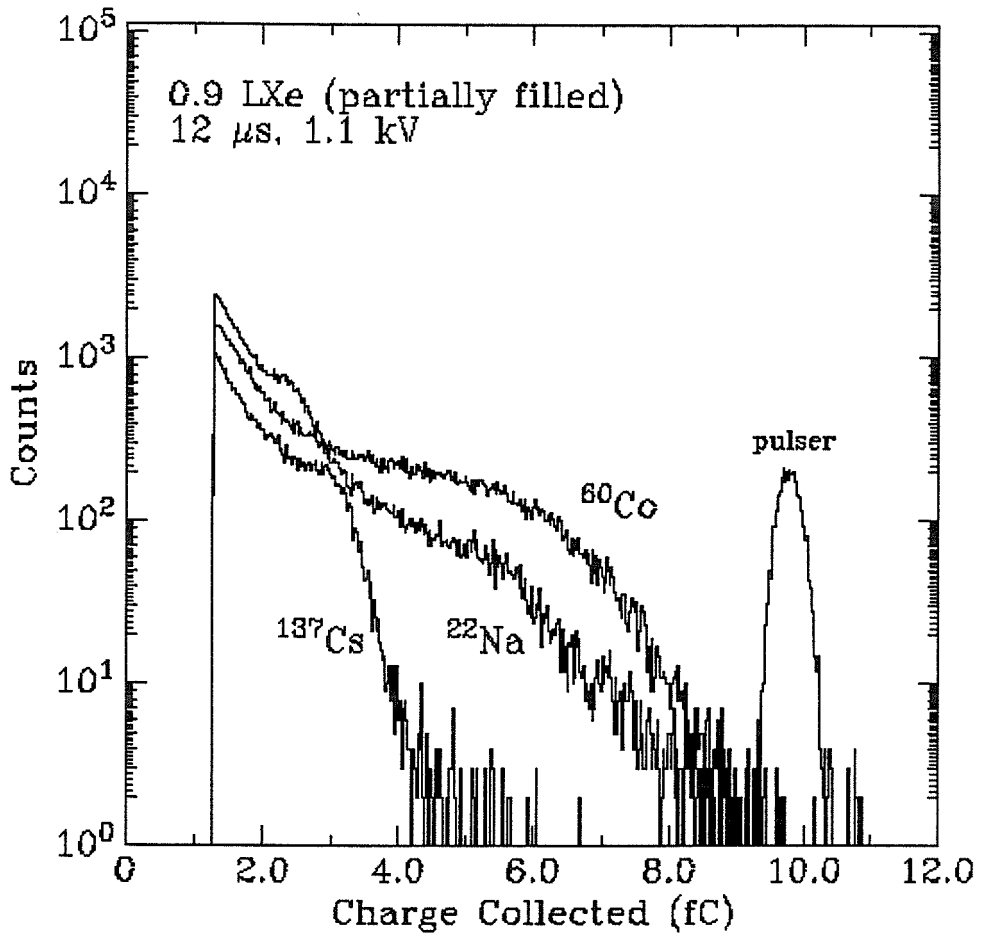


Figure D-30. Spectra taken with different sources in the 0.9 M detector partially filled with liquid xenon.

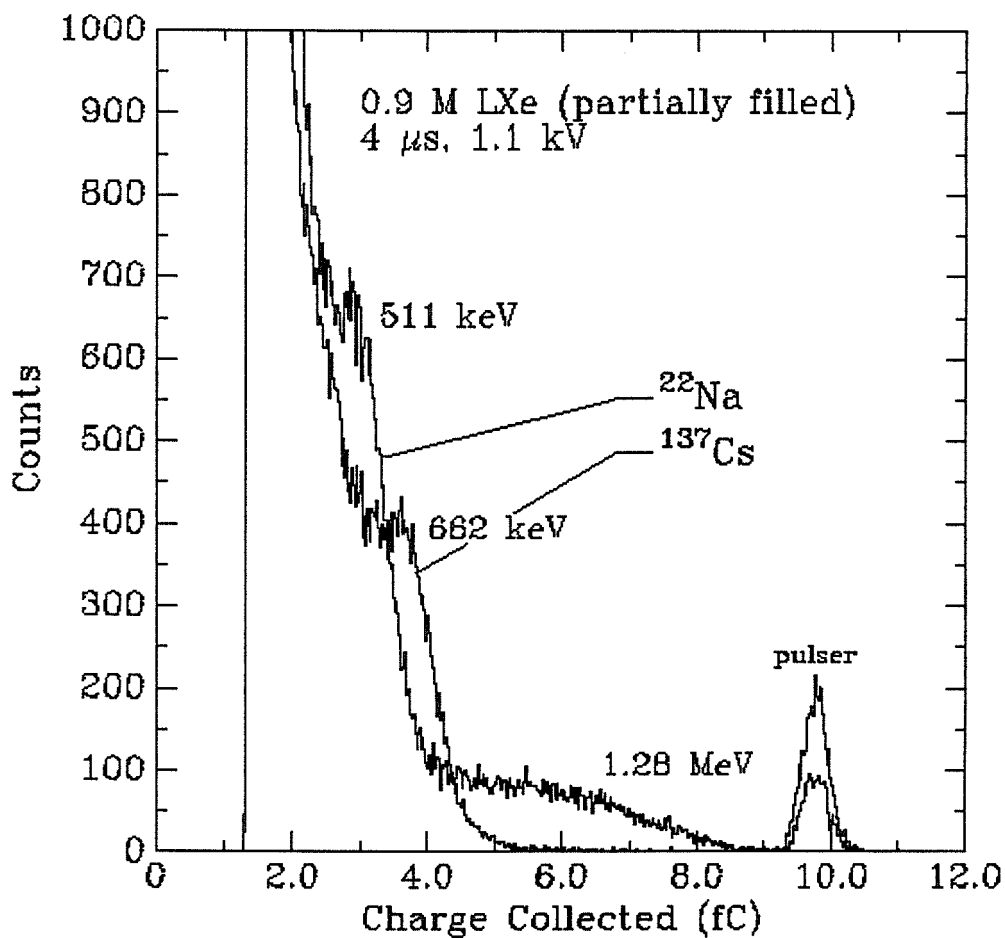


Figure D-31. Spectra taken with  $^{22}\text{Na}$  and  $^{137}\text{Cs}$  in the 0.9 M detector partially filled with liquid xenon. A linear scale has been used to display these spectra.



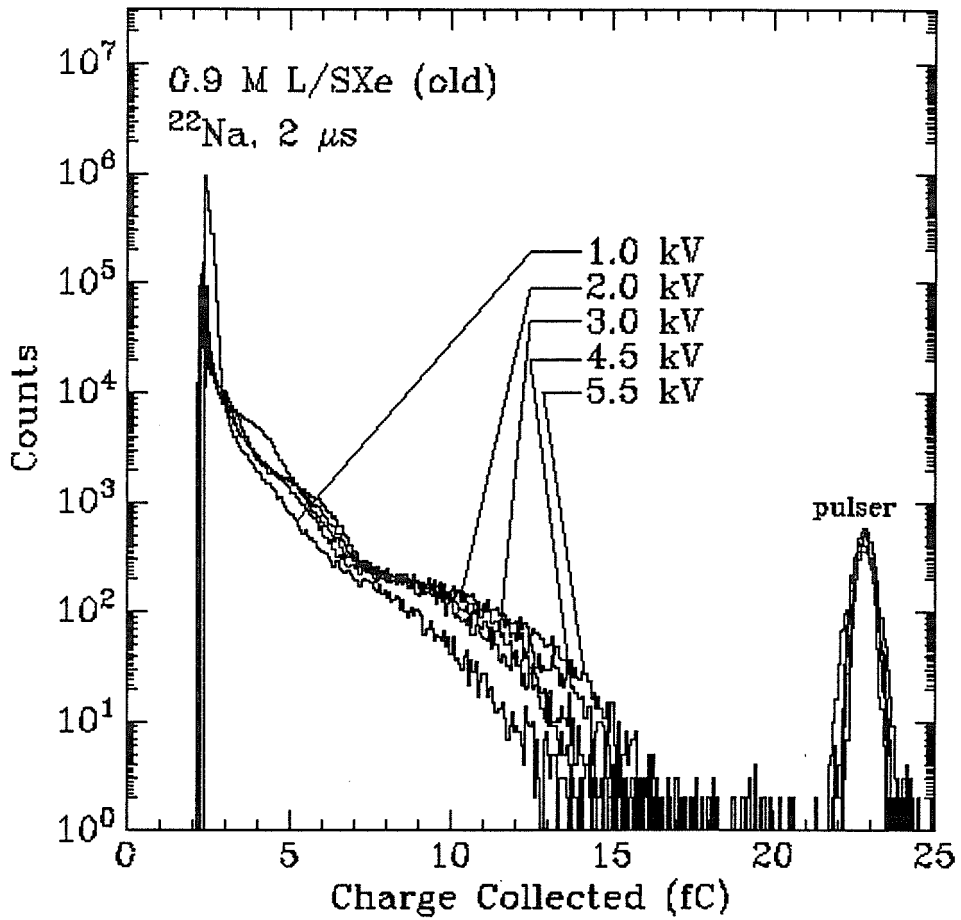


Figure D-32. Spectra taken at different voltages in the 0.9 M detector filled with liquid xenon, with a solid xenon core near the anode. This xenon was the old xenon which had been re-used often.

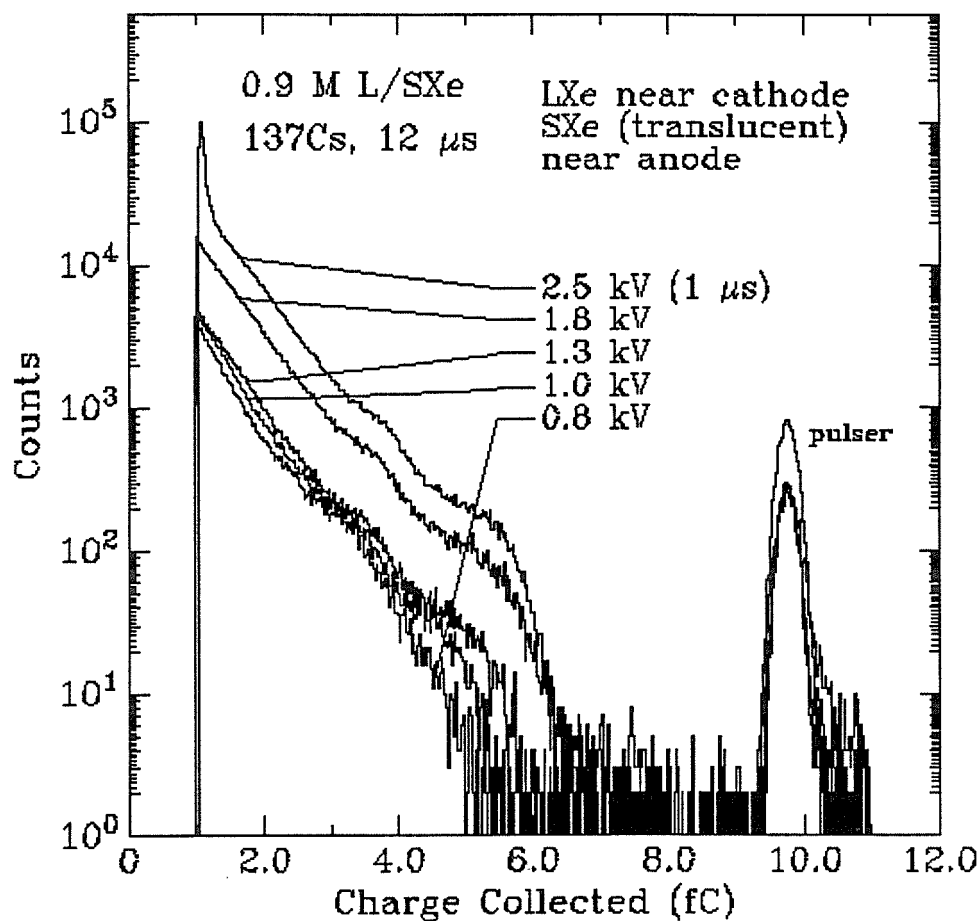


Figure D-33. Spectra taken at different voltages in the 0.9 M detector filled with liquid xenon and a solid xenon core near the anode. The shaping time constant for the spectrum taken at -2.5 kV applied to the cathode was 1  $\mu$ s. The shaping time constant for the other spectra in this figure was 12  $\mu$ s.

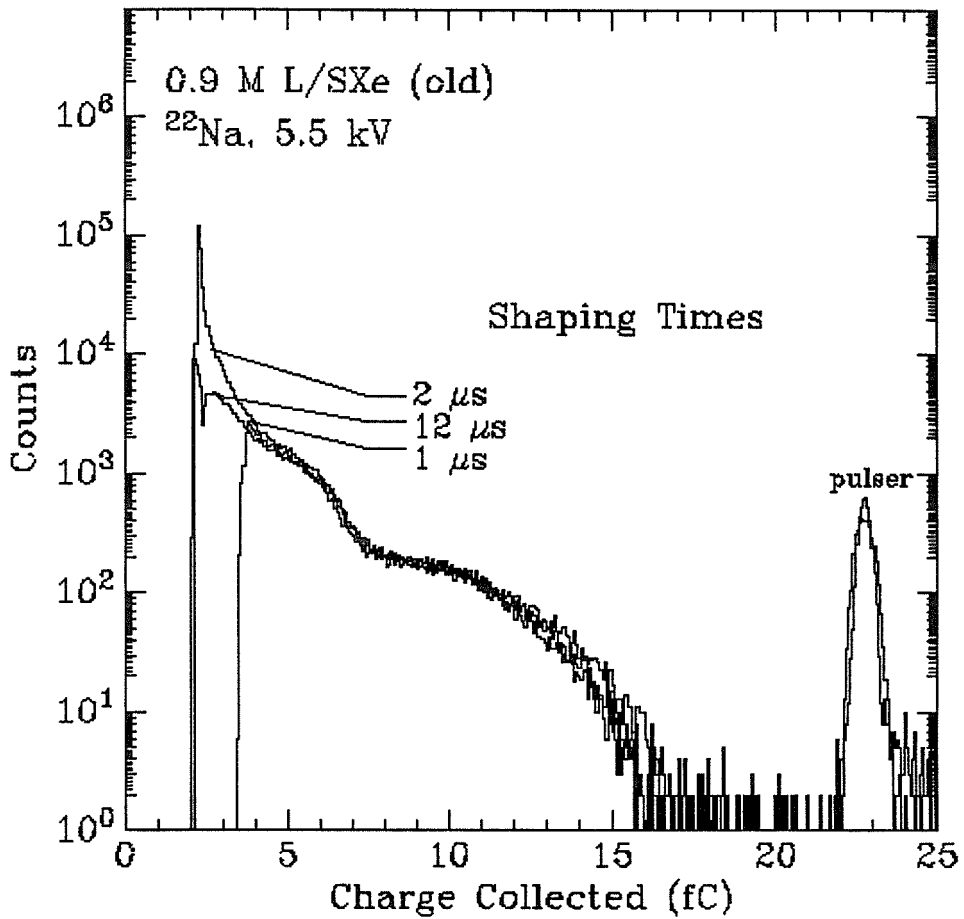


Figure D-34. The effect of different shaping time constants is displayed here for spectra taken in the 0.9 M detector filled with liquid xenon and a solid xenon core near the anode. The xenon used for these spectra was the old xenon. The applied voltage is  $-5.5\ \text{kV}$ .

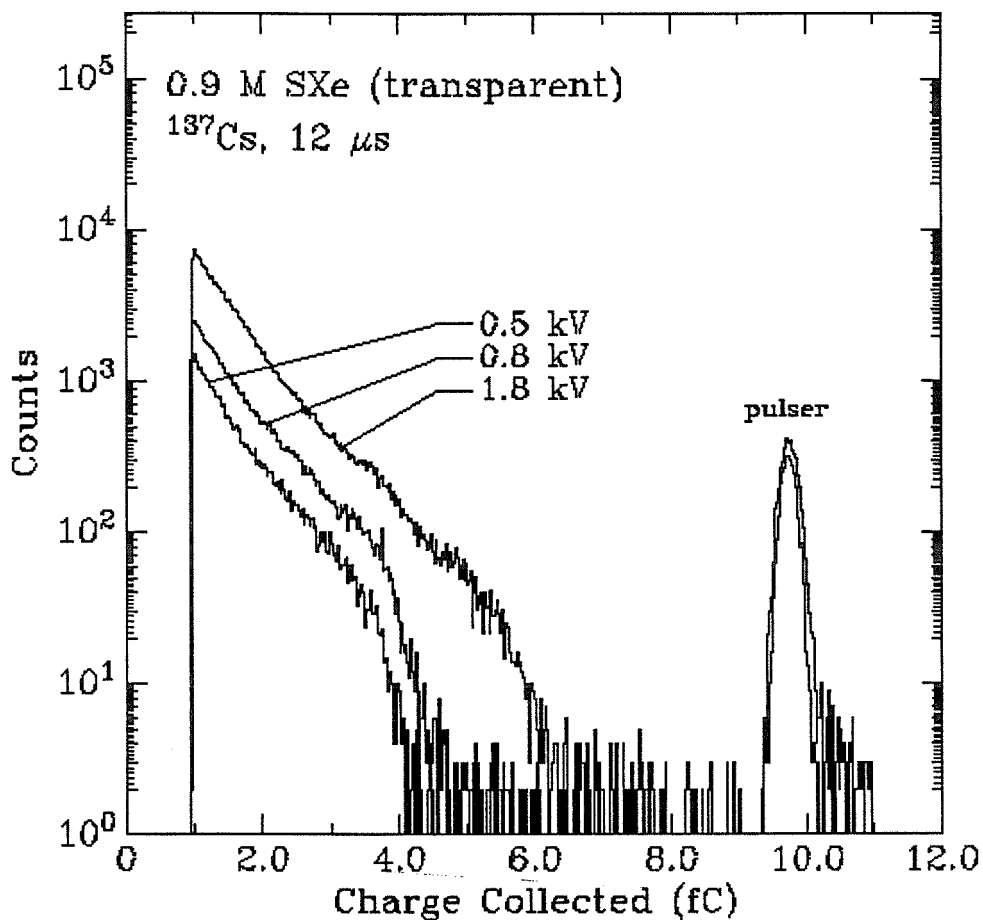


Figure D-35. Solid xenon spectra taken at different voltages in the 0.9 M detector with a  $^{137}\text{Cs}$  source. The crystal obtained for these spectra was transparent, unlike most of the solid xenon crystals, which were opaque.

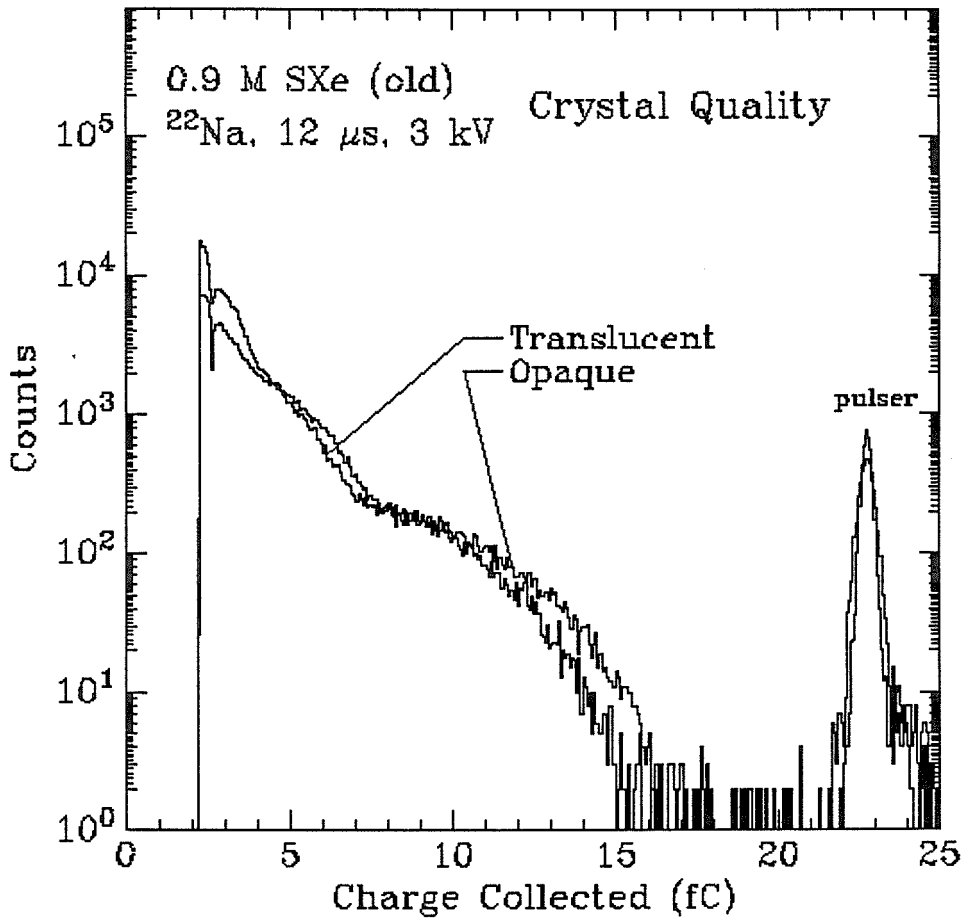


Figure D-36. Comparison of spectra in solid xenon with different crystal clarity using the 0.9 M detector.

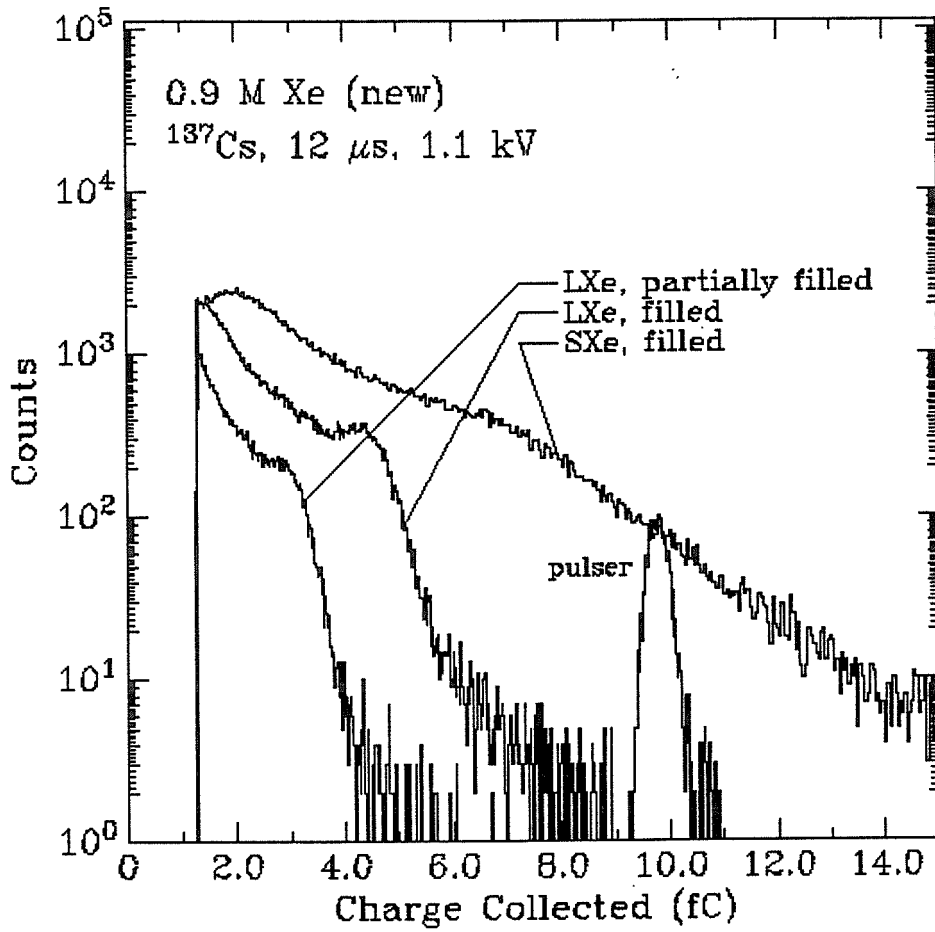


Figure D-37. Comparison of different xenon filling media for the 0.9 M detector.

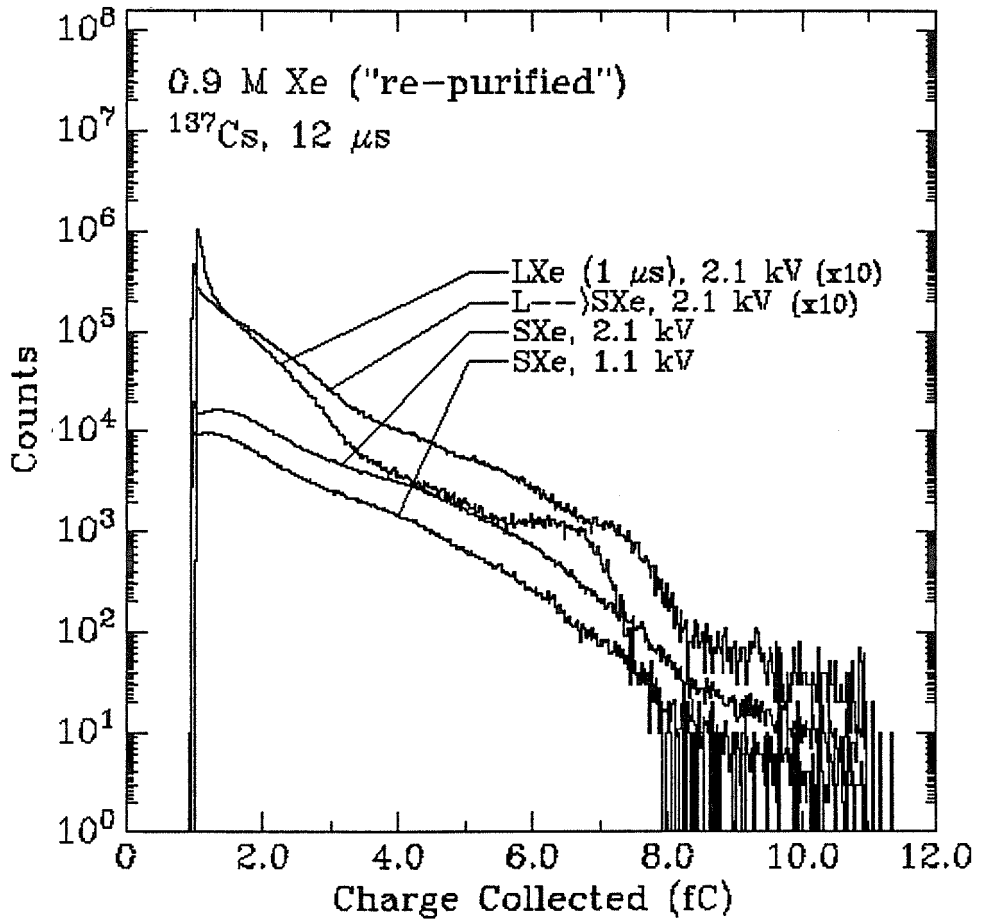


Figure D-38. Spectra taken in "re-purified" xenon, liquid and solid. (See text for discussion.)

References (Part I)

- <sup>1</sup> See, for example, K. Kleinknecht, *Detectors for Particle Radiation*, (Cambridge University Press, Cambridge, 1987).
- <sup>2</sup> E. Aprile and M. Suzuki, *IEEE Trans. NS-26*, 311 (1989).
- <sup>3</sup> G. Hademenos, E. Fenyves, D. Cline and M. Atac, *Nucl. Instrum. Methods B40/41*, 1235 (1989).
- <sup>4</sup> A. Barabash, V. Kuzminov, V. Lobashev, V. Novikov, B. Ovchinnikov and A. Pomansky, *Phys. Lett. B223*, 273 (1989).
- <sup>5</sup> A. Alessandrello, E. Bellotti, C. Cattadori, D. Camin, O. Cremonesi, E. Fiorini, C. Liguori, A. Pullia, L. Rossi, S. Ragazzi, P. Sverzellati and L. Zanotti, *Nucl. Instrum. Methods B17*, 411 (1986).
- <sup>6</sup> Bridget O'Callaghan-Hay, Ph.D. Thesis (California Institute of Technology, 1989).
- <sup>7</sup> E. Storm and H. Israel, *Nucl. Data Tables A7*, 565 (1970).
- <sup>8</sup> G. Pollack, *Rev. Mod. Phys.* **36**, 748 (1964).
- <sup>9</sup> T. Doke, *Portugal Phys.* **12**, 9 (1981).
- <sup>10</sup> T. Doke, A. Hitachi, S. Kubota, A. Nakamoto and T. Takahashi, *Nucl. Instrum. Methods* **134**, 353 (1976).
- <sup>11</sup> U. Fano, *Phys. Rev.* **72**, 29 (1947).
- <sup>12</sup> W.C. Haxton and G.J. Stephenson, *Prog. Part. Nucl. Phys.* **12**, 409 (1984).
- <sup>13</sup> F. Boehm and P. Vogel, *Physics of Massive Neutrinos* (Cambridge University



Press, Cambridge, 1987).

- <sup>14</sup> J. Engel, P. Vogel and M. Zirnbauer, *Phys. Rev.* **C37**, 731 (1988).
- <sup>15</sup> F. Boehm, private communication.
- <sup>16</sup> C. Lederer and V. Shirley, *Table of Isotopes* (Wiley, New York, 1978).
- <sup>17</sup> See, for example, E. Hennecke and O. Manuel, *Phys. Rev.* **C11**, 1378 (1975).
- <sup>18</sup> S. Elliott, A. Hahn and M. Moe, *Phys. Rev. Lett.* **59**, 2020 (1987).
- <sup>19</sup> Peter Fisher, Ph.D. Thesis (California Institute of Technology, 1988).
- <sup>20</sup> M. Edmiston and C. Gruen, *IEEE Trans. NS-25*, 352 (1978).
- <sup>21</sup> D.A. Imel and J. Thomas, *Nucl. Instrum. Methods* **A273**, 291 (1988).
- <sup>22</sup> J. Thomas and D.A. Imel, *Phys. Rev.* **A36**, 614 (1987).
- <sup>23</sup> J. Thomas, D.A. Imel and S. Biller, *Phys. Rev.* **A38**, 5793 (1988).
- <sup>24</sup> D.A. Imel and J. Thomas, *Nucl. Instrum. Methods* **B40/41**, 1208 (1989).
- <sup>25</sup> D.A. Imel, submitted to *Nucl. Instrum. Methods*, 1990.
- <sup>26</sup> Th. Lindblad, L. Bagge, Å. Engström, J. Bialkowski, C. Gruhn, W. Pang, M. Roach and R. Loveman, *Nucl. Instrum. Methods* **215**, 183 (1983).
- <sup>27</sup> K. Masuda, A. Hitachi, Y. Hoshi, T. Doke, A. Nakamoto, E. Shibamura and T. Takahashi, *Nucl. Instrum. Methods* **174**, 439 (1980).
- <sup>28</sup> E. Aprile, W. Ku, J. Park and H. Schwartz, *Nucl. Instrum. Methods* **A261**, 519 (1987).
- <sup>29</sup> All molecular sieve used was a 50%-50% mixture of 13X and 4A pellets, obtained from Union Carbide.
- <sup>30</sup> The electroformed mesh was obtained from Interconics, St. Paul, MN.
- <sup>31</sup> G. Knoll, *Radiation Detection and Measurement* (Wiley, New York, 1979).
- <sup>32</sup> L. Pages, E. Bertel, H. Joffre and L. Sklavenitis, *Atomic Data* **4**, 1 (1972).
- <sup>33</sup> O. Bunemann, T. Cranshaw and J. Harvey, *Can. J. Res.* **A27**, 191 (1949).

- <sup>34</sup> W. Hoffmann, U. Klein, M. Schulz, J. Spengler and D. Wegener, Nucl. Instrum. Methods **135**, 151 (1976).
- <sup>35</sup> R. Scalettar, P. Doe, H. Mahler and H. Chen, Phys. Rev. **A25**, 2419 (1982).
- <sup>36</sup> L. Miller, S. Howe and W. Spear, Phys. Rev. **166**, 871 (1968).
- <sup>37</sup> S. Suzuki, T. Doke, A. Hitachi, J. Kikuchi, A. Yunoki and K. Masuda, Nucl. Instrum. Methods **A245**, 366 (1986).
- <sup>38</sup> D. Anderson, Nucl. Instrum. Methods **A242**, 254 (1986).
- <sup>39</sup> *Argon, Helium and the Rare Gases*, edited by G. Cook (Interscience, New York, 1961), Vol. I.
- <sup>40</sup> M. Iqbal, B.O'Callaghan and H. Wong, Nucl. Instrum. Methods **A253**, 278 (1987).
- <sup>41</sup> Available, for example, from MDC High Vacuum Components Corporation, 23842 Cabot Boulevard, Hayward, CA 94545 or Nor-Cal Products, Inc., 1512 Southern Oregon Street, P.O. Box 518, Yreka, CA 96097.
- <sup>42</sup> SAES Getters/USA Inc., 1122 E. Cheyenne, Colorado Springs, CO 80906.
- <sup>43</sup> Henry Wong, private communication.
- <sup>44</sup> J. Marshall, Rev. Sci. Instrum. **25**, 232 (1954).
- <sup>45</sup> P. Doe, R. Allen, S. Biller, G. Bühler, W. Johnson and H. Chen, Nucl. Instrum. Methods **A258**, 170 (1987).
- <sup>46</sup> V. Grebinnik, V. Dodokhov, V. Zhukov, A. Lazarev, A. Nozdrin, A. Pisarev, V. Stolupin and V. Travkin, Sov. Phys. JETP **44**, 219 (1977).
- <sup>47</sup> J. Cobb and D. Miller, Nucl. Instrum. Methods **141**, 433 (1977).
- <sup>48</sup> E. Aprile, K. Giboni and C. Rubbia, Nucl. Instrum. Methods **A241**, 62 (1985).
- <sup>49</sup> A. Barabash, A. Golubev, O. Kazachenko, V. Lobashev, B. Ovchinnikov and B. Stern, Nucl. Instrum. Methods **A236**, 69 (1985).

- <sup>50</sup> E. Aprile and M. Suzuki, *IEEE Trans. Nucl. Sci.* **36**, 311 (1989).
- <sup>51</sup> E. Gullikson and B. Henke, *Phys. Rev. B* **39**, 1 (1989).
- <sup>52</sup> A. Pisarev, V. Pisarev and G. Revenko, *Sov. Phys. JETP* **36**, 828 (1973).
- <sup>53</sup> E. Gushchin, A. Kruglov and I. Obodovskii, *Sov. Phys. JETP* **55**, 650 (1982).
- <sup>54</sup> A. Bolotnikov, V. Dmitrenko, A. Romanyuk, S. Suchkov and Z. Uteshev, *Instrum. Exp. Tech.* **29**, 802 (1986).
- <sup>55</sup> K. Giboni, *Nucl. Instrum. Methods* **A269**, 554 (1988).
- <sup>56</sup> E. Aprile, W. Ku and J. Park, *IEEE Trans. Nucl. Sci.* **35**, 37 (1988).
- <sup>57</sup> S. Biller, D. Kabat, R. Allen, G. Bühler and P. Doe, *Nucl. Instrum. Methods* **A276**, 144 (1989).
- <sup>58</sup> I. Gradshteyn and I. Ryzhik, *Table of Integrals, Series, and Products*, Academic, Orlando (1980). See section 8.21 for a discussion of the exponential-integral and its infinite-series expansion.
- <sup>59</sup> *Handbook of Chemistry and Physics*, Chemical Rubber Co., (1972-1973). See page D-177 for low temperature liquid baths, and E-99 for thermocouple data.
- <sup>60</sup> Isotope Products Laboratories, Burbank, California.
- <sup>61</sup> Y. Chiba, I. Hayashibara, T. Ohsugi, T. Sakanoue, A. Taketani, N. Terunuma, T. Suzuki, A. Tsukamoto, H. Yamamoto, Y. Fukushima, T. Kohriki, S. Nakamura, M. Sakuda and Y. Watase, *Nucl. Instrum. Methods* **A269**, 171 (1988).
- <sup>62</sup> G. Jaffe, *Ann. Phys.* **42**, 303 (1913).
- <sup>63</sup> H. Kramers, *Physica* **18**, 665 (1952).
- <sup>64</sup> L. Onsager, *Phys. Rev.* **54**, 554 (1938).
- <sup>65</sup> K. Deiters, A. Donat, K. Lanius, R. Leiste, U. Röser, M. Sachwitz, K. Trützscher, E. Aprile, G. Motz, C. Rubbia, D. Koch and A. Staude, *Nucl.*

Instrum. Methods **180**, 45 (1981).

- <sup>66</sup> P. Doe, H. Mahler, H. Chen, U. Calif. Irvine Report No. 72, March 1982 (unpublished).
- <sup>67</sup> C. Gruhn and R. Loveman, IEEE Trans. Nucl. Sci. **26**, 110 (1979).
- <sup>68</sup> K. Yoshino, U. Sowada and W. Schmidt, Phys. Rev. Lett **40**, 407 (1978).
- <sup>69</sup> T. Takahashi, S. Konno, T. Hamada, M. Miyajima, S. Kubota, A. Nakamoto, A. Hitachi, E. Shibamura and T. Doke, Phys. Rev. **A12**, 1771 (1975).
- <sup>70</sup> *Rare Gas Solids*, edited by M. Klein (Academic, London, 1977), Vol. II.
- <sup>71</sup> E. Shibamura, A. Hitachi and T. Doke, Nucl. Instrum. Methods **131**, 249 (1975).
- <sup>72</sup> M. Iqbal, H. Henrikson, L. Mitchell, B. O'Callaghan, J. Thomas and H. Wong, Nucl. Instrum. Methods **A259**, 459 (1987).
- <sup>73</sup> J. Thomas and D.A. Imel, in *Proceedings of the Conference on Low Level Counting and Liquid Drift Detectors*, edited by D. Cline (UCLA, Los Angeles, 1987).
- <sup>74</sup> D. Ritson, *Techniques of High Energy Physics* (Interscience, New York, 1961).
- <sup>75</sup> H. Bethe, Phys. Rev. **89**, 1256 (1952).
- <sup>76</sup> I. Obodovskii and S. Pokachalov, Fiz. Nizk. Temp. **5**, 829 (1979) [Sov. J. Low Temp. Phys. **5**, 393 (1979)].
- <sup>77</sup> M. Cohen and J. Lekner, Phys. Rev. **158**, 305 (1967).

## PART II

SEARCH FOR MASSIVE NEUTRINOS IN THE  $\beta$ -DECAY OF  $^{35}\text{S}$

## CHAPTER ONE

### Introduction

#### 1.1 Neutrino Mass

A massive neutrino would have profound implications for our understanding of physics. Although the Standard Model adequately describes all observations of nature to the present, it does not explain the masses of the fermions. It is expected that at some point the Standard Model will be shown to be inadequate, and one of the competing Grand Unified Theories (GUT's) which can better motivate the masses will be selected as the correct theory. One common characteristic of most viable GUT's is that they predict a non-vanishing neutrino mass<sup>1</sup>. Moreover, neutrino mass presents one of the only solutions to the dark matter puzzle which involves particles which are known to exist. Thus, experiments which are sensitive to neutrino mass are among the most exciting in physics today. A good review of the types of experiments included in this category is given in Boehm and Vogel<sup>1</sup>. These include  $\beta\beta$ -decay with the emission of no neutrinos (see part I of this thesis), neutrino decay, neutrino oscillations and endpoint measurements of  $\beta$ -decay.

The electron neutrino's existence was first inferred from the electron spectrum of  $\beta^-$ -decay<sup>2</sup>:

$$(A, Z) \rightarrow (A, Z-1) + e^- + \bar{\nu}_e, \quad (1-1)$$

where A is the atomic mass and Z is the atomic number. Attempts<sup>1</sup> have been

made to determine the mass of the neutrino by measuring the shape of the  $\beta$ -decay spectrum near the endpoint of the decay. The difference between  $Q$ -value of the decay and the endpoint (maximum kinetic energy) of the electron spectrum gives the neutrino mass.

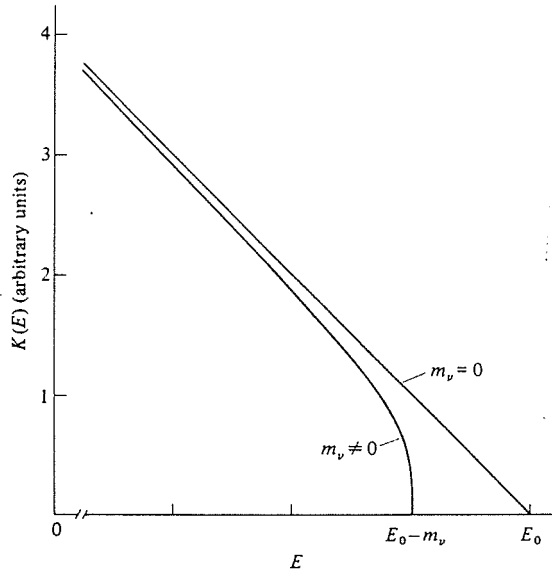


Figure 1-1. Kurie plot for nuclear  $\beta$ -decay. (From Ref. 1.) The slope becomes infinite near the endpoint in the case of a massive neutrino, but remains finite for  $\beta$ -decay with a massless neutrino.

In practice, one uses the slope of the Kurie plot<sup>3</sup>

$$K(E) \equiv \left[ \frac{dN/dE}{pE F(Z,E)} \right]^{\frac{1}{2}} \propto \left[ (E_0 - E) \left( (E_0 - E)^2 - m_\nu^2 \right)^{\frac{1}{2}} \right]^{\frac{1}{2}}, \quad (1-2)$$

where  $dN/dE$  is the  $\beta$ -decay rate as a function of electron energy,  $p$  and  $E$  are the electron momentum and energy, respectively,  $E_0$  is the endpoint energy of the decay ( $Q + m_e$ ),  $F$  is the Fermi function which corrects the decay rate for

Coulomb screening and finite nuclear size effects and  $m_\nu$  is the neutrino mass. As illustrated in Fig. 1-1, the slope of the Kurie plot becomes infinite near the endpoint of the electron spectrum for a non-zero neutrino mass. Lubimov<sup>4</sup> reports a value for  $m_\nu$  of about 30 eV, but this value has been excluded by recent experiments<sup>5</sup>.

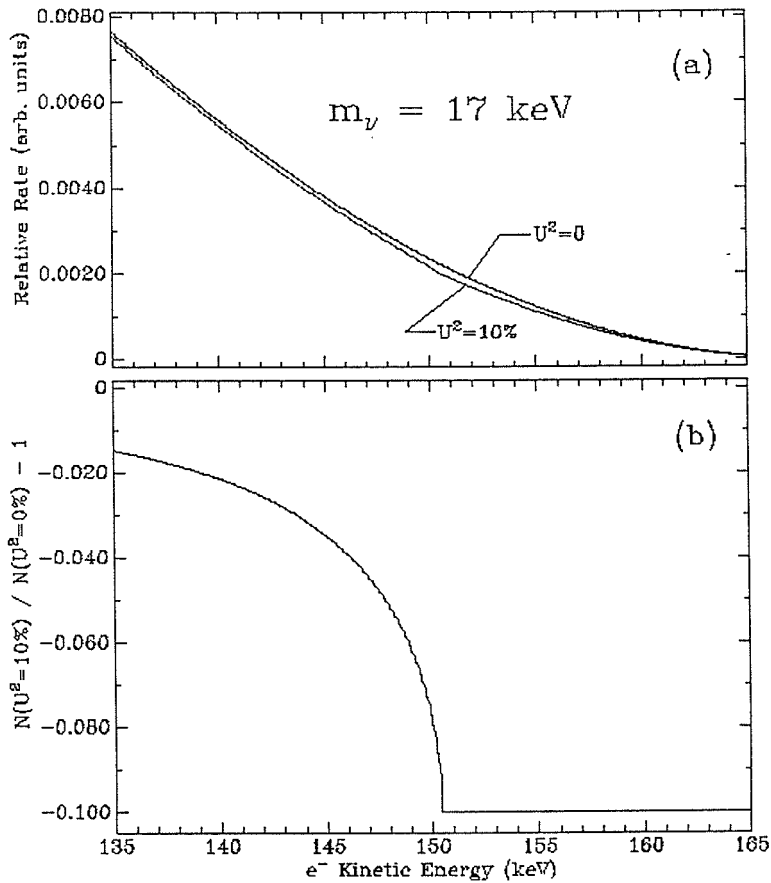


Figure 1-2. (a) Eq. (1-4) for the case of  $m_\nu = 17.0$  keV and  $|u|^2 = 0.10$  compared to the case of  $|u|^2 = 0$ . (b) The same comparison for Eq. (1-5). In the present experiment the range of interesting  $|u|^2$  will be about two orders of magnitude smaller.



In contrast to the above experiments, which attempt to measure the mass of the (light) electron neutrino, the present experiment is designed to be sensitive to a heavy neutrino admixture. It is possible that the neutrino is not a pure eigenstate of the weak interactions, but that it is a mixture of mass eigenstates  $\nu_i$ :

$$\nu_l = \sum_{i=1}^3 U_{li} \nu_i, \quad (1-3)$$

where  $U$  is the mixing matrix and  $l = e, \mu, \tau$ , in the case of three fermion families. In this case, although the dominant eigenstate may be one of small mass, there could be small admixtures of heavier mass ("subdominant") eigenstates. In what follows we restrict ourselves to the case of one heavy neutrino admixed in the electron neutrino. Then a  $\beta$ -decay electron spectrum would appear as the sum of two spectra, one with the electron endpoint at the  $Q$ -value of the decay, and one with the endpoint at  $Q - m_\nu$ . Thus, for an allowed transition:

$$\frac{dN}{dT_e} = A F(Z, T_e) p_e (T_e + m_e) (Q - T_e)^2 \times \left[ |u|^2 \left( 1 - \frac{m_\nu^2}{(Q - T_e)^2} \right)^{\frac{1}{2}} \Theta(Q - m_\nu - T_e) + (1 - |u|^2) \Theta(Q - T_e) \right], \quad (1-4)$$

where  $A$  is a constant,  $|u|^2$  is the mixing fraction of the heavy neutrino,  $T_e$  is the electron kinetic energy and  $\Theta(x)$  is the Heaviside step function. This spectrum is illustrated in Fig. 1-2a. By analyzing the function:

$$\frac{N(m_\nu \neq 0) - N(m_\nu = 0)}{N(m_\nu = 0)} \quad (1-5)$$

near the endpoint of the decay emitting the massive neutrino, one expects to find a threshold effect, or “kink” in the spectrum if a massive neutrino is admixed. (Fig. 1-2b.)

## 1.2 Previous Limits

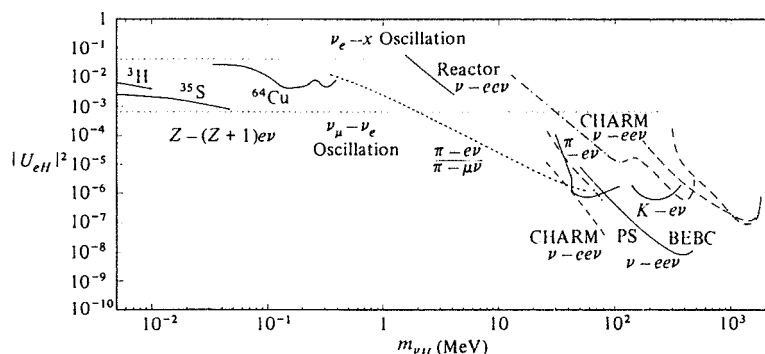


Figure 1-3. Exclusion plot for neutrino mass and admixture taken from Ref. 1.

The possibility of heavy neutrino admixtures stimulated several investigations. However, prior to 1985 no evidence for a massive neutrino admixed in  $\beta$ -decay had been observed, and the exclusion plot of mass and mixing angle achieved at the end of 1985 is shown in Fig. 1-3. In 1985, Simpson<sup>6</sup> announced evidence for a 17 keV neutrino admixed in the  $\beta$ -decay spectrum of  $^3\text{H}$ , with a mixing of about 3%. There are many difficulties in analyzing the spectrum of tritium ( $Q = 18$  keV); in fact this result was later reanalyzed<sup>7</sup> to give a mixing of about 1%. Meanwhile, since the effect of a heavy neutrino should occur in every  $\beta$ -decay, Simpson<sup>8</sup> and others<sup>9-13</sup> examined the spectrum of  $^{35}\text{S}$ . The spectrum of  $^{63}\text{Ni}$  was also studied<sup>14,15</sup>. ( $^{35}\text{S}$  and  $^{63}\text{Ni}$  were chosen since they have low  $Q$ -values<sup>16</sup> and are allowed decays for which the  $\beta$ -decay spectrum may be almost exactly calculated.) A discussion of the experiments in  $^{35}\text{S}$  will

be presented below.

### 1.3 Experimental Considerations

In order to see a threshold effect, data points with enough accuracy must be obtained. Roughly, to be sensitive to a “kink” of 0.7%, for example, data with statistical uncertainty of better than 0.7% must be acquired. In addition, several systematic uncertainties must be addressed.

The slope of the expected  $\beta$ -spectrum, to be compared with the experimental data, cannot be calculated with sufficient accuracy because it is very sensitive to the Q-value as well as the spectrometer response function which are not known or cannot be sufficiently accurately measured. Thus, in the fits, these parameters must be included as variables, leaving some ambiguity in the gross energy dependence of the spectrum. Therefore the resolution of the spectrometer must be sufficient to isolate the region of the spectrum near the threshold. Otherwise, the effect of a massive neutrino admixture will be indistinguishable from small changes in the fit parameters. Typically this means that resolution of 1-2 keV is required. In addition, one must take care that scattering in the detector and source and energy loss in the source do not spoil the resolution of the detection system. Thus, thin source backings are used so that backscattering in the source is negligible. Thin uniform sources are required, and must be deposited on a grounded, metallized surface to avoid energy shifts in the electrons emitted due to charging of the source. One should carefully measure the response function of the detector to electrons in the energy range of interest and gauge the effect of any low energy tail on the spectrum.

Pains must be taken to ensure the stability of the detector system. If a detector which is cooled accumulates material on its surface scattering and energy loss in transmission through the detector can be affected. In the case of magnetic spectrometers, the magnetic field stability, as well as the actual dimensions of the spectrometer during temperature changes, must be ensured constant. Otherwise a changing magnetic field or geometry will change the momentum slice observed, and smear out any threshold effect. For example, to obtain data which are accurate to  $10^{-4}$ , one must hold the magnetic field constant in the region of the electron path to about  $3 \times 10^{-5}$ .

#### 1.4 Evidence for a 17 keV neutrino

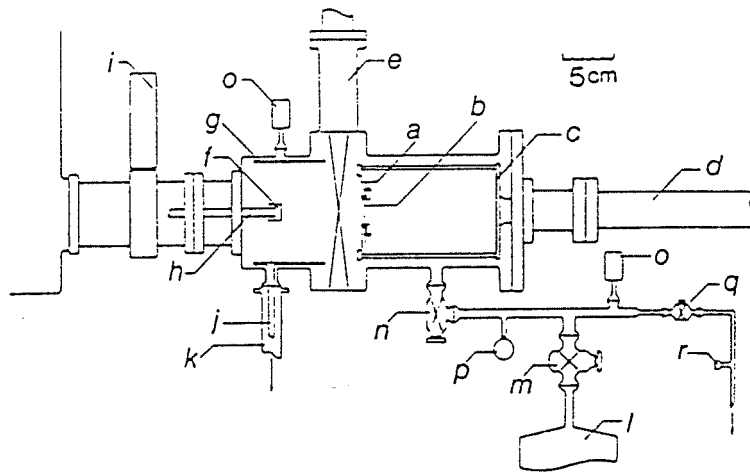


Figure 1-4. Simpson's experimental apparatus<sup>8</sup>. *a* is the acrylic source holder, *b* is the source, *c*, the source-holder mount, *d* is the source manipulator. *e*, *m*, *n*, *q* and *r* are vacuum valves; *f* is the Si(Li) crystal and *g*, the cryopanel. *h* and *j* are cold fingers. *i* is the preamplifier, *k* and *l* are sorption pumps, and *o* and *p* are vacuum gauges.

Simpson's experimental apparatus is shown in Fig. 1-4. He uses a cooled Si(Li) detector to observe the electron spectrum of a  $5 \mu\text{Ci } ^{35}\text{S}$  source deposited on a  $10 \mu\text{m}$  thick substrate covered with a thin metallic layer which is connected to ground. The mylar substrate is relatively thick, giving rise to a significant amount (2-3%) of backscattering in the substrate. Simpson allows the electron response function of the detector, measured with a  $^{57}\text{Co}$  source, to correct for this effect.

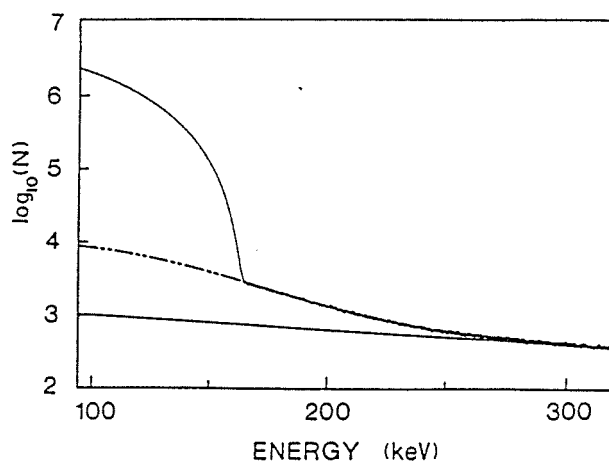


Figure 1-5.  $\beta$ -decay spectrum<sup>8</sup> from Simpson experiment in  $^{35}\text{S}$ . The background extends up to 330 keV, comprised of ambient background (smooth curve) and pile-up (dashed curve).

The calibration spectrum from this experiment shows an energy resolution (FWHM) of 0.77 keV for the  $\gamma$ -rays and about 1.5 keV for the K-conversion electron peaks. Fig. 1-5 is Simpson's  $\beta$ -spectrum, which shows backgrounds due to unrejected pile-up and natural background, the latter of which was measured and subtracted.

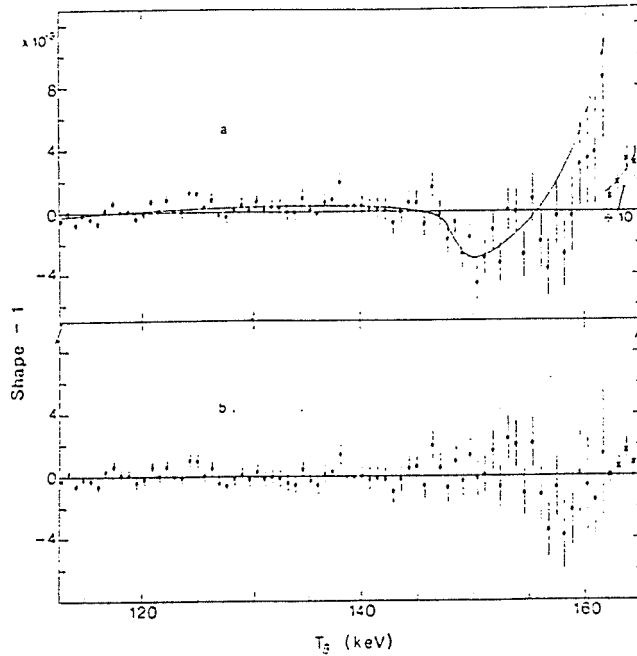


Figure 1-6. Data and fit<sup>8</sup> from Simpson experiment in <sup>35</sup>S. (a) Here the data are compared to a theoretical spectrum with  $|u|^2 = 0$ ;  $\chi^2/\nu = 2.0$ . The smooth curve is the shape expected for a 17 keV neutrino with  $|u|^2 = 0.8\%$ . In (b) the data are fit with  $m_\nu = 17$  keV and  $|u| = 0.75\%$  for which  $\chi^2/\nu = 1.0$ .

The data are compared (see (1-5) above) to theoretical  $\beta$ -decay spectra (1-4) which have been convoluted with the detector response function, in this case a Gaussian function with a flat tail extending to zero energy. Fig. 1-6 shows Simpson's <sup>35</sup>S spectrum compared to a spectrum without a heavy neutrino admixed and to a spectrum with a 17 keV neutrino admixed by 0.8%. The former spectrum shows a clear threshold effect at an energy 17 keV below the endpoint.

### 1.5 Exclusions of the 17 keV neutrino

Several subsequent investigations could not confirm the 17 keV neutrino postulated by Simpson. Datar<sup>9</sup> *et al.* deposited a Ba<sup>35</sup>SO<sub>4</sub> source on a 90 μg/cm<sup>2</sup> aluminized polypropylene foil and measured the β-spectrum of this source using a shielded, cooled Si(Li) detector with a resolution of 3.5 keV at 120 keV. They obtained the spectrum shown in Fig. 1-7a, for which they claim an upper limit on the admixture of a 17 keV neutrino of 0.6% at the 90% confidence level.

Ohi<sup>10</sup> *et al.* deposited <sup>35</sup>S between two foils of 0.5 μm thick Mylar and placed the source between two Si(Li) detectors, one of which was used to veto backscattered electrons from the other counter. Although the energy resolution for γ-rays in this detector was 1.7 keV FWHM, the response function for electrons is much wider and has an asymmetric tail due to energy loss of electrons in the Mylar film and incomplete back-scattering suppression. The comparison of the data with a theoretical spectrum assuming a massless neutrino is shown in Fig. 1-7b, for which Ohi claims an admixture upper limit in the mass range 10-50 keV of 0.3%.

Apalikov<sup>11</sup> *et al.* evaporated <sup>35</sup>S-tagged methionine onto a conducting glass substrate and placed the source in an iron-free toroidal magnetic spectrometer with a six-channel proportional chamber at the focus. The data and theoretical fit are shown in Fig. 1-7c. (No response function was provided in the report.) From this data they derive an upper limit of 0.2% on the admixture of the 17 keV neutrino.

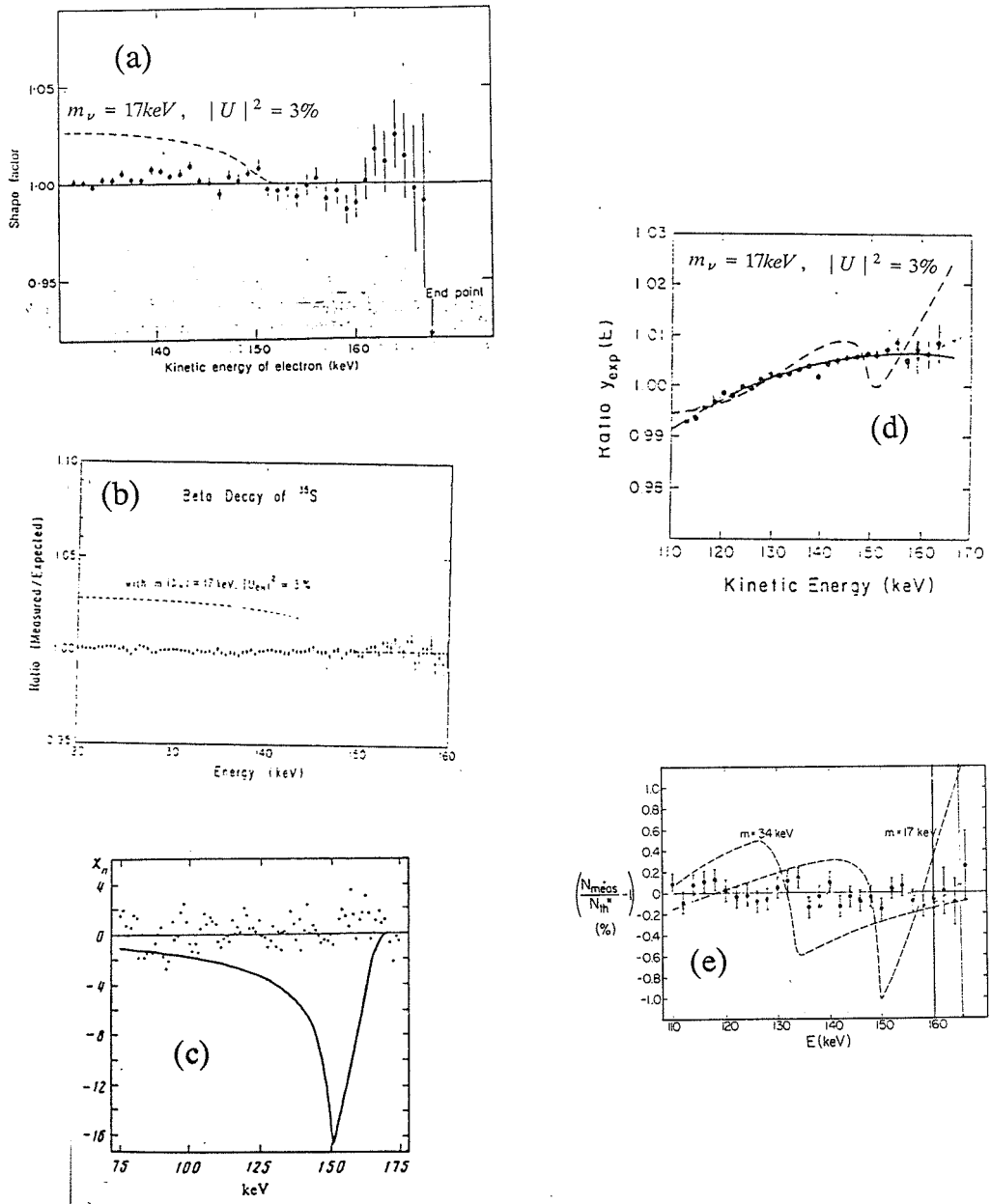


Figure 1-7. Data compared and fits from experiments using  $^{35}\text{S}$  which claim to exclude the Simpson result. (a) Datar<sup>9</sup>, (b) Ohi<sup>10</sup>, (c) Apalikov<sup>11</sup>, (d) Altitzoglou<sup>12</sup> and (e) Markey<sup>13</sup>. See text for discussion of these experiments.



Altitzoglou<sup>12</sup> *et al.* placed a  $^{35}\text{S}$  source in an iron-free intermediate-image magnetic spectrometer. A surface barrier detector was used to detect the electrons at the focus of the spectrometer. The rate at a given momentum setting was determined by extrapolating the low-energy tail to zero energy. The comparison of their data with theoretical spectra convoluted with a spectrometer response function (not shown in their report) and a quadratic shape factor is shown in Fig. 1-7d. For these data they claim an upper limit of the admixture of a 17 keV neutrino in  $\beta$ -decay of 0.4%.

Markey and Boehm<sup>13</sup> deposited 2 mCi of a  $\text{Na}_2^{35}\text{SO}_4$  solution onto a  $230 \mu\text{g}/\text{cm}^2$  Mylar foil and placed the source in the Caltech iron-free double-focusing magnetic spectrometer, to be described in more detail in chapter 2. A cooled Si(Li) detector was used at the focus of the spectrometer, and the rate at each momentum setting was determined by extrapolating detector spectrum to zero energy. The data from this experiment (Fig. 1-7e) yield an upper limit of 0.3% on the admixture of a 17 keV neutrino.

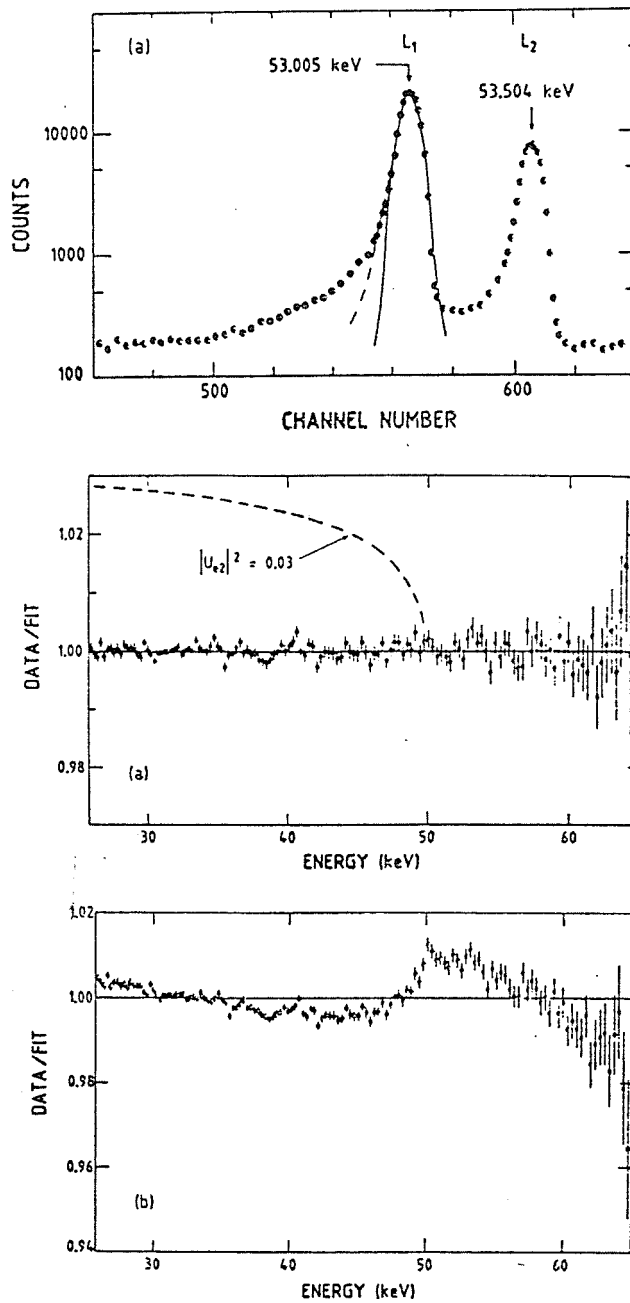


Figure 1-8. (a) Chalk River response function<sup>14</sup>. (b) Data from Chalk River experiment fit to  $|u|^2 = 0\%$  and (c) to  $|u|^2 = 3\%$ .

Two experiments were performed on  $^{63}\text{Ni}$ : one using the Chalk River iron-free double-focusing magnetic spectrometer<sup>14</sup> and one using the Caltech spectrometer<sup>15</sup>. The Chalk River experiment employed an array of 19 infinitely thick, electrostatically accelerated sources and an array of 22 proportional counters. The response function for this detector is shown in Fig. 1-8a and the  $\beta$ -decay data in Fig. 1-8b and c. These data yield an upper limit of 0.3% admixture of a 17 keV neutrino. The Caltech experiment used a Geiger counter with a  $2.5\ \mu\text{m}$  entrance window and placed an upper limit of 0.7% on the heavy neutrino admixture.

### 1.6 Remarks on the experiments

Simpson has provided criticism<sup>8</sup> of the above experiments. Specifically, the data analysis in the Ohi experiment appears to be flawed, in that the data were fit to a theoretical spectrum with no heavy neutrino admixture, and then a neutrino admixture was added to the spectrum, without refitting the other parameters of the experiment, such as the endpoint and response function. Simpson does this and finds their data to be consistent with an admixture of 1% at  $m_\nu = 17\ \text{keV}$ . The analysis by Datar<sup>10</sup> *et al.* seems to be similarly afflicted.

Two of the magnetic spectrometer  $^{35}\text{S}$  experiments employed shape factors, which Simpson warns can hide a “kink,” even though they are smooth corrections. In fact, the experiment by Apalikov<sup>11</sup> *et al.* seems to show a local distortion in the Kurie plot in the vicinity of 150 keV, where the threshold effect of a 17 keV neutrino would be expected to appear. Although the Markey<sup>13</sup> experiment did not have such a shape factor, the detector spectrum shows a backscattering tail which contains about 60% of the counts of the distribution,

about 2-3 times more than expected for normally incident electrons (and achieved in the present experiment). This implies that the spectrometer may have had serious scattering, which if included in the analysis would completely degrade the momentum resolution of the spectrometer and wipe out any threshold effect. At the very least, it makes the extrapolation to zero energy to obtain the rate at a given momentum setting very uncertain.

Clearly, it is still an open question as to whether or not a 17 keV neutrino exists, and more generally, whether there are any neutrinos in the mass range of 5 to 50 keV with mixing angles of less than 1%. Here I report on the progress of an experiment being carried out to explore just such a region.

## CHAPTER TWO

### Apparatus

In this chapter I present the experimental methods and equipment used to measure the  $\beta$ -spectrum of  $^{35}\text{S}$ .

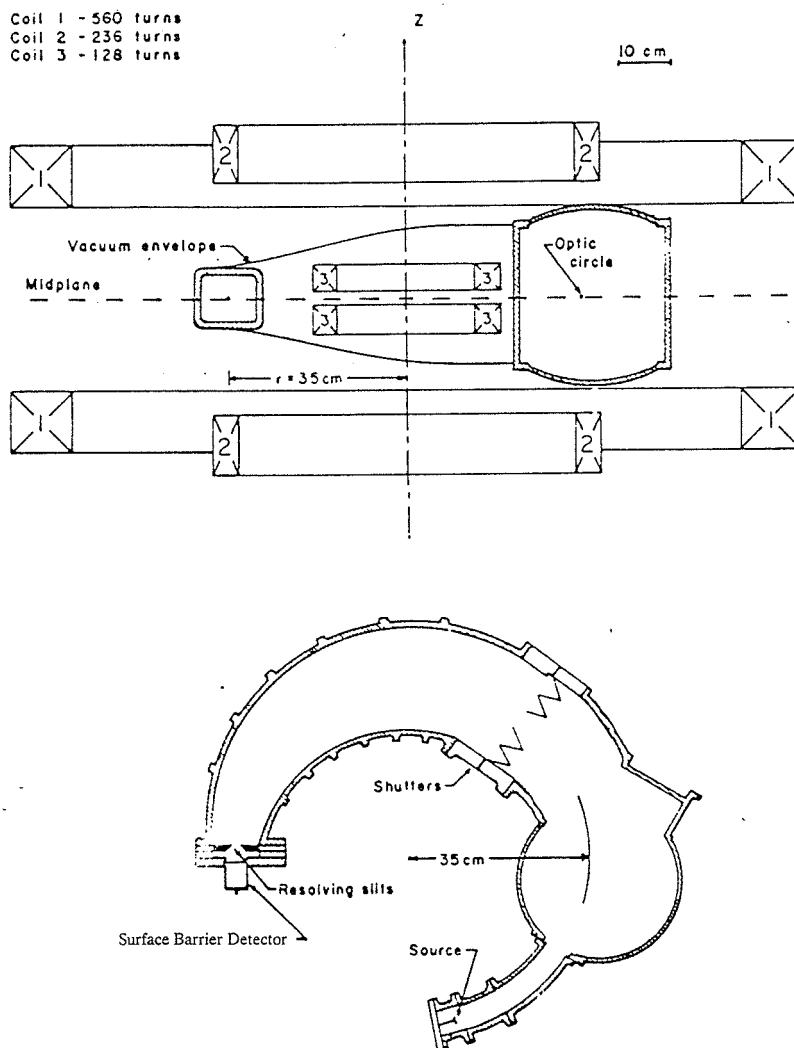


Figure 2-1. Schematic of Caltech iron-free double focusing  $\beta$ -spectrometer.

## 2.1 Spectrometer

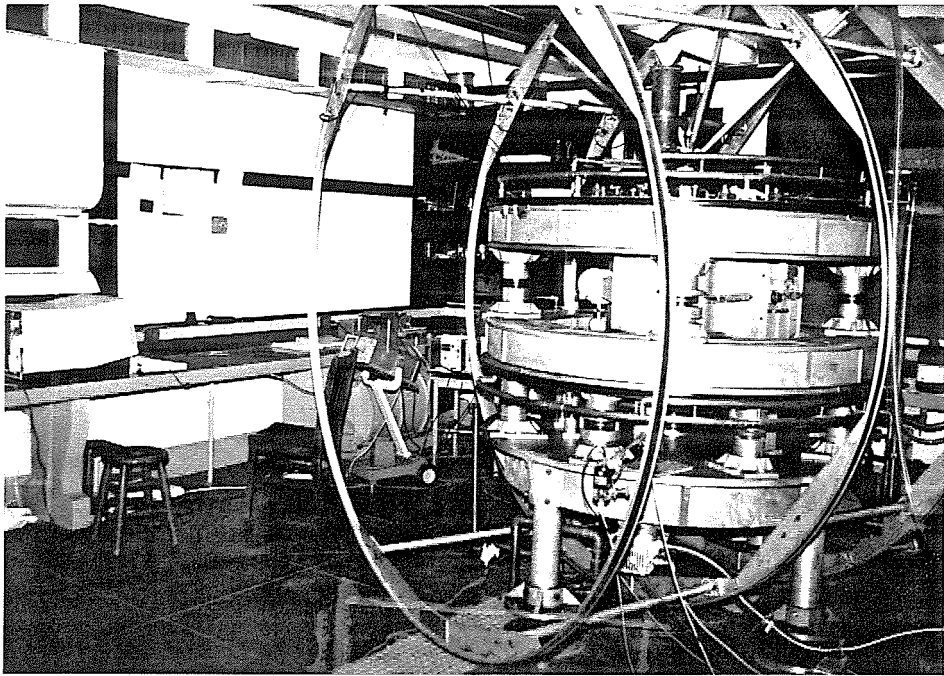


Figure 2-2. Picture of Caltech Spectrometer.

We employ the Caltech 35 cm radius  $\sqrt{2}\pi$  iron-free double-focusing beta spectrometer. For a discussion of beta spectrometer design and characteristics, see Siegbahn<sup>17</sup>. The spectrometer design is shown in Fig. 2-1, and a photograph is displayed in Fig. 2-2. In a double-focusing spectrometer the magnitude of the magnetic field (which is directed along the vertical) has a  $1/\sqrt{\rho}$  dependence, where  $\rho$  is the radial coordinate. This is accomplished by three sets of horizontal coils. The non-linear magnetic field bends the paths of electrons back towards the optic circle, so that all electrons meet at a focus after travelling  $\sqrt{2}\pi$  radians around the spectrometer. Shutters are employed to select a more narrow momentum distribution than that transmitted into the spectrometer and to serve as anti-scattering baffles, and the slit assembly

selects the electrons which hit the active region of the detector which is located at the focus of the spectrometer. For further detail on the beta spectrometer, see Ref. 18.

## 2.2 Source

Two radioactive sources,  $^{57}\text{Co}$  and  $^{35}\text{S}$ , were used for this experiment. The source dimensions are  $2\text{ mm} \times 20\text{ mm}$ , with the longer dimension in the vertical direction, i.e., the spectrometer was operated in the vertical mode. (In addition, a  $^{152}\text{Eu}$  source was used earlier in initial tests of the spectrometer and detector and to check the stability of the system.)

Ideally the source should be homogeneous and very thin to minimize energy loss in the source. Also the source backing should be very thin (and of low-Z material) to minimize backscattering in the foil. Previous experiments<sup>8-15</sup> employed sources which were deposited onto a foil. This can lead to crystallization of the source material, resulting in localized thick regions and correspondingly greater energy loss in the source. For this reason, we used vacuum deposition, which gives a uniform source thickness. The backing material must be metallic or metallized in order to prevent charging up of the source, which would alter the energy of the electrons being emitted into the spectrometer.

The sourceholder, designed to locate the source in the spectrometer to better than  $0.1\text{ mm}$ , is shown in Fig. 2-3. A  $1\text{ }\mu\text{m}$  thick Mylar foil was obtained from DuPont, stretched across an aluminum ring, epoxied in place and aluminized. A picture of a source foil is displayed in Fig. 2-4. The foil thickness was calculated<sup>19</sup> by measuring the energy loss of  $\alpha$ -particles from an  $^{241}\text{Am}$  source

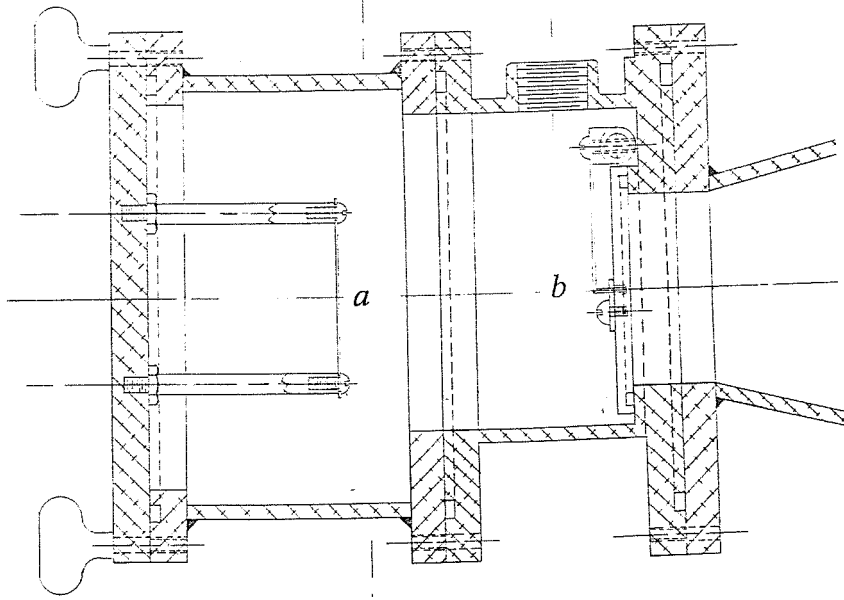


Figure 2-3. Schematic of sourceholder used in the spectrometer. The source is at *a*, and the vacuum shutter at *b*.

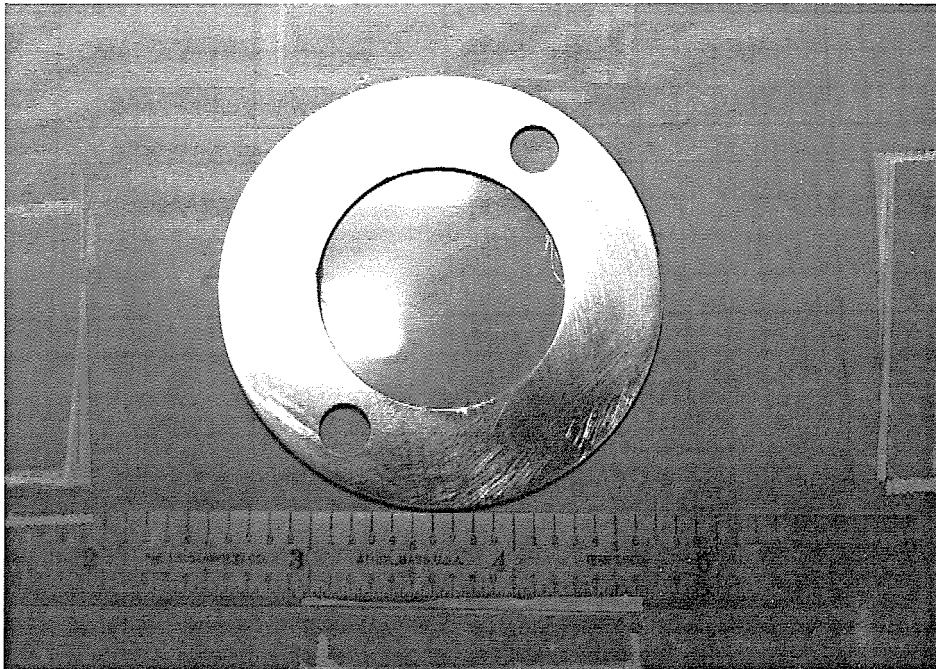


Figure 2-4. Picture of aluminum ring onto which is stretched a Mylar foil. The foil will be aluminized and then used as a backing for an evaporated source.



as they traverse the foil. The thickness of the Mylar backing is  $143 \pm 7 \mu\text{g}/\text{cm}^2$ , and the aluminum coating on the foil is less than  $20 \mu\text{g}/\text{cm}^2$  thick.

$^{57}\text{CoCl}_2$  was evaporated from a molybdenum boat which was carefully shaped to maximize the evaporation efficiency onto the foil in vacuum and used to calibrate the spectrometer and study its response function. 100 mCi of  $^{35}\text{S}$  in a  $\text{NH}_4(^{35}\text{SO}_4)_3$  aqueous solution were evaporated in vacuum from a tungsten boat onto a source foil, yielding a  $^{35}\text{S}$  source with an activity of about 2 mCi. The  $\text{NH}_4(^{35}\text{SO}_4)_3$  solution had a specific activity of 722 Ci/mmole, implying a source thickness of less than about  $1 \mu\text{g}/\text{cm}^2$  and an energy loss in the source of less than 3 eV. Further discussion of the quality of the evaporated sources is given in chapter 3.

### 2.3 Detector and Electronics

We chose to use a surface barrier detector in order to obtain good detector energy resolution (which assists in determining the count rate at a given momentum setting of the spectrometer) without extreme cooling of the detector, which can introduce instabilities as material is condensed onto the detector surface. Thus, a surface barrier detector ( $25 \text{ mm} \times 3 \text{ mm}$  (active area)  $\times 300 \mu\text{m}$  thick) was employed at the focus of the spectrometer. The detector is cooled using Peltier cooling to  $5^\circ\text{C}$ , which reduced the electronic noise width of the detector to 4.7 keV FWHM (Fig. 2-5). See chapter 3 for further discussion. An Ortec 142A preamplifier with the protection circuitry removed to improve the electronic noise is used to convert the charge signals to a voltage pulse, which is fed into a Canberra 2020 shaping amplifier. A BNC BH-1 precision pulser operated at 100 Hz is used to measure the dead time of the data acquisition system. The output from the amplifier and the pulser are fed into a

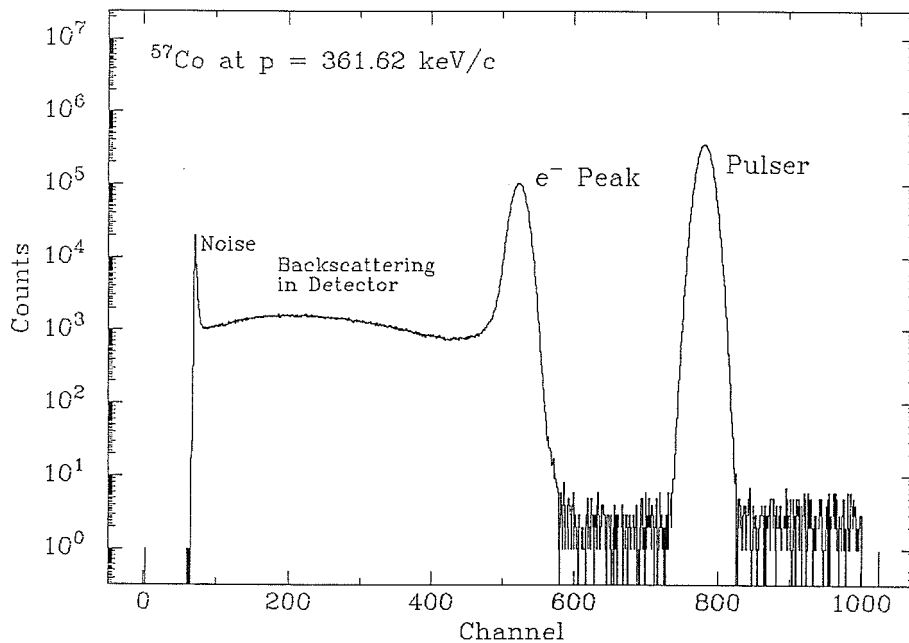


Figure 2-5.  $e^-$  spectrum (at  $p = 361.62$  keV/c,  $T = 115.01$  keV) from cooled surface barrier detector at the focus of the spectrometer using a  $^{57}\text{Co}$  source.

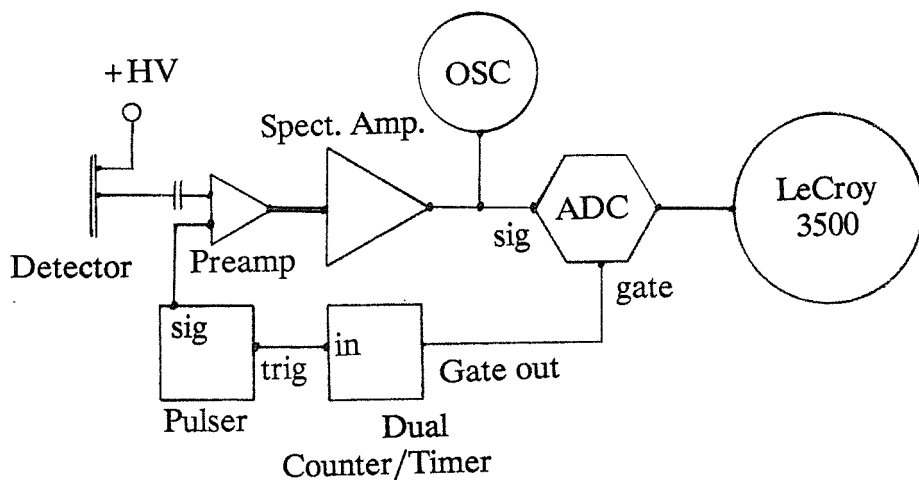


Figure 2-6. Schematic of spectrometer data acquisition system.

LeCroy 3500 used as a Multi-channel Analyzer which is gated by a counter/timer module. A schematic of the electronics system is shown in Fig. 2-6.

## 2.4 Power Supply and Stability

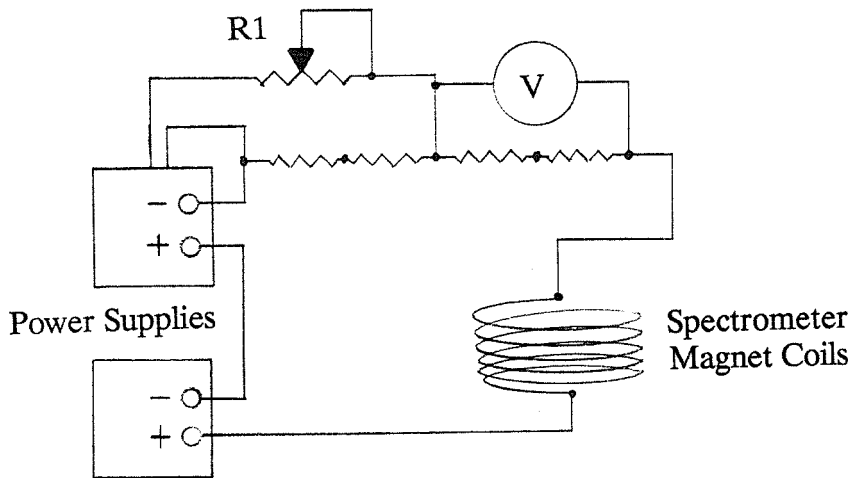


Figure 2-7. Schematic of power supply circuit for spectrometer magnet coils. R1 is actually an array of switches and precision resistors placed in an oil bath which allows the precise setting of the magnetic field.

Of critical concern in this experiment is the stability of the magnetic field and the detector. Because there is no simple way to directly measure the magnetic field ( $\leq 40$  G) in the spectrometer, one must rely on the correspondence between the current in the magnet coils and the magnetic field. In order to stabilize the current to about  $10^{-5}$ , two Kepco power supplies were used, one with a feedback loop to adjust the current. The schematic for the power supply

and current monitoring circuit is given in Fig. 2-7. Two temperature stable resistors ( $0.05 \Omega$ , 100 W) were used to set the current level with a feedback switch resistor, and the voltage drop across a separate pair of resistors was measured with a digital voltmeter (accuracy  $3 \times 10^{-5}$ ) to determine the current in the magnet coils. The switch resistors were placed in an oil bath and the sensing resistors were mounted to a large copper block, the temperature of which is monitored by a platinum resistor. The temperature in the magnet coils, also cooled by an oil bath, is similarly monitored.

In order to verify the stability of the system, the spectrometer was set to about the 50% point of the K-electron conversion line in  $^{57}\text{Co}$  at 385.9 keV/c. At this point, the steep slope of the conversion line amplifies a change in magnetic field, e.g., a change of  $10^{-5}$  in magnetic field produces a change of about 1% of the count rate into the detector.

Fig. 2-8 shows the count rate measured for a half an hour as a function of time at this value of momentum. After a two hour warm-up period, any large variation in count rate can also be seen as a drift in current in the magnet coils; no additional "hidden" instabilities such as changing coil dimensions or sensing resistor warm-up can be seen. The remaining variation, mainly due to offset voltage variations of the regulating op amp are within  $\pm 1.5 \times 10^{-5}$  and can be compensated, if necessary, by manually adjusting the current.

## 2.5 Spectrometer Settings

Five parameters must be determined for the spectrometer: the shutter horizontal and vertical openings, the slit assembly position, and the slit assembly horizontal and vertical openings. These must be set in such a way as to

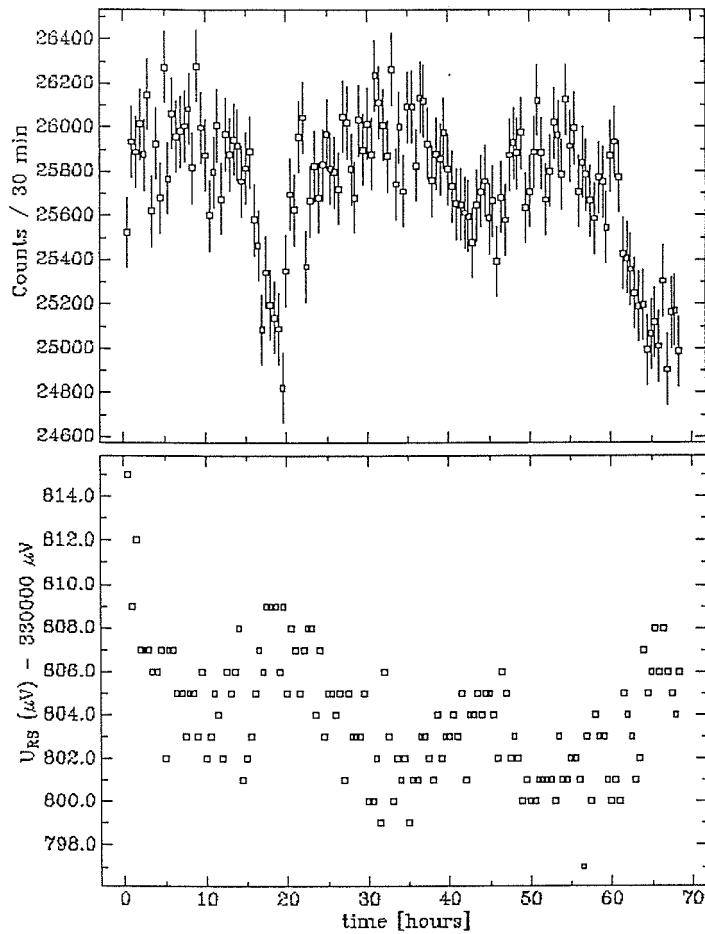


Figure 2-8. Current and count rate as a function of time.

provide a compromise between maximum transmission and good energy resolution, as well as minimum backscattering in the detector. For all of the following the spectrometer was tuned to the momentum of the 129.4 keV K-conversion electron line in  $^{57}\text{Co}$ .

First, the slit assembly was centered by scanning its horizontal position across the detector fixed at the spectrometer focus, with the magnetic field held constant. This was done for several values of the magnetic field, with the position of maximum transmission noted in each case. Fig. 2-9a shows the choice of slit position. One must remeasure at several values of the magnetic

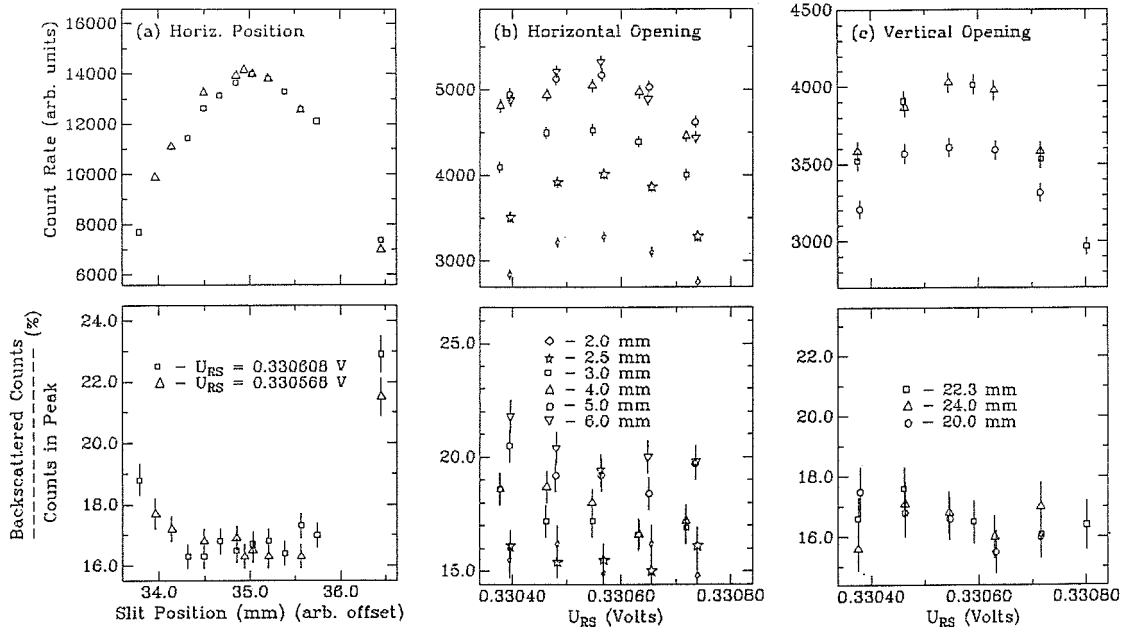


Figure 2-9. Determination of slit assembly settings. (a) Position: The region of low backscattering shows where the active region of the detector is, and the symmetric counting rate shows that the magnetic field is set to the peak of the conversion line for the placement of the detector. The slit position chosen was 34.93 mm. (b) Horizontal width: 2.5 mm was chosen as the opening which optimized the count rate with a low level of backscattering in the detector. (c) Vertical width: Similarly, 23 mm was chosen to maximize the count rate while maintaining a low level of detector backscattering.

field since the spectrometer focus moves with magnetic field.

In choosing the horizontal width opening, a similar procedure of measuring the conversion electron peak at different width settings was followed, and the setting that optimized transmission with minimum lower energy counts in the detector (which indicate that electrons are hitting the detector outside its active region) was chosen, Fig. 2-9b. The vertical width was similarly selected. The horizontal width is 0.5 mm wider than the source dimension, and the

vertical width is 3 mm wider than the source dimension, but both are narrower than the detector active area.

The shutters were opened to 9.3 cm horizontal opening and 25.2 cm vertical opening. This was a compromise between spectrometer resolution and scattering and the transmission of the spectrometer, Fig. 2-10.

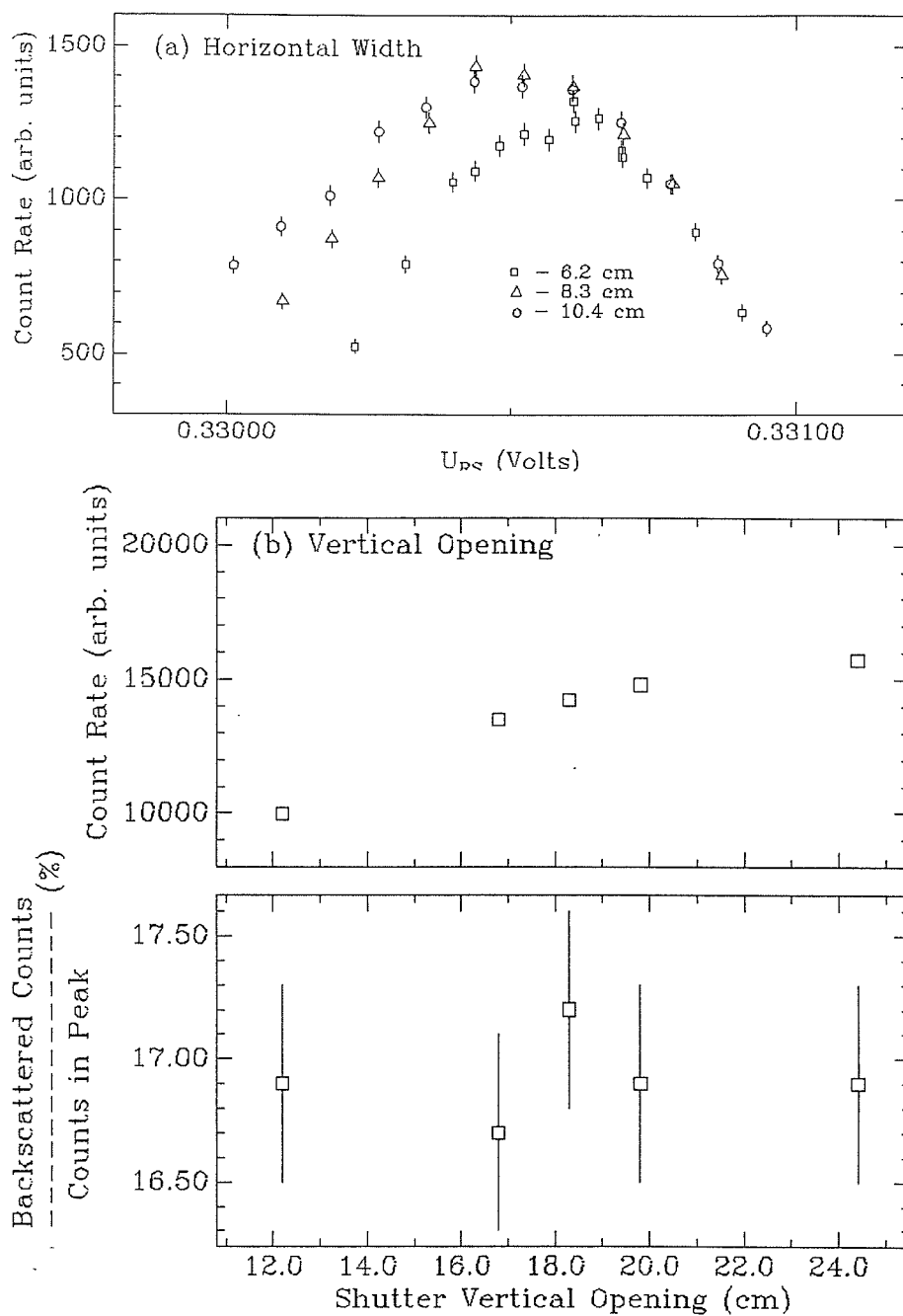


Figure 2-10. Determination of shutter openings. (a) The horizontal width is set to 9.3 cm which gives good transmission and fair momentum resolution. (See Fig. 3-3.) (b) Opening the vertical shutters slightly increased the transmission without affecting the resolution, so the spectrometer was operated at the maximum shutter vertical opening (25.2 cm).



## 2.6 Earth Field

The large set of four outer coils may be used to cancel the horizontal component of the earth's magnetic field. The resolution of the spectrometer was checked with and without the earth's field cancelled, and there was no improvement in the spectrometer resolution. Because of this, and in order not to introduce additional uncertainties, we chose not to cancel the earth's field. The vertical component of the earth's field will add a small offset to the momentum calibration of the spectrometer.

## CHAPTER THREE

### Data

#### 3.1 Calibration

$^{57}\text{Co}$  spectra were acquired at 139 different momentum settings to calibrate the spectrometer and measure its electron response function as well as the quality of the source. An example detector spectrum is shown in Fig. 3-1. The fraction of the spectrum contained in the backscattering tail (at 115 keV) is 21%. This is in fair agreement with data obtained with a surface barrier detector in a circular geometry by Planskoy<sup>20</sup>.

In order to determine the count rate at a given spectrometer momentum setting, we fit the  $e^-$  peak in the detector spectrum to a Gaussian peak with a linear backscattering tail which falls to zero under the peak:

$$y(x) = \frac{A}{\sqrt{2\pi\sigma^2}} e^{-\frac{(x-\mu)^2}{2\sigma^2}} + \begin{cases} a+bx, & x \leq -a/b \\ 0, & x > -a/b \end{cases} \quad (3-1)$$

Fig. 3-2 shows an example fit to the peak of a detector spectrum. The parameter  $A$  and its fit uncertainty (divided by acquisition time) give the count rate and its uncertainty. Fitting only the peak sacrifices some statistical accuracy but avoids difficulties in characterizing the scattering in the spectrometer for different incident electron energies.

Finally, to ensure the stability of the source, two spectra were acquired at the same momentum two days apart with high accuracy. The fall off in the

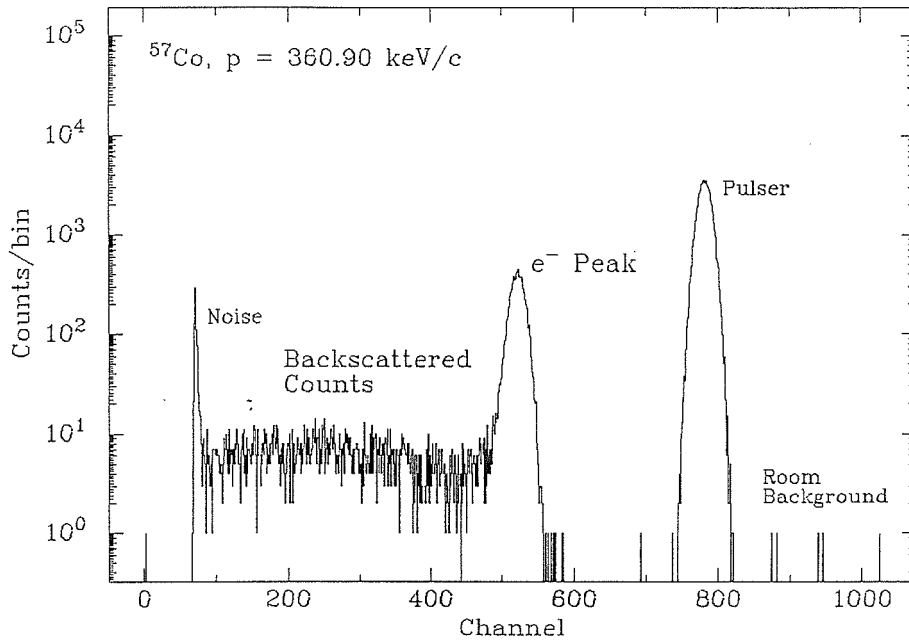


Figure 3-1. Typical detector  $e^-$  spectrum.

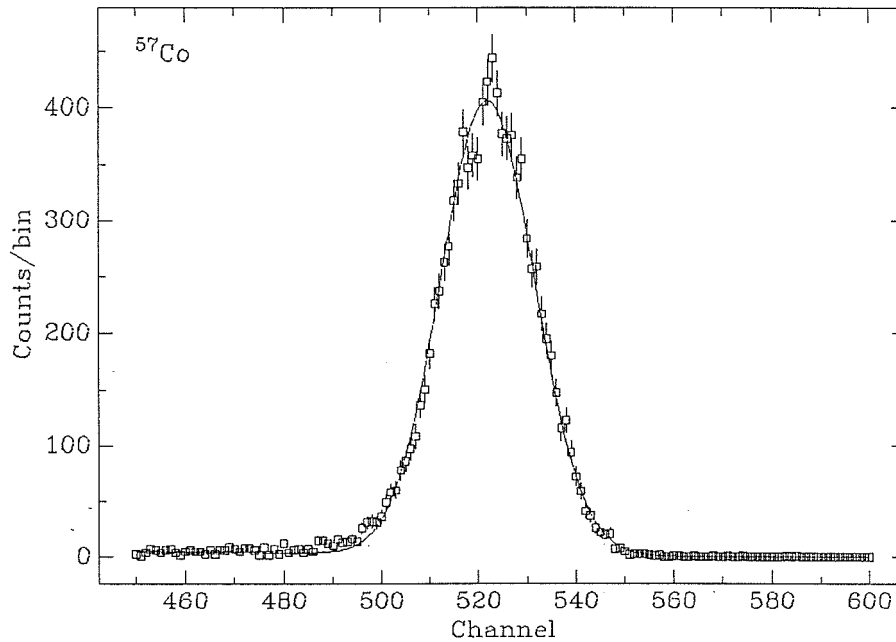


Figure 3-2. Fit of (3-1) to  $e^-$  peak in spectrum of Fig. 3-1.

count rate of the  $^{57}\text{Co}$  source was negligible over the measurement time period compared to the statistical accuracy required for the calibration. Thus, no correction for source stability was required.

Fig. 3-3 shows the  $^{57}\text{Co}$  spectrum calibration for the spectrometer. The response function is approximated by a Gaussian with an exponential tail superimposed on a linear background:

$$y(x) = \frac{\mu}{x}(a+bx) + \frac{\mu}{x} \times \begin{cases} H e^{-\frac{(x-\mu)^2}{2\sigma^2}}, & x \geq x_0, \\ H e^{-\frac{(x_0-\mu)^2}{2\sigma^2}} e^{-\frac{x-x_0}{\lambda}}, & x < x_0, \end{cases} \quad (3-2)$$

where  $\mu$  is the centroid of the response function and  $x_0$  is the point at which the function changes from being exponential to Gaussian. The best fit for this point was at the lower momentum half-maximum rate in each case. The calibration of the spectrometer was accomplished using the centroids,  $\mu$ , of the two K-conversion lines.

The resolution  $\Delta p/p$  is a constant function of  $p$  for a  $\beta$ -spectrometer. Thus,  $\sigma$  and  $\lambda$  both scale with  $p$ :

$$\frac{\lambda_2}{\lambda_1} \approx \frac{\sigma_2}{\sigma_1} \approx \frac{p_2}{p_1}. \quad (3-3)$$

Since the acceptance increases with momentum, the count rate for a given spectrometer momentum selection must be normalized by its momentum to recover a true  $\beta$ -spectrum shape. The response function for the spectrometer is (3-2), where, for  $p$  in keV/c:

$$\begin{aligned} \lambda &= 0.0011 \times p \\ \sigma &= 0.0012 \times p \end{aligned} \quad (3-4)$$

and the energy resolution is thus about 0.27% FWHM.

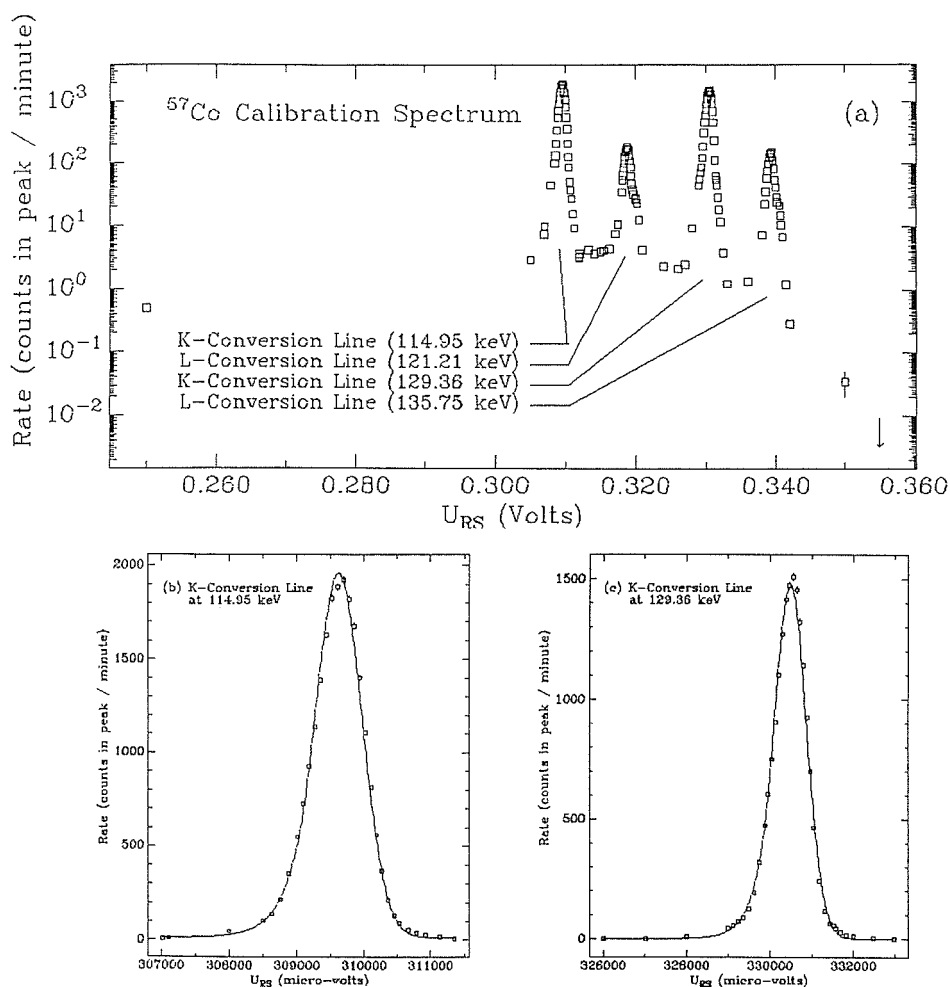


Figure 3-3. (a) Calibration spectrum of  $^{57}\text{Co}$ . The fits (a) and (b) for the K-lines are from (3-2), and are used to determine the calibration of the spectrometer.

Spectra taken at momenta between those of the conversion lines showed two  $e^-$  peaks in the detector. (Fig. 3-4.) This is due to scattering of the electrons from the conversion-electron peaks in the spectrometer. Using the energy information of the surface barrier detector, we can determine the relative contribution to the low energy tail of the response function of scattering in the spectrometer and scattering or energy loss in the source. The result of this analysis is that scattering in the detector is less than 0.1% of the count rate at the peak, and scattering or energy loss in the source is not observable at the

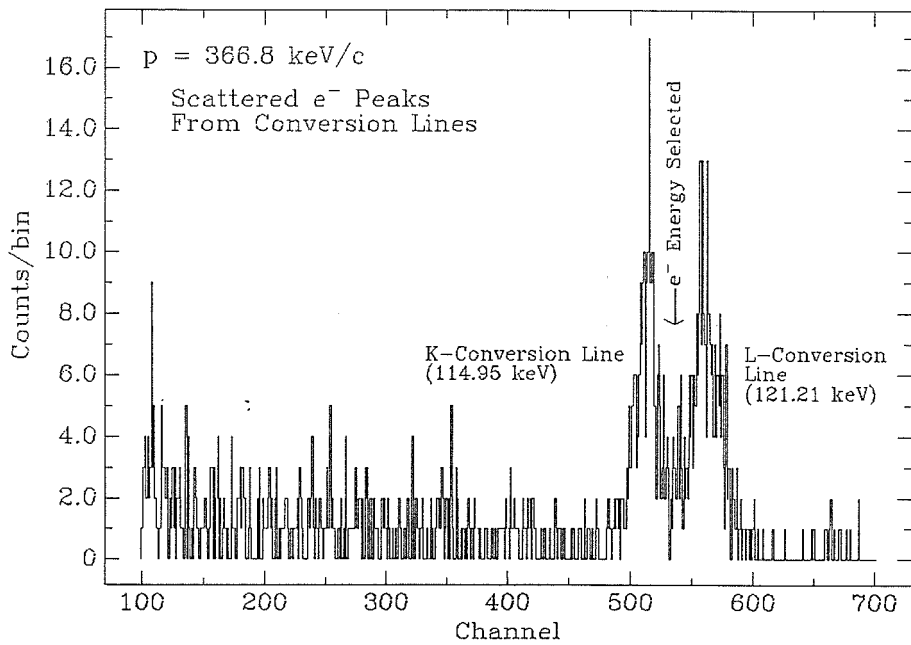


Figure 3-4. Spectrum taken at a momentum value (366.8 keV/c) between those of the conversion-electron lines in  $^{57}\text{Co}$ . The spectrum shows two peaks, indicating scattering of conversion electrons in the spectrometer.

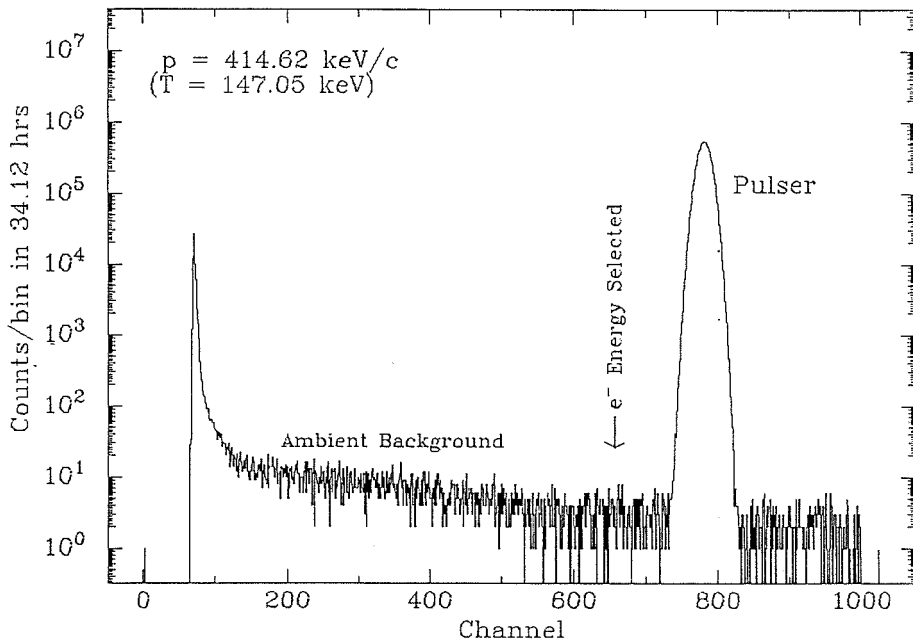


Figure 3-5. Spectrum taken at  $p = 414.6$  keV/c.

level of 0.01% of the count rate at the peak. We measured the background in the detector at a momentum setting of 414.62 keV/c, above the highest conversion line of the  $^{57}\text{Co}$  spectrum. The absence of a peak in this spectrum (Fig. 3-5) shows that no electrons are getting through the spectrometer at this momentum; the spectrum is purely ambient background, and the contribution to higher energies of electrons emitted with a given energy is less than 0.02%; i.e., if the entire count rate of the  $^{35}\text{S}$  source were somehow emitted with an energy of 136 keV, then the intensity at 150 keV of those electrons would contribute an equal share of counts as the normal intensity of the electrons emitted with 150 keV. Thus, contributions to each spectrum from lower momentum electrons will be negligible in the case of the  $^{35}\text{S}$  spectrum.

### 3.2 $^{35}\text{S}$ Spectrum

Preliminary data have been acquired using a 2 mCi  $^{35}\text{S}$  source. A minimum of  $10^5$  counts were accumulated in the  $e^-$  peak of the detector spectrum for each momentum setting. The data have been corrected for dead time as measured by the pulser and for the decay of  $^{35}\text{S}$ , and have been normalized by their momentum. For each datum the current in the spectrometer magnet coils was recorded continuously during the run. A sample detector spectrum from this data set is shown in Fig. 3-6. The count rate was estimated from the spectrum by summing over bins from 80% of the centroid to well-above the centroid. The data are plotted in Fig. 3-7a.

Fig. 3-7b shows the count rate as a function of time at the momentum setting of maximum emission from the  $^{35}\text{S}$  source. The count rate at this point, being a local extremum, is insensitive to changes in the magnetic field, and was used to monitor the source itself. Within the statistical accuracy of the data,

the source was stable (after correcting for the tabulated decay half-life of 87.4 days and correcting for the dead time measured by the pulser) during the time the data were acquired.



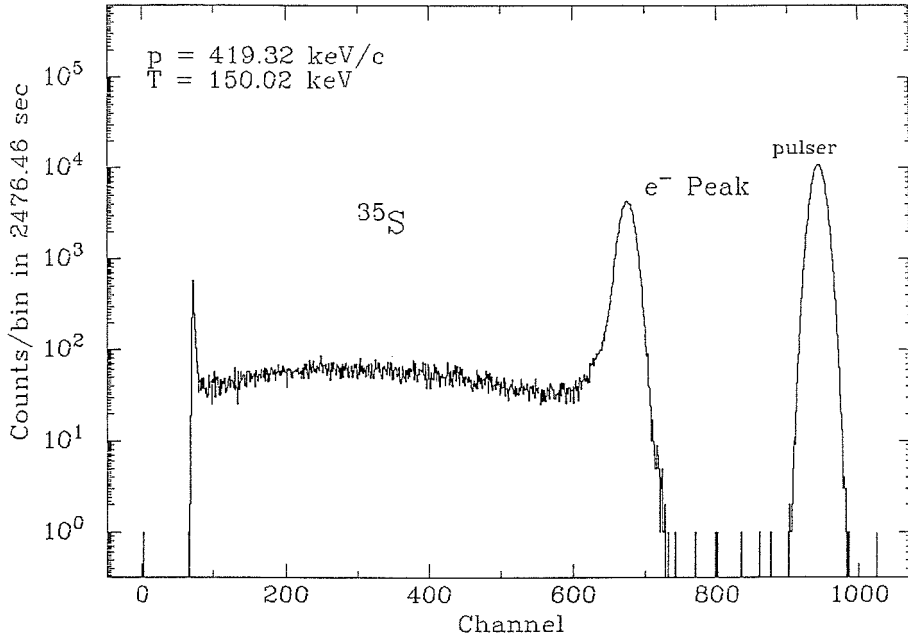


Figure 3-6. Example surface barrier detector spectrum of  $^{35}\text{S}$  for  $p = 419.32 \text{ keV/c}$ .

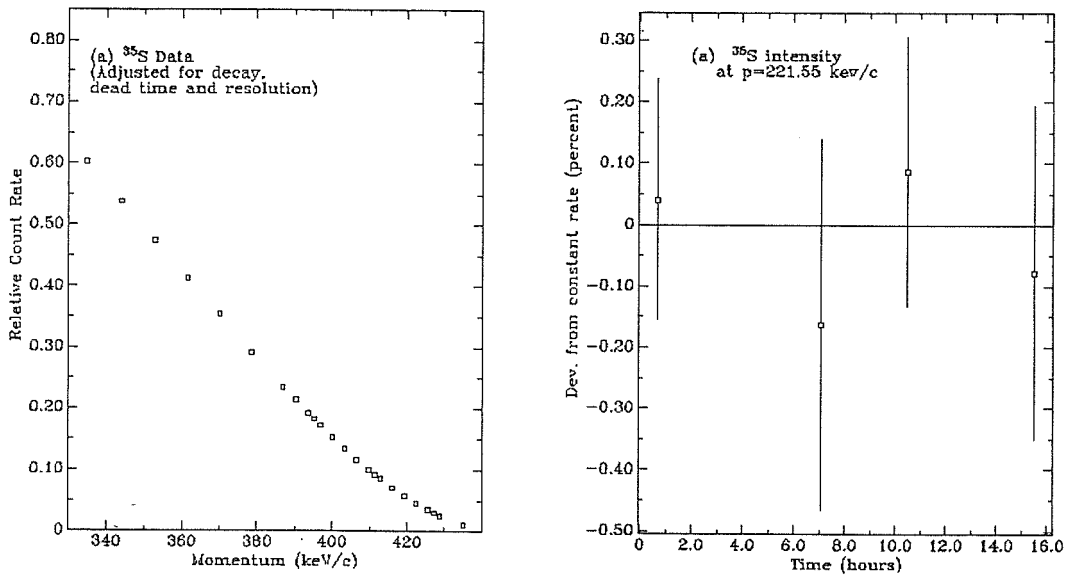


Figure 3-7. (a)  $\beta$ -spectrum of  $^{35}\text{S}$ . These data have been corrected for dead time, the decay of  $^{35}\text{S}$  ( $\tau_{1/2} = 87.4$  days) and the linear increase in resolution with momentum. (b) The count rate at the spectrum maximum ( $p = 221.55 \text{ keV/c}$ ) is stable within the statistical accuracy of the data for the duration of the period in which the data in (a) were acquired.

## CHAPTER FOUR

### Discussion

In this chapter I present a preliminary consistency check of the  $\beta$ -spectrum data in chapter 3 and provide a synopsis of how the data coming from this experiment will be analyzed. The chapter is concluded with a summary of what precision we expect to be able to achieve with the present apparatus.

#### 4.1 Discussion of Data

Fig. 4-1a shows a Kurie plot (1-2) of the data in chapter 3 fit to a straight line ( $\chi_{\text{red}}^2 = 1.1$ ), and Fig. 4-1b, the residual plot of the fit. The Q-value obtained from this plot is  $167.17 \pm 0.12$  keV (error bar from fit uncertainty only). The accepted Q-value of the  $^{35}\text{S}$   $\beta$ -decay from the tables of Wapstra and Audi<sup>21</sup> is  $166.68 \pm 0.2$  keV, signalling some systematic bias in the data, to be discussed below. Fig. 4-1b shows the approximate sensitivity of the data to a threshold effect. The statistical accuracy of the data is such that they should be sensitive to an admixture of greater than 0.6%. However, Fig. 4-1b itself does not exclude such an admixture. The solid curve in Fig. 4-1b shows the magnitude of Simpson's threshold effect compared to the statistical accuracy of the data, but does not constitute a fit to the data. The data have not been corrected for the effect of backscattering in the detector, which causes the fraction of events recorded in the  $e^-$  peak to be a function of energy, albeit a slowly varying one in the range of energies observed in the present experiment. In addition, the count rate from the detector spectra was calculated by

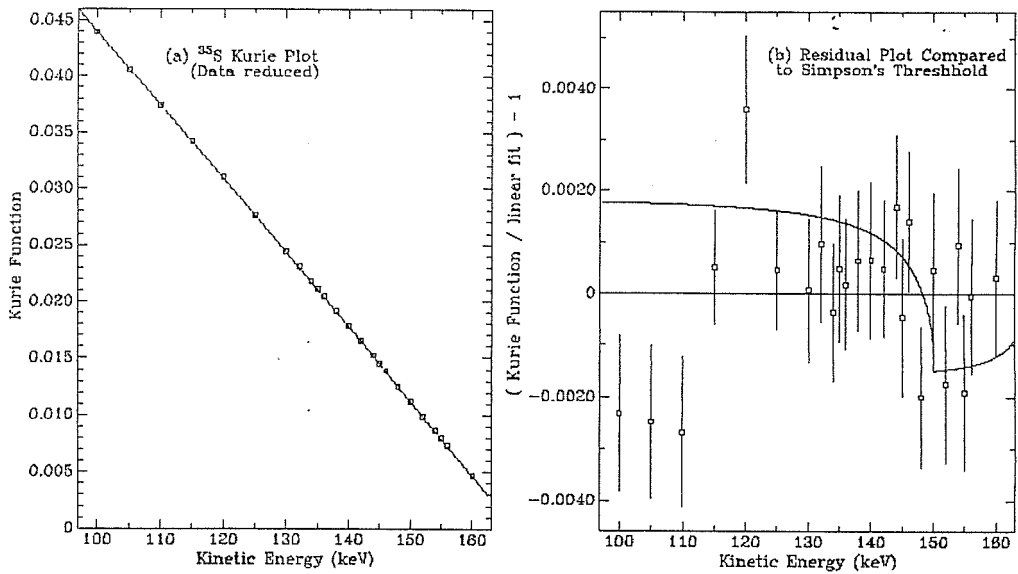


Figure 4-1. (a) The Kurie plot of data is fit ( $\chi^2_{\text{red}}$ ) to a straight line. The zero-count rate intercept is  $167.17 \pm 0.12$  keV. (b) The residual plot from (a). The statistical accuracy of the data is such that Simpson's threshold effect (solid curve) of 0.7% should be just visible, but cannot be excluded at a significant confidence level.

summing the data from 80% of the  $e^-$  peak centroid energy to an energy well above the centroid. Although the rate determined in this way is not sensitive to the upper integration limit (the background for these runs was negligible), it is very sensitive to the lower limit of integration, since count rate in the tail of the  $e^-$  peak is significant. This method undoubtedly introduces a systematic bias into the data, and a more systematic method will be used in the final data analysis. When these corrections are included, some experimental shape function which takes this and the exact response function of the spectrometer into account may be required to recover a straight line Kurie plot for the adjusted data. Thus, it appears that these two effects (systematic bias from count rate

determination method and fraction of events recorded in  $e^-$  peak) compensate each other, giving a linear Kurie plot with an offset  $Q$ -value. To place a limit on the admixture of a massive neutrino in this spectrum, a fitting procedure described in the next section must be performed.

## 4.2 Analysis Procedure

This section describes the analysis procedure we will employ for the data coming from this experiment. In order to compare the data to the theoretical spectrum, (1-4), we will convolute the theoretical spectrum with the response function of the detector:

$$\frac{dN^c}{dp}(p) = \int_0^{p(T_e=Q)} \frac{dN}{dp}(p') \times R(p-p') dp', \quad (4-1)$$

where the response function of the spectrometer,  $R(p)$ , is given by (3-2) (without the linear term) and (3-4), and may also include a polynomial shape function.

In a fit three parameters, the  $Q$ -value, the spectrum normalization and the massive neutrino admixture, will be varied for each value of the neutrino mass tested. In addition, shape function parameters may also be used and will be allowed to vary in the fit. It should be noted that although the shape parameters can drastically alter the shape of the spectrum, they can only do this in a slowly varying way, and cannot disguise a threshold effect if the data in a short energy range around  $Q-m_\nu$  are fit. For example, Fig. 4-2 shows the effect of a huge shape function on a simulated  $^{35}\text{S}$   $\beta$ -spectrum with a 17 keV neutrino admixed at the 0.5% level. Although the ratio of “experimental” data to the theoretical spectrum fit in this case has a huge variation over a large energy

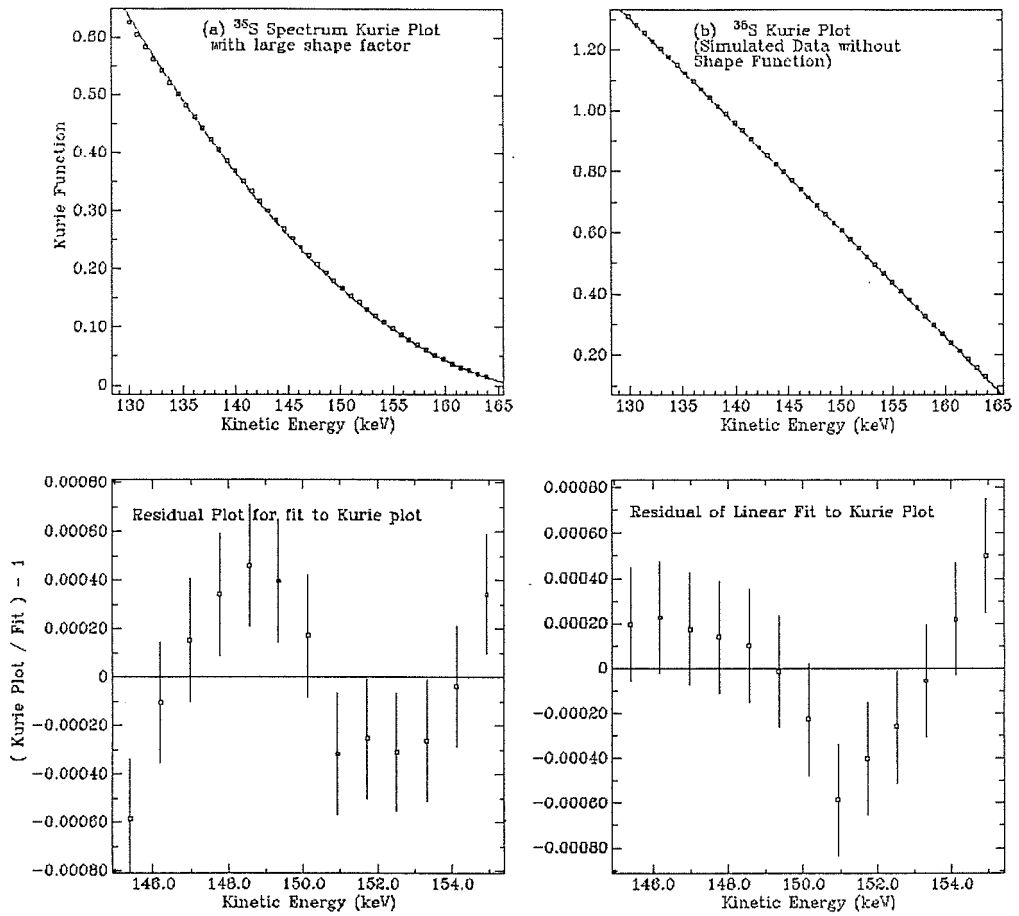


Figure 4-2. (a) Above, Kurie plot, and below, comparison (1-5) of calculated (error bars illustrate an uncertainty of 0.05% per datum)  $^{35}\text{S}$   $\beta$ -spectrum which includes a huge shape factor and a 0.5% admixture of a 17 keV neutrino to the theoretical spectrum with no such admixture. The quadratic shape factor used in this example varies 50 times more rapidly over the energy range 130-160 keV than that used by Altitzoglou<sup>12</sup> *et al.* The Kurie plot is fit to a quadratic function. (b) The same comparison for the calculated spectrum with no shape factor. The Kurie plot is fit to a line. Even with a large shape factor, the threshold effect is visible if a narrow energy range of data is selected.

range, the threshold effect is still visible if a narrow energy range is selected.

Once a best-fit value of the admixture is determined for the data, the magnitude of the admixture will be scanned through nearby (fixed) values while refitting the spectrum with all of the other parameters allowed to vary.  $\chi^2$  will be determined for each of these fits, and the error bar on the value (or upper limit) of the admixture will be calculated based on the variation of  $\chi^2$  around the best fit value.

### 4.3 Outlook

Initial data have been obtained at a lower statistical accuracy, and show that the  $^{35}\text{S}$  spectrum obtained with the source in the spectrometer is at least approximately consistent with the theoretical shape of the allowed spectrum. The data analysis software for this experiment has been written and debugged with simulated  $^{35}\text{S}$  spectra. Data runs with about three times the statistical accuracy of the data presented here are in progress, and should be sufficient to confirm or exclude the existence of the 17 keV neutrino Simpson claims to have observed.

## References (Part II)

- <sup>1</sup> F. Boehm and P. Vogel, *Physics of Massive Neutrinos* (Cambridge University Press, Cambridge, 1987).
- <sup>2</sup> W. Pauli, *Letter to the Physical Society of Tübingen*, unpublished; reproduced in L.M. Brown, *Physics Today*, **31**, 23 (1978).
- <sup>3</sup> C.S. Wu and S.A. Moszkowski, *Beta Decay* (Interscience, New York, 1966).
- <sup>4</sup> V. Lubimov in *86 Massive Neutrinos in Astrophysics and Particle Physics, Proc. 6th Moriond Workshop*, eds. O. Fackler and J. Tran Thanh Van, p. 441 (Paris: Editions Frontieres, 1986).
- <sup>5</sup> R. Robertson in *Fundamental Symmetries in Nuclei and Particles*, eds. H. Henrikson and P. Vogel, p. 86 (World Scientific, Singapore, 1990).
- <sup>6</sup> J.J. Simpson, *Phys. Rev. Lett.* **54**, 1891 (1985).
- <sup>7</sup> J.J. Simpson, *Phys. Rev.* **D39**, 1837 (1989).
- <sup>8</sup> J.J. Simpson, *Phys. Rev.* **D39**, 1825 (1989).
- <sup>9</sup> V. Datar, C. Baba, S. Bhattacharjee, C. Bhuinya and A. Roy, in a letter to *Nature* **318**, 547 (1985).
- <sup>10</sup> T. Ohi, M. Nakajima, H. Tamura, T. Matsuzaki, T. Yamazaki, O. Hashimoto and R. Hayano, *Phys. Lett.* **160B**, 322 (1985).
- <sup>11</sup> A. Apalikov, S. Boris, A. Golutvin, L. Laptin, V. Lyubimov, N. Myasoedov, V. Nagovitsyn, E. Novikov, V. Nozik, V. Soloshchenko, I. Tikhomirov and E. Tret'yakov, *Pis'ma Zh. Eksp. Teor. Fiz.* **42**, 233 (1985) [*JETP Lett.* **42**, 289

(1985)].

- <sup>12</sup> T. Altitzoglou, F. Calaprice, M. Dewey, M. Lowry, L. Piilonen, J. Brorson, S. Hagen and F. Loeser, *Phys. Rev. Lett.* **55**, 799 (1985).
- <sup>13</sup> J. Markey and F. Boehm, *Phys. Rev.* **C32**, 2215 (1985).
- <sup>14</sup> D. Hetherington, R. Graham, M. Lone, J. Geiger and G. Lee-Whiting, *Phys. Rev.* **C36**, 1504 (1987).
- <sup>15</sup> D. Wark and F. Boehm in *Nuclear Beta Decays and Neutrino*, Proc. Int'l. Sym. Osaka, Japan, June 1986, eds. T. Kotani, H. Ejiri and E. Takasugi (World Scientific, Singapore 1986).
- <sup>16</sup> C. Lederer and V. Shirley, *Table of Isotopes* (Wiley, New York, 1978).
- <sup>17</sup> K. Siegbahn in *Alpha-, Beta- and Gamma-Ray Spectroscopy*, vol. 1, ed. by K. Siegbahn, 79 (North-Holland, Amsterdam, 1965).
- <sup>18</sup> P. Alexander, J. DuMond and H. Henrikson, "Design and Construction of a 35 cm Radius  $\sqrt{2}\pi$  Iron-Free Beta Spectrometer," (unpublished) (1964).
- <sup>19</sup> L. Northcliffe and R. Schilling, *Nucl. Data Tables* **A7**, 233 (1970).
- <sup>20</sup> B. Planskoy, *Nucl. Instrum. Methods* **61**, 285 (1968).
- <sup>21</sup> A. Wapstra and G. Audi, *Nucl. Phys.* **A432**, 1 (1985).